

AD A074700

LEVEL

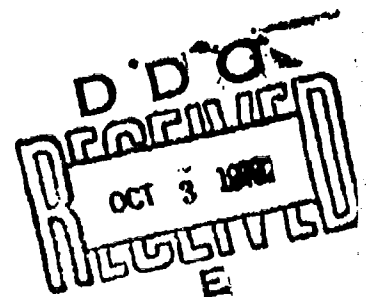
Bulletin 49
(Part 2 of 3 Parts)

THE SHOCK AND VIBRATION BULLETIN

Part 2
Modal and Impedance Analysis,
Human Response to Vibration and Shock,
Isolation and Damping, Dynamic Analysis

SEPTEMBER 1979

A Publication of
THE SHOCK AND VIBRATION
INFORMATION CENTER
Naval Research Laboratory, Washington, D.C.



Office of
The Director of Defense
Research and Engineering

Approved for public release; distribution unlimited.

DDC FILE COPY

79 10 01 009

SYMPOSIUM MANAGEMENT

THE SHOCK AND VIBRATION INFORMATION CENTER

Henry C. Pusey, Director

Rudolph H. Volin

J. Gordan Showalter

Barbara Szymanski

Carol Healey

Bulletin Production

**Graphic Arts Branch, Technical Information Division,
Naval Research Laboratory**

PAGES _____
ARE
MISSING
IN
ORIGINAL
DOCUMENT

Bulletin 49
(Part 2 of 3 Parts)

THE SHOCK AND VIBRATION BULLETIN

SEPTEMBER 1979

A Publication of
**THE SHOCK AND VIBRATION
INFORMATION CENTER**
Naval Research Laboratory, Washington, D.C.

The 49th Symposium on Shock and Vibration was held at the International Inn, Washington, DC on October 17-19, 1978. The NASA Goddard Space Flight Center, Greenbelt, Maryland, was the host.

Office of
The Director of Defense
Research and Engineering

CONTENTS

Accession For	NTIS GRA&I	DOC TAB	Unannounced	Justification
By				
Distribution/				
Availability Codes				
Dist.				
Avail and/or special				

PAPERS APPEARING IN PART 2

MODAL AND IMPEDANCE ANALYSIS

AN IMPEDANCE TECHNIQUE FOR DETERMINING LOW FREQUENCY PAYLOAD ENVIRONMENTS	1
K.R. Payne, Martin Marietta Corporation, Denver, CO	
A STATISTICAL LOOK AT MODAL DISPLACEMENT RESPONSE TO SEQUENTIAL EXCITATIONS	15
W.J. Kacena, Martin Marietta Corporation, Denver, CO	
ON DETERMINING THE NUMBER OF DOMINANT MODES IN SINUSOIDAL STRUCTURAL RESPONSE	19
W.L. Hallauer, Jr., and A. Franck, Department of Aerospace and Ocean Engineering, Virginia Polytechnic Institute and State University, Blacksburg, VA	
LATERAL AND TILT WHIRL MODES OF FLEXIBLY MOUNTED FLYWHEEL SYSTEMS	35
C.W. Bert and T.L.C. Chen, School of Aerospace, Mechanical and Nuclear Engineering, The University of Oklahoma, Norman, OK	

HUMAN RESPONSE TO VIBRATION AND SHOCK

WHOLE-BODY VIBRATION OF HEAVY EQUIPMENT OPERATORS	47
D.E. Wasserman, W.C. Asbury, and T.E. Doyle, National Institute for Occupational Safety and Health, Cincinnati, OH	
RESEARCH RELATED TO THE EXPANSION AND IMPROVEMENT OF HUMAN VIBRATION EXPOSURE CRITERIA	69
R.W. Shoenberger, Aerospace Medical Research Laboratory, Aerospace Medical Division, Wright-Patterson AFB, OH	

ISOLATION AND DAMPING

COMPUTER AIDED DESIGN OF PASSIVE VIBRATION ISOLATORS FOR AIRBORNE ELECTRO-OPTICAL SYSTEMS	81
P.W. Whaley, Air Force Institute of Technology, Wright-Patterson AFB, OH and J. Pearson, Air Force Flight Dynamics Laboratory, Wright-Patterson AFB, OH	
DESIGN OF TURBINE BLADES FOR EFFECTIVE SLIP DAMPING AT HIGH ROTATIONAL SPEEDS	87
D.I.G. Jones, Air Force Materials Laboratory, Wright-Patterson AFB, OH and A. Muszynska, Institute of Fundamental Technological Research, Polish Academy of Sciences, Warsaw, Poland	
A SIMPLE LOW-COST TECHNIQUE FOR MEASURING MATERIAL DAMPING BEHAVIOR	97
D.I.G. Jones, Air Force Materials Laboratory, Wright-Patterson AFB, OH	
THE EFFECTS OF FREQUENCY, AMPLITUDE, AND LOAD ON THE DYNAMIC PROPERTIES OF ELASTOMERS	105
J.E. Cole, III, Cambridge Acoustical Associates, Inc., Cambridge, MA	
LIQUID SPRING SHOCK ISOLATOR MODELING BY SYSTEM IDENTIFICATION	119
P.H. Sonnenburg, B.H. Wendler, and W.E. Fisher, The U.S. Army Corps of Engineers, Construction Engineering Research Laboratory, Champaign, IL	
A GENERALIZED DERIVATIVE MODEL FOR AN ELASTOMER DAMPER	135
R.L. Bagley and P.J. Torvik, Air Force Institute of Technology, Wright-Patterson AFB, OH	

SHOCK RESPONSE OF NON-LINEAR SYSTEMS	146
K. Peleg, School of Packaging, Michigan State University, East Lansing, MI	

DYNAMIC ANALYSIS

STABILITY ANALYSIS AND RESPONSE CHARACTERISTICS OF TWO-DEGREE OF FREEDOM NONLINEAR SYSTEMS	159
M. Subudhi and J.R. Curreri, Brookhaven National Laboratory, Upton, NY	
APPLICATION OF RANDOM TIME DOMAIN ANALYSIS TO DYNAMIC FLIGHT MEASUREMENTS	165
S.R. Ibrahim, Department of Mechanical Engineering and Mechanics, Old Dominion University, Norfolk, VA	
SHOCK SPECTRA DESIGN METHODS FOR EQUIPMENT-STRUCTURE SYSTEMS	171
J.M. Kelly and J.L. Sackman, University of California, Berkeley, Berkeley, CA	
A COMPUTATIONAL MODEL DESCRIBING THE INITIATION OF SILVER ACETYLIDE-SILVER NITRATE EXPLOSIVE BY AN INTENSE LIGHT SOURCE	177
F.H. Mathews, Sandia Laboratories, Albuquerque, NM	
TERMINAL VELOCITY AND ROTATION RATE OF A FLYER PLATE PROPELLED BY A TUBE-CONFINED EXPLOSIVE CHARGE	193
R.A. Benham, Sandia Laboratories, Albuquerque, NM	
A STABILITY THEOREM FOR A DYNAMICALLY LOADED LINEAR VISCOELASTIC STRUCTURE	203
D.W. Nicholson, Naval Surface Weapons Center, White Oak, Silver Spring, MD	
ANALOG DOUBLE INTEGRATION OF SHOCK PULSES	209
K. Peleg, School of Packaging, Michigan State University, East Lansing, MI and R.A. Lund, MTS Systems Corporation, Minneapolis, MN	

PAPERS APPEARING IN PART 1

FOREWORD

Henry C. Pusey, Director, Shock and Vibration Information Center, Naval Research Laboratory, Washington, DC

INVITED PAPERS

- THE DYNAMICS OF THE DOD SCIENCE AND TECHNOLOGY PROGRAM
Dr. George P. Milburn, Office of the Deputy Director of Research and Engineering (Research and Advanced Technology), Washington, DC
- THE DEVELOPMENT OF A METHOD FOR PREDICTING THE NOISE EXPOSURE OF PAYLOADS
IN THE SPACE SHUTTLE ORBITER VEHICLE
John F. Wilby and Larry D. Pope, Bolt Beranek and Newman, Inc., Canoga Park, CA

VIBRATION AND ACOUSTICS

- PROBABILITY OF FAILURE PREDICTION FOR STEP-STRESS FATIGUE UNDER
SINE OR RANDOM STRESS
R.G. Lambert, General Electric Company, Utica, NY
- ON THE USE OF COHERENCE FUNCTIONS TO EVALUATE SOURCES OF DYNAMIC EXCITATION
S. Barrett, Martin Marietta Corporation, Denver, CO
- STATUS OF CAVITY NOISE PHENOMENA MEASUREMENT AND SUPPRESSION
ON THE B-1 AIRCRAFT
A.G. Tipton and C.H. Hodson, Los Angeles Division, Rockwell International, El Segundo, CA
- SPACE SHUTTLE SOLID ROCKET BOOSTER AFT SKIRT REENTRY NOISE INDUCED
BY AN AERODYNAMIC CAVITY-FLOW INTERACTION
L.A. Schutzenhofer, P.W. Howard, W.W. Clever, and S.H. Guest, George C. Marshall Space Flight Center,
Marshall Space Flight Center, AL

BLAST AND SHOCK

SNAPS IN STRUCTURES

M. Zak, Jet Propulsion Laboratory, California Institute of Technology, Pasadena, CA

A SIMPLIFIED METHOD OF EVALUATING THE STRESS WAVE ENVIRONMENT OF INTERNAL EQUIPMENT

J.D. Colton and T.P. Desmond, SRI International, Menlo Park, CA

HIGH G PYROTECHNIC SHOCK SIMULATION USING METAL-TO-METAL IMPACT

M. Bai and W. Thatcher, Motorola Government Electronics Division, Scottsdale, AZ

AN EXPERIMENTAL DESIGN FOR TOTAL CONTAINER IMPACT RESPONSE MODELING AT EXTREME TEMPERATURES

V.P. Kobler, U.S. Army Missile Research and Development Command, Huntsville, AL and R.M. Wyakida,
J.D. Johannes, The University of Alabama in Huntsville, Huntsville, AL

EMPIRICAL PROCEDURES FOR ESTIMATING RECOILLESS RIFLE BREECH BLAST OVERPRESSURES

P.S. Westine and R.E. Ricker, Southwest Research Institute, San Antonio, TX

BLAST FROM BURSTING FRANGIBLE PRESSURE SPHERES

E.D. Esparza and W.E. Baker, Southwest Research Institute, San Antonio, TX

TEST EVALUATION OF SHOCK BUFFERING CONCEPT FOR HYDRODYNAMIC RAM INDUCED BY YAWING PROJECTILE IMPACTING A SIMULATED INTEGRAL FUEL TANK

P.H. Zabel, Southwest Research Institute, San Antonio, TX

PREDICTION OF FRAGMENT VELOCITIES AND TRAJECTORIES

J.J. Kulesz, L.M. Vargas, and P.I. Moseley, Southwest Research Institute, San Antonio, TX

PAPERS APPEARING IN PART 3

STRUCTURE MEDIUM INTERACTION

FAILURE OF UNDERGROUND CONCRETE STRUCTURES SUBJECTED TO BLAST LOADINGS

C.A. Ross, University of Florida Graduate Engineering Center, Eglin AFB, FL, P.T. Nash and G.R. Griner,
USAF Armament Laboratory, Eglin AFB, FL

OPTIMIZATION OF REINFORCED CONCRETE SLABS

J.M. Ferritto, Civil Engineering Laboratory, Naval Construction Battalion Center, Port Hueneme, CA

A NUMERICAL COMPARISON WITH AN EXACT SOLUTION FOR THE TRANSIENT RESPONSE OF A CYLINDER IMMERSED IN A FLUID

M.E. Giltrud and D.S. Lucas, Naval Surface Weapons Center, White Oak, Silver Spring, MD

CASE STUDIES IN DYNAMICS

FOIL SYSTEM FATIGUE LOAD ENVIRONMENTS FOR COMMERCIAL HYDROFOIL OPERATION

D.L. Graves, Boeing Marine Systems, Renton, WA

EVALUATION OF ROTOR-BEARING SYSTEM DYNAMIC RESPONSE TO UNBALANCE

R.E. Thaller and D.W. Ozimek, Aeronautical Systems Division, Wright-Patterson AFB, OH

SELECTED TOPICS FROM THE STRUCTURAL ACOUSTICS PROGRAM FOR THE B-1 AIRCRAFT

P.M. Belcher, Rockwell International Corporation, Los Angeles, CA

EXPERIMENTAL INVESTIGATION OF DYNAMIC CHARACTERISTICS OF TURBINE GENERATORS AND LOW-TUNED FOUNDATIONS

S.P. Ying and M.E. Forman, Gilbert/Commonwealth, Jackson, MI and R.R. Drumm, Pennsylvania Power
and Light Company, Allentown, PA

**COMBINED VIBRATION/TEMPERATURE/SIDELOAD ENVIRONMENTAL TESTING OF
UHF BLADE ANTENNAS**

R. Volker, McDonnell Douglas Corporation, St. Louis, MO

SHOCK ISOLATION PLATFORM FOR SEASPARROW LAUNCHER

P.V. Roberts, Raytheon Company, Bedford, MA

**TITLES AND AUTHORS OF PAPERS
PRESENTED IN THE
SHORT DISCUSSION TOPICS SESSION**

NOTE: These papers were only presented at the Symposium. They are not published in the Bulletin and are only listed here as a convenience.

RESEARCH IN COLLISION DYNAMICS OF SURFACE SHIPS

M.P. Pakstys, General Dynamics, Groton, CT

FORCED VIBRATION RESONATORS AND VIBRATIONS OF THE SHIP

G. Volcy, Bureau Veritas, Paris, France

RINGING PLATE SIMULATION OF PYROTECHNIC SHOCKS

S.H. Neff, Sandia Laboratories, Albuquerque, NM

QUARTZ CRYSTAL RESONATORS FOR HIGH G ENVIRONMENTS

R.L. Filler, ET&D Laboratory, Fort Monmouth, NJ

THE BENCHLESS LASER

J. Pearson, Air Force Flight Dynamics Laboratory, Wright-Patterson AFB, OH

PULSED HOLOGRAPHIC ANALYSIS OF LARGE VEHICLE COMPONENTS

G. Arutunian and G.R. Gerhart, U.S. Army Tank Automotive Research and Development Command, Warren, MI

CALIBRATION OF SHOCK AND VIBRATION MEASURING TRANSDUCERS

R.R. Bouche, Bouche Laboratories, Sun Valley, CA

**CRITICAL SPEEDS OF MULTITHROW NONUNIFORM CRANKSHAFTS USING SPATIAL FINITE LINE
ELEMENT TECHNIQUE**

C. Bagci, Tennessee Tech. University, Cookeville, TN

VIBRATION OF INPLANE LOADED ISOTROPIC AND ORTHOTROPIC RECTANGULAR PLATES

S.M. Dickinson, The University of Western Ontario, London, Ontario, Canada

ATTENUATION OF VIBRATIONS IN VISCOELASTIC SOLIDS CONTAINING MULTIPLE DEFECTS

M.P. Wnuk, South Dakota University, Brookings, SD

SOLVING PC-CARD VIBRATION PROBLEMS WITH UNIQUE DAMPING APPLICATIONS

W.J. Vitaliano, Harris GISD, Melbourne, FL

MINI COMPUTER SWEPT SINUSOIDAL DATA PROCESSING TECHNIQUES

F.E. Anderson, U.S. Army Missile R&D Command, Redstone Arsenal, AL

SHUTTLE PAYLOADS TEST FACILITIES

E.J. Kirchman, NASA Goddard Space Flight Center, Greenbelt, MD

AERODYNAMIC COUPLING BETWEEN CLOSELY SPACED PANELS

C.V. Stahel, Jr., General Electric Company, Philadelphia, PA

UPDATE ON COMBINED ENVIRONMENT GROWTH TESTING OF A BLACK BOX

J. Hutchinson, Vought Corporation, Dallas, TX

MODAL AND IMPEDANCE ANALYSIS

AN IMPEDANCE TECHNIQUE FOR DETERMINING LOW FREQUENCY PAYLOAD ENVIRONMENTS

Kenneth R. Payne
Martin Marietta Corporation
Denver, Colorado

An approximation method for determining low frequency payload environments is developed and compared to state of the art coupling/response routines. Problems in signal conditioning techniques and frequency domain analysis are discussed. Results from analytical simulations with a spring mass system and a math model of the Space Transportation System and Long Duration Facility are presented.

INTRODUCTION

Low frequency payload loads and environmental predictions can be a very lengthy and expensive task for complex booster payload configurations. Detailed mathematical models exhibiting sufficient resolution of the dynamic characteristics of both the payload and booster must be individually generated than mathematically coupled to form the final system models. The number of degrees of freedom associated with these individual models as well as the number of degrees of freedom describing the total system dynamic characteristics make analysis of this level of detail economically intimidating. This generally results in the analyst reducing the size of system models to cut down on cost. While some future payload models may legitimately be reduced in size for system analyses, the evident complexity of boosters, such as the Shuttle Transportation System (STS), and payloads, such as current concepts of Large Space Structures (LSS), will require enormous numbers of degrees of freedom for conventional system definition.

Furthermore, in most cases, booster models and external forcing functions are assumed to be constant, i.e., changes in the payload environments are assumed to be dependent on the payload characteristics, holding the external forces and booster characteristics constant for the most part. These assumptions do have some merit since a large number of payloads are carried on

a few common boosters. The result is some analyses are repeated over and over, often with very similar results.

A preferable technique, eliminating the necessity of creating detailed coupled models as well as decreasing the scope of an overall integration task, is described here. This approach, designated by the author as the "impedance technique", corrects the response of the booster/payload interface to reflect feedback changes associated with changes of the payload. All calculations are done in the frequency domain. The approach eliminates the necessity of computing the final coupled eigensolutions. The final equations are reduced to simple complex transfer functions. Furthermore, the booster dynamic characteristics required to compute these transfer functions consist of unloaded interface free-free modal data. Thus, by obtaining a "standard" set of booster model and input environmental data, the payload organizations should be able to calculate the expected low frequency environments at the interface of the booster/payload. Thus, the approach also reduces a large portion of the overall integration task.

The first purpose of this paper is to present the development of the impedance technique and emphasize some of its salient features. Since any analytical technique must pass a

demonstration test, the second purpose of this paper is to present the results of using the payload impedance technique on the future Long Duration Exposure Facility (LDEF) STS payload. This example serves as a cumulative evaluation and lends some insight into the value of the methodology.

DEVELOPMENT OF STANDARD MODAL COUPLING

Before discussing the development of the impedance methodology, a brief review of a standard modal coupling technique is in order. The coupling process begins with two or more discrete mathematical models depicting, for example, the structural properties of any booster and payload (Figure 1) system. The discrete equations of motion [1] for the payload uncoupled (free-free) could be written as:

$$[M_p] \{\ddot{x}_p\} + [K_p] \{x_p\} = \{0\} \quad (1)$$

where

$[M_p]$ = the discrete mass matrix of the payload
 $[K_p]$ = the discrete stiffness matrix of the payload
 $\{\ddot{x}_p\}, \{x_p\}$ = vectors of discrete motions of the payload.

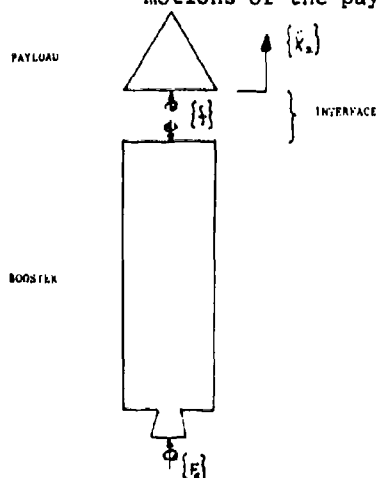


Fig. 1 - Schematic of Typical Payload/Booster System Showing Pertinent Accelerations and Loads.

Note here that the equations of motion shown in Eq. (1) do not include damping or any applied forces. These factors in the equations of motion will be considered later in the development. A similar set of equations can be written for the booster as,

$$[M_B] \{\ddot{x}_B\} + [K_B] \{x_B\} = \{0\} \quad (2)$$

where

$[M_B]$ = the discrete mass matrix of the booster
 $[K_B]$ = the discrete stiffness matrix of the booster
 $\{\ddot{x}_B\}, \{x_B\}$ = vectors of the discrete motions of the booster

Let us turn our attention to the payload model for the moment. Eq. (1) generally represents the structure as free-free, i.e., unconstrained at any point. A more convenient set of equations can be derived by writing the absolute motions of the payload as the sum of motion relative to the interface and that due to the motion of the interface itself. In matrix form, this can be written as:

$$\{\ddot{x}_p\} = \{\ddot{x}_I\} + [T] \{\ddot{x}_I\} \quad (3)$$

where

$\{\ddot{x}_p\}$ = the relative displacements of the payload points to the interface.
 $[T]$ = the static reduction matrix of all the payload degrees of freedom to the interface.
 $\{\ddot{x}_I\}$ = the discrete displacements at the payload/booster interface.

If the system can be assumed linear, the relationships shown in Eq. (3) will also hold for the velocities and accelerations. It should be pointed out that the relative motions of the payload are obtained by constraining the payload at the interface to the booster, and the reduction transformation $[T]$ becomes a rigid body transformation when the interface is statically determinate. Relative motion can be expressed in terms of the natural modes, $\{\phi\}$, of the constrained system. Then Eq. (3) becomes,

$$\{\ddot{x}_p\} = [\phi] \{\ddot{q}_p\} + [T] \{\ddot{x}_I\} \quad (4)$$

where

$\{\ddot{q}_p\}$ = modal coordinates of the constrained payload.

Transforming the payload energies into the Eq. (4) coordinate system, the equations of motion for the payload become

$$\begin{bmatrix} I & \phi_p^T M_p T^T \\ \text{sym} & T^T M_p T \end{bmatrix} \begin{Bmatrix} \ddot{q}_p \\ \ddot{x}_I \end{Bmatrix} + \begin{bmatrix} \omega_p^2 & 0 \\ 0 & 0 \end{bmatrix} \begin{Bmatrix} \ddot{q}_p \\ \ddot{x}_I \end{Bmatrix} = \begin{Bmatrix} 0 \\ 0 \end{Bmatrix} \quad (5)$$

where

$[I]$ = unity matrix representing the generalized mass,

$$[\phi_P^T M_P \phi_P] = [I]$$

$[\phi_P]$ = matrix of eigenvectors representing the constrained payload model.

$[\phi_P M_P T]$ = the inertial coupling matrix

$[\omega_P^2]$ = generalized stiffness matrix,

$$[\phi_P^T K_P \phi_P] = [\omega_P^2]$$

ω_P = eigenvalues of the payload in a constrained configuration.

Notice here that the equations of motion in Eq. (5) are still coupled. The upper set of equations represent noninterface payload dof and the lower set the interface dof between the payload and booster. Since the interface degrees of freedom $\{X_I\}$, are common to both the payload and the booster, the rigid body mass, $[T' M_P T]$, can be added to the booster separately before the final set of coupled equations are generated. Or,

$$[M_B + T' M_P T] \{\ddot{X}_B\} + [K_B] \{X_B\} = \{0\} \quad (6)$$

If modes, $[\phi_B]$, and frequencies, ω_B^2 , of Eq. (6) are calculated, Eq. (6) can be decoupled with the modal substitution approach and simplified to:

$$[I] \{\ddot{q}_B\} + [\omega_B^2] \{q_B\} = \{0\} \quad (7)$$

where

$\{\ddot{q}_B\}, \{q_B\}$ = modal coordinates of the booster.

Note that $\omega_B^2 = 0$ for every rigid body mode. Eqs. (5) and (7) can be combined to form the final modally coupled set of equations [2].

$$\begin{bmatrix} I & \phi_P^T M_P T S_I \phi_B \\ \text{sym} & I \end{bmatrix} \begin{Bmatrix} \ddot{q}_P \\ \ddot{q}_B \end{Bmatrix} + \begin{bmatrix} \omega_P^2 & \\ & \omega_B^2 \end{bmatrix} \begin{Bmatrix} q_P \\ q_B \end{Bmatrix} = \begin{Bmatrix} 0 \\ 0 \end{Bmatrix} \quad (8)$$

where S_I selects interface dof from the booster coordinates. These coupled equations of motion are then decoupled by modal substitution of a final set of eigenvalues, $[\phi_C]$, so that now the system equations are,

$$\begin{aligned} [I] \{\ddot{q}_C\} + [2\zeta_C \omega_C] \{\dot{q}_C\} \\ + [\omega_C^2] \{q_C\} \\ = [\phi_C^T] \begin{bmatrix} \phi_B^T T' T & \phi_B^T \\ \phi_P^T & \end{bmatrix} \{F_E\} \end{aligned} \quad (9)$$

where

$\{\ddot{q}_C\}, \{\dot{q}_C\}, \{q_C\}$ = coupled modal coordinates

$[2\zeta_C \omega_C]$ = coupled modal damping

$[\omega_C^2]$ = generalized stiffness for the coupled payload/booster system,

$$\phi_C^T \begin{bmatrix} \omega_P \\ \omega_C \end{bmatrix} \phi_C = \begin{bmatrix} \omega_P^2 \\ \omega_C^2 \end{bmatrix}$$

$\omega_C = 0$ for all rigid body modes

$\{F_E\}$ = vector of applied external forces.

Eq. (9) becomes the equation to be solved for vehicle responses and loads for external loading events, e.g., engine transients and staging events. The discrete responses of both the payload and booster are then computed by substituting back to the discrete domain.

DEVELOPMENT OF THE IMPEDANCE METHODOLOGY

While the above derivation was not completely rigorous, it does describe the basic assumptions and techniques of a modal coupling approach. But now let us return to Fig. 1. The methodology of the payload impedance technique is based on isolating the feedback of the payload from the coupled dynamic characteristics of the total payload/booster system. The key to the approach lies in the interface forces shown schematically in Fig. 1. The desired end result would be a method by which loads on a new payload can be determined from analysis or test of a prior payload for a set of loading conditions without

having to obtain a new set of coupled eigensolutions, or performing new time domain analyses.

Consider the interface accelerations, $\{\ddot{x}_i\}$, for the total free-free system (Fig. 1) as being the sum of the accelerations due to the external forces, $\{f\}$, and those due to the interface for $\{f\}$. Or,

$$\{\ddot{x}_i\} = \{\ddot{x}_i\}_E + \{\ddot{x}_i\}_f \quad (10)$$

$\{\ddot{x}_i\}_E$ = the accelerations at the interface due to the external forces $\{F_E\}$

$\{\ddot{x}_i\}_f$ = the accelerations at the interface due to the interface force, $\{f\}$

By substituting the appropriate expressions for the terms on the right-hand side of Eq. (10), the total interface accelerations will account for both the external forces being transferred through the booster and the dynamic feedback of the payload on the interface. The external forces of concern in this development include those such as engine thrusts and, in the case of an STS configuration, possibly landing loads. They do not, however, include any external loads applied directly to the payload.

First consider the accelerations due to the external forces applied to the booster. A set of free-free equations for the booster can be derived as:

$$\begin{aligned} [1] \{\ddot{q}_B\} + [2] \zeta_B \bar{\omega}_B \{\dot{q}_B\} \\ + [\bar{\omega}_B^2] \{q_B\} = [\phi_{FB}]^T \{F_E\} \end{aligned} \quad (11)$$

where

$\{\ddot{q}_B\}$ etc = modal coordinates of the unloaded booster model

$[2] \zeta_B \bar{\omega}_B$ = generalized damping matrix for the unloaded booster

$[\bar{\omega}_B^2]$ = generalized stiffness of the unloaded booster

$[\phi_{FB}]$ = modal amplitudes at the external force locations.

The termination "unloaded" means the payload body mass contribution $[r^T M_p r]$ in Eq. (6) is not added to the booster interface before the eigensolution is obtained. Eq. (11) can be converted to

the frequency domain by taking the Laplace Transform of both sides (1). With zero initial condition, the modal accelerations of the unloaded booster due to the applied external forces only can be expressed as,

$$\{\ddot{q}_B(s)\} = \left[\frac{s^2}{s^2 + 2\zeta_B \bar{\omega}_B s + \bar{\omega}_B^2} \right] [\phi_{FB}]^T \{F_E(s)\} \quad (12)$$

where

s = Laplacian variable

To convert to the frequency domain, substitute $j\omega$ for the variable, s , in Eq. (12). The result can be written in terms of the frequency ratio, λ as

$$\{\ddot{q}_B\}_i = \left[\frac{-\lambda_i^2}{(1-\lambda_i^2) + j(2\zeta_B \lambda_i)} \right] [\phi_{FB}]^T \{F_E(\lambda)\}_i \quad (13)$$

$i = 1, 2, \dots$ No. of input frequencies

where

$\lambda_i = \omega_i / \bar{\omega}_B$, the ratio of the i th frequency to the modal frequency
 $j = \sqrt{-1}$

Transforming back to the discrete coordinates of Eq. (10), an expression for the interface accelerations as a function of the input frequency is given by:

$$\{\ddot{x}_i\}_{E_i} = [\phi_{iB}] \left[\frac{-\lambda_i^2}{(1-\lambda_i^2) + j(2\zeta_B \lambda_i)} \right] [\phi_{FB}]^T \{F_E\}_i \quad (14)$$

Or simplifying,

$$\{\ddot{x}_i\}_{E_i} = [TADM]_i \{F_E\}_i \quad (15)$$

The coefficients matrix, $[TADM]_i$, represents the complex transfer admittance of the booster from the point of external force application to the payload interface.

Next, to derive the expression for the interface accelerations due to the interface forces, $\{f\}$, a set of differential equations similar to Eq. (11) can be written as,

$$\begin{aligned} & \{1\} \{\ddot{q}_B\} + [2\zeta_B \omega_B] \{\dot{q}_B\} \\ & + [\omega_B^2] \{q_B\} = [\phi_{fB}]^T \{-f\} \end{aligned} \quad (16)$$

where

$\{\ddot{q}_B\}$, $\{\dot{q}_B\}$, $\{q_B\}$ = modal coordinates associated only with the responses to the interface forces.

$[\phi_{fB}]$ = modal amplitudes at the interface.

Here the distinction in the booster modal responses is to separate those due to the external forces, $\{F_E\}$, (see Eq. (10)), from those due to the interface forces, $\{f\}$. Following the previous procedure for solving and simplifying the equations of motion in the frequency domain, the discrete accelerations at the interface due to the interface loads $\{f\}$, are:

$$\{\ddot{x}_I\}_{f_i} = [\phi_{IB}] \left[\frac{\lambda_i^2}{1 - \lambda_i^2 + j 2\zeta_B \lambda_i} \right] [\phi_{fE}]^T \{f\}_i \quad (17)$$

$i = 1, 2, \dots$ No. of input frequencies.

where

$[\phi_{IB}]$ = modal amplitudes at the interface

$\lambda_i = \frac{\omega_i}{\omega_B}$, ratio of the i th input frequency to the modal frequency.

or,

$$\{\ddot{x}_I\}_{f_i} = [PADM]_i \{f\}_i \quad (18)$$

Here the coefficients matrix, $[PADM]_i$, represents the complex transfer admittance of the booster from the point of interface force application (i.e., the interface) to the payload interface. This matrix contains the transfer function characteristics of the booster at that point due to the interface forces, $\{f\}$. Substituting Eqs. (15) and (18) into Eq. (10) yields.

$$\{\ddot{x}_I\}_1 = [TADM]_1 \{F_E\}_1 + [PADM]_1 \{f\}_1 \quad (19)$$

The feedback effect of the payload on these interface accelerations is contained in the second term of Eq. (19) which involves the interface forces, $\{f\}$. These forces will now be expressed as a function of the inertial responses of

the payload. Eq. (5) can be written to include damping as:

$$\begin{aligned} & \begin{bmatrix} 1 & \phi_p^T M_p T \\ \text{sym} & T^T M_p T \end{bmatrix} \begin{Bmatrix} \ddot{q}_p \\ \ddot{x}_I \end{Bmatrix} \\ & + \begin{bmatrix} 2\zeta_p \omega_p & 0 \\ 0 & 0 \end{bmatrix} \begin{Bmatrix} \dot{q}_p \\ \dot{x}_I \end{Bmatrix} \\ & + \begin{bmatrix} \omega_p^2 & 0 \\ 0 & 0 \end{bmatrix} \begin{Bmatrix} q_p \\ x_I \end{Bmatrix} = \begin{Bmatrix} 0 \\ f \end{Bmatrix} \end{aligned} \quad (20)$$

This equation now includes generalized damping and the force on the payload, $\{f\}$. Eq. (20) does imply a basic assumption. Notice that the damping and stiffness partitions corresponding to the interface degrees of freedom are null. This is not true if the interface is not statically determinate. In the case of the indeterminate interface, the following expressions are somewhat more complicated but are manageable. One may separate the upper set of equations in (20),

$$\begin{aligned} & \{1\} \{\ddot{q}_p\} + [2\zeta_p \omega_p] \{\dot{q}_p\} \\ & + [\omega_p^2] \{q_p\} = [\phi_p]^T [M_p] [T] \{x_I\} \end{aligned} \quad (21)$$

from the lower set,

$$\begin{aligned} & [T^T] [M_p] [\phi_p] \{\ddot{q}_p\} \\ & + [T^T M_p T] \{\ddot{x}_I\} = \{f\} \end{aligned} \quad (22)$$

Taking the Laplace transformation of Eq. (21) and simplifying as before, we have

$$\{\ddot{q}_p\}_1 = \left[\frac{\lambda_{p1}^2}{1 - \lambda_{p1}^2 + j 2\zeta_p \lambda_{p1}} \right] [\phi_p^T M_p T] \{\ddot{x}_I\}_1 \quad (23)$$

$i = 1, 2, 3, \dots$, No. of input frequencies.

Now substituting (23) into (22)

$$\left([T_{M_P}^T] \left[\frac{\lambda_{P1}^2}{1 - \lambda_{P1}^2 + j 2 \zeta_P \lambda_{P1}} \right] (\phi_{P M_P}^T) + [T_{M_P}^T] \right) \{\ddot{x}_I\}_1 = \{f_1\} \quad (24)$$

or

$$[IMP]_1 \{\ddot{x}_I\}_1 = \{f_1\}_1 \quad (25)$$

Here, the complex coefficients matrix $[IMP]_1$ represents the impedance of "complex inertia" of the payload at the payload/booster interface.

Now all of the complex transfer function characteristics that are necessary to fully describe the vehicle coupled response have been derived, and the final form of the coupled impedance can be generated. Substituting (25) into (19) yields,

$$\{\ddot{x}_I\}_1 = [TADM]_1 \{F_E\}_1 + [PADM]_1 [IMP]_1 \{\ddot{x}_I\}_1 \quad (26)$$

$i = 1, 2, 3, \dots$, No. of input frequencies.

Or, rearranging

$$([I] - [PADM]_1 [IMP]_1) \{\ddot{x}_I\}_1 = [TADM]_1 \{F_E\}_1 \quad (27)$$

$i = 1, 2, 3, \dots$, No. of input frequencies.

In this form of the impedance equation the left hand side matrix of complex coefficients for the interface accelerations represents the coupled impedance of the payload/booster combination, and the right hand side represents the complex "pseudo" generalized force. Since the external forces, $\{F_E\}$, are in complex spectral form, and the coefficient matrices are complex as well, the desired spectral interface acceleration can be obtained with Eq. (26) using nothing more than complex multiplication. This simplicity greatly reduces the cost of generating the low frequency environmental predictions. If we now consider some new payload for the same booster with the same interface and same set of external force/torque vectors (Fig. 2), then the interface accelerations for the new payload will be:

$$\{\ddot{x}_I\}_{2_1} = ([I] - [PADM]_1 [IMP]_{1_1})^{-1} ([I] - [PADM]_1 [IMP]_{1_1}) \{\ddot{x}_I\}_{1_1} \quad (28)$$

$i = 1, 2, 3, \dots$, No. of input frequencies.

where "1" & "2" designate different payloads.

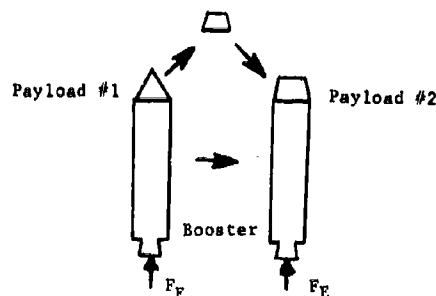


Fig. 2 - Schematic of Impedance Technique for Replacing One Payload Feedback With Another

The advantages of analyzing the interface environments in this manner appear to be significant. The resultant set of coefficients for $\{\ddot{x}_I\}_1$ in Eq. (28) act as a coupled analytical filter that modifies the environment for payload number 1 to arrive at an environment for payload number 2. A payload organization could obtain the complex impedance from the proposed data bank that corresponds to the previous interface accelerations and generate new flight predictions for the desired interface. Notice that the basic equations of this technique do not require a coupled set of eigensolutions discussed in Eq. (9). Thus, it appears that either Eq. (27) or (28) could be utilized to significantly reduce the life-cycle cost of loads analyses.

The assumptions with the most impact on the technique involve the use of Eq. (28). Neither are the forcing functions applied to the vehicle exactly repeatable nor are the transfer characteristics the same for all booster configurations. In the case of a booster system like the (STS), these characteristics change for each location in the Orbiter bay.

EVALUATION OF THE IMPEDANCE TECHNIQUE

To assess the accuracy of the technique, specifically the calculated results of Eq. (26), time domain results were compared with those from the impedance technique for a simple system (Fig. 3). This evaluation using this simplified model proved beneficial in a number of areas. (The degree of freedom X_2 was used to describe the interface motion for this check case, with the external forces, F_E , applied at M_2 .) Time histories of a number of forcing functions were used to force the model (see Fig. 3). Differential equations similar to those depicted in Eq. (9) were then solved using standard time domain techniques. The discrete accelerations of the assumed interface were used for comparison with the impedance results. The forcing functions used in the frequency domain analysis were obtained by converting the time histories of F_E to Fourier spectra with a Fast Fourier Transform (FFT) algorithm.

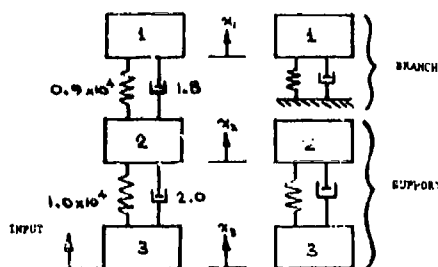


Fig. 3 - Schematic of Three Mass Check Model

One discrepancy pertaining to the modal damping became apparent from the beginning. Various techniques have been tried to obtain the correct damping for

a modally coupled model. For example, one technique used on the Viking Program involved calculating the triple matrix product of the coupled set of modes and the uncoupled diagonal damping matrices and discarding the resulting off-diagonal terms to maintain an uncoupled set of equations. This generalized damping is then used in Eqs. (9) for the time domain solutions. This assumption does force the coupled damping to be a function of the coupled modes but discards, in essence, the coupling effect from mode to mode. The manner in which the damping is measured and assumed for a payload and booster presents the problem. If the damping is measured for a typical payload in a modal survey, the recorded damping is a function of the test boundary conditions. When the payload is physically attached to the booster, a new set of boundary conditions exist and, therefore, a new set of relative motions or mode shapes also exist. For small damping, less than 1%, the previous philosophies about how to generate coupled damping may be adequate for determining payload loads and environments in the time domain. Generally speaking, significant changes in damping make very little difference in time domain peak response. Since the impedance technique is a frequency domain approach, changes in damping have a large impact on the transfer function characteristics. The impedance method never computes the final set of eigensolutions, therefore the transfer functions from modal coupling and the impedance technique will never be the same. In order to get comparable transfer functions for both the impedance check and the coupled time domain check, discrete dampings were assumed as shown in Fig. 3. Thus, the resulting functions were the same regardless. This point is important in light of future comparisons of existing loads analysis techniques and those similar to the impedance methodology developed above.

Use of the FFT in obtaining the spectral data also presents some problems as discovered by experimenting with the sample problem. The FFT is more commonly used for spectral analysis, e.g., auto-spectral densities, coherence, etc., of random data [3, 4]. Certain errors are introduced by signal truncation of time histories. In random data analysis, these errors are usually minimized by taking a number of averages or statistical degrees of freedom [4]. The effects of truncation on transient or complex signals cannot be averaged out since the signals are of finite length and do not repeat themselves. These truncation errors can be significant in generating Fourier spectra,

especially when these spectra are used to drive a system. The system transfer function has a certain value at a certain frequency and thus responds to the input at that frequency regardless of the error of that input.

Two separate force time histories were applied to the model depicted in Fig. 3. One force time history consisted of a decaying sine wave shown in Fig. 4. The same decaying sine function with a dc (steady-state) shift is shown in Fig. 5. These two forcing functions characterize one of the most common truncation effects [5]. The force time history represented in Fig. 4 could represent a lateral force at a payload/booster interface extracted from recorded flight data. Fig. 5 could be obtained in a like manner and represent a longitudinal interface load.

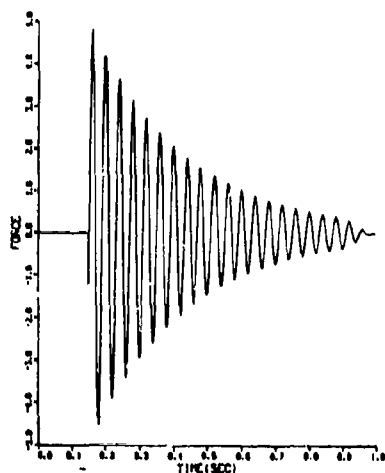


Fig. 4 - Decaying Sine Forcing Function With No Steady State

The forcing function shown in Fig. 4 was used to drive the 3 mass check model and obtain the acceleration as a function of time for the middle mass at degree of freedom number 2 (see Fig. 3). In addition, the Fourier transform of the forcing function in Fig. 4 was generated using an FFT after the time history was "windowed" by a Tukey window [5]. This Fourier transform was then used to drive the model using Eq. (27) to calculate the response of degree of freedom number 2. The spectral results of the impedance analysis is shown in Fig. 6. But for the true comparison this spectral response was

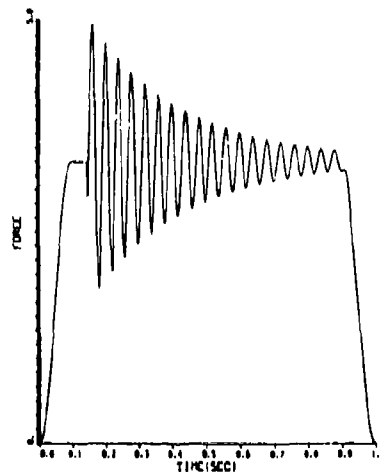


Fig. 5. - Decaying Sine Forcing Function With Steady State

inverse Fourier transformed to obtain a time history to correlate with the time domain response. This correlation is shown in Fig. 7.

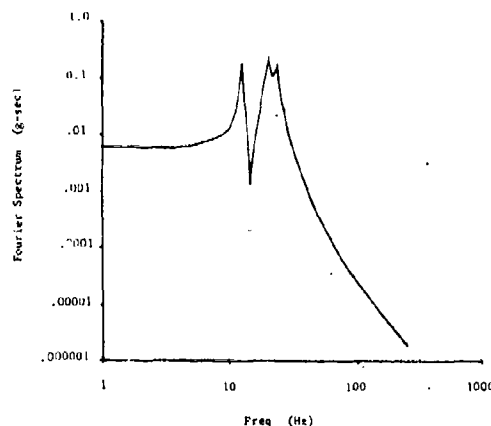


Fig. 6 - Spectral Response of Mass No. 2 To Decaying Sine With No Steady State

The effect of the window is more obvious when the model is driven in the frequency domain with the force in Fig. 5. Figs. 8 and 9 show the Fourier spectral response of degree of freedom

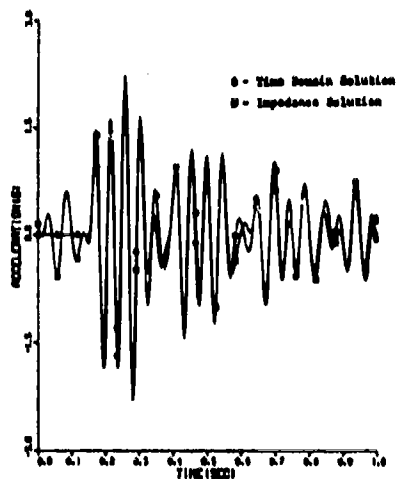


Fig. 7 - Time Domain Comparisons of Impedance Technique Responses And Time Domain Responses to Decaying Sine With No Steady State

2 with and without a Tukey window. Figs. 10 and 11 again depict a comparison of both sets of frequency domain response to the time domain response. It is obvious from these plots that for this case the Tukey window improves the response correlations.

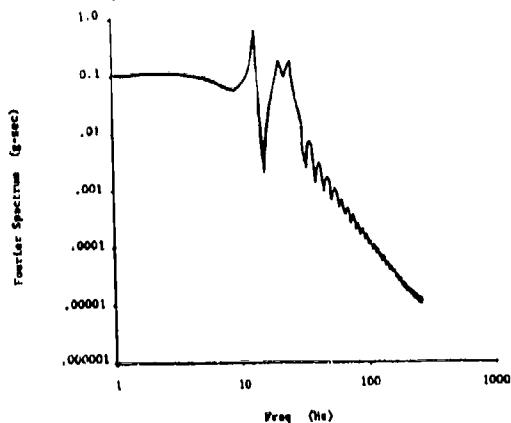


Fig. 8 - Fourier Spectrum of Response to Decaying Sine With Dc But No Tukey Window

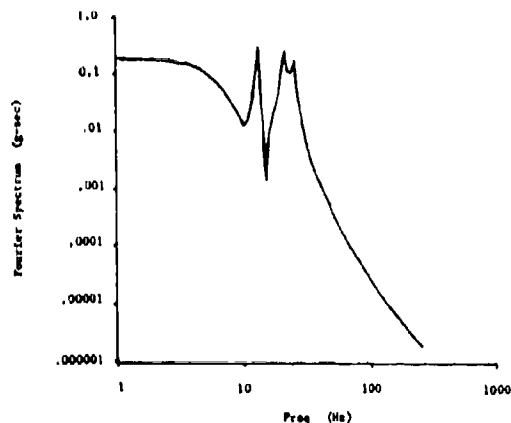


Fig. 9 - Fourier Spectrum of Response to Decaying Sine With Dc and With A Tukey Window

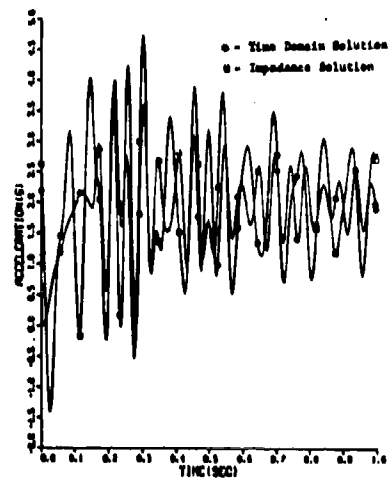


Fig. 10 - Time Domain Comparisons of Impedance And Time Domain Solutions Without a Tukey Window

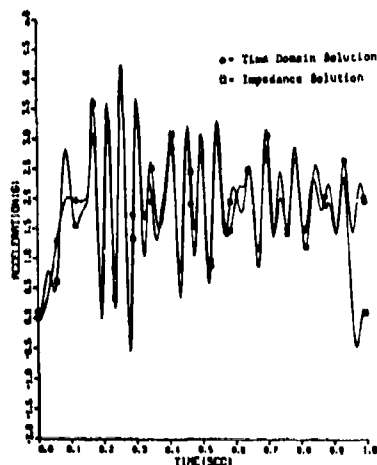


Fig. 11 - Time Domain Comparisons of Impedance And Time Domain Solutions With A Tukey Window

It is apparent from the results obtained that the low frequency environments can be predicted with the impedance technique. Better correlation with the time domain solutions could possibly be made with a different window or increasing the frequency resolution, however, enough correlation is apparent to attempt to use the technique for more complicated systems.

As a further demonstration of the impedance technique, interface accelerations were computed for a future STS payload. The primary objective of this analysis was to compare results with other current environmental predictions from state-of-the-art techniques.

The models used for this set of analyses were chosen to be consistent with those used for the loads cycles done by the STS project [6]. They were obtained through Langley Research Center (LRC) and were comprised of NASTRAN eigenvalues and eigenvectors for the STS finite element models of the liftoff and landing configurations. Two hundred eigenvectors were used for each configuration which included the models of the Development Flight Instrumentation (DFI) and Space Pallet (SP). All modes for each loads case were assumed to have a modal damping ratio of 1%.

The Long Duration Exposure Facility (LDEF) was chosen as the payload for these analyses. Forty eigenvalues

and eigenvectors were again furnished by LRC. The discrete mass matrix for the LDEF, necessary for the generation of the inertial coupling coefficients matrix was not available and had to be generated from discrete model data with our finite element routines. Orthogonality checks were calculated to ensure that the modes and regenerated mass matrix were consistent. Like the booster models, the LDEF modes were assumed to have 1% damping throughout.

Two loading events, liftoff and landing, were chosen to demonstrate the impedance technique. The liftoff event analyzed was case LP501R [6] which is defined as a "high performance fast timing" engine thrust with a mismatch between right and left SRBs. The SRB mismatch in this case was 0.098 sec. A more detailed description of the flight conditions can be found in [6].

A total of 62 discrete forcing functions were used to drive the analytical model for liftoff. Each defined time history was 10.0 sec in length. To obtain the Fourier spectrum of each force, they were first digitized, i.e., linearly interpolated, at 102.4 samples per second. This resulted in a total number of samples of 1024 with a Nyquist frequency of approximately 50 Hz. The same Tukey window discussed previously was used for the liftoff forcing functions. A Fourier spectrum of a representative force was plotted and is shown in Fig. 12.

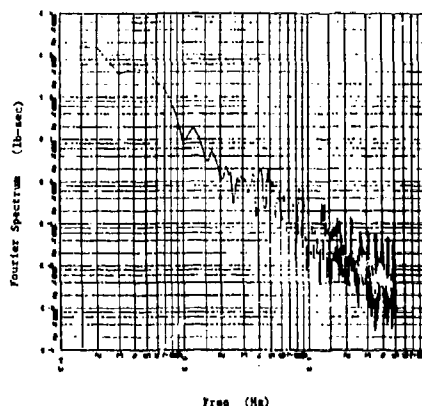


Fig. 12 - Typical Fourier Spectrum of "1-cos" Wind Load Used For Liftoff Analysis

An example of the spectral results of the impedance predictions for the liftoff event is shown in Fig. 13. For a check with previous predictions, the complex Fourier spectra were inverse transformed to obtain a time history for amplitude and frequency content comparisons. An inverse Fourier transform time history is presented in Fig. 14. Shown also on the plot are the corresponding peak accelerations (transcribed from [7]) resulting from a time domain analysis.

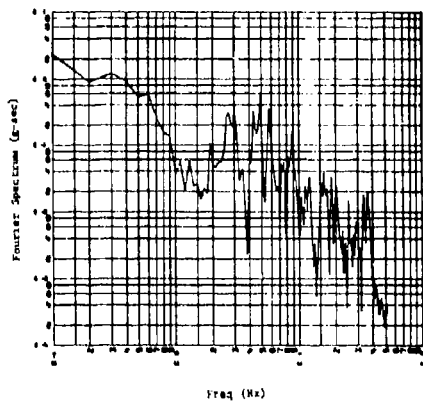


Fig. 13 - Fourier Spectrum of X Response At Forward Attach Point Right Hand Side For Liftoff

The Tukey window effect on the resulting time histories is best shown in Fig. 14 which is the longitudinal acceleration at a forward LDEF attach point. Because of the window, this response begins and ends at approximately zero amplitude. However, since this windowing technique of signal conditioning does not alter the signal in the remaining areas, its effect can be ignored.

The correlation of the impedance technique results and the time domain solutions show generally good comparisons. Transcribing the peaks of the time domain accelerations to the inverse transform plots is agreed not to be a conclusive comparison technique. However, the peaks do appear to occur at the same points in time for both cases, indicating a minimal phase error. The largest discrepancy is shown in amplitude comparisons. Even in this area some of the amplitudes calculated with

the impedance technique compare quite well. The best comparisons occurred in the longitudinal accelerations.

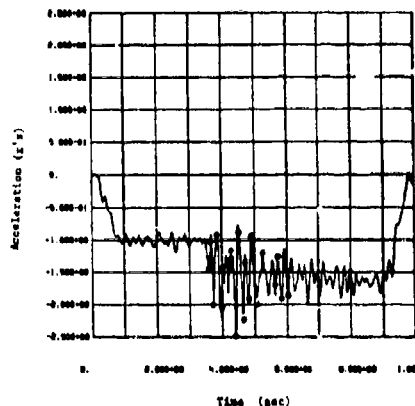


Fig. 14 - Inverse Transform Response X Forward Attach Right Hand Side For Liftoff

The final event analyzed with the impedance technique was a landing case (LM 550 in [7]). For this event 266 Fourier spectra were calculated for discrete forcing functions for the orbiter. The event can generally be described as a high angle of attack with symmetric landing conditions.

The problems encountered in analyzing the landing event resulted in further definition of analytical requirements for the use of the impedance technique for low frequency predictions. The analysis of this event pointed out the pitfalls of frequency resolution. The time histories of the forcing function for landing were of two different lengths. These are two basic external forces on the orbiter for landing [7]: the landing gear strut loads; and the aerodynamic loads due to such things as ground effects, etc. The strut force time histories were 2.0 seconds in length and all other loads were only 0.8 seconds in length. Since the behavior of the aerodynamic loads were not known past 0.8 seconds and since it appeared that all oscillatory characteristics of the strut forces had diminished by 0.8 sec., the decision was made to truncate the strut forces at 0.8 seconds for the analysis. The resulting sample rate based on the 512

data points used was 640 samples per second with a Nyquist frequency of 320 Hz.

The important thing of note, however, was that the frequency resolution for the 0.8 second signal was only 1.25 Hz. This resolution would be sufficient for describing characteristics of higher frequencies. However, the orbiter model contains low frequency bending modes at or around 5 Hz. With the assumed 1% modal damping ratio, this mode may have a bandwidth of 0.1 Hz. Thus, it is obvious that frequency descriptions of the input forces with a frequency resolution of 1.25 Hz could and did give erroneous answers.

The decision was made to discard the aerodynamic loads and perform the analysis with the full 2.0 second time history of the strut loads only. This decision of neglecting the aerodynamic forces was based on the general assumption that the aerodynamic forces contribute only a small part to the low frequency environment at the payload interface. The resulting resolution with only the strut forces becomes 0.5 Hz, which comes somewhat closer to the desired 0.1 Hz.

Representative results of the analysis with only the strut loads are shown in Figs. 15 and 16. Here again the time domain peaks from [7] were transcribed to the plots for comparison.

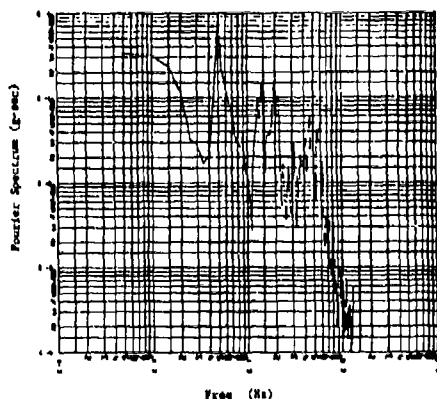


Fig. 15 - Fourier Spectrum of X Response At Forward Attach Point Right Hand Side For Landing Due To Strut Force Only

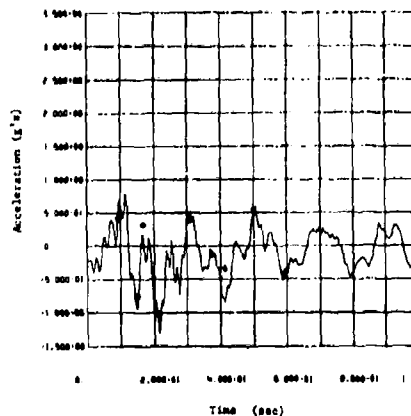


Fig. 16 - Response X Forward Attach Right Hand Side For Landing Due To Strut Forces Only

These comparisons were not expected to be as good as the liftoff case generally because of the absence of aerodynamic loads. The worst comparisons are most evident in the "z" direction acceleration, as expected, since this is the direction of the general aerodynamic forces. Also, the correlation seems to get worse from about 0.3 to 0.4 seconds on. This again is when the aerodynamic forces are the most active.

DISCUSSION AND CONCLUSIONS

These results do point out one important point: determining the low frequency environment from a pure spectral standpoint is quite difficult. Frequency domain analysis is too sensitive to damping for example. As the results of the STS analysis show, additional and more meaningful information is gained from the time history obtained from the inverse transforms.

The Analysis of the liftoff event for the LDEF by far showed the best results. Even these results can be improved, however. As discussed in the previous sections, the differences in coupled damping versus the resulting damping of the impedance technique will never go away. The differences in damping due to changes in boundary conditions will always be there. However, with in-flight information on the true transfer characteristics, these problems could be minimized.

The set of analysis performed with the impedance technique for the liftoff case included loads that were applied somewhat incorrectly. The steady-state winds and gust loads are represented by a steady state level with a "1-cos" gust function. In normal time domain solutions the necessary initial conditions are derived to place the vehicle in equilibrium before the time domain solutions begin. In the spectral analysis of the impedance technique, these forces were applied at time zero, forcing the model to respond to an "imaginary" transient at time zero. Therefore, the responses shown will be changed when the winds are done correctly.

The landing event analysis probably had the most meaningful results for the intent of this study. These results, when compared to the time domain analysis prediction, show not only the effects of the aerodynamic forces but, more importantly, give insight into the errors caused by inadequate frequency resolution.

Neither the liftoff or landing results shown should be used in any manner for design purposes. Discrepancies in the models used in these analyses versus the latest design revisions, or, what was used in [7] may cause drastic differences in response. In addition, assumptions made in the impedance technique analysis, e.g., neglecting aerodynamic loads, for evaluation purposes cause the results to be somewhat unconservative.

Based on the results of all of the analyses performed, a limited evaluation of the technique for the use of future payloads can be made. It appears that this technique can be used for any coupled payload system in a very inexpensive manner. As stated before, the ratioing of the acceleration from one flight to the next, as developed in Eq. (28), probably has the least use for STS payloads due to the variety of interface locations in the bay. It does appear as an appealing analytical approach for changing pallets or pallet mounted experiments.

However, the best use can be to achieve the removal of an integration role with a final set of eigensolutions. This can be achieved in much the same way as was done in this study. In the future, payload projects can obtain a data tape from the STS project that contains the best STS model and flight event cases. The payload designer can then perform the analysis to evaluate

the design. This philosophy merely requires continual update of the STS dynamic characteristics and the latest flight data information.

Having calculated the predicted low frequency environment for a particular payload, the evaluation can be made for the necessity of a more extensive loads and/or response analysis for the payload based on the spectral content of the interface environment and the payload impedance. If there is concern about the design margin, the impedance technique programs should give some insight into the modal degrees of freedom of the generalized forces that are contributing most to the environment at that frequency bandwidth. This information should then be used to reduce the size of the models involved and again cut costs.

In summary, based on the results of this study, with reusable boosters and an environmental data bank, payload organizations can use the impedance technique to:

1. Eliminate the necessity of integrated coupled analysis;
2. Perform their own low cost environment predictions;
3. Reduce analytical effort with spectral evaluation of coupled response; and,
4. In the event more detailed analysis is necessary, reduce the size of the dynamic models.

REFERENCES

1. Hurty, W. C., and Rubinstein, M. F.: Dynamics of Structures. Prentice Hall, N.J., 1964.
2. Benfield, W. A., and Hrudu, R. F.: Vibration Analysis of Structures by Component Mode Substitution. AIAA Journal, July 1971, pp 1255-1261.
3. Otnes, R. K., and Enochson, L.: Digital Time Series Analysis. Wiley-Interscience, New York, 1972.
4. Bendat, J. S., and Piersol, A. G.: Random Data Analysis and Measurement Procedures. Wiley-Interscience New York, 1971.
5. Childers, D., and Durling, A.: Digital Filtering and Signal Processing. West Publishing Co., New York, 1975.

6. Martens, M. A., Dartilo, D. O., and Metan, R.: Shuttle Static and Dynamic Models with Forcing Functions for MMS and LDEF Payloads. SD77-SH-0083, Rockwell International Space Division, July 1977, NAS9-14000.
7. Martens, M. A., Henkel, E. E., and Metsa, R.: Load Data Bo9k for Long Duration Exposure Facility, Development Flight Demonstration and Spacelab Single Pallet Cargo System. SD79-SH-0116, Rockwell International Space Division, April 1977, NAS9-1400.

A STATISTICAL LOOK AT MODAL DISPLACEMENT RESPONSE TO SEQUENTIAL EXCITATIONS

William J. Kacena
Martin Marietta Corporation
Denver, Colorado

The residual displacement response to a sequence of simple excitations separated by nearly equal time intervals is evaluated on a statistical basis. Mean plus three-sigma responses are plotted as a function of the number of sequential excitations for a range of damping values. The curves were derived for parametric evaluation of the vibratory pointing error for a maneuvering spacecraft, but they can be applied to other sequential excitation problems where the residual displacement in a key mode is the response parameter of interest.

INTRODUCTION

Maneuver excited vibration of a spacecraft can cause oscillatory pointing errors of sensitive optical instruments. Reference [1] shows that a simple residual displacement shock spectrum of the maneuver's rotational acceleration time history is a powerful analysis tool for bounding these errors. The spectrum envelope curve at each modal frequency combined with an appropriate modal constant predicts the worst case error associated with each mode of vibration. This analysis technique both identifies which vibration modes produce significant errors and calculates the magnitude of the worst case undamped error in each mode due to a single maneuver excitation.

When sequential excitations are applied, the accumulated response may be many times the response introduced by a single worst case excitation. However, such factors as damping, the probability of a worst case excitation and the probability of badly phased excitations all reduce the cumulative response from the worst case upper bound (the number of excitations times the worst case undamped effect from a single excitation). This paper presents the results of a statistical study of this sequential response problem.

Each excitation in a sequence is assumed to have a simple waveform, and random selection of each excitation's time duration results in a statistical representation of how well the excitation is tuned to the response frequency. Similarly, the random selection of times between excitations provides a statistical look at how the response is affected by arbitrary phasing among excitations. These two random time selections are combined with a damped response analysis for a scenario of N sequential excitations, and the worst case residual

responses from each of M such scenarios are evaluated statistically (mean and standard deviation). The statistical worst case response (mean plus three-sigma) is normalized to the worst case response from a single excitation and plotted as a function of the number sequential excitations. Parametric curves for various values of damping are represented using a decay constant parameter that is a function of modal damping, modal frequency, and the average values of the random time parameters.

The curves presented provide a useful nomograph for evaluating the probable residual displacement response of a single vibration mode when excited by a sequence of simple forcing functions spaced at nearly equal time intervals. Although the results apply directly to the evaluation of residual pointing error of a maneuvering spacecraft, they can be applied to any vibration problem (forced or base motion) where residual displacement in a key mode is the important response parameter.

NOMENCLATURE

- A maximum response to a single excitation
- D decay constant parameter, $e^{-2\pi\zeta f(t_0 + \tau_0)}$
- F slope of forcing function
- f modal frequency (Hz)
- g normalized response parameter
- M number of sequences considered statistically
- n nth excitation in a sequence
- N number of sequential excitations
- t time variable and time between excitations (seconds)
- t_0 avg. time between excitations (seconds)

T a time period (seconds)
X response displacement
 β fraction parameter
 ζ modal damping ratio
 τ actual excitation time (seconds)
 τ_0 average time during an excitation (seconds)

DAMPED RESPONSE CHARACTERISTICS

The response of a single degree-of-freedom system with natural frequency, f , and damping ratio, ζ , experiences exponential decay such that

$$|X| \leq A e^{-2\pi\zeta ft} \quad (1)$$

If equation (1) bounds the response to a single worst case excitation, then the combined response to this excitation and a second identical excitation at a time T after the first is bounded by

$$|X| \leq A (e^{-2\pi\zeta ft} + e^{-2\pi\zeta f(t+T)}) \quad (2)$$

For $t = 0$ and N identical excitations spaced at equal time intervals, T ,

$$\frac{|X|}{A} \leq \sum_{n=0}^{N-1} (e^{-2\pi\zeta fT})^n \quad (3)$$

If τ_0 is the average excitation time and t_0 is the average time between excitations, $T = t_0 + \tau_0$; and equation (3) can be rewritten as

$$\frac{|X|}{A} \leq \sum_{n=0}^{N-1} D^n \quad (4)$$

where D is a decay constant parameter,

$$D = e^{-2\pi\zeta f(t_0 + \tau_0)} \quad (5)$$

From handbook data on infinite series [2]

$$\sum_{n=0}^{\infty} D^n = \frac{1}{1-D}, \quad 0 \leq D \leq 1 \quad (6)$$

The expression in (6) is a simple representation for the upper bound damped response to a sequence of excitations. For $D = 0.5$, the maximum response is limited to twice the worst case single excitation response. However, as D approaches unity, the response becomes large, and the simple upper bound expression may be overconservative. Since the decay parameter D is the key damping term for an infinite sequence of responses, we anticipate that D will be an independent damping parameter when a finite sequence of responses is evaluated. The following statistical results confirm this hypothesis.

STATISTICAL ANALYSIS

Figure 1 shows the undamped residual displacement response spectrum for a simple symmetric excitation. A change in the time duration of the excitation causes the spectrum peaks and valleys to shift accordingly in frequency. This indicates that there is a statistical relationship between the excitation time period and the expected response magnitude. In addition, the times between excitations dictate the phase relationship between subsequent responses. Hence, there is a statistical relationship between the time between excitations and the expected accumulation of the response.

This statistical response analysis uses a random number generator to select the maneuver time period, τ , and the time between excitations, t , of Figure 2 on an arbitrary uniform distribution basis:

- 1) given modal frequency, f
- 2) assume $f\tau \gg 1$
- 3) assume $ft \gg 1$
- 4) $(\tau_0 - 1/f) < \tau < (\tau_0 + 1/f)$
- 5) $(t_0 - .5/f) < t < (t_0 + .5/f)$

Residual Response

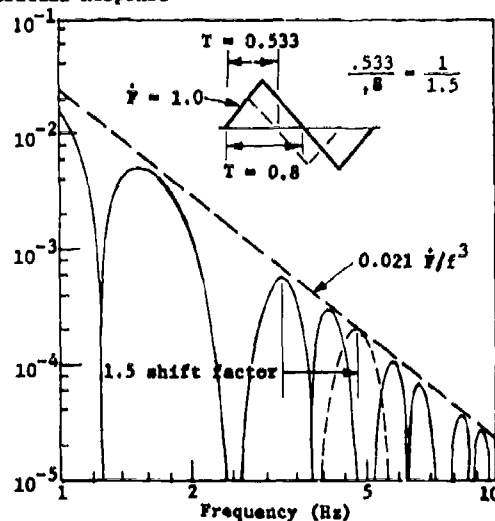


Figure 1. Typical Triangular Waveform Spectra

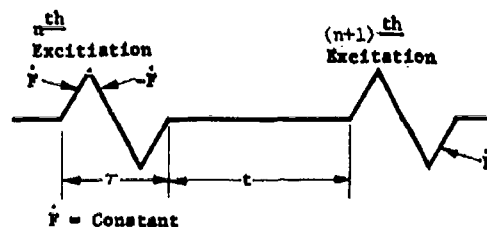


Figure 2. Sequential Excitation Parameters

The assumptions in 2) and 3) above indicate that the particular problem of interest here and the results presented are for excitation and quiescent times that are much longer than a cycle of the dominant vibration mode. The random selection of τ over a two cycle range of the modal frequency yields statistical response results that reflect one cycle of the double peak/valley recurrence in the spectral plot of Figure 1. Hence, the selection of τ does not bias the response statistics to either a spectral peak or valley. Similarly, the random selection of t , in 5) above, within one cycle of the modal frequency makes the phase relationship between the initial conditions and the impending response strictly arbitrary.

Figure 3 summarizes the results of this study by plotting a normalized residual displacement response parameter versus the number of sequential excitations. The response parameter is normalized such that unity is the response to a single worst case excitation as defined in [1]. The top curve represents the stacked worst case undamped response to sequential excitations, and the next curve illustrates that the mean plus three-sigma undamped response for random time selections is significantly less than the worst case. The mean plus three-sigma response statistics are computed by calculating the absolute maximum residual displacement response for M scenarios each having N excitations, and then computing the statistical representation from the array of M maxima.

The equation of the statistical response for zero damping (determined empirically from Figure 3) is only a function of the number of excitations, N .

$$\text{Statistical Undamped Normalized Response} = (2N)^{1/2} \text{ for } N \geq 2 \quad (7)$$

The statistical damped response results in Figure 3 are presented as a family of curves for various values of the decay constant parameter, D . This parameter (ranging from 0 to unity) was selected because it is the average exponential decay of the response between excitations. Sufficient analyses were conducted to verify that D provides a general representation independent of the relative magnitudes of ζ , f , τ_0 and t_0 .

The curves are not defined for more than 40 sequential excitations as computational expense becomes a restriction for large values of N . However, an upper bound on the normalized response can be estimated using the infinite series expression of equation (6). It is refreshing to observe that equation (6) does indeed bound the curves for all values of D . However, as D approaches unity, use of this upper bound may be overconservative. For this reason, a technique for extrapolating the data of Figure 3 has been developed.

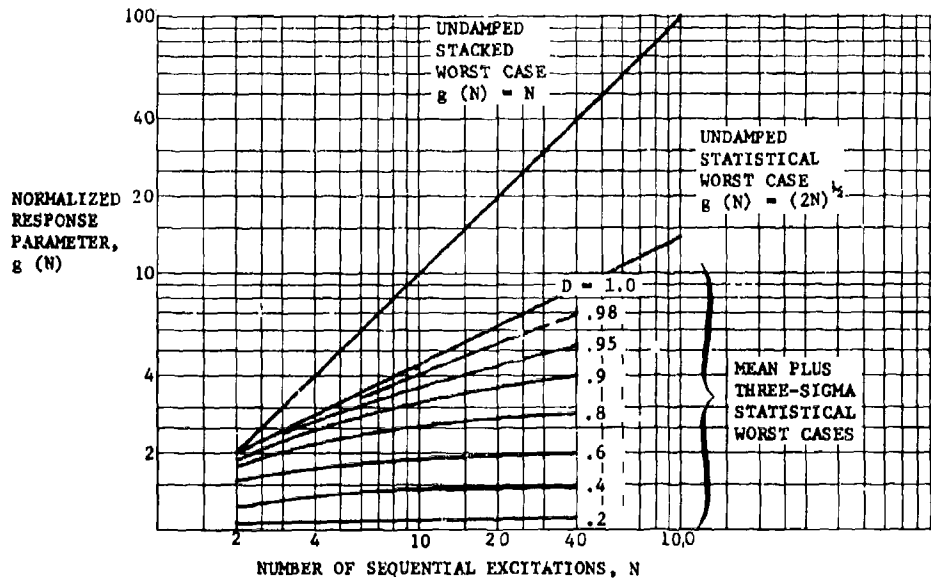


Figure 3 Statistical Response Results for Sequential Excitations

EXTRAPOLATION APPROACH

The fraction of the stacked worst case undamped response represented by equation (6) is $[N(1-D)]^{-1}$. One might suspect that the statistical results are a fraction of the undamped statistical curve also related to the function $[N(1-D)]^{-1}$. Based on equations (6) and (7), assume that

$$\frac{\text{Statistical Damped}}{\text{Normalized Response}} = \beta(2N)^{.45} \quad (8)$$

where β is a function of $[N(1-D)]^{-1}$.

Returning to Figure 3, constant values of β are lines parallel to the undamped curve $(2N)^{.45}$. When such lines are drawn for various values of β , each constant β line intersects several of the constant D lines. When the parameter $[N(1-D)]^{-1}$ is calculated at each intersection for a given value of β , it is approximately constant, too. Figure 4 plots the observed relationship, which is well-behaved for $[N(1-D)]^{-1} < 1$. The extrapolation method was checked for two simple example cases ($D=.95$, $N=100$ and $D=.98$, $N=150$) and found to be extremely accurate, as illustrated in Figure 4.

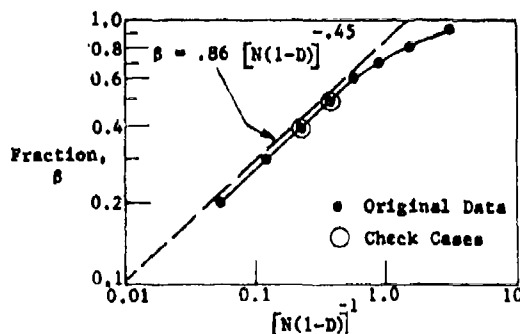


Figure 4 Extrapolation Parameter

RECOMMENDED USE OF RESULTS

- 1) Based on ζ , f , τ_0 and t_0 , calculate

$$D = e^{-2\pi\zeta f(t_0 + \tau_0)}$$
- 2) Use N and D and direct interpolation of Fig. 3 to get the normalized response. If extrapolation of Figure 3 is required, get the normalized response as follows: use equation (6) for $D \leq .5$, and for $D > .5$ use Figure 4 to get β and then apply equation (8).
- 3) Calculate the worst case residual response to a single excitation using the method described in reference [1], and multiply by the results of 2) above to get the mean plus three-sigma response.

DISCUSSION

The results described herein apply to the residual displacement response of a vibration mode excited by a sequence of simple forcing functions. The only forcing functions evaluated in this study are lower in frequency than the dominant response mode being investigated. For relatively high frequency excitations, the statistical results do not apply because the uniform distribution assumed for τ is no longer equally likely to correspond to spectral peaks and valleys. In addition, the results presented assume that all sequential excitations have the same rise time parameter, \bar{F} from Figure 2. If \bar{F} varies from excitation to excitation, the statistical analysis approach described here may be repeated accounting for the specific \bar{F} probability distribution. Although these results are derived specifically for triangular waveforms, the probability of τ corresponding to a spectral peak or valley is similar for other waveforms and the results should not be seriously compromised by this factor. For these results to apply, it is more important that all excitations in the sequence are similar to one another than it is for them to resemble the triangular wave.

REFERENCES

1. W. J. Kacena, "Use of Shock Spectra to Evaluate Jitter of a Flexible Maneuvering Spacecraft," The Shock and Vibration Bulletin, Vol. 48, Part 3, pp 39-47, September 1978.
2. Handbook of Chemistry and Physics, 40th Edition, p 296, March 1959.

ON DETERMINING THE NUMBER OF DOMINANT MODES
IN SINUSOIDAL STRUCTURAL RESPONSE

W. L. Hallauer, Jr. and A. Franck
Department of Aerospace and Ocean Engineering
Virginia Polytechnic Institute and State University
Blacksburg, Virginia 24061

This paper addresses the problem of using structural dynamic transfer function data to determine the number of vibration modes dominant in response at a given frequency. If two or more modes are closely spaced or if response is influenced strongly by distant modes, then the number of dominant modes may not be evident from examination of transfer function plots, and quantitative methods may be required. Two relatively simple methods which have been used previously are reviewed, and a more effective new method, called the vector-fit method, is described in detail. Applications of these methods are given with the use of numerically simulated transfer function data.

1. INTRODUCTION

At any particular frequency of excitation, the steady-state sinusoidal response of a structure is dominated by only a few of its indefinitely large number of vibration modes. The objective of modal testing is to measure specific parameters of the dominant modes such as natural frequencies, damping values, and mode shapes. When applicable, the best method for determining the number of dominant modes in a frequency band is simply to count resonance peaks on transfer function plots. In such a situation, modal parameters can then be calculated rather easily by modern curve-fitting algorithms, most of which require the number of dominant modes as an input value. However, if two or more modes are closely spaced, or if response is influenced strongly by modes whose resonances are outside the frequency band of interest, then peak counting may not reveal the true number of dominant modes, and subsequent curve fitting of transfer function data may produce incorrect modal parameters and/or miss modes entirely. But a quantitative method for determining the number of dominant modes may succeed where peak counting fails. If such a method should reveal the presence of previously undetected modes, then careful curve fitting or some other modal testing technique, such as multiple-shaker tuning, might successfully separate the modes.

The problem of determining the number of dominant modes was discussed extensively some years ago in connection with the number of shakers required to separate modes in multiple-shaker modal testing. Traill-Nash [1] intro-

duced the "effective number of degrees of freedom" at a given frequency, which he defined as being the number of motion coordinates required to represent with accuracy structural response at that frequency. He concluded that the number of shakers must equal or exceed the effective number of degrees of freedom. Bishop and Gladwell [2] suggested a relationship between Traill-Nash's effective number of degrees of freedom and the number of dominant modes; subsequently, Asher [3] implicitly equated these two numbers. He then stated, in effect, that the number of shakers required equals the number of dominant modes. This contention is not generally true; the number of distinct generalized force distributions must equal the number of dominant modes, but there is no necessary relationship between the number of generalized force distributions and the number of discrete forces. Nonetheless, Asher made a significant contribution by proposing probably the first quantitative methods to determine the number of dominant modes by analysis of transfer function data.

This paper describes the theoretical basis for such a quantitative method, reviews the methods discussed by Asher, proposes a new and more effective method, and illustrates these methods with the use of numerically simulated transfer function data.

II. THEORETICAL BACKGROUND

Consider a linear structure discretized to n degrees of freedom, the time-dependent

responses of which are elements of the $n \times 1$ column matrix \ddot{x} . (Notation is listed at the end of the paper.) The governing matrix equation of motion is

$$[m] \ddot{x} + [c] \dot{x} + [k] x = f \quad (1)$$

where $[m]$, $[c]$, and $[k]$ are the $n \times n$ inertia, damping, and stiffness matrices, respectively, and f is the column matrix of time-dependent forcing. We specify that all forces vary sinusoidally at the same frequency, ω , and that all have 0° or 180° phase,

$$f = F \cos \omega t = \operatorname{Re} \left\{ F e^{i\omega t} \right\} \quad (2a)$$

After starting transients have decayed away, response is steady-state sinusoidal,

$$x = \operatorname{Re} \left\{ X e^{i\omega t} \right\} \quad (2b)$$

where the elements of amplitude vector X are generally complex, reflecting phase differences between excitation and response. The linear, frequency-dependent relationship between excitation amplitude and complex response amplitude is defined by the $n \times n$ transfer function matrix $[H(\omega)]$,

$$X = [H(\omega)] F \quad (3)$$

The standard real modal analysis solution of equation (1) for $[H(\omega)]$ begins with calculation of the real undamped natural frequencies ω_r , $r = 1, 2, \dots, n$, and the associated real mode shape vectors ϕ_r , which are the columns of modal matrix $[\phi]$ (Meirovitch [4]). Subsequently, response coordinates X_i are transformed into normal coordinates which diagonalize the mass and stiffness matrices of equation (1); then the normal coordinates are calculated by matrix inversion, and X is calculated from the normal coordinate solution in the form

$$X = [\phi] [S(\omega)] F$$

where $[S(\omega)]$ is an $n \times n$ complex matrix. Hence, the transfer function matrix is

$$[H(\omega)] = [\phi] [S(\omega)]$$

and any column, say the j th, of $[H(\omega)]$ can be written as

$$H_j(\omega) = \sum_{r=1}^n S_{rj}(\omega) \phi_r, \quad j = 1, 2, \dots, n \quad (4)$$

Thus, each column of the transfer function matrix can be expressed as a summation of the n linearly independent mode shape vectors. If we consider some subset $p < n$ of degrees of freedom and define the corresponding $p \times 1$ incomplete j th transfer function column as

$H_j^*(\omega)$, then equation (4) gives

$$H_j^*(\omega) = \sum_{r=1}^p S_{rj}(\omega) \phi_r^*, \quad j = 1, 2, \dots, n \quad (5)$$

where the degrees of freedom included in each $p \times 1$ incomplete mode shape vector ϕ_r^* are the same as those included in H_j^* . Although the summation in equation (5) extends over all modes, only p of the n ϕ_r^* vectors are independent.

If damping matrix $[c]$ were to couple the undamped normal modes (i.e., if $[\phi]^t [c] [\phi]$ were not diagonal), then the use of undamped normal modes as outlined above would be computationally inefficient, and we would probably solve for the transfer function matrix with an appropriate complex modal analysis employing complex eigenvalues and mode shape vectors. Nevertheless, the solution for each column of the transfer function matrix could still be expressed in the forms of equations (4) and (5), that is, as linear summations of n mode shape vectors, where in this case the ϕ_r would be complex vectors. The important fact, expressed in the language of matrix theory, is that each transfer function column H_j is an element in the n -dimensional vector space spanned by the n mode shape vectors, whether they be real or complex; similarly, each incomplete column H_j^* is an element in the p -dimensional vector space spanned by any p linearly independent incomplete mode shape vectors.

A useful general characteristic of structural dynamic behavior is that very few of a structure's many vibration modes are sensitive to excitation at any given frequency. These few modes then dominate the response at that frequency. If there are q such dominant modes at frequency ω , then the mathematical statements of their dominance, from equations (4) and (5), are

$$H_j(\omega) \approx \sum_q S_{rj}(\omega) \phi_r, \quad j = 1, 2, \dots, n \quad (6)$$

$$H_j^*(\omega) \approx \sum_q S_{rj}(\omega) \phi_r^*, \quad j = 1, 2, \dots, n \quad (7)$$

where \sum_q denotes summation over only the q dominant modes.

In equation (6), the q mode shape vectors associated with the dominant modes generate a q -dimensional subspace of the original n -dimensional vector space. The approximate equality in equation (6) means that

each $H_j(\omega)$ column can, with small error, be considered an element of the subspace. In equation (7), the $p \times 1$ incomplete mode shape vectors associated with the dominant modes generate a q -dimensional subspace of the original p -dimensional vector space, provided that $p > q$. Again, the approximate equality means that each $H_j(\omega)$ column is approximately an element of the subspace.

Most current methods of modal testing are capable of measuring incomplete transfer function column vectors over a frequency band of interest. The j th column H_j^* represents physically the complex response amplitude of motion sensors at p stations on the test structure due to sinusoidal forcing excitation of unit amplitude at the j th station, which does not necessarily coincide with any of the motion sensor stations. If excitation is applied successively to k different stations, then vectors H_j^* , $j = 1, 2, \dots, k$, can be measured. They are the columns of the $p \times k$ incomplete transfer function matrix $[H^*]$. (It is generally impossible to measure the complete matrix $[H]$, since a continuous structure has an indefinitely large number of degrees of freedom.)

If the structure being tested responds linearly, then each H_j^* column is represented mathematically by equation (7), which, therefore, is the basis of the methods discussed in Section III below for determining the number of dominant modes from experimental transfer function data. Each method estimates the number q of dominant vectors ϕ_r^* in equation (7), given k experimental $p \times 1$ vectors H_j^* .

One practical requirement for the correct use of equation (7) in the present context is immediately evident: since p must exceed q , as discussed above, the test engineer must guess an upper bound q_{\max} for the number of dominant modes likely to be encountered, and then he must install more than q_{\max} distinct motion sensors. This requirement does not present a significant practical obstacle, since q_{\max} for most structures should be on the order of ten or less. It is assumed in the remainder of the paper that the number of motion sensor measurements available for analysis is always greater than the number of dominant modes.

In vehicle modal testing, it is usually feasible to install a substantial number of motion sensors, but the number of exciters or excitation stations is often much smaller due to practical limitations. Hence, we assume that $k \leq p$ in most of what follows.

III. QUANTITATIVE METHODS FOR DETERMINING THE NUMBER OF DOMINANT MODES

III.1 TRANSFER FUNCTION DETERMINANT METHOD

This method involves analysis of square transfer function matrices, which are formed by the use of only k of the p available motion sensor measurements. Thus, $[H^*]$ is a $k \times k$ matrix. If, in the first case, the number of exciters is less than or equal to the number of dominant modes, $k \leq q$, then according to equation (7), the k columns of $[H^*]$ generally will be linearly independent; hence $[H^*]$ will be non-singular and its determinant will be non-zero, $\det [H^*] \neq 0$ for $k \leq q$. But if the number of exciters is increased until it just exceeds the number of dominant modes, $k = q + 1$, then the k columns will be approximately dependent, so that $[H^*]$ will be nearly singular and its determinant will be close to zero, $\det [H^*] \approx 0$ for $k > q$. The strategy for application of this method, therefore, is to add rows and columns of data to the transfer function matrix in unit steps until the value of k is found for which $\det [H^*] \approx 0$; then the conclusion is that $q = k - 1$.

This is a very simple method to apply, but it has some deficiencies. First, transfer function determinants are complex, so one must assess the possibly non-monotonic progression toward zero of a sequence of complex numbers. Second, the restriction to square transfer function matrices is undesirable because it prevents the use of all available motion sensor data. Both of these deficiencies are eliminated with little additional effort by the use of the Gram determinant method described below, so there appears to be no reason to develop further or test the transfer function determinant method. We note that Ibrahim and Mikulcik [5] employed a similar method, but with filtered transient response data, and found it quite satisfactory.

III.2 GRAM DETERMINANT (GRAMIAN) METHOD

This method involves analysis of a rectangular $p \times k$ transfer function matrix, $[H^*]$. The Gram matrix of $[H^*]$ is defined to be a matrix product,

$$[G_k] = [H^*]^t [H^*]$$

where the overbar indicates complex conjugacy. By this definition, the Gram matrix is a $k \times k$ Hermitian matrix. The Gram determinant, or Gramian, is defined to be

$$c^{(k)} = \det [G_k]$$

It can be proved that the Gramian is real and non-negative.

The Gramian of a transfer function matrix is a quantitative measure of the degree of linear dependence of the column vectors, H_j^* , $j = 1, 2, \dots, k$. Specifically, the set of vectors is linearly dependent if and only if the Gramian is zero (Hildebrand [6]). Moreover, it is reasonable to expect that if the set of vectors is almost but not precisely linearly dependent, then the Gramian should be nearly zero. As is discussed in Section III.1, any q or fewer columns of $[H^*]$ generally are linearly independent and, hence have non-zero Gramians, $G^{(k)} > 0$ for $k = 1, 2, \dots, q$. But any set of more than q columns will be approximately dependent and have very small or zero Gramians, $G^{(k)} \approx 0$ for $k > q + 1$. Therefore, the basic strategy for application of this method is to add columns of data to the transfer function matrix in unit steps until the value of k is found for which $G^{(k)} \approx 0$; then, the conclusion is that $q = k - 1$.

It is necessary in applying this method to separate the change in Gram determinant value due to change in degree of linear dependence from that due simply to change in determinant size. If, for example, all Gram matrix elements are numerically of order 10^{-2} , then, without change in degree of linear dependence, $G^{(1)}$ will be of order 10^{-2} , $G^{(2)}$ of order 10^{-4} , $G^{(3)}$ of order 10^{-6} , and so forth. This characteristic of determinants will obviously mask the Gramian test for linear dependence unless Gram matrix elements are of order 1. In applications of the Gramian method, the authors have attempted to minimize the masking by normalizing each column of $[H^*]$ so that the corresponding diagonal element of the Gram matrix is 1, i.e., $(H_j^*, H_j^*) = 1$, $j = 1, 2, \dots, k$, where H_j^* here denotes the normalized column rather than the original column in physical units. The numerical results of Section IV.3 suggest that this *ad hoc* measure is effective in filtering out Gramian variation with Gram matrix size.

Asher [3] described and discussed both the transfer function determinant and the Gram determinant methods. He recognized that in applying either method, one might find it difficult to decide how small a generally non-zero determinant value must be in order to indicate linear dependence correctly. The numerical results of Section IV.3 confirm that the absence of a definite smallness criterion is indeed a weakness of the Gramian method. Even though all Gramian values are referenced to $G^{(1)} = 1$ by virtue of the normalization procedure described above, examples for different situations show Gramian values $G^{(q+1)}$ of orders 10^{-1} , 10^{-2} , and even 10^{-3} .

Another deficiency of the Gramian method is that it can correctly indicate linear dependence, yet underestimate the number of dominant modes. To understand how this can happen, consider a simple example in which there are two dominant modes. The analysis of three given, distinct transfer function vectors, denoted v_1 , v_2 , and v_3 , then should indicate two modes. The set of three vectors is linearly dependent, but suppose also that v_1 and v_2 are independent and v_1 and v_3 are dependent. If the transfer function matrix is defined as $[H^*] = [v_1, v_2, v_3]$, then $G^{(1)} = 1$, $G^{(2)} > 0$, and $G^{(3)} = 0$, leading to the correct conclusion that $q = 2$. If, on the other hand, we define $[H^*] = [v_1, v_3, v_2]$, then $G^{(1)} = 1$ and $G^{(2)} = G^{(3)} = 0$, leading to the incorrect conclusion that $q = 1$. An instance of this particular case occurring in a realistic situation is presented in Section IV.3. (See Figures 12b,c and the associated discussion.) It is clear that the ordering of vectors in the $p \times k$ transfer function matrix affects all Gramian values except $G^{(1)} = 1$ and $G^{(k)}$, which is invariant with column and row ordering.

The Gramian method then has some serious weaknesses. Perhaps for this reason, it apparently has not been employed widely. The authors have located only one published application, that by Klosterman [7]. The vector-fit method to be discussed next is, to a considerable extent, free of the weaknesses of the Gramian method.

III.3 VECTOR-FIT METHOD

A concept analogous to the number of dominant modes of a vibrating structure is that of a "best approximating subspace". Cliff [8] discussed this concept in the context of control theory. Given a set of k p -dimensional vectors, one can calculate the particular m -dimensional basis ($m < k$) which, among all possible m -dimensional bases, does the best job of approximately spanning the set of k vectors, with error minimized in the least-squares sense. In other words, the k vectors are "fit" to the best approximating m -dimensional subspace. The method developed here to solve for the number of dominant modes follows Cliff's general approach; hence, it is referred to as the vector-fit method.

Given the $p \times k$ transfer function matrix $[H^*]$ for frequency ω , the general stepwise procedure for application of the vector-fit method is as follows:

1. A particular p -dimensional complex unit vector u_j is calculated from $[H^*]$. Among all possible unit vectors, u_j alone

has the property of producing the best, in a sense to be defined, set of one-term approximations to the transfer function columns. This set of approximations takes the form

$$H_j^* = C_{j1} u_1, j = 1, 2, \dots, k$$

where the C_{j1} generally are complex constants. Next, the real scalar error $E^{(1)}$ associated with this set of approximations is calculated.

2. A second unit vector u_2 is calculated. It is orthogonal to u_1 . Among all possible unit vectors orthogonal to u_1 , u_2 alone has the property of producing, in conjunction with u_1 , the best set of two-term approximations to the transfer function columns. This set takes the form

$$H_j^* = \sum_{i=1}^2 C_{ji} u_i, j = 1, 2, \dots, k$$

Next, error $E^{(2)}$ associated with this set of approximations is calculated.

.

- m. The mth unit vector u_m is calculated. It is orthogonal to all other u_i , $i = 1, 2, \dots, m-1$. Vector u_m has the property of producing, in conjunction with u_1, u_2, \dots, u_{m-1} , the best set of m-term approximations to the transfer function columns. This set takes the form

$$H_j^* = \sum_{i=1}^m C_{ji} u_i, j = 1, 2, \dots, k$$

Next error $E^{(m)}$ associated with this set of approximations is calculated.

.

Each step introduces a refinement of the approximation, so the error diminishes in each step, $E^{(m)} \leq E^{(m-1)}$. If, after $m > 1$ steps of this procedure, we find that $E^{(m)} \approx 0$ relative to $E^{(1)}$, then we may reasonably conclude that the set of transfer function vectors

is spanned approximately, with very small error, by an m-dimensional basis. According to equation (7), then, there are m dominant modes at frequency ω , i.e., $q = m$. It is quite unlikely that the vectors u_i will be identical to the mode shape vectors ϕ_i^* of equation (7), since the u_i are orthogonal by definition while the ϕ_i^* need not and generally will not be orthogonal. Nonetheless, it is certain that both sets u_i and ϕ_i^* span the same q-dimensional vector space.

If $p < k$ and the procedure is carried through p steps, then $E^{(p)} \approx 0$ since the p independent u_i exactly span p-dimensional space. If, on the other hand, $k < p$ and the procedure is carried through k steps, then $E^{(k)} \approx 0$ since the k independent u_i exactly span the subspace defined by the k transfer function column vectors. (This case is simply orthogonalization of a vector set, similar to the Gram-Schmidt procedure.) Hence, in order for the vector-fit method to produce a correct evaluation of the number of dominant modes, it is necessary that p and k each must exceed q. That is, the test engineer must provide both more motion sensors and more excitation stations than the maximum number of dominant modes likely to be encountered. In application, the method itself indicates if too few motion sensors or excitation stations have been used, and this is illustrated in Section IV.3.

It is worthy of note that each of the three methods described for identification of the presence of q dominant modes requires a minimum of q + 1 motion sensors and q + 1 excitation stations.

The theory associated with the calculations discussed above is developed next. Let a basis for p-dimensional space of complex vectors consist of p orthogonal unit vectors u_1, u_2, \dots, u_p , which are unknown at this point. Any transfer function column vector H_j^* , $j = 1, 2, \dots, k$, can be expressed as the summation

$$H_j^* = \left(\sum_{i=1}^m + \sum_{i=m+1}^p \right) (\bar{u}_i, H_j^*) u_i$$

The basis vectors are orthogonal in the Hermitian sense, so

$$(\bar{H}_j^*, H_j^*) = \left(\sum_{i=1}^m + \sum_{i=m+1}^p \right) (\bar{u}_i, H_j^*) (\bar{H}_j^*, u_i)$$

Hence, we may define as follows the squared scalar error associated with approximation of H_j^* as a series sum in only the first m basis vectors,

$$\begin{aligned} (e_j^{(m)})^2 &= \sum_{i=m+1}^p (\bar{u}_i, H_j^*) (\bar{H}_j^*, u_i) \\ &= (\bar{H}_j^*, H_j^*) - \sum_{i=1}^m (\bar{u}_i, H_j^*) (\bar{H}_j^*, u_i) \end{aligned}$$

The appropriate total or global error, defined in the least-squares sense over all H_j^* , is

$$E^{(m)} = \left[\sum_{j=1}^k (e_j^{(m)})^2 \right]^{1/2} = \left[\sum_{j=1}^k (\bar{H}_j^*, H_j^*) - \sum_{j=1}^k \sum_{i=1}^m (\bar{u}_i, H_j^*) (\bar{H}_j^*, u_i) \right]^{1/2}$$

For given m , we wish to determine the basis vectors u_i so as to minimize $E^{(m)}$ by maximizing the double-summation term. With a few steps of matrix algebra, that term is cast into the more useful form

$$\sum_{j=1}^k \sum_{i=1}^m (\bar{u}_i, H_j^*) (\bar{H}_j^*, u_i) = \sum_{i=1}^m \bar{u}_i^t [A] u_i$$

where $[A] = [H^*] [H^*]^t$ is a $p \times p$ Hermitian matrix with p real non-negative eigenvalues $\lambda_1 \geq \lambda_2 \geq \dots \geq \lambda_p \geq 0$ and p corresponding complex, mutually orthogonal unit eigenvectors $\psi_1, \psi_2, \dots, \psi_p$. Thus, for given m , we wish to minimize

$$E^{(m)} = \left[\sum_{j=1}^k (\bar{H}_j^*, H_j^*) - \sum_{i=1}^m \bar{u}_i^t [A] u_i \right]^{1/2}$$

Consider first $m = 1$. The maximum value assumed by the Hermitian quadratic form $\bar{u}_1^t [A] u_1$ is equal to the largest eigenvalue λ_1 , and this maximum results if $u_1 = \psi_1$ (Franklin [9]). Hence, the minimum associated error is

$$E_{\min}^{(1)} = \left[\sum_{j=1}^k (\bar{H}_j^*, H_j^*) - \lambda_1 \right]^{1/2}$$

Next, for $m = 2$ we wish to minimize

$$E^{(2)} = \left[\sum_{j=1}^k (\bar{H}_j^*, H_j^*) - \lambda_1 - \bar{u}_2^t [A] u_2 \right]^{1/2}$$

For all possible u_2 orthogonal to $u_1 = \psi_1$, the maximum value assumed by quadratic form $\bar{u}_2^t [A] u_2$ is equal to the second eigenvalue λ_2 , and this maximum results if $u_2 = \psi_2$ (Franklin [9]). Thus,

$$E_{\min}^{(2)} = \left[\sum_{j=1}^k (\bar{H}_j^*, H_j^*) - \sum_{i=1}^2 \lambda_i \right]^{1/2}$$

This reasoning can be extended easily to show that the minimum error for arbitrary m ($1 \leq m \leq p$) is

$$E^{(m)} = \left[\sum_{j=1}^k (\bar{H}_j^*, H_j^*) - \sum_{i=1}^m \lambda_i \right]^{1/2} \quad (8)$$

where $u_i = \psi_i$. To simplify notation, it is understood in equation (8) and in the discussion and numerical examples to follow that $E^{(m)}$ denotes the minimum error, even though subscript min is deleted.

We can now reiterate and summarize the vector-fit method for determining the number q of dominant modes at a given frequency. From the $p \times k$ transfer function matrix $[H^*]$, the $p \times p$ Hermitian matrix $[A] = [H^*] [H^*]^t$ is formed. It is necessary that $p \geq q + 1$ and $k \geq q + 1$. Next, the real eigenvalues of $[A]$, $\lambda_1 \geq \lambda_2 \geq \dots \geq \lambda_p \geq 0$, are calculated. Next, for $m = 1, 2, \dots, p$, the minimum error values are calculated from equation (8). The smallest integer m for which $E^{(m)} \approx 0$ relative to $E^{(1)}$ then is equal to the number q of dominant modes. Note that the eigenvectors of $[A]$, $\psi_1, \psi_2, \dots, \psi_p$, need not be calculated.

It can be proved easily that the error values $E^{(m)}$ are entirely independent of the numbering or ordering schemes used to identify motion sensors and exciters or to arrange elements in the transfer function matrix. In other words, any of the rows of $[H^*]$ can be interchanged and/or any of the columns can be interchanged without changing the values of $E^{(m)}$. Hence, the vector-fit method has no weakness comparable to the dependence on vector ordering of the Gramian method.

IV. NUMERICAL SIMULATION STUDY

Two mathematical models have been used for numerical simulation of experimental application of the vector-fit and Gramian methods. The models were designed to have frequency bands of high modal density with prescribed numbers of dominant modes. The basic objective of the numerical study then was to determine if the vector-fit and Gramian methods are capable of correctly determining the number of dominant modes. Other objectives were to compare the two methods and to develop guidelines for applying the methods and interpreting the results.

To simplify calculations, it was specified that each model have hysteretic damping which does not couple the undamped normal modes. Hence, transfer function matrix elements were calculated exactly from the equation

$$H_{ij} = \sum_{r=1}^n \frac{\phi_{ir} \phi_{jr}}{M_r \omega_r^2 \left[\left(1 - \frac{\omega^2}{\omega_r^2}\right) + i g_r \right]}$$

where ϕ_{ir} is the i th element of the complete mode shape vector ϕ_r , $M_r = \phi_r^T [m] \phi_r$ is the generalized mass of the r th normal mode, and ω_r and g_r are, respectively, the natural frequency and hysteretic damping of the r th mode.

IV.1 TEN-MODE MODEL

The mode shapes of this model are those of the first ten out-of-plane vibration modes of the uniform stretched membrane shown on Figure 1,

$$\phi_{ir} = A_r \sin \left(\frac{m_r \pi x_i}{1.3} \right) \sin \left(\frac{n_r \pi y_i}{1.0} \right)$$

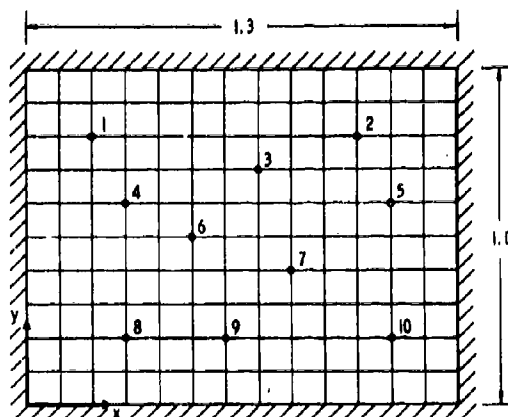


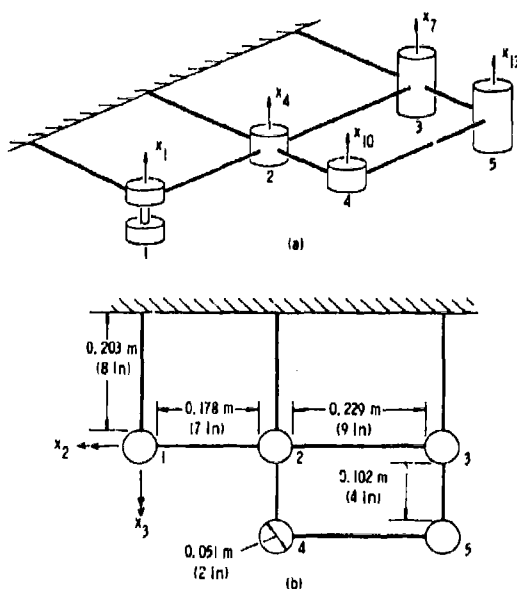
Fig. 1 Stretched membrane for mode shapes of ten-mode model

where integers m_r and n_r are the numbers of half-wavelengths for the r th mode listed in Table 1, x_i and y_i are coordinates of the motion sensor/exciter stations shown on Figure 1, and constant A_r for the r th mode is chosen so that the numerically largest mode shape element equals one. Other modal parameters, as listed in Table 1, are not those of the uniform membrane, but rather were selected to produce a mathematical model with four very closely spaced modes in the vicinity of 100 on the frequency scale and six more modes outside the region of high modal density. Thus, $q = 4$ in a frequency band of roughly three units centered at 100, so the methods under study, if successful, should indicate accordingly. Since this model has limited physical significance, all quantities are considered to be dimensionless.

TABLE 1

Parameters of ten-mode model

r	1	2	3	4	5	6	7	8	9	10
ω_r	67.6	82.0	91.2	98.9	99.4	100.1	101.4	110.7	117.6	132.3
g_r	0.015	0.017	0.017	0.021	0.019	0.023	0.024	0.026	0.027	0.03
M_r	0.02	0.009	0.01	0.012	0.011	0.01	0.009	0.011	0.013	0.009
m_r, n_r	1,1	2,1	1,2	3,1	2,2	3,2	1,3	4,1	2,3	4,2



Figs. 2 Fifteen-degree-of-freedom model: (a) pictorial view with translation dof; (b) plan view

IV.2 FIFTEEN-DEGREE-OF-FREEDOM MODEL

This model, unlike the ten-mode model, is based entirely on a physical structure, the cantilevered, rectangular plane grid shown on Figures 2a and b. The model was designed to have two modes with nearly identical natural frequencies, as shown in Table 2. To achieve such close modes, an optimization technique similar to that of Hallauer *et al.* [10] was used.

Each elastic member of the model is a steel bar having Young's modulus $E = 200 \text{ GPa}$ ($29 \times 10^6 \text{ psi}$), shear modulus $G = 82.7 \text{ GPa}$ ($12 \times 10^6 \text{ psi}$), and diameter of 6.35 mm (0.25 inch). (The fundamental units of pounds inches, and seconds were used in all calculations.) Each bar may twist about its axis and bend out of the grid plane, and each is clamped at both ends by either the rigid support wall or a rigid cylindrical joint member of 0.051-m (2-inch) diameter. The five node points of the model are the intersections of the bar centerlines in the grid plane. The fifteen degrees of freedom then consist of one out-of-plane translation and two out-of-plane rotations of each node point. The translations are identified in Figure 2a, and the rotations of node 1, for example, are identified in Figure 2b. The nodal lumped mass and moment of inertia (for both rotational dof) associated with each rigid joint are listed in Table 2. To account approximately for distributed inertia of the bars, finite element consistent mass matrices were used, with bar density taken to be 7859 kg/m^3 ($7.3536 \times 10^{-4} \text{ lb-sec}^2/\text{in}^4$). Modal hysteretic damping constants g_r were specified to be 0.015 for modes 1 and 2, 0.018, 0.022, and 0.026 respectively for modes 3, 4, and 5, 0.03 for modes 6-10, and 0.035 for modes 10-15.

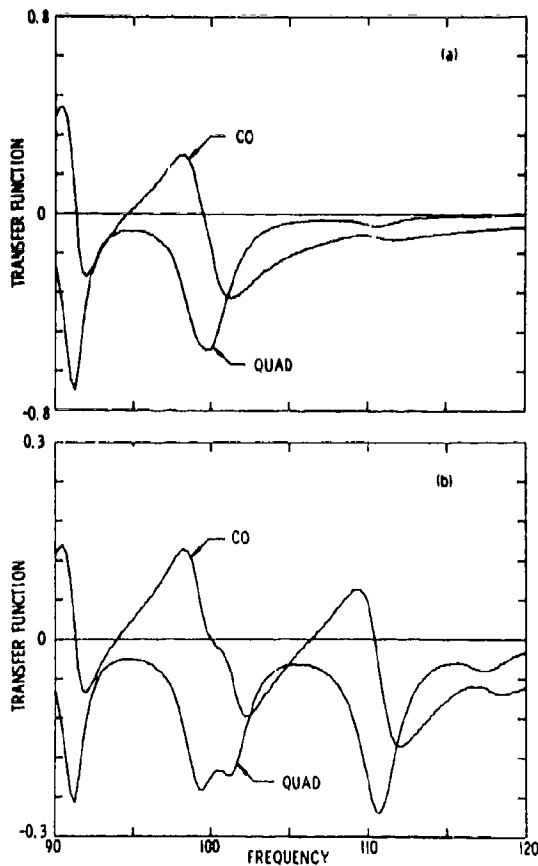
IV.3 RESULTS AND DISCUSSION

Consider first the ten-mode model. Typical transfer functions are shown on Figures 3a and b, with the coincident (co) or real parts and the quadrature (quad) or imaginary parts plotted separately. Qualitative inspection of these and other transfer functions seems to indicate the presence of only two dominant modes in the vicinity of frequency 100. But there are actually four dominant modes in that region, as listed in Table 1.

TABLE 2

Inertia parameters and close modes of fifteen-dof model

Node	Inertia parameters		Close modes		
	Mass kg	Moment of inertia 10^{-3} kg-m^2	r $\omega_r(r/s)$	3	4
1	0.5114	0.5570	$\phi_{1,r}$	1.000	1.000
2	1.4994	1.7199	$\phi_{4,r}$	0.031	-0.274
3	2.0390	4.1627	$\phi_{7,r}$	0.446	-0.444
4	0.4756	0.1154	$\phi_{10,r}$	-0.421	-0.236
5	2.0424	4.1833	$\phi_{13,r}$	-0.151	0.216



Figs. 3 Typical transfer functions for the ten-mode model: (a) $H_{3,3}(w)$; (b) $H_{7,7}(w)$

To begin numerical application of the vector-fit method, we examine first errors calculated from the complete 10×10 transfer function matrix. Such a large matrix will not generally be required, but examining this case first establishes a reference and provides guidelines for interpreting the error values and, more generally, for applying the method. Since transfer functions are usually plotted versus excitation frequency, it seems natural and, in fact, proves advantageous also to calculate and plot error values versus excitation frequency. Errors $E^{(m)}$, $m = 1, 2, \dots, 10$, for the complete transfer function matrix were calculated from equation (8) and are plotted on Figure 4. Note the relatively large variations with frequency and the peaking of $E^{(1)}$, $E^{(2)}$, and $E^{(3)}$. Note also that $E^{(4)}$ is on the order

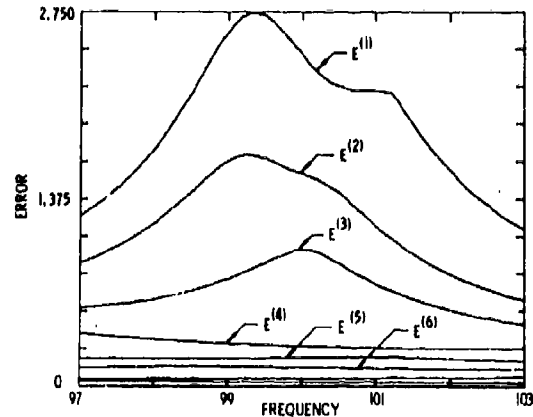
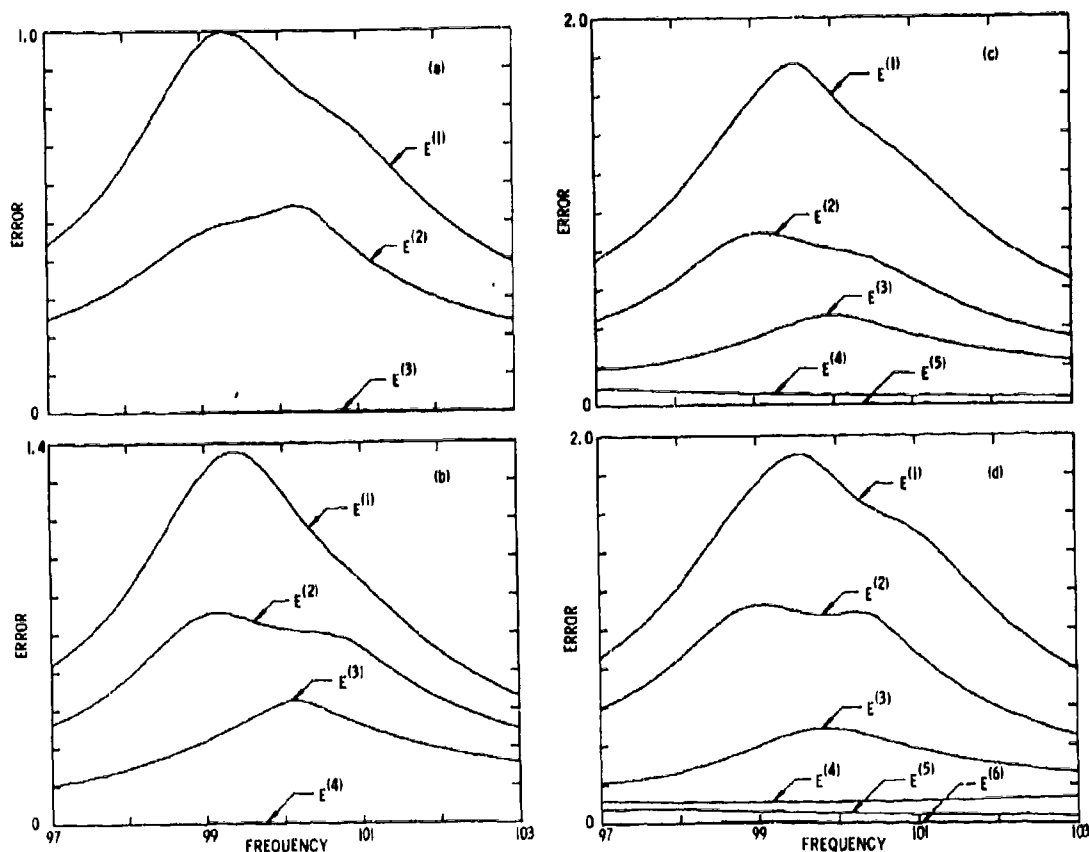


Fig. 4 Reference error graph for the ten-mode model with all motion sensors and all exciters

of 10% of the maximum value of $E^{(1)}$, and that $E^{(4)}$ varies only slightly with frequency. As stated in Section III.3, the result that $E^{(4)} \ll E^{(1)}$ indicates that there are four dominant modes. But it is also important that $E^{(4)} \neq 0$ and that $E^{(4)}$, $E^{(5)}$, etc. vary slowly with frequency in comparison with $E^{(1)}$, $E^{(2)}$, and $E^{(3)}$. From these observations, we conclude that four modes dominate but do not completely describe the response in this narrow frequency band, and that the contributions of distant modes remain relatively constant in this band. Both conclusions are quite reasonable in view of the nature of the ten-mode model. Thus, this reference case suggests that in examining graphs of error versus frequency, we should use not only the basic criterion $E^{(q)} \ll E^{(1)}$, but also the additional criteria that $E^{(q)} \neq 0$, that $E^{(q)}$, $E^{(q+1)}$, etc. should vary slowly with frequency in comparison with $E^{(1)}$, $E^{(2)}$, ..., $E^{(q-1)}$, and that plots versus frequency of $E^{(1)}$, $E^{(2)}$, ..., $E^{(q-1)}$ should exhibit peaks. An exceptional case for which all these criteria might not apply is that of a distant mode contributing significantly to response. In this case, we might expect to find a relatively large, slowly varying, and non-peaking $E^{(m)}$ for $m < q$.

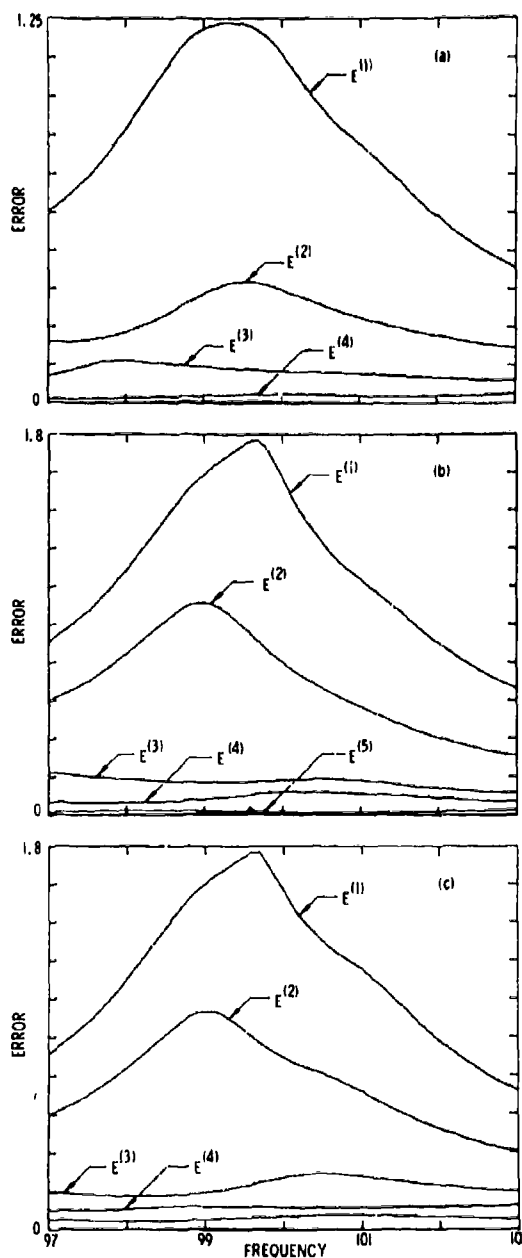
Figures 5 a-d are plots of errors calculated from responses at seven motion sensor locations due successively to excitation at three, four, five and six locations. This simulates a realistic testing approach in which



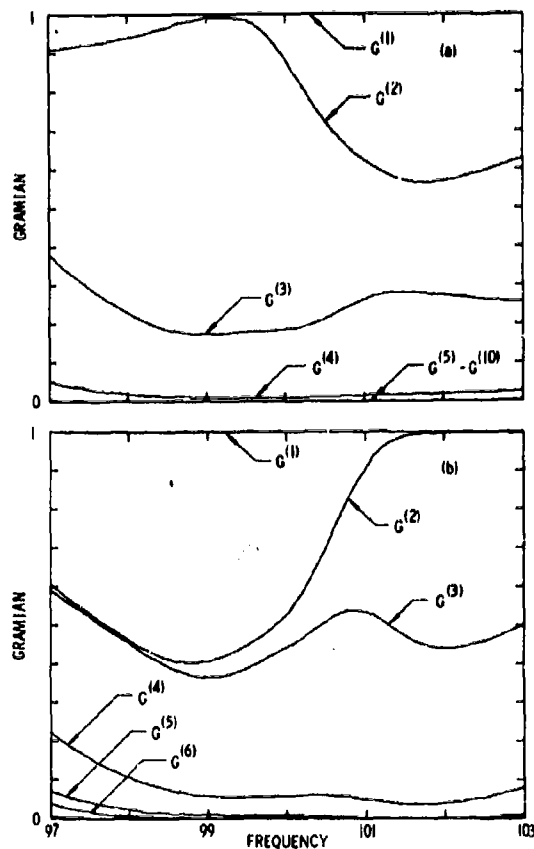
Figs. 5 Error graphs for the ten-mode model with motion sensors 1, 2, 5, 6, 8, 9, 10: (a) exciters 1, 6, 9; (b) exciters 1, 2, 6, 9; (c) exciters 1, 2, 6, 8, 9; (d) exciters 1, 2, 6, 8, 9, 10

very few exciters are applied initially, and additional exciters are applied as required. In Figure 5a for three exciters, $E^{(2)}$ is not much smaller than $E^{(1)}$, and $E^{(3)} = 0$, as required by the theory of Section III.3. (The very small non-zero values on this and other computer-generated plots are due to round-off errors.) Clearly, more exciters are required to indicate correctly the number of dominant modes. The addition of a fourth exciter (i.e., another column in $[H^*]$) leads to Figure 5b, which also indicates the need for at least one more exciter. With five exciters, however, Figure 5c shows that $E^{(4)}$ varies slowly with frequency and is non-zero yet much smaller than $E^{(1)}$. We conclude, therefore, that $q = 4$. Figure 5d for six exciters substantiates the conclusion.

Unfortunately, interpretation of the error plots is not always as unambiguous as it appears to be with Figures 4 and 5. There is a definite dependence on the motion sensor and exciter locations represented in the transfer function matrix. These points are illustrated on the error plots of Figures 6 a,b, and c, which were calculated for different sets of motion sensor/exciter locations than those of Figures 4 and 5. Figure 6a for five motion sensors and five exciters can be interpreted as indicating four dominant modes; but this interpretation is substantially weaker here than for Figures 4 and 5c,d since $E^{(3)}$ on Figure 6a is only slightly peaked and is very small relative to $E^{(1)}$. Figure 6b for six motion sensors and six exciters is ambiguous; one might infer that it indicates three, four, or five dominant modes, with three being perhaps



Figs. 6 Error graphs for the ten-mode model: (a) motion sensors/excitors 2, 3, 4, 7, 8; (b) motion sensors/excitors 2, 3, 4, 7, 8, 10; (c) motion sensors/excitors 2, 3, 4, 6, 8, 10

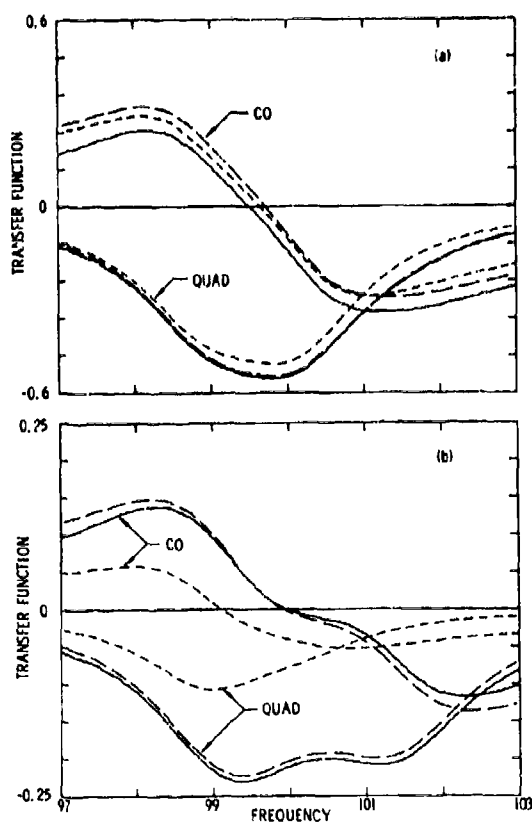


Figs. 7 Gramian graphs for the ten-mode model with all ten motion sensors: (a) all ten exciters applied in forward order, 1, 2, . . . , 10; (b) all ten exciters applied in reverse order, 10, 9, . . . , 1

the most likely interpretation. Figure 6c, also with six motion sensor/exciter locations but one different location than Figure 6b, permits a somewhat more certain interpretation of four dominant modes.

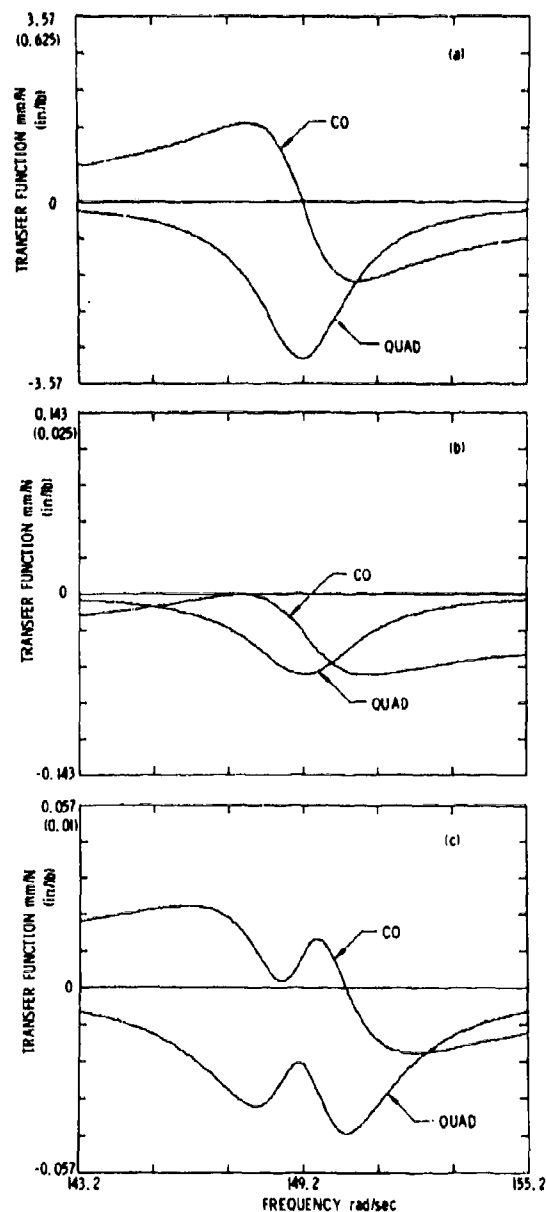
One can observe from the vertical axis scales on Figures 4 - 6 that all non-zero error values tend to increase as columns are added to the transfer function matrix. This tendency appears not to have any useful significance.

Next, we examine the Gramian method as applied to the ten-mode model. Figure 7a is a graph of Gramians plotted versus frequency in the region of high modal density. Gramians $G(1) - G(10)$ were calculated from complete

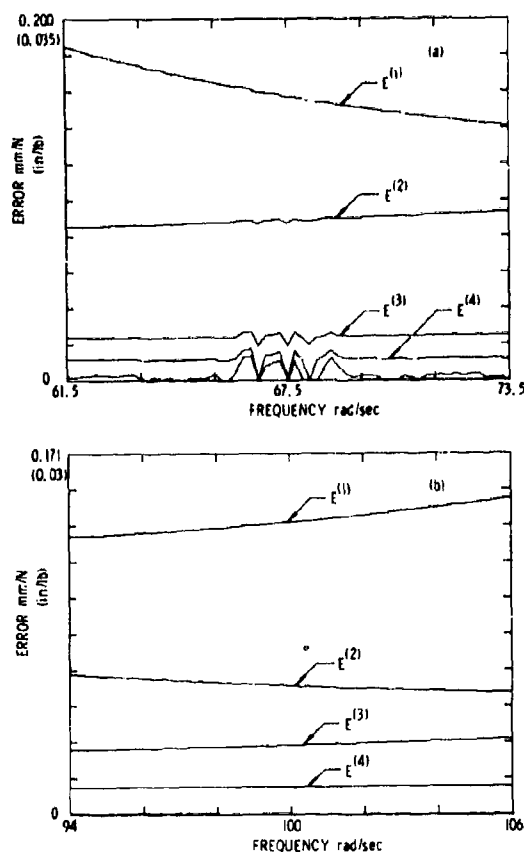


Figs. 8 Comparisons of exact and approximate transfer functions for the ten-mode model, with solid lines for exact values, long dashes for modes 4, 5, 6, and 7, and short dashes for modes 4 and 6: (a) $H_{3,3}(\omega)$; (b) $H_{7,7}(\omega)$

10 x 1 transfer function vectors, with the vectors applied in the order of the station numbering shown on Figure 1, i.e., 1, 2, ..., 10. Recall that the identification criterion for this method is $G^{(q+1)} \approx 0$, where $G^{(1)} = 1$ by virtue of transfer function vector normalization. So $G^{(5)}$ should be nearly zero in this case. A tabulation (not included) of $G^{(5)}$ for Figure 7a shows values in the ranges 10^{-3} and 10^{-4} . Figure 7b is a graph of Gramians $G^{(1)} - G^{(10)}$ also calculated from 10 x 1 transfer function vectors, but with the vectors applied in reverse order of the station numbering, i.e., 10, 9, ..., 1. Values of $G^{(5)}$ for Figure



Figs. 9 Transfer functions for the fifteen-dof model: (a) $H_{1,1}(\omega)$; (b) $H_{4,10}(\omega)$; (c) $H_{1,13}(\omega)$



Figs. 10 Error graphs for the fifteen-dof model with motion sensors/exciters 1, 4, 7, 10, 13: (a) in the region of a single isolated mode; (b) in a region of very little modal activity

7b are in the ranges 10^{-1} and 10^{-2} . The vast differences between the curves on Figure 7a and those on Figure 7b illustrate the vector-ordering dependence of the Gramian method, and the different magnitudes of $G^{(5)}$ on the two graphs illustrate the indefiniteness of the smallness criterion, $G^{(q+1)} \approx 0$.

Finally for the ten-mode model, Figures 8a and b demonstrate the significance on typical transfer function plots of the dominance of four modes. These graphs show exact coincident and quadrature values of $H_{3,3}(\omega)$ and $H_{7,7}(\omega)$, approximate values calculated from only the four dominant modes, and approximate values calculated from only modes four and

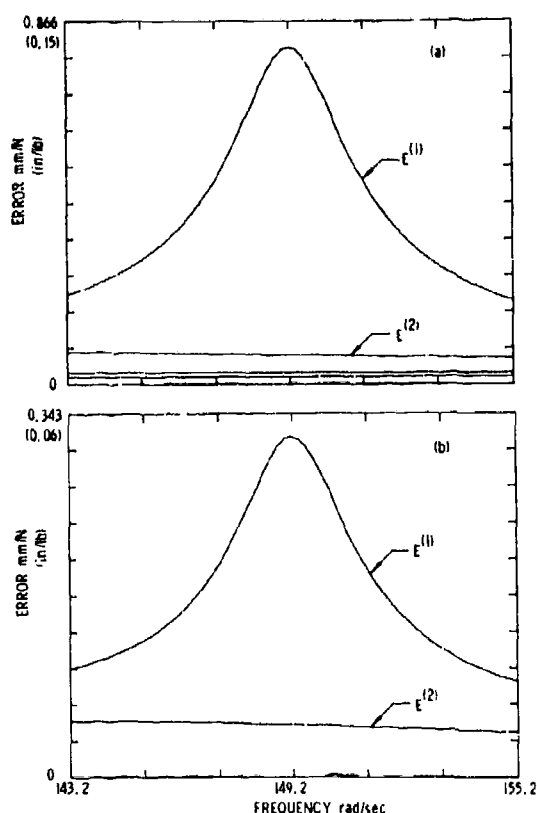
six, two of the dominant modes. Whereas modes four and six alone dominate $H_{3,3}$, all four of the close modes make comparable contributions to $H_{7,7}$.

Consider next the fifteen-dof model, which has the pair of close modes listed in Table 2. In testing of this model, it would be natural to instrument and to provide forcing excitation at the five translation degrees of freedom shown on Figure 2a, so we will analyze the 5×5 incomplete transfer function matrix associated with those degrees of freedom.

Figures 9a,b, and c are selected transfer functions in a narrow band about the close natural frequencies. Figure 9a for $H_{1,1}(\omega)$ has the character of most transfer function elements in this frequency band, namely, it seems to indicate only a single, isolated mode. Figure 9b for $H_{4,10}(\omega)$ suggests the presence of more than one mode, but the asymmetry of the coincident response curve would probably be attributed to a distant mode rather than to close modes. Of all the elements of the 5×5 $[H^*]$, only $H_{1,13}(\omega)$ shown on Figure 9c provides definite evidence of the presence of two close modes. But both $H_{4,10}$ and $H_{1,13}$ have such small magnitudes relative to $H_{1,1}$ that, in actual testing, they would probably be lost in noise or ignored. So it is fair to say that qualitative examination of the transfer functions indicates the presence of only a single mode at 149.2 rad/sec.

Before examining error plots in the region of the two close modes, it is useful to have as a reference an example of error plots at and near a single isolated mode. The second mode of this model, with a natural frequency of 67.5 rad/sec, is quite distant from all other modes. Figure 10a is the graph of error values around this mode for the 5×5 $[H^*]$. For comparison, Figure 10b is the graph of error values in a region of almost no modal activity between the second and third modes. The error scales of both Figures 10a and b are quite small (relative to that of Figure 11a discussed below), and neither figure has any error peaks. The only significant difference in character between the two figures is the numerical noise at and near the natural frequency in Figure 10a, due to accumulated round-off error in eigenvalue calculations.

Figures 11a and b are graphs of error values in a band around the pair of close modes, the former for excitation at all five translation degrees of freedom, and the latter for excitation at only three. On the basis of all criteria developed previously and in

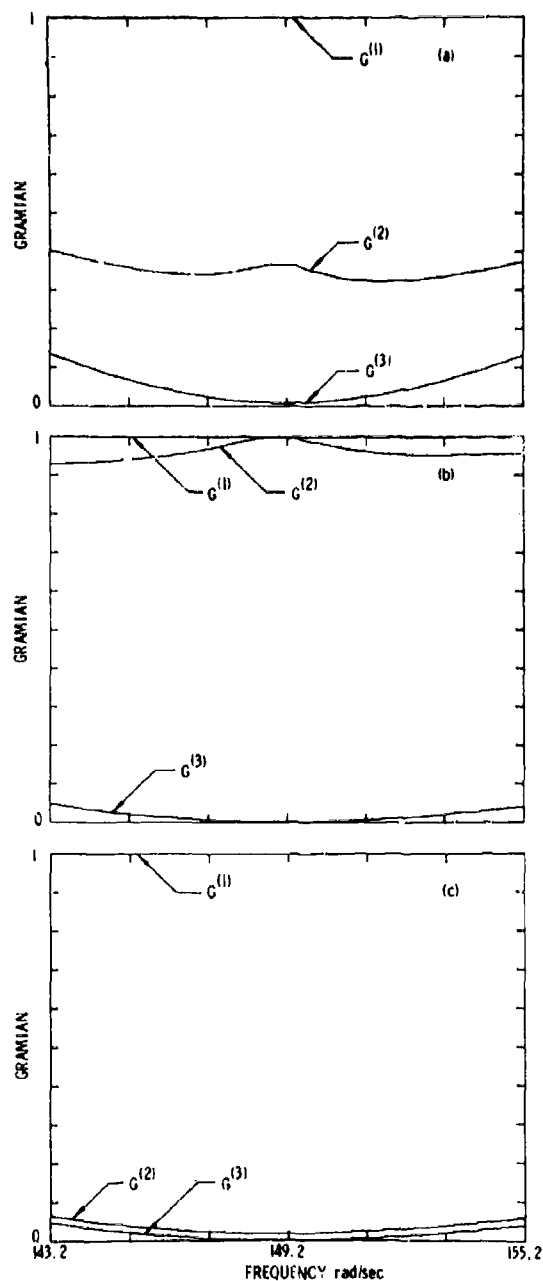


Figs. 11 Error graphs for the fifteen-dof model with motion sensors 1, 4, 7, 10, 13: (a) exciters 1, 4, 7, 10, 13; (b) exciters 1, 10, 13

comparison with Figure 10a, these graphs indicate clearly and indisputably the presence of two dominant modes.

Figures 12 a, b, and c are graphs of Gramians in the region of close modes. Figure 12a for five exciters applied in the order 1, 4, 7, 10, 13 seems to indicate clearly that $q = 2$. So also does Figure 12b for three exciters applied in the order 13, 1, 10. However, Figure 12c for the same three exciters applied in the order 1, 10, 13 seems to indicate just as clearly, though incorrectly, that $q = 1$.

In summary of the discussion of theory and the numerical simulation study, the vector-fit method is distinctly superior to the Gramian method for the purpose of determining the number of dominant modes. The only advantage of the Gramian method is that it requires substantially less computation time. As has been



Figs. 12 Gramian graphs for the fifteen-dof model with motion sensors 1, 4, 7, 10, 13: (a) five exciters applied in the order 1, 4, 7, 10, 13; (b) three exciters applied in the order 13, 1, 10; (c) three exciters applied in the order 1, 10, 13

demonstrated, the vector-fit method can produce error plots which are difficult to interpret correctly. But results of the simulation study suggest that the use of a large number of motion sensors in calculation of the error values will reduce the likelihood of mistaken interpretations. Theoretically, a minimum number of $q+1$ motion sensors are required; however, it would seem prudent and usually practical to estimate q and then to use several times that number of motion sensors in calculating error values.

We note that the vector-fit method is valid regardless of the type of motion sensor employed in testing, since the form of equation (7) remains the same for displacement, velocity, or acceleration transfer functions.

V. CONCLUDING REMARKS

The vector-fit method for determining the number of dominant vibration modes from structural transfer functions has been derived theoretically, illustrated with a numerical simulation study, and compared with other methods. The method works well with exact, noiseless, simulated data. However, its practical applicability has not been evaluated. The logical next step is to test the method with real data. If it should prove applicable, it would be a useful analysis tool for modal testing. Regardless of the type of testing employed, the vector-fit method could provide an independent check on whether or not all significant modes had been detected.

ACKNOWLEDGMENTS

This work has been sponsored by NASA Langley Research Center under Research Grant NSG 1276. The authors are most grateful to E. M. Cliff, who contributed the theoretical basis for the vector-fit method from his research in control theory, and to Paul Conti, who assisted in the study.

BASIC NOTATION

(\cdot)	column matrix, vector
$\text{Re}(\cdot)$	real part of (\cdot)
$[\cdot]^t, (\cdot)^t$	transpose of $[\cdot], (\cdot)$
$(\bar{\cdot})$	complex conjugate of (\cdot)
$\det[\cdot]$	determinant of $[\cdot]$
$(\bar{u}, v) = \bar{u}^t v$	Hermitian scalar product
$[A] = [H^*][R^*]^t$	$p \times p$ Hermitian matrix
$[C]$	$n \times n$ damping matrix
$[G_k] = [R^*]^t [H^*]$	$k \times k$ Gram matrix
$[H]$	$n \times n$ transfer function matrix
$[H^*]$	$p \times k$ incomplete transfer function matrix

$[k]$	$n \times n$ stiffness matrix
$[m]$	$n \times n$ inertia matrix
$[\phi]$	$n \times n$ modal matrix
$[S]$	an unspecified $n \times n$ complex matrix
F	force-amplitude vector
H_j	j th column of $[H]$
H_j^*	j th column of $[H^*]$
ϕ_r	r th column of $[\phi]$
ϕ_r^*	$p \times 1$ sub-vector of ϕ_r
ψ_i	i th complex unit eigenvector of $[A]$
u_i	$p \times 1$ complex unit basis vector
$x(t)$	$n \times 1$ time-dependent response vector
\bar{x}	$n \times 1$ complex response-amplitude vector
C_{ij}	unspecified complex constant
$E(m)$	m th real error value
$G(k) = \det[G_k]$	Gram determinant, Gramian
g_r	hysteretic damping constant of r th mode
$i = \sqrt{-1}$	
k	number of dof subjected to forcing excitation
λ_i	i th eigenvalue of $[A]$
M_r	generalized mass of r th normal mode
m_r, n_r	numbers of half-wavelengths for the ten-mode model
n	total number of dof
ω	frequency of excitation
ω_r	natural frequency of r th normal mode
p	number of dof instrumented with motion sensors
q	number of dominant modes
S_{ij}	element of $[S]$

REFERENCES

1. Traill-Nash, R. W., "On the Excitation of Pure Natural Modes in Aircraft Resonance Testing", *J. Aero/Space Sci.*, Dec. 1958, pp. 775-778.
2. Bishop, R. E. D. and Gladwell, G. M. L., "An Investigation into the Theory of Resonance Testing", *Phil. Trans. of the Royal Society of London, Series A, Vol. 255, Math. and Phys. Sci.*, 1963, pp. 241-280.
3. Asher, G. W., "A Note on the Effective Degrees of Freedom of a Vibrating Structure", *AIAA Journal*, Vol. 5, No. 4, April 1967, pp. 822-824.
4. Meirovitch, L., *Elements of Vibration Analysis*, McGraw-Hill, 1975, Chapter 4.

5. Ibrahim, S. R. and Mikulcik, E. C., "The Experimental Determination of Vibration Parameters from Time Responses", The Shock and Vibration Bulletin, Bulletin 46, Part 5, 1976, pp. 187-193.
6. Hildebrand, F. B., Methods of Applied Mathematics, 2nd ed., Prentice-Hall, 1965, Chapter 1.
7. Klosterman, A. L., "On the Experimental Determination and Use of Modal Representations of Dynamic Characteristics", Ph.D. Dissertation, University of Cincinnati, 1971.
8. Cliff, E. M., "Essential Uncontrollability of Discrete Linear, Time-invariant, Dynamical Systems", Proceedings of the IFAC 75, International Federation of Automatic Control, 6th World Congress, August 24-30, 1975, Boston/Cambridge, Mass., Part 1, Section 9.3, pp. 1-6.
9. Franklin, J. N., Matrix Theory, Prentice-Hall, 1968, Chapter 6.
10. Hallauer, W. L. Jr., Weisshaar, T. A., and Shostak, A. G., "A Simple Method for Designing Structural Models with Closely Spaced Modes of Vibration", J. Sound and Vibration, Vol. 61, No. 2, Nov. 1978.

LATERAL AND TILT WHIRL MODES OF FLEXIBLY MOUNTED FLYWHEEL SYSTEMS*

C. W. Bert and T. L. C. Chen[†]
School of Aerospace, Mechanical
and Nuclear Engineering
The University of Oklahoma
Norman, Oklahoma

High-performance, composite-material flywheel systems under current development for energy-storage purposes differ from turbine and compressor systems in that the flywheel rim is flexibly attached to the hub. Thus, for whirling with gyroscopic action, an axisymmetric flywheel system has four degrees of freedom, two associated with lateral translation and two with tilting. In the Sandia Livermore spin-test facility, the above system was driven by an air turbine which added two more degrees of freedom. A six-degree-of-freedom analysis of such a system is presented here and applied to two versions of a specific design presently being developed.

INTRODUCTION

Current engineering interest in the flywheel as an energy-storage mechanism for either stationary or vehicular applications has directed attention to the dynamics of such a system [1]*. One flywheel configuration currently under investigation by Sandia Laboratories is a high-rotational-speed system consisting of a composite-material rim attached by means of flexible composite-material bands (or spokes) to a hub of finite mass which in turn is attached to a relatively flexible shaft [2]. In the spin tests conducted at Sandia-Livermore test facility [3], the flywheel shaft is essentially supported as a cantilever at its top end by rigid attachment to the turbine shaft, which in turn, is supported by a pair of ball bearings. A schematic diagram of such a system is shown in Fig. 1.

For this system both translational and tilting motions take place. The translation contributes to the development of a lateral force due to centrifugal action, while the tilting produces an inertial couple, including gyroscopic action, about a diameter of the flywheel. The sense of this couple is such that it effectively stiffens the system for modes corresponding to retrograde (or backward) precession. This gyroscopic effect on rotor

whirling was first investigated by Stodola [4] in 1918. See also [5].

Due to the flexible nature of the flywheel bands, flywheel shaft, and turbine shaft, as well as the finite mass of the rim, hub (54% of the rim mass) and turbine, the system is considered as a three-mass system. A few analyses of multi-mass disk-shaft systems have appeared in the literature; see, for instance [6-8]. Unfortunately, however, these analyses are all applicable to only the case where the flexible members (portions of the shaft) connect to ground. In the present system, one flexible member (the bands) connects to an otherwise free mass (the flywheel rim). To the best of the present investigators' knowledge, the only analyses even remotely applicable to such a configuration are [9-11]. However, the analyses in [9-10] are applicable only to a thin-plate wheel, while McKinnon's analysis [11] considered a two-mass system with only three degrees of freedom, since he considered the radial flexibility of the rim-to-hub connector to be negligible.

The present analysis considers three masses (rim, hub, and turbine) and six degrees of freedom (translation and tilting for each mass, as shown in Fig. 1).

* The research reported here was supported by the Department of Energy through a contract from Sandia Laboratories, Albuquerque, New Mexico.

[†] Presently at the Engineering Mechanics Department, Research Laboratories, General Motors Technical Center, Warren, MI.

* Numbers in brackets designate References at end of paper.

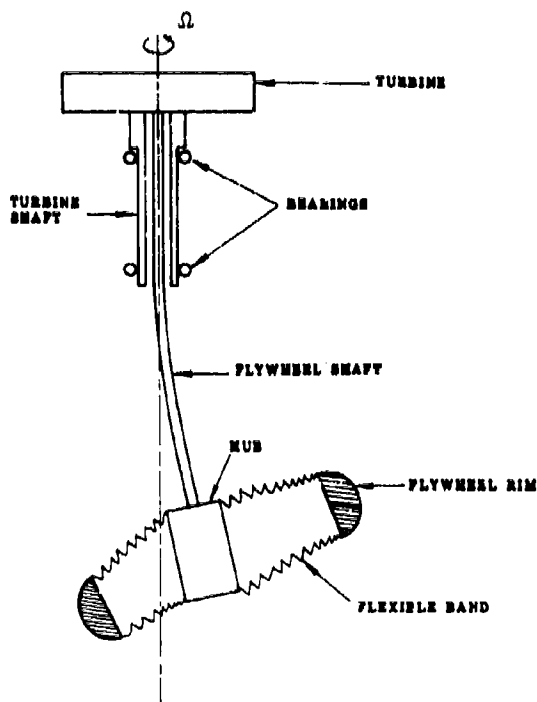


Fig. 1. Schematic diagram of the Sandia fly-wheel system, as installed in the Sandia-Livermore spin-test facility.

ANALYSIS

The system is depicted schematically in Fig. 1, which has three masses and six generalized displacements $\{q_i\} = (r_r, \phi_r, r_h, \phi_h, r_t, \phi_t)^T$. It is noted that r and ϕ are respective translational and tilting displacements, while subscripts r, h, t refer to rim, hub, and turbine respectively. The compliance equations can be written in matrix form as follows:

$$\{q_i\} = [\alpha_{ij}] \{Q_j\} \quad i, j = 1, 2, \dots, 6 \quad (1)$$

Here the generalized forces are $\{Q_i\} = (F_r, M_r, F_h, M_h, F_t, M_t)^T$ and the α_{ij} are the compliances. Due to the nature of the connection between the rim and hub as well as the necessary symmetry of the array as required by Maxwell's reciprocal principle, some of the compliance terms are repeated in the array, which can thus be written as follows:

$$\begin{bmatrix} \alpha_{11} & \alpha_{12} & \alpha_{33} & \alpha_{12} & \alpha_{15} & \alpha_{16} \\ \alpha_{12} & \alpha_{22} & \alpha_{12} & \alpha_{44} & \alpha_{25} & \alpha_{66} \\ \alpha_{33} & \alpha_{12} & \alpha_{33} & \alpha_{12} & \alpha_{15} & \alpha_{16} \\ \alpha_{12} & \alpha_{44} & \alpha_{12} & \alpha_{44} & \alpha_{25} & \alpha_{66} \\ \alpha_{15} & \alpha_{25} & \alpha_{15} & \alpha_{25} & \alpha_{55} & \alpha_{25} \\ \alpha_{16} & \alpha_{66} & \alpha_{16} & \alpha_{66} & \alpha_{25} & \alpha_{66} \end{bmatrix} \quad (2)$$

with

$$\alpha_{11} = \alpha_{33} + 1/K_{bip} \quad (3)$$

$$\alpha_{22} = \alpha_{44} + 1/K_{bop}$$

where K_{bip} and K_{bop} are band stiffnesses to resist respective relative in-plane translation and out-of-plane tilting between rim and hub. The values of K_{bip} and K_{bop} increase not only with the initial winding tension in the bands but also with rotational speed due to the centrifugal stiffening effect. The values of α_{ij} can be obtained by using elementary beam theory; however, shear flexibility is included in obtaining turbine shaft stiffnesses due to its high diameter/length ratio. For the purpose of completeness, equations for calculating compliances and band stiffnesses are presented in Appendices A and B respectively.

The generalized forces are given by

$$\begin{aligned} F_r &= m_r \omega^2 r_r, & M_r &= (I_{mdr} \omega - I_{mar} \Omega) \omega \phi_r \\ F_h &= m_h \omega^2 r_h, & M_h &= (I_{mdh} \omega - I_{mah} \Omega) \omega \phi_h \\ F_t &= m_t \omega^2 r_t, & M_t &= (I_{mdt} \omega - I_{mat} \Omega) \omega \phi_t \end{aligned} \quad (4)$$

where m_r, m_h , and m_t are respective rim, hub, and turbine masses; I_{mar}, I_{mah} and I_{mat} are respective rim, hub, and turbine mass moments of inertia about the axis of rotation; I_{mdr}, I_{mdh} and I_{mdt} are the respective mass moments of inertia about a diametral axis; Ω is the rotational speed; and ω is the whirling frequency.

Inverting Eq. (1) and using Eqs. (4), one obtains the following equation:

$$([M_{ij}] \omega^2 - [N_{ij}] \omega - [K_{ij}]) \{q_i\} = 0 \quad (5)$$

$$(i, j = 1, 2, \dots, 6)$$

where $[K_{ij}]$ is the inverse of $[\alpha_{ij}]$, $[M_{ij}]$ and $[N_{ij}]$ have zero elements except for the following

$$\begin{aligned}
M_{11} &= m_r & M_{22} &= I_{mdr} & M_{33} &= m_h & \\
M_{44} &= I_{mdh} & M_{55} &= m_t & M_{66} &= I_{mdt} & (6) \\
N_{22} &= I_{mar} \Omega & N_{44} &= I_{mah} \Omega & N_{66} &= I_{mat} \Omega
\end{aligned}$$

One can reduce Eq. (5) to a standard-type eigenvalue problem, which minimizes the computations, by introducing the following definition:

$$\{\hat{P}_1\} = \omega \{q_1\} \quad (7)$$

Using Eq. (7) in Eq. (5) and omitting the subscripts, one obtains the following equation

$$\begin{bmatrix} [0] & [I] \\ [M]^{-1} [K] & [M]^{-1} [N] \end{bmatrix} \begin{Bmatrix} \{q_1\} \\ \{\hat{P}_1\} \end{Bmatrix} = \omega \begin{Bmatrix} \{q_1\} \\ \{\hat{P}_1\} \end{Bmatrix} \quad (8)$$

Eq. (8) is in the form of a standard-type eigenvalue problem. Thus, it can be solved by using an existing eigenproblem code at each rotational speed Ω .

NUMERICAL RESULTS AND DISCUSSION

The numerical values of the various mass and inertia parameters for two different composite-material flywheel systems are listed in Table 1**. Each of the two systems have the same rim, which is constructed of hoop-wound graphite-epoxy composite material and is designed to achieve an energy-storage capacity of 0.56-kwh at 31,500 rpm.

System A has flat-band-type spokes of aramid-epoxy unidirectional composite material and is shown in Fig. 2. There are six complete bands, i.e. the bands are located 30 degrees apart around the circumference. The bands are wound with an initial tension of 360 lb and pass through and are bonded to slots in the hub.

System B differs from System A primarily in the fact that System B has upokes which are wound flat on to the rim but undergo a 90-degree twist to be wound on to axially oriented pins at the hub. This twist and a lower initial winding tension in the bands (90 lb for System B) results in higher in-plane compliance of the bands. However, the tilting compliance is smaller.

TABLE 1
Mass and Inertia Parameters for Systems A and B

Quantity	Symbol	Units	System	
			A	B
Rim mass	m_r	N-sec ² /cm (lb-sec ² /in)	0.075 (0.043)	0.075 (0.043)
Hub mass	m_h	" "	0.041 (0.0235)	0.045 (0.0258)
Turbine mass	m_t	" "	0.035 (0.020)	0.035 (0.020)
Rim mass moment of inertia about its axis	I_{mar}	N-cm-sec ² (lb-in-sec ²)	36.33 (3.215)	36.33 (3.215)
Hub mass moment of inertia about its axis	I_{mah}	" "	0.610 (0.054)	0.836 (0.074)
Turbine mass moment of inertia about its axis	I_{mat}	" "	0.757 (0.067)	0.757 (0.067)
Rim mass moment of inertia about a centroidal diameter	I_{mdr}	" "	18.485 (1.636)	18.485 (1.636)
Hub mass moment of inertia about a centroidal diameter	I_{mdh}	" "	2.791 (0.247)	2.689 (0.238)
Turbine mass moment of inertia about a centroidal diameter	I_{mdt}	" "	0.452 (0.040)	0.452 (0.040)

** The numerical values of compliances are given in Appendix A.

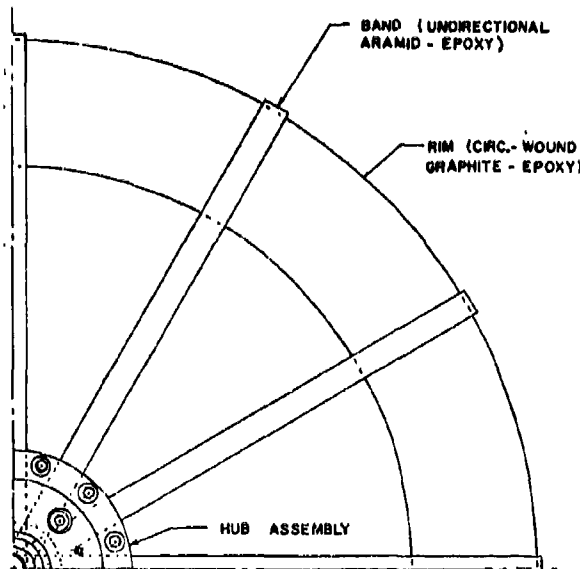


Fig. 2 Plan view of one quarter of the Sandia thick-ring flywheel (System A).

Both System A and System B have been spin-tested at the Sandia Livermore spin test facility, in which the flywheel hub is mounted to a shaft which is cantilevered from the Barbour-Stockwell air-turbine drive assembly.

Solving the eigenvalue problem represented by equation (8) by means of routine EIGRF [12] on an IBM 370, Model 158J digital computer, one obtains modal frequencies as a function of the rotational speeds. Plots of these relationships for Systems A and B are shown in Figs. 3 and 4. These figures are plotted in log-log form in order to get them on the paper. All six modes, with forward and retrograde branches for each, are shown for completeness. It should be mentioned that the retrograde branches correspond to negative whirling speeds, i.e., the direction of rotation of the whirling is a direction opposite to the direction of the running speed.

The intersections of the ω vs. Ω curves with straight lines of the form $\omega = n\Omega$ determine the so-called critical speeds (Ω_{cr}) which correspond to the values of running speed Ω at which dynamic instability may take place. The value $n (= \omega/\Omega)$ is called the order of the critical speed and it is usually either a positive or negative integer or its reciprocal. Lines corresponding to $n = \pm 1$ and $n = \pm 2$ are shown in Figs. 3 and 4.

Critical speeds of positive orders are always associated with forward precession, in which the whirling phenomenon takes place in the same direction as the shaft rotation. In

contrast, critical speeds of negative orders are always associated with retrograde precession, in which the whirling phenomenon travels in a direction opposite to the direction of shaft rotation.

There does not appear to be any unanimity concerning which orders of critical speeds are the most critical ones. For example, Stodola [4, 5], Biezono and Grammel [7], and Hartog [13] emphasize the first order ($n = 1$). Also ref. [7] claims that backward-precession critical speeds are less dangerous than forward-precession ones. However, Yamada [14] observed experimentally retrograde as well as forward critical speeds of orders up to 8. Recently Thomson et al. [1] reported on experiments with single-mass flywheel systems. They had difficulty detecting the lower whirl phenomena, although they did detect one first-order, lower-mode critical speed. For the upper mode they detected critical speeds of retrograde orders 1, 2, 3, and 5 on one system and 1 and 3 on the other, as well as forward orders 2, 3, 4, and 5 on both systems.

It is noted that in Fig. 3 there are shown fourteen first- and second-order critical speeds in the rotational speed range up to 50,000 rpm: six forward and eight retrograde. According to the reasoning of [7] and [13], the most important critical speeds would be the first-order forward ones at about 650 rpm and 34,000 rpm. In contrast, the experience of [1] and [11] suggest that higher mode forward critical speeds of second order are most dangerous. It is noted that the amplitude ratios ϕ_r/ϕ_h and r_r/r_h increase rapidly as the running speed approaches the third-mode, second-order forward critical speed (approximately 23,000 rpm). This is consistent with comparison between the present results and the experimental results in [3] as discussed in the next section, which suggests that perhaps the second forward critical speed at the third mode is the most important one for System A.

The curious triple-curvature behavior (two inflection points) of the second-mode forward branch in the proximity of the third-mode forward branch (i. e. in the vicinity of $\omega = 45,000$ cpm, $\Omega = 23,000$ rpm) is reminiscent of the curve-veering phenomenon discussed by Leissa [15] and was also found by McKinnon [11], who reported that an experimental wheel failed in the vicinity of these conditions.

The major differences in System B as compared to System A are smaller out-of-plane band compliance and larger hub mass and axial moment of inertia (m_h , I_{mah}). Again there are fourteen first- and second-order critical speeds up to 50,000 rpm: six forward and eight retrograde as shown in Fig. 4. The first order forward critical speeds are at 700 rpm and 36,000 rpm, while the most important one of the second-order forward critical speeds is approximately 23,500 rpm.

It should also be mentioned that a 4 DOF analysis presented in [17] predicted corresponding second-order critical speeds much higher than the present analysis. The considerable decrease exhibited in the present 6 DOF analysis is believed to be due to the close proximity of the band tilting and turbine-shaft translation modes (i.e. the 3rd. and 4th. modes in Figs. 3 and 4). Thus, it must be concluded that an analysis with at least 6 DOF is required to accurately portray the system behavior.

Some parametric studies were carried out for System A in which either the hub assembly or the bands, or both were redesigned. Values of the third 2nd.-order critical speed for different designs are presented in Table 2. It is interesting to see that this particular critical speed can be increased more significantly by increasing the band thickness (with fixed cross-sectional area) than by changing the material.

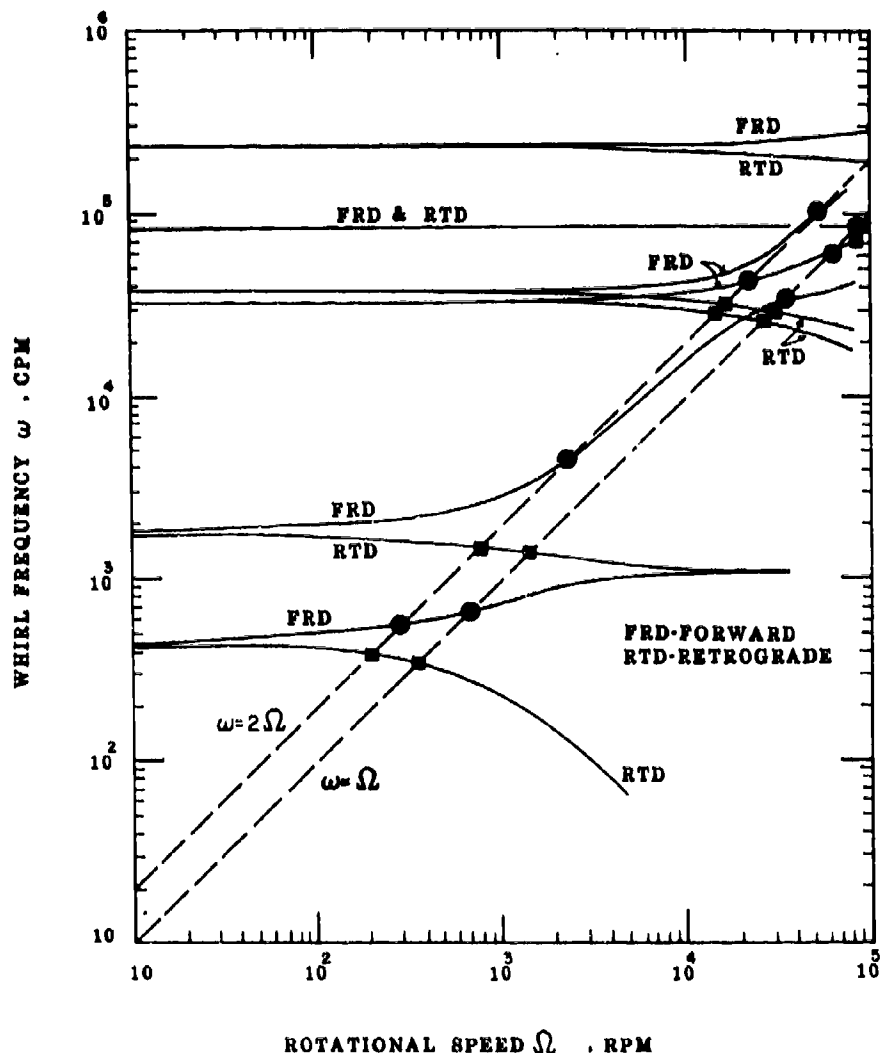


Fig. 3 System A whirl frequency vs. rotational speed for all six modes with gyroscopic effects. Circles denote potential forward critical speeds and squares denote potential retrograde critical speeds.

COMPARISON WITH EXPERIMENTAL RESULTS

In the spin tests of the two Sandia flywheel systems (denoted here as Systems A and B) tested by Sandia personnel at the Sandia Livermore Laboratory [3], x and y coordinates of the hub position in the horizontal plane were picked up by proximity gages and displayed on an oscilloscope.

The System A flywheel displayed considerable vibrational amplitude in the low-speed range. (The excessive amplitude may have been

indicative of the predicted critical speeds in the vicinity of 650 and 2,000 rpm.) Starting at about 14,000 rpm, there was a gradually increasing buildup in amplitude which accelerated rapidly starting at 18,000 rpm. Especially sudden increases in amplitude were noted at 20,200 rpm and 20,900 rpm. These sudden jumps while the rotational speed was gradually increased may be indicative of the nonlinear jump phenomenon associated with a "softening" restoring force [16]. It is also possible that these sudden increases were due to any one of

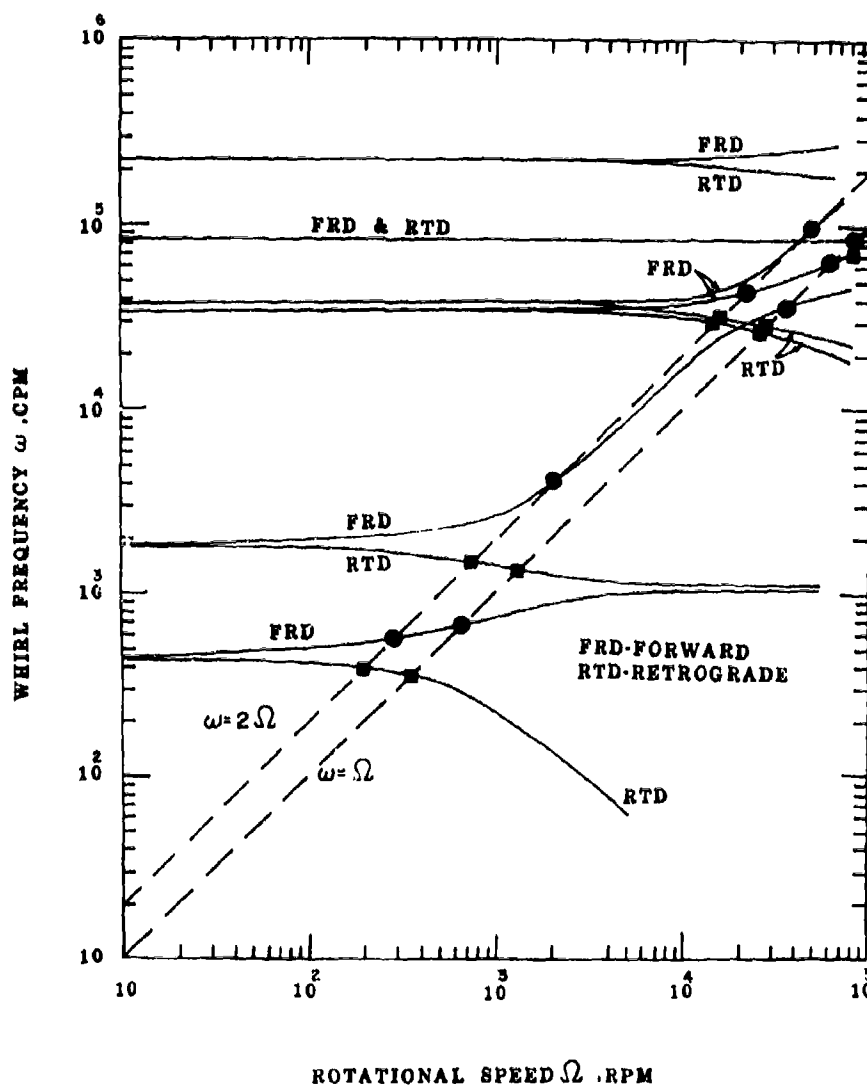


Fig. 4 System B whirl frequency vs. rotational speed for all six modes with gyroscopic effects. Circles denote potential forward critical speeds and squares denote potential retrograde critical speeds.

TABLE 2
Comparison of the Third-Mode Second-Order Critical Speeds for Various Designs
of System A

Case	Specific Design	.Critical Speed (rpm)	Remarks
1.	Basic design given in Table 1	23,000	frequency map shown in Fig. 3 total cross-sectional area unchanged
2.	Change band material to graphite/epoxy ^{††}	24,000	
3.	Change hub assembly ^{‡‡}	24,000	
4.	Combination of cases 2 and 3	24,500	
5.	Change number of sets of bands from 6 to 2 but with triple thickness perpendicular to the rim	24,500	
6.	Combination of cases 3 and 5	24,600	

^{††} Young's modulus in fiber direction = 18.0 msi (124.2 GPa)
Specific weight = 0.054 pci (0.015 N/cm³)

^{‡‡} New hub parameters are $m_h = 0.0183 \text{ lb-sec}^2/\text{in}$ (0.032 N-sec²/cm)
 $I_{mdh} = 0.2012 \text{ lb-in-sec}^2$ (2.273 N-cm-sec²)
 $J_{mah} = 0.0432 \text{ lb-in-sec}^2$ (0.488 N-cm-sec²)

these causes: (1) sudden failure of a band, (2) slippage of the bands in the vicinity of the hub, or (3) rapid opening of delamination in the rim. The flywheel shaft broke due to excessive amplitude when a speed of approximately 22,100 rpm was reached.

By ultrasonic and radiographic means it had been found prior to the spin test that this particular flywheel rim appeared to have some localized areas of fiber buckling. An earlier test of another flywheel of the System A design has achieved 17,900 rpm before the lead balance weights were thrown off and the test stopped. Surface flaws, but no significant internal flaws, were detected in it prior to test, and post-failure examination showed that it had separated in the vicinity of the surface irregularity.

In summary, it appears that the calculated third-mode, second-order forward critical speed of 23,000 rpm for System A is in good agreement with the observed failure due to excessive amplitude at 22,100 rpm. This agreement was surprising, since all of the stiffness values used were calculated ones, some of which were based on boundary-condition assumptions which may not have been sufficiently realistic.

The System B flywheel exhibited a generally smoother ride (less vibrational amplitude) than did System A. A possible explanation for this could be the inherently more

symmetric stiffness distribution of the band geometry in System B. Pronounced sudden decreases in amplitude, indicative of nonlinear jump phenomena associated with a "hardening" restoring force [16], were observed at approximately 22,000 rpm and 24,800 rpm. There was a gradual increase in amplitude starting at about 27,500 rpm, with sudden increases in amplitude at approximately 29,000 rpm and 30,000 rpm. There was a loud report associated with the first of these, and final failure was at 30,100 rpm. Post-failure examination of this flywheel indicated that the rim still retained its structural integrity, but many of the bands had failed near their attachment to the rim. It is not known which of the following phenomena directly caused failure of these bands: (1) snapping of some of the bands due to excessive steady centrifugal and aerodynamic loads, (2) excessive dynamic mechanical loads resulting from the system dynamics causing the bands to snap, or (3) excessive abrasion due to rubbing after the flywheel dropped into the spin pit following failure of the reduced-section break-away shaft. An earlier test of the System B design had displayed dynamic instability at 29,000 rpm and the test was discontinued at that point.

In summary, it appears that the calculated third-mode, second-order forward critical speed of 23,500 rpm for System B was not associated with the excessive amplitudes, during spin tests, in the vicinity of 29,000-30,000 rpm.

However, there is a calculated first-order forward critical speed for the second mode (associated with flywheel-shaft rotatory flexibility) at approximately 34,000 rpm. It may be tentatively conjectured that the System A flywheel failed at a second-order critical speed (23,000 rpm) due to stiffness asymmetry of the bands, while System B could have gotten beyond this speed only to encounter excessive amplitude at the next higher first-order critical speed (30,000 rpm⁺).

CONCLUSIONS

Based on the present study, it is concluded that perhaps the most important critical speed for flywheel System A is the second-order forward one at the third mode. Due to the nature of the coupling involved, an analysis with at least 6 DOF is required to accurately predict this system behavior rather than a 4 DOF analysis. Increasing the band thickness in the flywheel shaft direction is a practical way to increase the above mentioned critical speed.

For System B, the most important critical speed is less certain. However, there is a distinct possibility that it could be a first-order forward one at the second mode. Two practical ways to increase this critical speed are to increase the flywheel shaft stiffness and to decrease the hub's diametral mass moment of inertia.

ACKNOWLEDGMENTS

The authors wish to acknowledge the constant encouragement of Dr. E. D. Reedy, Jr. of Sandia-Albuquerque, the spin-test data provided by Sandia-Livermore, and helpful comments by C. A. Kocay of the University of Oklahoma.

REFERENCES

1. W.T. Thomson, F.C. Younger, and H.S. Gordon, "Whirl Stability of the Pendulously Supported Flywheel System," *Journal of Applied Mechanics*, Vol. 44, Trans. ASME, Vol. 99E, No. 2, pp. 322-328, June 1977.
2. E.D. Reedy, Jr., "A Composite-Rim Flywheel Design," *SAMPE Quarterly*, Vol. 9, No. 3, pp. 1-6, Apr. 1978.
3. E.D. Reedy, Jr. and H.K. Street, "Composite-Rim Flywheels: Spin Tests," Sandia Laboratories, Albuquerque, NM, to be published.
4. A. Stodola, "New Critical Shaft Speeds as Effects of the Gyroscopic Disc-Action," *Engineering*, Vol. 106, pp. 665-666, Dec. 13, 1918.
5. A. Stodola, *Steam and Gas Turbines*, pp. 1113-1122, Vol. 2, transl. from German, McGraw-Hill, New York, 1927.
6. R.B. Green, "Gyroscopic Effects on the Critical Speeds of Flexible Rotors," *Journal of Applied Mechanics*, Vol. 15, Trans. ASME, Vol. 70, pp. 369-376, Dec. 1948.
7. C.B. Biezeno and R. Grammel, *Engineering Dynamics*, Vol. III: *Steam Turbines*, pp. 225-230, Blackie and Son Ltd., London, 1954.
8. H.F. Black, "Lateral Vibration of Shafts Having Radial Symmetry and Appreciable Gyro-Action," *Journal of Mechanical Engineering Science*, Vol. 6, No. 1, pp. 53-63, Mar. 1964.
9. D.R. Chivens and H.D. Nelson, "The Natural Frequencies and Critical Speeds of a Rotating, Flexible Shaft-Disk System," *Journal of Engineering for Industry*, Trans. ASME, Vol. 97B, pp. 881-886, Aug. 1975.
10. J.A. Dopkin and T.E. Shoup, "Rotor Resonant Speed Reduction Caused by Flexibility of Disks," *Journal of Engineering for Industry*, Trans. ASME, Vol. 96B, No. 4, pp. 1328-1333, Nov. 1974.
11. C.N. McKinnon, Jr., "Rotor Dynamics Analysis," Appendix B of "Evaluation of Selected Drive Components for a Flywheel Powered Commuter Vehicle," LMC Corp., Final Report, Contract EY-76-C-02-1164, Phase I, June 30, 1977.
12. IMSL Library 1, 6th ed., International Mathematical and Statistical Libraries, Inc., 1977.
13. J.P. den Hartog, *Mechanical Vibrations*, 4th ed., Sec. 6.8, McGraw-Hill, New York, 1956.
14. Y. Yamada, "On the Critical Speeds of a Rotor System Having an Asymmetrical Disc," *Proc. 4th Japan National Congress of Applied Mechanics*, pp. 381-384, 1954.
15. A.W. Leissa, "On a Curve Veering Aberration," *Journal of Applied Math. and Physics (ZAMP)*, Vol. 25, pp. 99-111, 1974.
16. C. Hayashi, *Nonlinear Oscillations in Physical Systems*, p. 119, McGraw-Hill, New York, 1964.
17. C.W. Bert, T.L.C. Chen and C.A. Kocay, "Critical Speeds and Natural Frequencies of Rim-Type Composite-Material Flywheels," University of Oklahoma, Research Report OU-AMNE-78-3, Sept. 1978.
18. C.W. Bert, "Deflections in Stepped Shafts," *Machine Design*, Vol. 32, No. 24, pp. 128-133, Nov. 24, 1960.

APPENDIX A. ELEMENTS OF COMPLIANCE MATRICES

Detailed derivation for the stiffnesses of the flywheel shaft and the turbine shaft are

given in [17]. Using such stiffnesses, one can derive the compliances appropriate to the present design configuration as follows:

$$\begin{aligned} a_{12} &= K_{sc}^{-1} - K_{tc}^{-1} + L_s K_{tr}^{-1} \\ a_{15} &= K_{tf}^{-1} + L_s K_{tc}^{-1} \\ a_{16} &= -K_{tc}^{-1} + L_s K_{tr}^{-1} \\ a_{25} &= -K_{tc}^{-1} \\ a_{33} &= K_{sf}^{-1} + K_{tf}^{-1} - 2 L_s K_{tc}^{-1} + L_s^2 K_{tr}^{-1} \\ a_{44} &= K_{sr}^{-1} + K_{tr}^{-1} \\ a_{55} &= K_{tf}^{-1} \\ a_{66} &= K_{tr}^{-1} \end{aligned} \quad (A-1)$$

Here the first subscripts s and t refer to the respective flywheel shaft and turbine shaft; the second subscripts f and r are referring to the respective flexural translational and flexural rotatory stiffnesses; while c refers to the coupling stiffness to resist translational motion due to a bending couple applied on the shaft. The following numerical values are used in both Systems A and B:

$$\begin{aligned} K_{sf} &= 564.3 \text{ N/cm (322.2 lb/in)} ; \\ K_{sr} &= 134,705 \text{ N-cm/rad (11,923 lb-in/rad)} ; \\ K_{sc} &= 10,346 \text{ N/rad (2,326 lb/rad)} ; \\ K_{tf} &= 9.751 \times 10^6 \text{ N/cm (5.568} \times 10^6 \text{ lb/in)} ; \\ K_{tr} &= 1.583 \times 10^7 \text{ N-cm/rad (1.401} \times 10^6 \text{ lb-in/rad)} ; \\ K_{tc} &= 1.629 \times 10^6 \text{ N/rad (9.301} \times 10^5 \text{ lb/rad)} ; \\ L_s &= \text{length of flywheel shaft} = 27.94 \text{ cm (11 in)} \end{aligned}$$

APPENDIX B. EXPRESSIONS FOR COMPUTING BAND STIFFNESSES

Determination of band stiffnesses K_{bip} and K_{bop} for System A are derived in [17] and are summarized here for completeness.

The in-plane stiffness of the system of bands is

$$K_{bip} = 12 A_b E_b / L + 12 K_b \quad (B-1)$$

The first term on the RHS (right-hand side) is the integrated stiffness caused by the axial membrane stretching in each band; while the second term is due to resistance to in-plane

motion caused by lateral force applied on each band. Stiffness K_b is given as Eq. (A-21) in [17] and is reproduced here as follows:

$$K_b = (kP \sinh kL)[2(1 - \cosh kL) + kL \sinh kL]^{-1} \quad (B-2)$$

where $k \equiv (P/E_b I_1)^{1/2}$; P is the sum of initial winding tension and centrifugal tension in each band (see [17] for details)*; A_b is the cross-sectional area in each band; E_b is the band Young's modulus in the fiber direction; L is the band unsupported span length; I_1 is the area moment of inertia relative to an axis parallel to the flywheel shaft.

The out-of-plane stiffness of the system of bands is

$$K_{bop} = 12 A_b E_b b^2 / L + 12 (E_b I_2 P)^{1/2} (R_1 / L - 1) \quad (B-3)$$

where b is one half of the hub axial length; R_1 is the inside radius of the rim.

Again the first term on the RHS is associated with the axial membrane stretching in the bands. The second term is associated with bending of the bands about their own centroids out of the plane which is perpendicular to the axis of revolution of the hub.

For System B, the bands are wound flat on to the rim but undergo a 90-degree twist to be wound on to axially oriented pins at the hub. Bands in such systems are shown in Fig. 5(a). Application of Eq. (B-1) is not valid unless a modification is carried out. Physically the first term on RHS of Eq. (B-1), which is associated with stretching in axial direction, is unaffected. However, the second term should be decreased due to reduction of moment of inertia along x .

If the force applied at the right-hand side is Q as shown in Fig. 5(a), the moment distribution is

$$M(x) = -Q(L - x) \quad (B-4)$$

Using the same approach as that as presented in [18], the translational deflection at the point where Q is applied can be expressed as follows by neglecting the shear flexibility:

$$y_p = \int_0^L [(M \frac{\partial^2 M}{\partial Q^2}) / EI(x)] dx \quad (B-5)$$

where $I(x)$ is the moment of inertia at position x .

* $P \equiv$ initial winding tension (P_1) + centrifugal tension (P_c);

$$P_c = 4,017 \times \left(\frac{\text{rpm}}{32,000} \right)^2$$

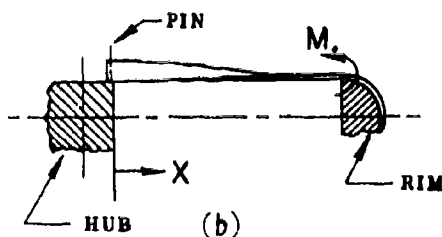
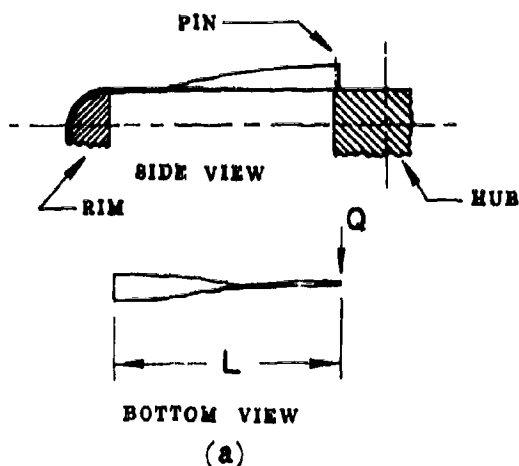


Fig. 5 Schematic diagrams showing that the bands of System B have been twisted by an angle of $\pi/2$ at the end attached to the hub.

Assuming that the angle twisted is linearly dependent on x , the following relation can be obtained

$$I(x) = I_1 \cos^2 \bar{x} + I_2 \sin^2 \bar{x} \quad (B-6)$$

$$\text{where } I_1 \equiv ta^3/12 ; \quad I_2 \equiv at^3/12 ;$$

$\bar{x} \equiv \pi x/2L$; t is band thickness; a is band width.

Inserting Eqs. (B-4) and (B-6) into Eq. (B-5), one obtains

$$(y_p/Q)_{\text{twisted}} = \int_0^L [(L-x)^2/E_b(I_1 \cos^2 \bar{x} + I_2 \sin^2 \bar{x})] dx \quad (B-7)$$

For the case when the bands are not pretwisted, the value of y_p/Q can be obtained by using the following equation.

$$(y_p/Q)_{\text{nontwisted}} = \int_0^L [(L-x)^2/E_b I_1] dx \quad (B-8)$$

The ratio of the translational stiffness for the above two different configurations can be obtained as follows:

$$\begin{aligned} (K_b)_{\text{twisted}} / (K_b)_{\text{nontwisted}} \\ = (y_p/Q)_{\text{nontwisted}} / (y_p/Q)_{\text{twisted}} \end{aligned} \quad (B-9)$$

Using the values pertinent to the present geometry and integrating numerically, one obtains the following result:

$$(K_b)_{\text{twisted}} = 0.678 (K_b)_{\text{nontwisted}}$$

This implies a destiffening effect due to 90° pretwisting. Combining the present result with that given as Eq. (B-1), one can compute K_{bip} , by using the following equations

$$K_{bip} = 12(A_b E_b / L + 0.678 K) \quad (B-10)$$

As far as the K_{bop} is concerned, Fig. 5(b) should be used. If a moment M_o , instead of a force Q , is applied at one end, the moment distribution would be

$$M(x) = M_o \quad (B-11)$$

The slope at the point of application of M_o can be deduced from the following equation.

$$\begin{aligned} (\phi/M_o)_{\text{twisted}} \\ = \int_0^L [1/E_b (I_2 \cos^2 \bar{x} + I_1 \sin^2 \bar{x})] dx \end{aligned} \quad (B-12)$$

$$\text{where } \bar{x} \equiv \pi(L-x)/2L$$

For the case where the bands are not pretwisted, the value of ϕ/M_o is

$$(\phi/M_o)_{\text{nontwisted}} = \int_0^L (1/E_b I_2) dx \quad (B-13)$$

Combining Eqs. (B-12) and (B-13), one obtains

$$(\phi/M_o)_{\text{twisted}} / (\phi/M_o)_{\text{nontwisted}} = 5.0$$

This represents a stiffening effect through pretwisting. Thus, the second term on RHS of Eq. (B-3) should be multiplied by 5 in order to incorporate the stiffening effect. However, the first term is unaffected since it accounts for the membrane stretching effect along the axis of the bands. Bearing this in mind, one has

$$K_{bop} = 12 A_b E_b b^2 / L + 60 (E_b I_2 P)^{1/2} (R_1 / L - 1) \quad (B-14)$$

In the present paper, the following data are used

$$\begin{aligned} A_b &= 0.05 \text{ in}^2 (0.323 \text{ cm}^2) \\ a &= 0.5 \text{ in} (1.27 \text{ cm}) \\ b &= 1.5 \text{ in} (3.81 \text{ cm}) \\ E_b &= 11 \times 10^6 \text{ psi} (75.87 \text{ GPa}) \\ L &= 5.375 \text{ in} (13.65 \text{ cm}) \\ R_1 &= 7.625 \text{ in} (19.37 \text{ cm}) \\ t &= 0.1 \text{ in} (0.254 \text{ cm}) \end{aligned}$$

APPENDIX C. NOMENCLATURE

A_b	cross-sectional area of one band
a	width of band in plane of rotation
b	one half of the hub axial length
E_b	elastic modulus of band along its length
F_h, F_r, F_t	centrifugal forces of hub, rim, and turbine, respectively
$I(x)$	distribution of rectangular area moment of inertia of band along the length of a twisted band
I_1, I_2	major and minor rectangular area moments of inertia of band
$I_{mah}, I_{mar}, I_{mat}$	mass polar moments of inertia about the axis of revolution for the hub, rim and turbine, respectively
$I_{mdh}, I_{mdr}, I_{mdt}$	mass polar moments of inertia about a diametral axis for the hub, rim and turbine, respectively
K_b	translational flexural stiffness of one band in a plane perpendicular to the plane of rotation
K_{bip}	in-plane translational stiffness of the entire system of bands
K_{bop}	out-of-plane rotatory stiffness of entire system of bands
$[K_{ij}]$	inverse of $[a_{ij}]$

K_{sc}, K_{sf}, K_{sr}	flywheel-shaft stiffnesses: translational-rotatory coupling, translational, and rotatory, respectively
K_{tc}, K_{tf}, K_{tr}	turbine-shaft stiffnesses: translational-rotatory coupling, translational, and rotatory, respectively
k	tie-bar parameter $(\cong P/E_b I_1)^{1/2}$
L	unsupported length of band (from hub to rim)
L_h	length of flywheel shaft
M	bending moment at position x on the band
M_h, M_r, M_t	inertial moments of hub, rim, and turbine, respectively
$[M_{ij}]$	inertia matrix with elements defined in Eqs. (6)
M_o	bending moment applied at end of band
m_h, m_r, m_t	mass of hub, rim, and turbine, respectively
$[N_{ij}]$	gyroscopic-action matrix with elements defined in Eqs. (6)
n	the order of a critical speed $(\cong \omega/\Omega)$
P	total tension in one band $(\cong P_c + P_1)$
P_c	centrifugal tension in one band
P_1	initial winding tension in one band
$\{\hat{P}_1\}$	pseudo-velocity column vector $(\cong \omega \{q_1\})$
Q	applied shear force on band, acting normal to the band and in the plane of rotation
$\{Q_j\}$	generalized force column vector $\equiv (F_r, M_r, F_h, M_h, F_t, M_t)^T$
$\{q_i\}$	generalized displacement column vector $\equiv (r_r, \phi_r, r_h, \phi_h, r_t, \phi_t)^T$
R_1	inside radius of rim where the bands are attached to it
r_h, r_r, r_t	translation in plane of rotation for the hub, rim, and turbine

t thickness of band in direction of axis of rotation of flywheel
 x position along the band, measured from the hub
 \bar{x}, \bar{z} $\pi x/2L, \pi(L-x)/2L$
 y_p deflection of band at rim relative to the hub, in a direction normal to the band and in the plane of rotation
 $[\alpha_{ij}]$ compliance matrix with elements defined by Eqs. (A-1)
 ϕ_h, ϕ_r, ϕ_t tilt angles (slopes) of the hub, rim, and turbine, respectively.
 Ω rotational speed
 ω whirling frequency

HUMAN RESPONSE TO VIBRATION AND SHOCK

WHOLE-BODY VIBRATION OF HEAVY EQUIPMENT OPERATORS

D.E. Wasserman, W.C. Asbury, T.E. Doyle
National Institute for Occupational Safety and Health
Cincinnati, Ohio

Approximately 6.8 million United States workers are exposed to whole-body vibration. A vibration field study was made of one of these groups -- heavy equipment operators. Several types of machines (track-type tractors, scrapers, motor graders, loaders, backhoes, compactors, skidders, and dump trucks) were operated by one or two of four operators with differing degrees of experience. Vibration data were obtained from the following locations: vehicle floor, man-seat interface, as well as from the operator's knee, shoulder, and head. Results of analyzing the vibration spectrum indicate that for the different types of machines little difference could be attributed to the experience or body mass of the operator and that most of the higher level vibration occurred below the 4 to 8 Hz "human-body resonance band," much of it at less than 1 Hz.

INTRODUCTION

From data compiled in plant site and workplace studies performed by the National Institute for Occupational Safety and Health (NIOSH) we can estimate that there are some eight million workers in the United States who are exposed to occupational vibration. (1) Of these, some 6.8 million are estimated to be exposed to so-called "whole-body" vibration (i.e., vibration impinging on the entire body, head-to-toe) such as would be experienced while driving a moving vehicle, for example. Another 1.2 million workers are exposed to "hand-arm" (i.e., segmental) vibration, which is locally applied vibration such as would be experienced while operating vibratory hand tools (e.g., pneumatic chipping hammers, grinders, chain saws, etc.).

Whole-body vibration is considered a "generalized stressor." (2) Since it impinges on multiple body organs simultaneously, both the acute and chronic physiological effects of such exposure are difficult to define. With regard to the work situation, information about chronic effects are paramount since a worker working in the same vibratory

job for 30 years, 50 weeks per year, at a conservative 30 hours per week, would be exposed 45,000 hours. To answer some of the questions relating to chronic vibration exposure in the workplace, NIOSH has completed a series of epidemiological morbidity studies of key vibration-exposed occupations: heavy equipment operation (3, 4), bus driving (5), and truck driving (6). In addition, a series of laboratory animal studies (7, 8) and human studies (9) were performed.

Heavy equipment operation was the subject for this first series of field studies because this large group of workers (about 500,000) is chronically exposed to occupational vibration and has been epidemiologically studied and because the Union of Operating Engineers Local # 3 (San Francisco based), which assisted in the previous epidemiological studies, offered us the use of their unique training facility (Rancho-Murielita, near Sacramento, California).

As part of this series, we undertook engineering field studies to quantify and describe the vibration exposure received by workers while they operated various types of heavy equipment vehi-

cles under actual work conditions. Future biological laboratory and medical field studies combined with vibration dose data, such as that reported here, will eventually give the final answers to the health and safety consequences of this exposure. In this paper the instrumentation, the study methods, and the data collection and processing of the engineering field study are described. An example of the vibration data is also presented.* Only the results of the analysis of the vibration data is presented in this report; physiological, noise, and other data obtained in this study will be reported elsewhere.

INSTRUMENTATION

The vibration exposure experienced by the worker must be measured at various points on the vibratory source, as well as on the man, because the dose a worker receives depends on such multiple factors as:

- o worker orientation and the degree of body coupling to the vibratory source;
- o frequency filtering by vehicular seats, worker clothing, vehicle suspension, vehicle tire pressure;
- o multiple vibratory sources, e.g., dual engines on some types of earth-moving scrapers;
- o vehicle speed and the type of road terrain being traveled;
- o the worker's age, body mass, and exposure time on the job.

Multiple simultaneous measures need to be taken to characterize the vibration dose. Because vibration is often accompanied by noise, heat, fumes, and dust, it is necessary to attempt to account for these additional stressors.

SOURCE OF DATA - The Target Vehicle

The system developed and used in these field studies is depicted in Figures 1a-1c. Each heavy equipment vehicle operator was "wired," using various transducers, to a multi-channel

* The complete details of this study have been reported in "Whole-Body Vibration Exposure of Workers During Heavy Equipment Operation," D.E. Wasserman, T.E. Doyle, and W.C. Asbury, DHEW (NIOSH) Publication No. 78-153, April, 1978.

multiplexed FM/FM (4 watt) telemetry transmitter operating at 216.5 MHz. Data were transmitted to a nearby mobile unit where it was demodulated and FM tape recorded for later data analysis. Vibration acceleration measures were taken in accordance with the accepted biodynamic coordinate system designated in ISO 2631 (Figure 2). Data were collected from the following locations:

- o Vibration acceleration at:
 - Target vehicle floor (vertical axis);
 - Man-seat interface (i.e., worker's buttocks) (vertical, horizontal, and lateral axis) (Figures 3, 4);
 - Worker's knee (vertical axis);
 - Worker's head (vertical axis) (Figures 5 and 6).
- o Environment:
 - "A" weighted noise (at the worker's ear level) using a sound level meter;
 - Temperature and relative humidity (manually obtained).
- o Physiology:
 - Electrocardiogram (EKG) using disposable silver-silver chloride electrodes;
 - Electromyograms (EMG, 2 channels, bilateral sacrospinalis muscles) using the above type electrodes.
- o Other:
 - Road profiles traversed by the target vehicle (using a monochrome vidicon TV camera and video tape recorder mounted at the operator's eye level observing and recording the road terrain the operator actually observed) and continuous observations of the operator and his vehicle motion (using a second monochrome vidicon TV camera and video tape recorder);
 - Target-vehicle speed (Doppler radar);
 - Target-vehicle tire pressure (where applicable);
 - Two-way radio communication between target-vehicle operator and mobile unit.

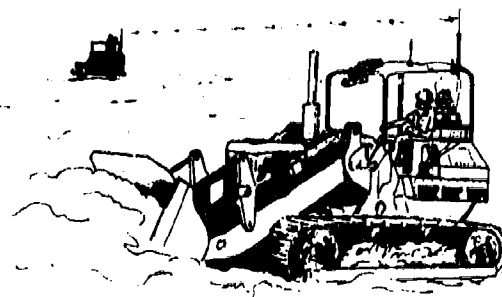


Figure 1a.
Heavy equipment vehicle
operator "wired" for
transmitting measured
data.

Figure 1b.
Vibration mobile unit
obtaining vibration,
environmental, and
physiological data.

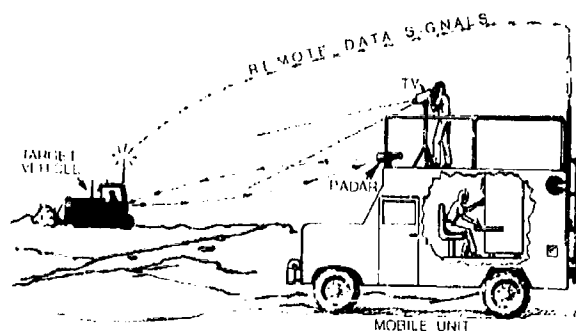


Figure 1c.
Vibration mobile unit
and target vehicle (v)
at test site.

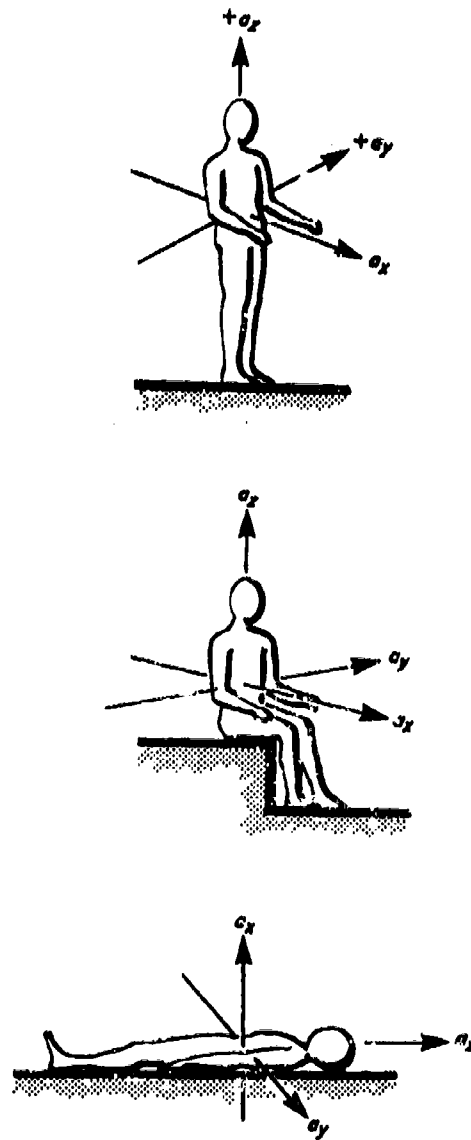


Figure 2. Biodynamic coordinate system acceleration measurements (ISO 2631).
 a_x , a_y , a_z = acceleration in the direction of the x, y, and z axes;
 x axis = back-to-chest;
 y axis = right-to-left;
 z axis = foot-to-head.

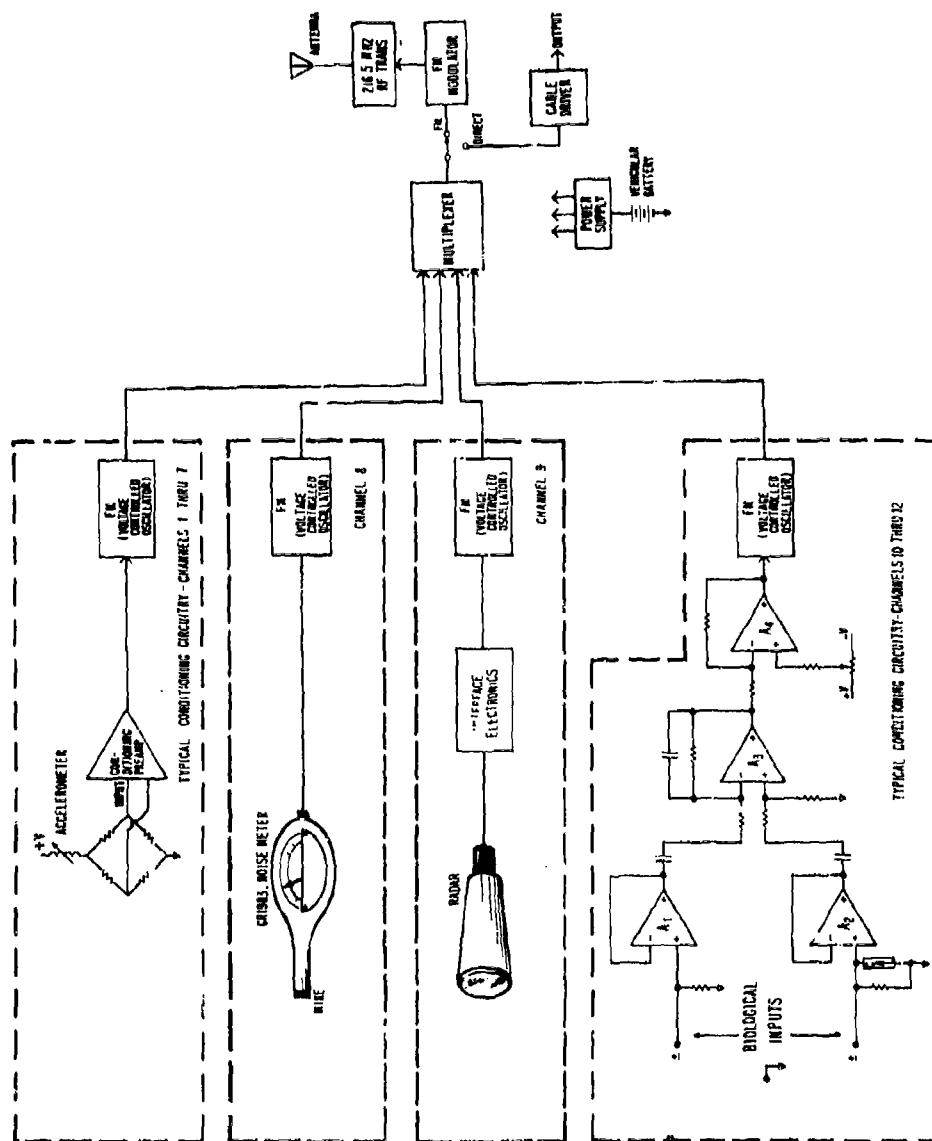


Fig. 3 - Functional diagram of Fm/FM telemetry transmitter used during field studies

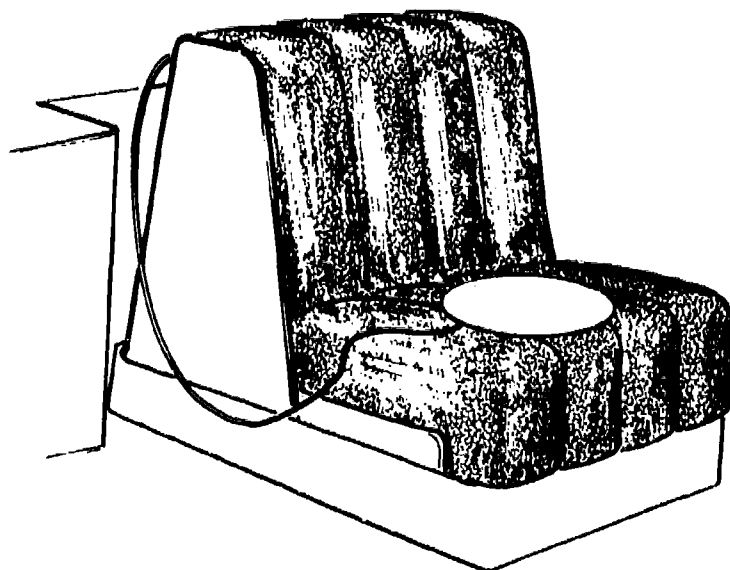


Fig. 4 - Seat accelerometer disk
is use during field study

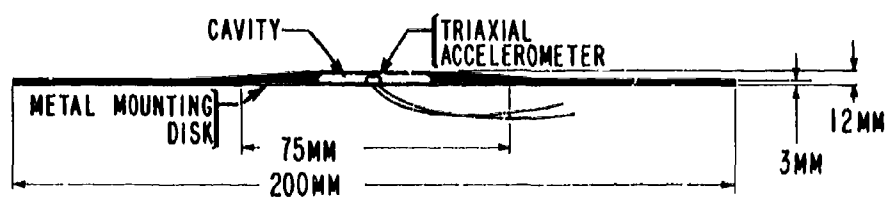


Fig. 5 - Triaxial accelerometer embedded in molded rubber disk. The disk is taped to the surface of the driver's seat cushion to receive man/seat acceleration data.



Fig. 6 - Bite bar in use during
field study

The heart of the data acquisition system was a ruggedized FM/FM telemetry system. The basic transmitter capacity was up to 14 multiplexed channels. This permitted a variety of data inputs and the system was designed so as to allow us to custom design a variety of conditioning electronics modules and to interface these into the multiplexer. In these field tests we chose to transmit 12 data channels (with the remaining two channels at the receiving end tape recorder used for data reduction purposes - a time marker channel and reference oscillator). Thus, the transmitter data were:

- o seven vibration data channels,
- o one "A" weighted noise channel,
- o two electroyogram (EMG) channels,
- o one electrocardiogram (EKG) channel.

The transmitter was designed so that it could be used in a radio frequency (RF) mode or in a direct (hard-wired) mode with the RF section off. All inputs were individually conditioned and multiplexed; this multiplexed signal could be transmitted either directly (through a 1000 foot cable driver amplifier to the mobile unit) or through the RF mode, with a transmitting distance of 2 to 4 miles, depending on the terrain. A simplified schematic diagram of the transmitter is depicted in Figure 3.

Because of the limited number of data channels, we were unable to use three accelerometers at each vibration position. (Three accelerometers would have been needed to reasonably define the multiple directions of vibration impinging on an object at a given point.) Three orthogonal directions were measured only at the man-seat interface (Figures 4 and 5); thus, at the floor, knee, and bite bar (Figures 6 and 7) only vertical acceleration was measured.

Equipment power was obtained using a single 12 volt auxillary automotive battery.

A list of the major commercial equipment used in this study is given in Table I.

VIBRATION DATA RECEIVER - Vibration Mobile Unit

A versatile, rugged, on-off road mobile unit that could be used virtually anywhere under any road condition was needed as a mobile control and data acquisition center. To meet these needs

a four-wheel-drive military ambulance was customized (Figures 8 and 9) which included a 5000-watt alternator for the instrumentation power.

All of the data from the target vehicle were simultaneously multiplexed and transmitted to this receiving mobile unit where it was received, demodulated, and, finally, FM tape recorded with some preliminary data processing (i.e., Fourier Spectrum Analysis) being produced on-line. The target vehicle was continuously under video monitoring from the portable black and white TV camera located on top of the mobile unit. This video information was taped and synchronized with all the incoming data. The speed of the target vehicle was continuously monitored and recorded using a police-type Doppler radar unit. In addition, an independent RF audio communication link maintained two-way communication between the two vehicles.

The mobile unit normally carried a three-man crew: one to operate the major electronics system, one to operate the roof video camera chain, and the third to double as driver and operator of the Doppler speed-measuring unit.

STUDY METHODS AND DATA COLLECTION

Four professional heavy equipment operators were used in the tests of the different pieces of heavy equipment of various U.S. manufacturers (Table II). In many cases, it was possible to obtain data from two drivers as they sequentially operated a given machine, each repeating the same type of work cycle over the same terrain under the same environmental conditions. Where two drivers were used sequentially, one driver was the "seasoned professional" (the driver who actually taught the proper use of that machine). Because the other instructor did not use that particular machine but could operate it he was considered the "new driver." This was done because about one-third of the heavy equipment workforce contains relatively new operators. All had at least 20 years of experience operating various heavy equipment vehicles.

Routes and work cycle schedules were mapped out for each machine. When multiple machines of the same type were used each machine was operated over the same terrain and under the same work conditions. Each day an operator was wired into a heavy equipment vehicle, system calibration and checks performed, tape recorded, and logged. Operators were instructed to perform their normal

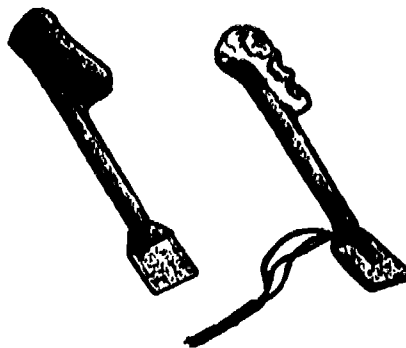


Fig. 7 - Metal bite bar (left), with accelerometer and dental impression (right)

TABLE I

Major Commercial Equipment Used in Study*

(Transmitting) Target Vehicle Equipment

Aydin-Vector by power FM/FM transmitter (216.5 MHz, Xtal controlled)
 Sony, Model AVC-3400, portable monochrome Vidicon camera and video tape recorder system
 Bectin-Dickinson, "Dispos E1" silver-silver chloride electrodes
 ENTRAN, Model EGAL-125, piezo resistive accelerometers
 Pace, Model 100 ASA, voice communications transmitter/receiver (21.575 MHz)

(Receiving) NIOSH Mobile Unit Equipment

Microdyne, Model CPR-101, phase-locked loop receiver
 Metraplex, Model 122-2, Subcarrier FM demodulators
 Honeywell, Model 5600-B, multichannel FM tape recorder
 Sony, Model AVC-3400, portable monochrome Vidicon camera and video tape recorder system
 Honeywell-Saicor, Model SAI51A, Fourier analyzer
 Custom Signals, Model MR-7, moving Doppler speed radar system (10.525 GHz)
 Generac, Model XP-5014C, 6207-5, 5000-watt alternator

* Mention of commercially available equipment does not necessarily imply U.S. Government endorsement.

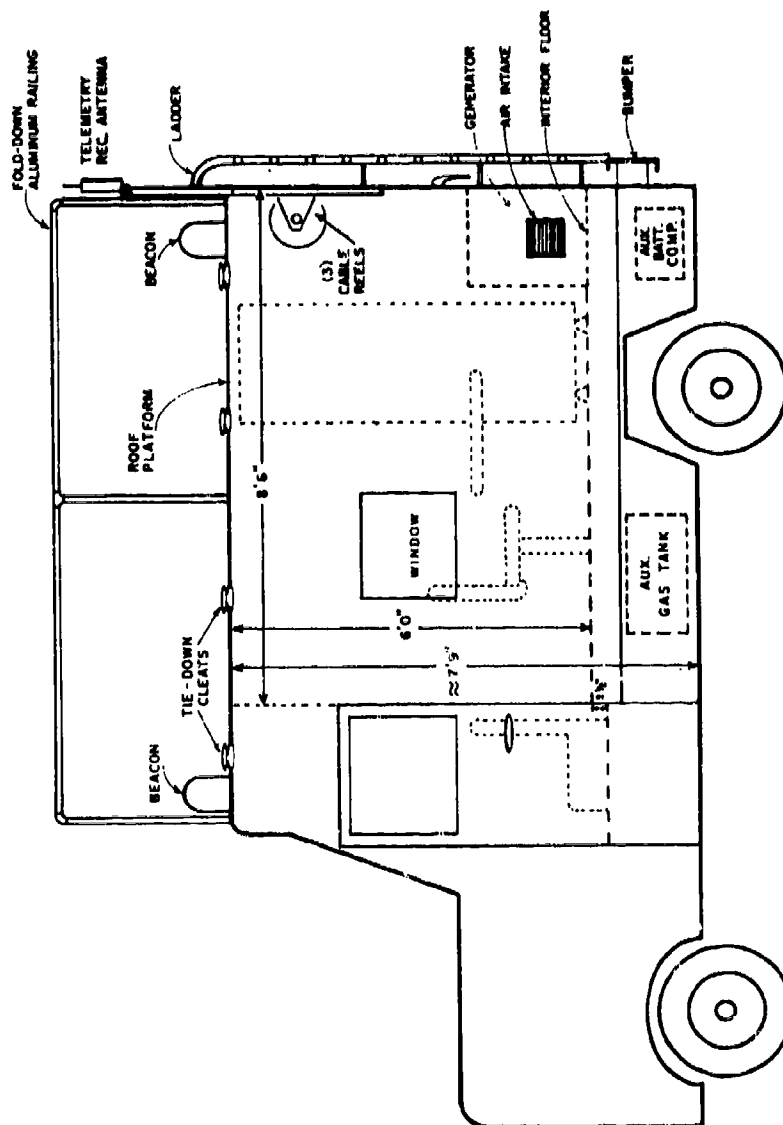


Fig. 8 - Vibration mobile unit--side view of exterior

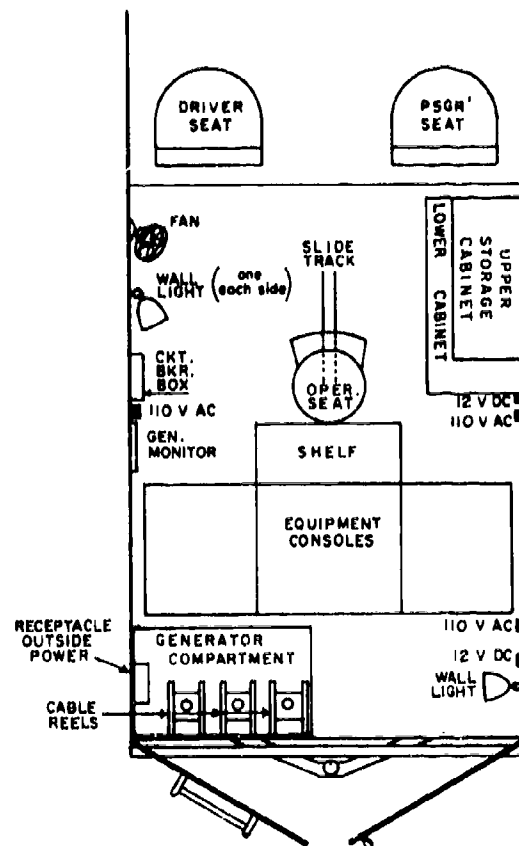


Fig. 9 - Vibration mobile unit--interior plan

work tasks in the same manner they would if testing were not taking place. Data collection began and the same work cycle using the same machine was repeated using another operator later in the same day.

Where possible, types of machines were later categorized into their appropriate SAE classification system also shown in Table II.

DATA PRESENTATION AND ANALYSIS

During the course of this study, we gathered spectral data from accelerometers placed in seven different positions. We classified these data into various matching categories and obtained a maximum of seven spectral plots for each data group.

As an example, Figure 10 illustrates seven plots for one of the machines and one of the operators (Data Group C). The computer code number in the upper left hand corner of each spectral plot indicates the machine type (Society of Automotive Engineers (SAE) classification and document number), the position of the accelerometer (e.g., the seat, knee, etc.), the number of computer averages used in each plot, and the driver code number. To read a given spectral plot for each peak in the spectra, read "frequency" horizontally (25 Hz full scale) and read peak linear acceleration in "g" units vertically (for RMS, multiply each peak value by 0.707), using the appropriate vertical scale factor as indicated in each plot.

In Table III, the predominate frequencies for the six Hz bands for Data Group C are discussed. In Table IV, the maximum and minimum peaks within the six frequency bands for Data Group C are tabularized. In Table V are found the major spectral peaks by machines and type of operator for all of the machines used in the field tests.

Because the heavy equipment machines have been categorized into an approved SAE classification system the vibration data processing has centered around this classification scheme. The first attempt at data reduction resulted in some 2,400 data plots. In the second attempt only linear vibration spectra, grouped according to the SAE classification where possible, was used. This resulted in the linear spectral plots, an example of which is contained in Figure 10 for Data Group C.

The following steps were taken to derive these linear spectra plots using an HP Model 5451 Fourier computer. To

compute a power spectra of a random process it was first necessary to generate a positive quantity that could be averaged. The resulting average was a measure of the energy in each frequency comprising the spectrum band. The vibration data can be regarded as a typical random process yielding a Fourier transform that will have both positive and negative, real and imaginary values, randomly distributed across the spectrum. If this transform were averaged without time synchronization, the result would be zero. Thus, the Fourier transform was first conjugate multiplied to yield a positive quantity at each frequency. A number of such spectra were summed and then each frequency was divided by that number to achieve the desired average. To obtain linear spectra from power spectra, the square root of the power spectra was taken. In the computing process the result yields a real part containing magnitude data with the imaginary part containing phase information. The magnitudes are then summed as repeated averages are taken and stored in the computer. The phase values randomly sum and, thus, must be disregarded.

The computer processing methods are summarized in Table V.

SUMMARY

The summary and conclusions given herein cover all the machines and operators indicated in Table VI. Without being overly specific, it appears we can indicate the following for the major vibration peaks:

1. For track type machines (tractors and crawler loaders) with virtually no suspension and limited speed, the major frequency peaks extend discontinuously from about 0.12 Hz to about 20 Hz, with peak acceleration levels at approximately 0.01g to 0.25g. About 25 percent of the major frequency peaks occur in the 4-8 Hz human body resonance band, whereas about 50 percent of the major peaks occur at frequencies less than 0.15 Hz. The majority of these latter peaks appear in the vertical a_z direction.

2. For rubber tire type machines (scrapers, motor graders, and loaders) that have suspension systems and moderate speed capability, the major frequency peaks extend discontinuously from about 0.10 Hz to about 5.25 Hz,

* A complete list of all spectral plots is given in the previously cited NIOSH publication 78-153.

TABLE II
Heavy Equipment Machine Data Groupings

Data group no.	Computer file code	Machine type	Mfg. and model	SAE class	SAE doc. no.	Comments and conditions
A	21	Track type tractor	CAT D9 CAT D8 Terex G6	C-8	J1039	A single operator, operating a different machine each day, doing the same job, over the same terrain conditions; then repeated by a second operator.
B	26	The combined data of two operators from data group A (above) operating same track type tractors.				
C	24	Rubber-tired, self-propelled scrapers, 2 axle, 1 and 2 axle drive.	Michigan 110 CAT 627B CAT 631 B, C Terex TS-14	50,000- to 100,000-lb. wt. class 150,000-lb. wt. class	J1198	A single operator, operating a different machine each day, doing the same job, over the same terrain conditions; then repeated by a second operator.
D	27	The combined data of two operators from data group C above operating same rubber tired scrapers.				
E	25	Rubber-tired, self-propelled grader	Wabco 666 CAT 12E CAT 14C	35,000-lb. wt. class 55,000-70,000 wt. class	J236A	A single operator, operating a different machine each day, doing the same job, over the same terrain conditions; then repeated by a second operator.
F	28	The combined data of two operators from data group E (above) operating self-propelled graders.				
G	23	Rubber-tired, front end loader	Michigan 125 CAT 968 CAT 988 Hough-Int'l	36,000- to 70,000-lb. wt. class	J237A	A single operator, operating a different machine each day, doing the same job, over the same terrain conditions.
H	55	Vibrating drum type compactor	Tampo RS-28	---	---	Single operator operating a single machine; then repeated by second operator.
I	29	The combined data of two operators from data group H (above) operating a vibrating compactor.				
J	54	Hydraulic excavator (backhoe)	Deere 690B	38,000-lb. wt. class	---	Single operator operating a single machine; then repeated by a second operator.
K	51	Wheel type compactor	CAT 825	---	---	Single operator operating a single machine.
L	7	Crawler loader, front engine (track type)	CAT 955 CAT 941	C-6 C-5	J1057 J1039	Single operator operating a single machine. Single operator operating a single machine.
M	22	Log skidder	CAT	---	---	Single operator operating a single machine.
P	56	Off-on highway dump truck	MAKX RJ685	---	---	Single operator operating a single machine
Q	53	Off highway dump truck	CAT 769	100,000- to 200,000-lb. wt. class	J166	Single operator operating a single machine.

SELF-PROPELLED RUBBER TIRE SCRAPERS
 (MICHIGAN 110; CAT 627B, 631B, 631C;
 TEREX TS-14)
 OPERATOR NO. 1, EXPERIENCED

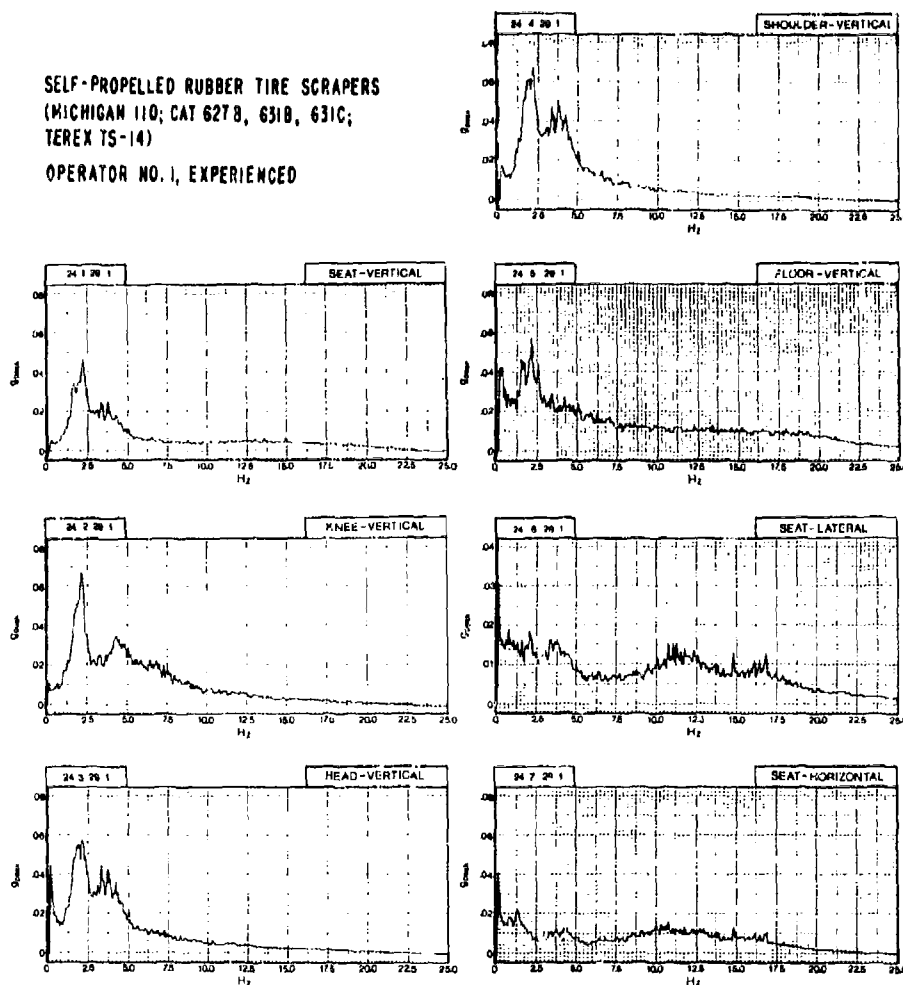


Fig. 10 - Data Group C

TABLE III

Example of Discussion of Data (Data Group C)

Data Group "C" (Computer File Code 24)

TYPE OF MACHINE: Self-propelled rubber tire scrapers (Michigan 110, CAT 627B and 631 B, C, Terex TS-14); both traditional and newer vibration reducing design.*

OPERATORS: One experienced and one inexperienced; each operating machines on separate days, doing the same job over same terrain.

WORK SEQUENCE: 1. Roading empty on blacktop (10-20 mph); 2. Filling bowl with dirt and rock (30-40 seconds fill time); 3. Roading loaded on semi-smoothhaul road (20 mph); 4. Gradually dumping load while moving (5 mph); 5. Road-ing unloaded on same haul road (30 mph); 6. Push-pull loading of another scraper; 7. Roading unloaded on access road (30 mph).

SPECTRAL PLOTS: 14; 7 for each operator.

HIGHEST AND LOWEST VIBRATION FREQUENCY PEAKS:

Experienced operator (summarized in Table C-1)

In the 0-3.99 Hz band, 2.12 Hz appears as a maximum peak at every vertical transducer position. It also appears in the lateral seat direction at about half the amplitude of the principle peak of 0.13 Hz. The principle peak of the seat in the horizontal direction is 0.31 Hz.

In the 4-7.99 Hz human-body resonance band, components of 4 Hz appear maxi-mally at all transducers.

In the 8-11.99 Hz band, 8 Hz components appear vertically at each transducer; 10-11 Hz components appear at the seat in the lateral and horizontal positions.

In the 12-15.99 Hz band, major components of 12-13 Hz appear at the floor, head, knee, and the seat laterally. Minor components of the 12-13 Hz band appear at the seat vertically with the highest peak occurring at 14.87 Hz; similarly, the seat horizontally has a 14.87 major component. Shoulder data do not appear.

In the 16-19.99 Hz band, major components of 16-18 Hz appear at each trans-ducer except at the head and shoulder.

In the 20-23.99 Hz band, only the floor and lateral seat direction appear to have spectra.

In summary, the overall major peak appears at 2.12 Hz at the shoulder. It also appears that the seats (in the vertical) direction tend to remove frequencies above 16 Hz.

*The data are a combination of data for scrapers of traditional and newer design. The primary spectral difference is that the vibration reducing designs exhibit vertical vibration levels of about one-half that of the traditional designs in the frequency range of 1.5 to 2.5 Hz.

Example of Tabularized Minimum and Maximum Peaks (Data Group C, Experienced Operator, Track Type Tractor

Plot	Frequency Bands												Total No. peaks in spectral plot
	0-3.99 Hz		4-7.99 Hz		8-11.99 Hz		12-15.99 Hz		16-19.99 Hz		20-23.99 Hz		
	max	min	max	min	max	min	max	min	max	min	max	min	max
24-1-19-1 (seat, vert az)	2.12Hz 0.640g 0.0050g	0.13Hz 0.62Hz 0.0050g	4.25Hz 0.425Hz 0.0180g	6.87Hz 7.12Hz 0.0050g	8.75Hz 9.75Hz 0.0050g	9.12Hz 10.73Hz 0.0050g	14.87Hz 13.09Hz 0.0050g	17.37Hz 16.50Hz 0.0050g	19.62Hz 19.25Hz 0.0050g	20.37Hz 20.12Hz 0.0050g	22.75Hz 22.75Hz 0.0050g	23.99Hz 23.99Hz 0.0050g	40
24-2-29-1 (knee, vert az)	2.12Hz 0.9670g 0.0050g	0.50Hz 0.100g 0.0050g	4.25Hz 0.0350g 0.0050g	7.87Hz 0.140g 0.0050g	8.25Hz 0.130g 0.0050g	11.37Hz 0.0050g 0.0050g	12.12Hz 15.62Hz 0.0050g	15.25Hz 17.87Hz 0.0050g	17.87Hz 19.62Hz 0.0050g	19.62Hz 20.12Hz 0.0050g	22.75Hz 22.75Hz 0.0050g	23.99Hz 23.99Hz 0.0050g	63
24-3-29-1 (head, vert az)	2.12Hz 0.0580g 0.0150g	0.62Hz 0.87Hz 0.0150g	4.12Hz 0.360g 0.0150g	7.50Hz 0.0070g 0.0050g	8.25Hz 0.0090g 0.0050g	11.62Hz 12.25Hz 0.0050g	12.62Hz 12.50Hz 0.0050g	15.62Hz 17.87Hz 0.0050g	17.87Hz 19.62Hz 0.0050g	19.62Hz 20.12Hz 0.0050g	22.75Hz 22.75Hz 0.0050g	23.99Hz 23.99Hz 0.0050g	37
24-4-29-1 (shoulder, vert, az)	2.12Hz 0.0670g 0.0130g	0.62Hz 0.87Hz 0.0130g	4.12Hz 0.430g 0.0130g	7.50Hz 0.0070g 0.0050g	8.25Hz 0.0090g 0.0050g	11.62Hz 12.25Hz 0.0050g	12.62Hz 12.50Hz 0.0050g	15.62Hz 17.87Hz 0.0050g	17.87Hz 19.62Hz 0.0050g	19.62Hz 20.12Hz 0.0050g	22.75Hz 22.75Hz 0.0050g	23.99Hz 23.99Hz 0.0050g	31
24-5-29-1 (floor, vert az)	2.12Hz 0.0570g 0.0130g	3.75Hz 0.0220g 0.0130g	4.25Hz 0.0250g 0.0130g	7.50Hz 0.0070g 0.0050g	8.25Hz 0.0090g 0.0050g	11.62Hz 12.25Hz 0.0050g	12.62Hz 12.50Hz 0.0050g	15.62Hz 17.87Hz 0.0050g	17.87Hz 19.62Hz 0.0050g	19.62Hz 20.12Hz 0.0050g	22.75Hz 22.75Hz 0.0050g	23.99Hz 23.99Hz 0.0050g	60
24-6-29-1 (seat, lateral, az)	0.13Hz 0.010g (2.12Hz)	2.50Hz 0.0120g 0.0180g	4.12Hz 0.0130g 0.0180g	7.06Hz 0.0065g 0.0155g	10.75Hz 11.25Hz 0.0155g	12.25Hz 12.25Hz 0.0155g	14.87Hz 15.62Hz 0.0155g	17.87Hz 19.62Hz 0.0155g	19.62Hz 20.12Hz 0.0155g	22.75Hz 22.75Hz 0.0155g	23.99Hz 23.99Hz 0.0155g	23.99Hz 23.99Hz 0.0155g	81
24-7-29-1 (seat, hori- zontal, az)	0.31Hz 0.0410g	2.50Hz 3.00Hz	4.20Hz 4.30Hz	6.00Hz 0.0050g	10.75Hz 0.0150g	12.25Hz 12.25Hz	14.87Hz 15.62Hz	17.87Hz 19.62Hz	19.62Hz 20.12Hz	22.75Hz 22.75Hz	23.99Hz 23.99Hz	23.99Hz 23.99Hz	54

TABLE V
Summary of Data Analysis

Method	Fast Fourier Transform (FFT)
Analyzer	Hewlett-Packard 5451 Digital Fourier Analyzer
Parameters:	
Analysis range	0.25 Hz
Block size	1024
Sample time	1.62 minutes
Δf - constant bandwidth -	.0488 Hz
Hanning window	Used once
Hanning correction factor	2.0

TABLE VI
Complete Distribution of Major Spectral Peaks of All Machines Tested by Type of Operator

Machine type	Data group	File code	Table	Maximum values	Transducer position	Operator	Number of plots
Track type tractors	A	21	A1	0.13 Hz @ .125g	floor	experienced	7
Track type tractors	A	21	A2	0.12 Hz @ .25g	floor	inexperienced	7
Combined data of group A	B	26	B	0.13 Hz @ .189g	floor	-----	7
Rubber tire scrapers	C	24	C1	2.12 Hz @ .067g	shoulder, knee	experienced	7
Rubber tire scrapers	C	24	C2	0.13 Hz @ .130g 3.75 Hz @ .128g 5.25 Hz @ .095g	floor, seat (lateral, a_y) seat (horizontal, a_x) seat (horizontal, a_x)	inexperienced	7
Combined data of group C	D	27	D	0.05 Hz @ .078g 0.10 Hz @ .080g 1.85 Hz @ .0740g	seat (lateral, a_y) floor knee	-----	7
Rubber tire motor graders	E	25	E1	2.45-2.50 Hz @ .066-.0760g	seat (vertical, a_z), shoulder, head	experienced	6
Rubber tire motor graders	E	25	E2	2.55-2.60 Hz @ .042-.043g	head, shoulder	inexperienced	6
Combined data group E	F	28	F	2.37-2.48 Hz @ .052-.056g	seat (vertical, a_z), shoulder, head	-----	6
Rubber tire loaders	G	23	G	0.13 Hz @ .056-.11g 2.37 Hz @ .04-.05g	floor, seat, all three directions knee, head, shoulder, seat (vertical, a_z)	experienced	7

TABLE VI (continued)

Complete Distribution of Major Spectral Peaks of All Machines Tested by Type of Operator

Machine type	Data group	File code	Table	Maximum values	Transducer position	Operator	Number of plots
Track type tractors	A	21	A1	0.13 Hz @ .125g	floor	experienced	7
Track type tractors	A	21	A2	0.12 Hz @ .25g	floor	inexperienced	7
Combined data of group A	B	26	B	0.13 Hz @ .189g	floor	-----	7
Rubber tire scrapers	C	24	C1	2.12 Hz @ .067g	shoulder, knee	experienced	7
Rubber tire scrapers	C	24	C2	0.13 Hz @ .130g 3.75 Hz @ .128g 5.25 Hz @ .095g	floor, seat (lateral, a_y) seat (horizontal, a_x) seat (horizontal, a_x)	inexperienced	7
Combined data of group C	D	27	D	0.05 Hz @ .078g 0.10 Hz @ .080g 1.85 Hz @ .0740g	seat (lateral, a_y) floor knee	-----	7
Rubber tire motor graders	E	25	E1	2.45-2.50 Hz @ .066-.0760g	seat (vertical, a_z) shoulder, head	experienced	6
Rubber tire motor graders	E	25	E2	2.55-2.60 Hz @ .042-.043g	head, shoulder	inexperienced	6
Combined data of group E	F	26	F	2.37-2.48 Hz @ .057-.056g	seat (vertical, a_z) shoulder, head	-----	6
Rubber tire loaders	G	23	G	0.13 Hz @ .056-.11g 2.37 Hz @ .04-.05g	floor, seat, all three directions knee, head, shoulder, seat (vertical, a_z)	experienced	7

TABLE VI (continued)

Complete Distribution of Major Spectral Peaks of All Machines Tested by Type of Operator

Vibrating drum compactor	H	55 H1	.010 Hz @ .070g .012 Hz @ .055g	shoulder head	experienced	6
Vibrating drum compactor	H	55 H2	3.62 Hz @ .0810-.090g	head, shoulder	inexperienced	6
Combined data of group H	I	29 I	0.13 Hz @ .0191-.27g 14.13-15.28 Hz @ .004-.01g	knee, seat (vertical, a_z), head, shoulder all locations except horizontal seat	---	6
Hydraulic excavator	J	54 J1	0.12-0.15 Hz @ .065-.54g 15.25 Hz @ .027g	seat (vertical, a_z), head knee	experienced	7
Hydraulic excavator	J	54 J2	0.18-0.20 Hz @ .026-.051g 14.62-15.35 Hz @ .01-.027g	floor, knee, head all locations except horizontal seat and head	inexperienced	7
Wheel type compactor	K	51 K	0.13 Hz @ .025-.037g 14.95 Hz @ .064g	seat (lateral, a_x ; horizontal, a_z) seat (horizontal, a_x)	experienced	3
Track type crawler loader	L	7 L	0.12-0.13 Hz @ .016-.039g 6.50 Hz @ .034g 19.75 Hz @ .065g	seat (horizontal, a_x and lateral, a_y) head, knee seat (horizontal, a_x)	experienced	5
Track type crawler loader	N	22 N	0.12 Hz @ .018-.023g 4.12 Hz @ .014g 8-10.25 Hz @ .011g	seat (lateral, a_y ; horizontal, a_x) seat (lateral, a_y) seat (lateral, a_y)	experienced	3
Log skidder	N	52 N	1 Hz @ .130g 2.62 Hz @ .06g 4.15 Hz @ .074g	seat (lateral, a_x) seat (vertical, a_z) seat (lateral, a_y)	experienced	3
Off-on highway dump truck	P	56 P	2.50 Hz @ .0195-.03-0g 12.12 Hz @ .0151g	head, shoulder, floor seat (horizontal, a_x)	experienced	6
Off highway dump truck	Q	53 Q	0.12 Hz @ .0155-.048g 5.1-5.3 Hz @ .01-.037g 11.60 Hz @ .021g	seat (horizontal, a_x) all seat locations seat (lateral, a_y)	experienced	3

TABLE VI (continued)

Complete Distribution of Major Spectral Peaks of All Machines Tested by Type of Operator

Vibrating drum compactor	H	55 H1	.010 Hz @ .070g .012 Hz @ .055g	shoulder head	experienced	6
Vibrating drum compactor	H	55 H2	3.62 Hz @ .0810-.090g	head, shoulder	inexperienced	6
Combined data of group H	I	29 I	0.13 Hz @ .0191-.27g 14.13-15.28 Hz @ .004-.03g	knee, seat (vertical, a_z), head, shoulder all locations except horizontal seat	—	6
Hydraulic excavator	J	54 J1	0.12-0.15 Hz @ .065-.54g 15.25 Hz @ .027g	seat (vertical, a_z), head knee	experienced	7
Hydraulic excavator	J	54 J2	0.18-0.20 Hz @ .026-.051g 15.62-15.35 Hz @ .01-.027g	floor, knee, head all locations except horizontal seat and head	inexperienced	7
Wheel type compactor	K	51 K	0.13 Hz @ .025-.037g 15.95 Hz @ .064g	seat (lateral a_y ; horizontal, a_x) seat (horizontal a_x)	experienced	3
Track type crawler loader	L	7 L	0.12-0.13 Hz @ .016-.029g 6.50 Hz @ .034g 19.75 Hz @ .065g	seat (horizontal a_x and lateral a_y) head, knee seat (horizontal a_x)	experienced	5
Track type crawler loader	M	22 M	0.12 Hz @ .018-.023g 4.12 Hz @ .014g 8-10.25 Hz @ .011g	seat (lateral, a_y) horizontal, a_x seat (lateral, a_y) seat (lateral, a_y)	experienced	3
Log skidder	N	52 N	1 Hz @ .130g 2.62 Hz @ .08g 4.15 Hz @ .074g	seat (lateral, a_y) seat (vertical, a_z) seat (lateral, a_y)	experienced	3
Off-on highway dump truck	P	56 P	2.50 Hz @ .0195-.0340g 12.12 Hz @ .0151g	head, shoulder, floor seat (horizontal, a_x)	experienced	6
Off highway dump truck	Q	53 Q	0.12 Hz @ .0155-.048g 5.1-5.3 Hz @ .01-.037g 11-60 Hz @ .021g	seat (horizontal a_x) all seat locations seat (lateral, a_y)	experienced	3

with peak acceleration levels at approximately 0.04g to 0.130g. In the 4-8 Hz human body resonance band, only a single peak at 5.25 Hz at 0.095g in the horizontal (a_x) seat position occurs. About 25 percent of the major peaks occur in the 2.12-2.6 Hz range. The majority of these latter peaks appear in the vertical a_z direction.

3. For the vibrating drum type machine compactors, the spectra spread from 0.1 Hz broadly to 15.28 Hz, with acceleration levels ranging from 0.004g to 0.09g. In the 4-8 Hz human body resonance band there were no major peaks; however, a peak at 3.62 Hz appears at 0.09g. The majority of the spectra peaks appear in the vertical direction.

For the wheel type compactor (where we have available only a limited amount of data) seat data, 0.13 Hz and 14.95 Hz appear predominant with accelerations ranging from 0.025g to 0.064g.

4. For the hydraulic excavator (a track machine without a suspension) there appear to be two distinct groups of peaks: one group at very low frequencies (0.12-0.20 Hz at 0.026g to 0.54g) and another group at higher frequencies (14.6-15.3 Hz at 0.01g to 0.027g). Once again, the majority of these peaks occur vertically and no major peaks occur in the 4-8 Hz human body resonance band.

5. The limited available seat data for the log skidder (a very specialized forestry type machine) range from 1-4.15 Hz, with acceleration levels from 0.07g to 0.130g peaks.

6. For the case of the two dump trucks, we found a spectrum extending from 0.12-12.12 Hz (0.01g to 0.048g). In the 4-8 Hz resonance band, about 37 percent of the major peaks occur. Once again, the majority of all peaks appear in the vertical a_z direction.

CONCLUSIONS

Recognizing the constraints on the data obtained in this study as well as our small operator sample size, it would appear that certain limited and tentative concluding comments can be made:

1. From these limited data there appears to be little difference between experienced and inexperienced operators.

2. From these limited data, there appears to be little difference in spectra between operators of differing

body masses. (This would appear to confirm an observation by Barton et al. (10).)

3. From these limited data, there appears to be a single vibration transmission path to the operator's upper torso and head from the vehicle occurring directly through the operator's seat and torso. In the case of the operator's seat, the vibration impinging on the upper torso is modified by the filtering characteristics of the seat.

4. Most of the higher acceleration levels measured occur in frequency bands below the 4-8 Hz human body resonance band with much of the data occurring at less than 1 Hz.* We believe these very low frequency peaks are due to changes in vehicle path or speed, such as accelerating the vehicle and braking, steering through turns, and changing grades or side slopes in the terrain.

ACKNOWLEDGEMENTS

The authors would like to extend their thanks to the following: (NIOSH) Dr. E.S. Harris, M. Curry, D. Ring, and S. Adams; (Union of Operating Engineers - Local # 3) D. Marr, J. Martin, and A. Burch; (Caterpillar Tractor Co.) J.C. Burton; (Structural Dynamics Research Corp.) Steve Beck; and (NAMRL) Dr. J.C. Guignard for their advice and assistance during the course of this study.

* Frequencies below 1 Hz are reported (11, 12) to cause motion sickness; however, the subjects in this study have never reported this problem while operating the heavy equipment machines. Recent work has shown that human exposure from 0.1-0.7 Hz (measured at the accelerometers in the order of 0.19g) as reported here are generally associated with motion sickness in susceptible people when the motion is sustained (as on a ship) and has an on-going periodicity. (13) This does not generally happen in this situation because of the non-recurring nature of the motion.

REFERENCES

1. Wasserman, D.E., D.W. Badger, T.E. Doyle, and L. Margolies: Industrial Vibration - An Overview. ASSE Journal 19(6):38-43 (1974).
2. Guignard, J.C. and P.F. King: Aeromedical Aspects of Vibration and Noise. AGAR, No. 151 (1972).
3. Milby, T.E. and R.C. Spear: Relationship Between Whole-Body Vibration and Morbidity Patterns Among Heavy Equipment Operators. DHEW Publication No. (NIOSH) 74-131 (1972).
4. Spear, R.D., C. Keller, V. Behrens, M. Hudes and D. Tartar: Morbidity Patterns Among Heavy Equipment Operators Exposed to Whole-Body Vibration. DHEW Publication No. (NIOSH) 77-120 (Nov. 1976).
5. Gruber, G.J. and H.H. Ziperman: Relationship Between Whole-Body Vibration and Morbidity Patterns Among Motor Coach Operators. DHEW Publication No. (NIOSH) 75-104 (Sept. 1974).
6. Gruber, G.J.: Relationship Between Whole-Body Vibration and Morbidity Patterns Among Interstate Truck Drivers. DHEW Publication No. (NIOSH) 77-168 (June 1977).
7. Sturges, D.V., D.W. Badger, R.N. Slarve and D.E. Wasserman: Laboratory Studies on Chronic Effects of Vibration Exposure. Paper B10-1, AGARD Conference on Vibration and Combined Stress in Advanced Systems, Oslo, Norway (April 1974).
8. Badger, D.W., D.V. Sturges, R.N. Slarve, and D.E. Wasserman: Serum and Urine Changes in Macaca mulatta Following Prolonged Exposure to 12 Hz, 1.5g Vibration. Paper B11-1, AGARD Conference on Vibration and Combined Stress in Advanced Systems, Oslo, Norway (April 1974).
9. Cohen, H., D. Wasserman, and R. Hornung: Human Performance and Transmissibility Under Sinusoidal and Mixed Vertical Vibration. Ergonomics 20(3):207-216 (1977).
10. Barton, J.C. and R.E. Hefner: Society of Automotive Engineers. Whole-Body Vibration Levels: A Realistic Baseline for Standards. Paper 760415, Earthmoving Industry Conference, Peoria, Illinois (April 1976).
11. Goto, D., and H. Kanda: Motion Sickness Incidence in the Actual Environment. Research Institute, Heavy Industries Company, Tokyo, Japan (Working Group Paper ISO/TC/08/SCH/WG2-63, (Aug. 1977).
12. Guignard, J.C.: Recent Research in the U.S. Germaine to International Standard, ISO2631-1974 and to its Proposed Extension to Frequencies Below 1 Hz. U.K. Informal Group on Human Response to Vibration, Northampton, England (Sept. 1977).
13. Guignard, J.C.: (private communication).

RESEARCH RELATED TO THE EXPANSION AND IMPROVEMENT OF HUMAN VIBRATION EXPOSURE CRITERIA

Richard W. Shoenberger

Aerospace Medical Research Laboratory, Aerospace Medical Division
Wright-Patterson Air Force Base, Ohio 45433

A program of research directed toward improvement of the validity and generality of human vibration exposure criteria is described. A psychophysical matching technique was used to investigate the perceived intensity of various types of vibration environments. Experiments conducted to date are of two types: comparisons of sinusoidal and non-sinusoidal vibrations, and comparison of translational and angular vibrations. Results discriminate between alternate methods for evaluating the severity of non-sinusoidal vibrations, and indicate relationships between translational and angular vibrations needed for the expansion of vibration criteria to include angular motions.

Standards for human exposure to whole-body vibration [1, 3, 8] are intended to be applied to real-world situations in which the motion environments are composed of complex waveform vibrations containing multiple frequencies or broadband random inputs. These may occur in any of three translational and three rotational directions, either independently or simultaneously in any combination of the six possible degrees-of-freedom. However, the experimental data base from which such standards are derived consists primarily of studies in which the vibration inputs were single sinusoids applied in one or another of the three translational axes. To improve the validity and generality of vibration exposure criteria, research is needed comparing single-axis sinusoidal and various kinds of non-sinusoidal, angular, and multi-degree-of-freedom vibrations. A program of research in the Biodynamic Effects Branch, Biodynamics and Bioengineering Division of the Aerospace Medical Research Laboratory, investigating the perceived intensity of various types of vibration environments, is directed toward this goal.

This paper is divided into two sections: experiments comparing sinusoidal vibrations with various kinds of non-sinusoidal vibrations, and experiments comparing

translational vibrations with angular vibrations. Although the detailed experimental designs varied slightly from one experiment to another, the technique used was fundamentally the same for all experiments -- a psychophysical matching procedure in which the subjects matched their perceptions of the intensity of one type of vibration by adjusting the physical intensity of another type of vibration. Similar techniques have proved successful for comparing the subjective intensities of vibrations with different frequencies [5], different translational axes [6], and different spectral compositions [7].

Comparisons of Sinusoidal and Non-Sinusoidal Vibrations

Current human vibration exposure standards [1, 3, 8] specify two procedures for evaluating non-sinusoidal vibration environments. The preferred method treats each component frequency of a multifrequency environment or each third-octave band of a random environment independently, while the alternative method involves a weighting technique. These two methods yield different results except when all the vibration energy is within a single third-octave band. Under the weighting method, the severity rating of the vibration increases with the number

of third-octaves in the spectrum; but under the independent component method, the rating is determined solely by the criterion level of the most intense third-octave and is, therefore, independent of the bandwidth. The greatest difference occurs when the vibration spectrum has the shape of the criterion curves.

In the three experiments reported below, the vibration stimuli were constituted so that they contained either one, two, three or four components, each at a particular criterion level and each in a different third-octave band. Under the independent component method the severity of the stimuli would be rated the same no matter how many components they contained, but under the weighting method the severity rating would increase as the number of components increased. The experimental procedure was essentially the same in each experiment, but the composition of the vibration stimuli varied between experiments. In Experiment I, the stimuli were composed from sinusoids with frequencies from 11 to 63 Hz; in Experiment II they were made up of third-octave bands of random vibration with center frequencies from 16 to 40 Hz; and in Experiment III they were synthesized from sinusoids from 2.6 to 16 Hz.

METHOD

Subjects: In all three experiments the subjects were male Air Force military personnel, who were physically qualified volunteer members of a vibration panel. They received incentive pay for participation in vibration experiments. Ten subjects participated in Experiment I, 12 subjects in Experiment II, and 14 subjects in Experiment III.

Apparatus: In Experiment I vibration was produced by an MB Electronics electromagnetic vibrator (Model C-5), and in Experiments II and III an Unholtz-Dickie electromagnetic vibrator (Model MA 250D) was used to produce the vibration stimuli. In all three experiments a lightweight aluminum seat was rigidly mounted on the moving element of the vibrator, and transmitted the vibration directly to the subject without cushioning or padding. The Unholtz-Dickie seat included arm and foot rests, but the MB seat did not. The subject

was seated upright and secured to the seat by a lap belt and shoulder harness. He was also provided with a hand-held potentiometer with which he controlled the amplitude of the matching vibration. The acceleration of the vibrating seat was displayed on a true RMS meter, and the acceleration of the matching vibration was read from this meter and recorded by the experimenter for each matching response. Photographs of the experimental setup for both vibrators and additional details concerning the production of the vibration stimuli are available in reference 7.

Vibration: In all three experiments, vibration was in the Z-axis. Vibration stimuli in Experiment I were composed of four sinusoidal frequencies (11, 17, 40 & 63 Hz) presented either singly or in all possible combinations of two, three or four frequencies. Twenty-five Hz (the matching frequency) was also presented as a stimulus to provide a check on possible biases or errors in the matching response when the stimulus and response frequencies were identical. The frequencies used were approximately the preferred center frequencies of every other third-octave band from 10 to 63 Hz. However, slight departures from some of these center frequencies were made to avoid harmonic relationships between frequencies. This resulted in constantly changing phase relationships between the frequencies in all combinations, rather than the fixed phasing which would occur for harmonically related frequencies. All frequencies were presented at accelerations corresponding to the ISO 25-min Fatigue-Decreased Proficiency (FDP) level [3]. Table I lists all of the stimuli used in Experiment I, and specifies their frequencies and RMS accelerations.

In Experiment II the vibration stimuli were made up of five third-octave bands of random vibration, with center frequencies of 16, 20, 25, 31.5 and 40 Hz, presented either singly or in combinations of two, three, or four bands. The 25 Hz sinusoidal matching frequency was also presented as a stimulus, as it was in Experiment I, to check on possible response biases. All third-octave bands were presented at acceleration levels corresponding to the

TABLE I
Vibration Stimuli (Exp. I, 25-min FDP)

Number of Components	Stimulus Code	Frequency (Hz)	Acceleration (RMS G_z)
One	A	11	0.25
	B	17	0.39
	25	25	0.57
	C	40	0.92
	D	63	1.43
Two	AB	11 + 17	0.46
	AC	11 + 40	0.95
	AD	11 + 63	1.45
	BC	17 + 40	0.99
	BD	17 + 63	1.48
	CD	40 + 63	1.70
Three	ABC	11 + 17 + 40	1.03
	ABD	11 + 17 + 63	1.50
	ACD	11 + 40 + 63	1.72
	BCD	17 + 40 + 63	1.74
Four	ABCD	11 + 17 + 40 + 63	1.76

ISO 1-hr FDP level [3]. It was necessary to use a lower acceleration level than that used in Experiment I (25-min FDP) because the random stimuli contained occasional peaks which were considerably higher than the peak accelerations for the sinusoidal and multifrequency stimuli. All possible combinations of four sinusoids were used to produce the stimuli in Experiment I, while selected combinations of five third-octave bands were used in Experiment II (reasons for this difference are discussed in reference 7). Table II lists all of the stimuli used in Experiment II, and specifies their center frequencies and RMS accelerations.

In the third experiment, the two methods for evaluating non-sinusoidal vibrations were compared at frequencies which spanned the Z-axis body resonance range. The vibration stimuli were composed of five sinusoidal frequencies (2.6, 4.1, 6.3, 10, and 16 Hz) presented either singly or in combinations of two, three, or four frequencies. In this case, 6.3 Hz was used as the matching frequency. All frequencies were presented at accelerations corresponding to the ISO

1-hr FDP level [3]. Table III lists all of the stimuli used in Experiment III and specifies their frequencies and RMS accelerations.

Procedure: In all three experiments, each subject matched his perception of the intensity of each of the stimulus vibrations by adjusting the intensity of a sinusoidal matching frequency (25 Hz in Experiments I and II and 6.3 Hz in Experiment III) until he felt that its subjective intensity was the same as the subjective intensity of the stimulus vibration he had just experienced. Each match involved a 30-second exposure to the stimulus vibration and a subsequent exposure to the matching vibration which lasted approximately 15 to 30 seconds, depending on how quickly the subject achieved a match.

When each subject arrived at the laboratory, the nature of the experiment and the intensity-matching procedure were explained. The subject was then seated in the vibration chair and given a short practice session to familiarize him with the operation of the equipment and the matching

TABLE II
Vibration Stimuli (Exp. II, 1-hr FDP)

Number of Third-Octave Bands	Stimulus Code	Center Frequency (Hz)	Acceleration (RMS G_z)
(Sinusoidal)	25	25	0.38
One	A	16	0.24
	(B -----	20 -----	0.30)*
	C	25	0.38
	(D -----	31.5 -----	0.47)*
	E	40	0.60
Two	AE	16 + 40	0.65
	BC	20 + 25	0.48
	BD	20 + 31.5	0.56
	CD	25 + 31.5	0.60
Three	ABC	16 + 20 + 25	0.54
	ACE	16 + 25 + 40	0.75
	CDE	25 + 31.5 + 40	0.85
Four	ABCD	16 + 20 + 25 + 31.5	0.72
	ABDE	16 + 20 + 31.5 + 40	0.86
	BCDE	20 + 25 + 31.5 + 40	0.90

*The 20 Hz and 31.5 Hz bands were not used as individual third-octave stimuli.

technique. He then matched each of the vibration stimuli for a particular experiment. The series of stimuli was presented to each subject in a different random order. After a short rest break of about 5 minutes, the stimulus series was presented again and the subject matched each stimulus a second time.

RESULTS AND DISCUSSION

The mean matching responses obtained when the stimulus frequency was the same as the matching frequency were 0.58 RMS G_z for Experiment I, 0.36 RMS G_z for Experiment II, and 0.13 RMS G_z for Experiment III. These values are nearly identical to the respective stimulus accelerations and demonstrate that the matching procedure had no inherent response biases.

Table IV presents the mean acceleration of the matching responses for stimuli containing the same number of components (i.e., one, two, three, or four) for each

of the three experiments. The difference in the magnitude ranges of the matching responses between experiments are the result of the different FDP levels and frequency ranges of the stimuli and the different frequencies of the matching responses used in the three experiments.

Each of the three experiments was designed to investigate the relationship between perceived vibration intensity and the number of criterion-level components in the vibration stimulus. Under the independent component method for evaluating complex vibrations, the acceleration of the matching response should be independent of the number of components in the stimulus. On the other hand, under the weighting method, the acceleration of the matching response should increase with the number of components in the stimulus. Inspection of Table IV indicates that in all three experiments the acceleration of the matching response increased almost linearly as the number of sinusoids

TABLE III
Vibration Stimuli (Exp. III, 1-hr FDP)

Number of Components	Stimulus Code	Frequency (Hz)	Acceleration (RMS G_z)
One	A	2.6	0.15
	B	4.1	0.12
	C	6.3	0.12
	D	10	0.15
	E	16	0.24
Two	AE	2.6 + 16	0.28
	BC	4.1 + 6.3	0.17
	BD	4.1 + 10	0.19
	CD	6.3 + 10	0.19
Three	ABC	2.6 + 4.1 + 6.3	0.23
	ACE	2.6 + 6.3 + 16	0.31
	CDE	6.3 + 10 + 16	0.31
Four	ABCD	2.6 + 4.1 + 6.3 + 10	0.27
	ABDE	2.6 + 4.1 + 10 + 16	0.34
	BCDE	4.1 + 6.3 + 10 + 16	0.33

TABLE IV
Mean Acceleration of Matching Responses (RMS G_z)

Number of Components	Exp. I	Exp. II	Exp. III
One	0.64	0.36	0.12
Two	0.88	0.47	0.16
Three	1.11	0.59	0.19
Four	1.31	0.67	0.22

(Exps. I & III) or third-octave bands (Exp. II) in the stimulus increased. In each experiment there was roughly a doubling of response acceleration as the number of components in the stimulus increased from one to four. In order to test the significance of the changes in response as a function of the number of components in the stimulus, an analysis of variance was performed for each experiment. The results of all three analyses showed that the increases in the mean accelerations of the matching responses as a

function of the number of components in the stimulus were highly significant ($p \ll 0.001$ for each experiment). The similarity of results in spite of differences in the three experiments (e.g., types of vibration waveforms; acceleration levels; vibration seats; and frequency ranges, spacing and sampling of stimulus components) suggests considerable generality for the fundamental relationship shown in these experiments; namely, that the perceived intensity of complex vibration inputs increases as a function of the number of

criterion-level components in the stimulus.

An increase in subjective intensity as more components are added to the stimulus is not predicted by the independent component method for evaluating complex vibrations but is predicted by the weighting method. Moreover, if the weighted accelerations of the matching responses are compared with the weighted accelerations of the input vibrations, additional support for the weighting method is provided, since the correspondence is quite good for all three experiments. For each experiment, Figure 1 shows the mean weighted response acceleration as a function of the mean weighted stimulus acceleration for stimuli containing one, two, three, or four components. If the correspondence were perfect, the data points would lie along the diagonal line. It is evident from the figure that the data fall quite close to the diagonal.

The results indicate that the independent component method for evaluating non-sinusoidal vibrations tends to underestimate the severity of complex vibration environments and that the degree of underestimation increases as the number of components in the vibration input increases. The fact that the matching acceleration increased by roughly a factor of two as the number of stimulus components increased from one to four suggests that the difference in subjective intensity is great enough to have practical significance. For example, a doubling of acceleration represents a change in severity in terms of the ISO standard from the Fatigue-Decreased Proficiency Boundary to the Exposure Limit. The findings of these experiments also indicate that the subjective intensity of non-sinusoidal vibration environments is more accurately reflected by the weighting method and provide evidence in favor of adopting the weighting method as the preferred

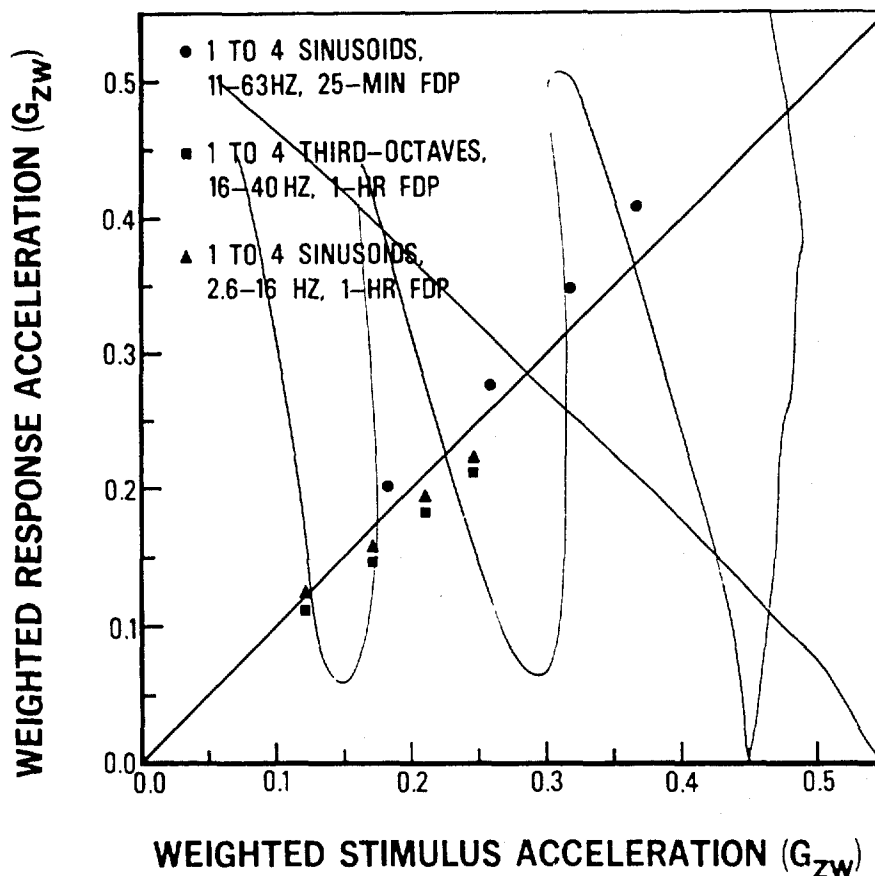


Figure 1. Weighted response acceleration as a function of weighted stimulus acceleration for each experiment

procedure when a vibration environment contains energy in more than one third-octave band.

Comparisons of Translational and Angular Vibrations

In addition to non-sinusoidal vibrations, operational environments contain vibration components in all six spatial degrees-of-freedom--linear motions along the three translational axes (X, Y and Z), and angular motions around each of these axes in roll, pitch and yaw. To be applicable to all vibration environments, vibration standards must provide criteria for all six of these directions of motion. However, existing criteria for human exposure to whole-body vibration [1, 3, 8] are limited to translational vibrations along the X, Y and Z axes.

Very little information is available concerning human response to angular vibration. Even if a significant body of knowledge existed on angular vibration effects, specific data on the comparability of translational and angular vibrations would be needed. A contributing factor is that vibration intensity is measured in different physical units for the two types of vibration - m/s^2 (or G) for translational vibration, and rad/s^2 for angular vibration. Although these are both units of acceleration there is no physical way to equate them.

One way to obtain information on the equivalence of linear and angular vibrations is through a psychophysical matching technique similar to the one used in the experiments described above. In this case the subjects matched their perceptions of the intensity of translational stimulus vibrations in the vertical direction (Z axis) by adjusting the physical intensity of angular response vibrations in the roll axis. The purpose of the experiment was to obtain comparative data on the subjective intensity of translational and angular vibrations, necessary for the inclusion of angular oscillatory motions into human vibration exposure criteria.

METHOD

Subjects: The subjects were again from the vibration panel

described above. Eleven subjects participated in this experiment.

Apparatus: Whole-body vibration was produced by the AMRL six degree-of-freedom motion device (SIXMODE). The SIXMODE is capable of motion in all six degrees-of-freedom and has a payload capacity of 1,000 lbs. The vibration seat was rigidly constructed of aluminum and bolted directly to the vibration platform. The subject was restrained by means of a lap belt and shoulder harness, and was seated on a standard F-105 seat insert made up of a parachute container and seat pad. Previous research [2] has shown that this setup provides a stiff but comfortable coupling between the seat and subject, that has a negligible effect on vibration transmission to the subject over the frequency range from 2 to 10 Hz.

The vibration table was instrumented with accelerometers which measured the acceleration of the table in all six degrees-of-freedom. These acceleration signals were recorded on six channels of a strip-chart recorder. In addition, the signals for the vertical and roll directions were fed to true RMS meters, providing a digital readout for the Z-axis input accelerations, in RMS G, and the roll-axis response accelerations, in RMS rad/s^2 .

The subject was also provided with a hand-held potentiometer with which he controlled the intensity of the roll-axis matching vibration, and a headset and microphone connected to an intercom system, for communications between the subject, experimenter, and SIXMODE operator.

Vibration: Z-axis stimulus vibrations were presented at each of the following frequencies: 2.5, 3.15, 4, 5, 6.3, 8 and 10 Hz. Each of these seven frequencies was presented at three different acceleration levels: the 2.5-hr. FDP level [3], the 1-hr. FDP level, and the 25-min. FDP level (see Table V). The roll-axis response vibrations were presented at the same frequencies and were adjusted in intensity by the subjects. Preliminary evaluations of the motion produced by the SIXMODE, within the vibration regime to be used, showed that cross-axis motion was generally quite small, except when

the machine was operated in roll at 10 Hz. At this frequency, driving the machine in roll produced considerable cross-axis motion, especially in the Y axis. The amplitude of the Y-axis motion was related to the roll amplitude, so that at high roll accelerations Y-axis acceleration became quite large. It was anticipated that this was likely to affect the subject's matching response at 10 Hz, and the results showed that it did. This point will be considered further in the results and discussion section.

One additional point must be noted in connection with the vibration environment produced when the vibrator is operated in roll. As a consequence of the way that the SIXMODE table is connected to the hydraulic actuators that produce its motion, the axis of rotation for angular motions in roll (and in pitch as well) is located approximately 22.9 cm (9 in) below the table. Adding the thickness of the table and the height of the seat results in the subject being seated approximately 81.3 cm (32 in) above the axis of rotation. Therefore, the resultant translational accelerative forces acting on the subject are somewhat greater than they would be if he were seated at the axis of rotation. However, such an arrangement is not unrealistic, since it is representative of configurations found in many operational situations.

Procedure: Each subject was required to match his perception of the intensity of each of the Z-axis stimulus vibrations listed in Table V by adjusting the intensity of vibration in the roll axis until he felt that its subjective intensity was the same as the stimulus vibration he had just experienced. For each match the frequency of the matching roll vibration was the same as that of the particular stimulus vibration being matched. Each match involved a 30-second exposure to the Z-axis stimulus vibration and a subsequent exposure to the matching roll vibration that lasted approximately 20 to 45 seconds, depending on how quickly the subject achieved a match.

When each subject arrived at the test facility, he was given a set of written instructions which

explained the nature of the experiment and the intensity-matching procedure. He was then seated in the vibration chair and given a short practice session to familiarize him with the operation of the equipment and the matching technique. The subject then experienced a series of matching runs (pairs of stimulus and matching vibrations) consisting of two matches at each of the seven frequencies at one of the three acceleration levels (see Table V). Testing was carried out during three test sessions, with a different acceleration level in each session. Sessions were scheduled at approximately one week intervals. The order of acceleration levels across sessions and the order of frequencies within a session were randomized for each subject.

RESULTS AND DISCUSSIONS

Table VI gives the mean acceleration of the matching responses (2 matches for each of 11 subjects) for each of the 21 vibration stimuli listed in Table V. The same data are also presented in Figure 2, which shows response acceleration as a function of frequency, with stimulus intensity (FDP level) as a parameter. As mentioned previously, roll motion at 10 Hz was always accompanied by appreciable Y-axis motion, especially at higher roll acceleration levels (approximately 0.25 RMS G at 4 RMS rad/s² roll). This means^y that the subject matched the 10 Hz Z-axis stimuli with a response vibration that was a combination of angular motion in roll and translational motion in the Y-axis. The effect of this artifact on the magnitude of the roll matching response at 10 Hz is readily apparent in Figure 2. Therefore, the least squares lines, fitted to the means for each of the three FDP levels, in Figure 2 are limited to the frequencies from 2.5 through 8.0 Hz, and the 10 Hz data are excluded from all subsequent analyses.

Although the 10 Hz data are not a valid representation of the roll acceleration required to match the 10 Hz Z-axis stimuli, they do indicate that the Y-axis motion and the roll motion interact in their effects on perceived vibration intensity. This suggests that simultaneous motions in more than

TABLE V
Vibration Stimuli (Roll Exp.)

Frequency (Hz)	Acceleration (RMS G_z)		
	2.5-hr FDP	1-hr FDP	25-min FDP
2.5	.092	.153	.228
3.15	.082	.135	.204
4.0	.072	.120	.183
5.0	.072	.120	.183
6.3	.072	.120	.183
8.0	.072	.120	.183
10.0	.092	.153	.228

TABLE VI
Mean Response Acceleration
(RMS rad/s^2) for Each Stimulus Condition

Frequency (Hz)	Stimulus Level		
	2.5-hr FDP	1-hr FDP	25-min FDP
2.5	0.63	1.09	1.48
3.15	0.68	1.33	1.93
4.0	0.91	1.55	2.79
5.0	1.05	2.11	3.86
6.3	1.64	2.92	4.94
8.0	2.06	3.74	5.74
10.0	2.23	3.05	4.02

one axis should be evaluated on the basis of their combined effects, rather than independently as recommended in paragraph 4.3 of the ISO standard [3].

Inspection of Figure 2 indicates that the mean acceleration of the roll-axis matching response increased both as a function of frequency and as a function of the intensity level of the Z-axis stimulus vibrations. It is also apparent that the mean responses for each intensity level are fit very well by straight lines in a log-log plot of roll acceleration as a function of frequency. To test the statistical significance of these results, log transforms were calculated for the data for each subject for each of the stimulus conditions (excluding 10 Hz), and an analysis of variance was performed based on the logs. The analysis of variance showed highly significant effects for frequency ($F=104.22$, $p \ll .001$) and

for intensity level ($F=65.70$, $p \ll .001$). This means that the acceleration of the roll-axis matching response increased significantly with frequency and with the intensity level of the Z-axis stimulus vibrations.

The results of this experiment demonstrate that perception of the subjective intensity of oscillatory motions in roll, as indicated by the acceleration of roll-axis matching responses, is significantly related to both the frequency and intensity of the Z-axis stimulus vibrations. Since the stimuli were chosen from Z-axis equal intensity contours specified by current vibration exposure standards, the mean matching responses obtained define equivalent contours of equal subjective intensity for roll vibrations, for the conditions under which the experiment was conducted. Of course, the exact level and perhaps the slope of the curves may be affected by a number of factors which were not

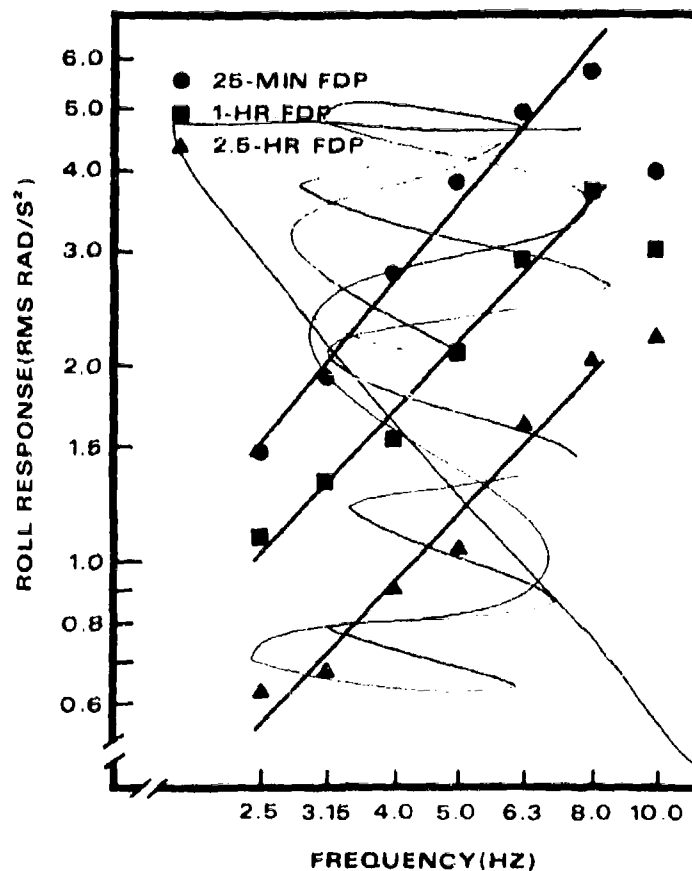


Figure 2. Mean acceleration of roll response as a function of frequency, for each level of stimulus intensity.

investigated; for example, the configuration of the vibration seat, whether or not the subject is restrained, or the distance of the subject from the axis of rotation. However, the basic relationship between the matching response and the intensity and frequency of the stimulus vibrations should still hold. (Indeed, in a study in which the subjects sat unrestrained on a flat seat with no backrest and were asked to set levels of vibration that they felt were "uncomfortable" [4], the roll curves showed essentially the same relationship to frequency as found here.) These results provide information on the relationship between Z-axis vibra-

tions, measured in translational acceleration units of G, and roll vibrations, measured in angular acceleration units of rad/s^2 . The determination of such relationships is essential for the development of improved and expanded vibration exposure criteria applicable to complex vibration environments consisting of both angular and translational motions.

Experimentation is currently underway comparing angular vibration in the pitch axis with Z-axis translational vibration. The experimental design is the same as in the roll experiment just described, but the matching vibration is in pitch rather than roll.

Future investigations in this area will include additional assessments of angular vibrations in comparison to translational vibrations, and evaluations of the effects of simultaneous vibrations in (or around) more than one axis. Results from this program of research will improve the validity and applicability of vibration exposure criteria in complex real-world motion environments.

Acknowledgements

This research was conducted by personnel of the Aerospace Medical Research Laboratory, Aerospace Medical Division, Air Force Systems Command, Wright-Patterson Air Force Base, Ohio 45433. Reprints of this paper are identified by the Aerospace Medical Research Laboratory as AMRL-TR-78-106. The voluntary informed consent of the subjects used in this research was obtained as required by Air Force Regulation 80-33.

Instrumentation and operation of the vibration machines, and production, synthesis, analysis and calibration of the vibration stimuli were accomplished by personnel of the University of Dayton Research Institute, under Contract F33615-76-C-0401.

References

1. Air Force Systems Command. 1972. Evaluation of Human Exposure to Whole-Body Vibration. AFSC Design Note 3E1, Design Handbook 1-3, Series 1-0.
2. Allen, R.W., H.R. Jex, and R.E. Magdaleno. 1973. Manual Control Performance and Dynamic Response During Sinusoidal Vibration. AMRL-TR-73-78, Aerospace Medical Research Laboratory, Wright-Patterson Air Force Base, Ohio.
3. International Organization for Standardization. 1974. Guide for the Evaluation of Human Exposure to Whole-Body Vibration. ISO 2631-1974.
4. Parsons, K.C., and M.J. Griffin. 1978. The Effect of the Position of the Axis of Rotation on the Discomfort Caused by Whole-Body Roll and Pitch Vibrations of Seated Persons. Journal of Sound and Vibration. 58:127-141.
5. Shoenberger, R.W., and C.S. Harris. 1971. Psychophysical Assessment of Whole-Body Vibration. Human Factors. 13: 41-50.
6. Shoenberger, R.W. 1973. A Comparison of Judgements of Vibration Intensity for Chest-to-Back (X Axis) and Side-to-Side (Y Axis) Exposures. AMRL-TR-73-32, Aerospace Medical Research Laboratory, Wright-Patterson Air Force Base, Ohio.
7. Shoenberger, R.W., 1976. Comparison of the Subjective Intensity of Sinusoidal, Multifrequency, and Random Whole-Body Vibration. Aviat. Space Environ. Med. 47: 856-862.
8. U.S. Department of Defense. 1974. Military Standard 1472B, Human Engineering Design Criteria for Military Systems, Equipment and Facilities. Washington, D.C.: Government Printing Office.

ISOLATION AND DAMPING

COMPUTER AIDED DESIGN OF PASSIVE VIBRATION ISOLATORS FOR AIRBORNE ELECTRO-OPTICAL SYSTEMS

P. W. Whaley, Assistant Professor
Air Force Institute of Technology
Wright-Patterson AFB, Ohio

and

Jerome Pearson, Project Engineer
Air Force Flight Dynamics Laboratory
Wright-Patterson AFB, Ohio

Fuselage nodalization has been used to reduce vibration levels in helicopters with good results. (See Shipman, White, and Cronkhite, "Fuselage Nodalization," Presented at the 28th Annual National Forum of the American Helicopter Society, Washington, DC, May 1972). The concept of nodalization for jet-powered, winged aircraft was examined at the Flight Dynamics Laboratory using a simply supported beam loaded with a lumped mass at each end and supported by two passive isolators located arbitrarily along the beam. The Fibonacci numerical search routine was used to minimize the sum of the mean squared angular vibration responses of the two ends. For symmetric loading (end masses identical), the optimum attachment locations were the nodes of the free-free beam. The vibration reduction was several orders of magnitude compared to isolators at the ends.

LIST OF SYMBOLS

English:

A	beam cross sectional area
A_1, A_2, \dots, A_{12}	arbitrary constants in beam solution
c_1	left end damper coefficient
c_2	right end damper coefficient
E	beam Young's modulus
$F(\omega)$	beam forcing function frequency response
$f(t)$	time part of beam forcing function
I	beam cross section moment of inertia
J_1	left end mass moment of inertia
J_2	right end mass moment of inertia
k_1	left end spring constant
k_2	right end spring constant
k_n	wave number, $\omega_n^2 = k_n^4 / EA$
L	beam length
M_1	left end mass

M_2	right end mass
M	beam bending moment
$P(x)$	beam forcing function spatial orientation
PI	optimization performance index
t	time
V	beam shearing force
x	position along beam
x_1	distance from left end to left isolator
x_2	distance from right end to right isolator
y	beam transverse vibration
z_1	left end vibration disturbance
z_2	right end vibration disturbance

Greek:

β	beam damping coefficient
ρ	beam mass density
ω	forcing frequency
ω_n	system natural frequency
ϕ	system mode shapes

INTRODUCTION

Airborne electro-optical packages must operate in the noisy aircraft vibration environment and maintain strict accuracy requirements. This presents a formidable problem due primarily to two deficiencies: 1) very little information is available concerning the angular vibration of airframes, a major source of optical disturbances, and 2) active and passive vibration isolation techniques are relatively underdeveloped compared to other areas of electro-optics technology. This paper is primarily concerned with the second constraint, although the interested reader is referred to references 1-4 for information concerning the angular vibration environment. Active vibration control techniques were recently surveyed and a design procedure was reported in Reference [5]. That work represents a significant advance in vibration isolation techniques for airborne optical packages.

The basic approach presented in Reference [5] is to design active vibration isolation systems for installation of existing laser systems into existing airframes at known locations. This approach will work, no doubt, but does not provide for the inherent structural properties of the airframe and the loading provided by the optical package. A better approach would be to consider a laser system whose design is not as yet finalized, and a candidate aircraft on which the exact laser location remains to be determined. The basis of this approach is to consider the best position on the airframe for laser attachment and also the best manner of attachment.

Fuselage nodalization is a concept that has been used on helicopters for several years [6]. This approach is to attach the rotor and engine system to the helicopter airframe at node points associated with the airframe first natural frequency. Since the forcing spectrum of helicopters is largely sinusoidal at the blade passage frequencies, this nodalization results in a significant reduction in the vibratory energy transmitted to the airframe by the rotor and engine. This particular approach will probably not work nearly as well for jet-powered, winged aircraft because their vibratory response patterns are largely stochastic. However, by nodalizing the first structural mode of the optical system, one should significantly reduce the vibration level at that frequency as that mode is suppressed. Since lower frequencies generally have a higher vibration amplitude, nodalization should provide a reduction in the Root Mean Squared (RMS) disturbance transmitted to the electro-optical package. This paper is a preliminary analysis of nodalization to evaluate the degree of additional vibration isolation which is possible. It is not anticipated that nodalization alone will provide adequate isolation, but rather will take its place along with active and passive vibration isolation techniques as a tool for the designer.

The basic model to be used in this analysis is a beam with a mass at each end and two isolators attaching the beam to a vibrating mount at arbitrary points along the beam length. Thus, the linear and angular vibratory response can be evaluated as a function of added mass, attachment points, and isolator parameters.

MODEL DEVELOPMENT

Mode Shapes and Natural Frequencies

A simplified airborne electro-optical package may be thought of as a source (laser) which bounces a beam off of a pointing mirror. Figure 1 illustrates this model where the springs k_1 and k_2 and dampers c_1 and c_2 act as passive isolators.

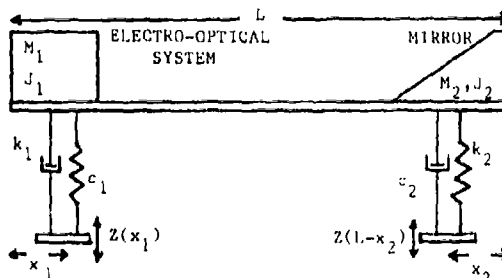


Fig. 1 - Beam Model of an Airborne Electro-Optical Package

The equation of motion for the model of Figure 1 is:

$$EI \frac{\partial^4 y}{\partial x^4} + 2B \frac{\partial y}{\partial t} + \rho A \frac{\partial^2 y}{\partial t^2} = k_1 [z_1 - y(x_1, t)] \delta(x - x_1) + k_2 [z_2 - y(L - x_2, t)] \delta(x - L + x_2) \quad (1)$$

E = Young's Modulus

I = Cross Section Moment of Inertia

ρ = Mass Density

A = Cross-sectional Area

B = Damping Coefficient

δ = Dirac delta function

The moving supports are approximated using the base excitation theory for one degree-of-freedom systems [7]. The added masses and attaching springs are considered in the boundary conditions [8]. Since beams are typically lightly damped, the damping is ignored in the solution for natural frequencies and mode

shapes.

Figures 2 and 3 show detailed free-body diagrams from which boundary condition equations are derived.

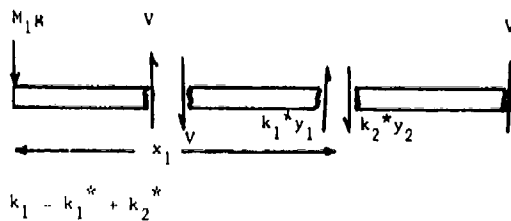


Fig. 2 - Free-Body Diagram of Left Half of the Beam

The beam is analyzed in three segments:

For $0 \leq x \leq x_1$, (left of both supports)

$$y_1(x, t) = [A_1 e^{k_n x} + A_2 e^{-k_n x} + A_3 \sin k_n x + A_4 \cos k_n x] e^{j\omega t} \quad (2)$$

where $k_n^4 = \omega_n^2 \rho \frac{A}{EI}$

For $x_1 \leq x \leq L - x_2$ (between the supports)

$$y_2(x, t) = [A_5 e^{k_n x} + A_6 e^{-k_n x} + A_7 \sin k_n x + A_8 \cos k_n x] e^{j\omega t} \quad (3)$$

For $L - x_2 \leq x \leq L$ (right of both supports)

$$y_3(x, t) = [A_9 e^{k_n x} + A_{10} e^{-k_n x} + A_{11} \sin k_n x + A_{12} \cos k_n x] e^{j\omega t} \quad (4)$$

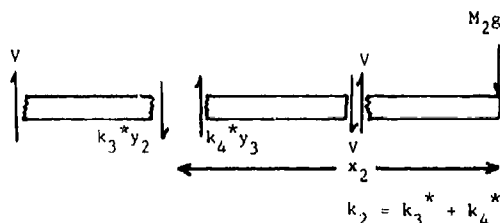


Fig. 3 - Free-Body Diagram of Right Half of Beam

Boundary conditions are as follows:

From Figure 2,

at $x = 0$

$$V = -EI \frac{\partial^3 y_1}{\partial x^3} = -M_1 \frac{\partial^2 y_1}{\partial t^2} \quad (5)$$

$$M = -EI \frac{\partial^2 y_1}{\partial x^2} = -J_1 \frac{\partial^3 y_1}{\partial x \partial t^2} \quad (6)$$

at $x = x_1$

$$y_1 = y_2 \quad (7)$$

$$\frac{\partial y_1}{\partial x} = \frac{\partial y_2}{\partial x} \quad (8)$$

$$\frac{\partial^2 y_1}{\partial x^2} = \frac{\partial^2 y_2}{\partial x^2} \quad (9)$$

$$EI \left(\frac{\partial^3 y_1}{\partial x^3} - \frac{\partial^3 y_2}{\partial x^3} \right) = k_1 y_1 \quad (10)$$

From Figure 3,

at $x = L - x_2$

$$y_2 = y_3 \quad (11)$$

$$\frac{\partial y_2}{\partial x} = \frac{\partial y_3}{\partial x} \quad (12)$$

$$\frac{\partial^2 y_2}{\partial x^2} = \frac{\partial^2 y_3}{\partial x^2} \quad (13)$$

$$EI \left(\frac{\partial^3 y_2}{\partial x^3} - \frac{\partial^3 y_3}{\partial x^3} \right) = k_2 y_2 \quad (14)$$

at $x = L$

$$-V = EI \frac{\partial^3 y_1}{\partial x^3} = -N_2 \frac{\partial^2 y_1}{\partial x^2} \quad (15)$$

$$M = -EI \frac{\partial^2 y_1}{\partial x^2} = -J_2 \frac{\partial^3 y_1}{\partial x \partial t^2} \quad (16)$$

Equations 5, 6, 15 and 16 come from force and moment balances at the ends. Equations 7 and 11 arise from continuity of displacement at the spring attachment points, and Equations 8 and 12 come from continuity of slope. Likewise, Equations 9 and 13 come from continuity of moment at the spring attachment points, and Equations 10 and 14 come from continuity of force.

Equations 1-12 are to be solved simultaneously for frequency, not a trivial task since these equations are highly transcendental. The frequencies which make the determinant of the matrix of coefficients zero are the natural frequencies, and the corresponding set of A_i , $i = 1, \dots, 12$, give mode shapes. A FORTRAN IV code was developed which searches for these frequencies and Table I shows the results of a few sample calculations.

The first three columns of Table 1 are solutions for the first natural frequency using the direct analysis described here, the

TABLE 1
Some Example Solutions Compared to Exact and Finite Element Answers

Natural Frequencies, Hz						
Direct Analysis	Exact	Finite Element	$k_1 = k_2$ N/m	x_1, x_2 m m	$M_1 = M_2$ Kg	$J_1 = J_2$ Kg-m ²
462.42	462.42	457.4	6.8×10^{13}	0 0	0	0
1032.2	1048.45	1256.2	0	0 0	4.5×10^{-3}	3.7×10^{-3}
446.1		403.3	6.8×10^5	.18 .457	.045	1.1×10^{-2}

$$L = 1.8 \text{ m}$$

$$E = 6.8 \times 10^{10} \text{ N/m}^2$$

$$I = 7.7 \times 10^{-7} \text{ m}^4$$

$$\rho = 2.63 \times 10^3 \text{ kg/m}^3$$

$$A = 8.2 \times 10^{-4} \text{ m}^2$$

exact solution available in some cases, and a finite element solution. For $k_1 = k_2 = 6.8 \times 10^{13} \text{ N/m}$, the boundary condition is approximately simply supported. For $k_1 = k_2 = 0$, the boundary condition is free-free. Rows 1 and 2 of Table 1 show excellent agreement for these two cases. The third row is for a different loading condition, showing good agreement with the finite element solution.

Forced Response

The angular disturbances transmitted to the laser and mirror are thought to be the major corrupting influence on system performance. In order to evaluate the advantages of nodalization, the angular vibration forced response must be calculated. Given the set of natural frequencies ω_n , and the mode shapes ϕ_n , the forced response is [9]:

$$\frac{\partial y(x,t)}{\partial x} = \sum_{n=1}^{\infty} \frac{d\phi_n(x)}{dx} \int_0^L \frac{P(x)}{\rho} \phi_n(x) dx \quad (17)$$

$$\int_0^t \frac{f(\tau)}{\omega_n} \sin \omega_n(t-\tau) d\tau$$

In the design of vibration control systems, the frequency response of Equation 17 is often more useful. Taking the Fourier Transform of 17, the result is:

$$Y(x,\omega) = \sum_{n=1}^{\infty} \frac{d\phi_n(x)}{dx} \int_0^L \frac{P(x)}{\rho} \phi_n(x) dx \frac{F(\omega)}{\omega_n^2 - \omega^2 + j2\eta\omega} \quad (18)$$

The frequency response can be approximated in the frequency bands of interest by considering only the natural frequencies which lie in that band.

The proper form for the forcing spectrum, $F(\omega)$ may be estimated from the amplitude ratio computed from base excitation theory [7]. For a spring-mass system excited by vibration of the case, the ratio of the mass response to

the base excitation is:

$$\frac{Y}{Z} = \frac{\omega_1^2}{\omega_1^2 - \omega^2 + j2\eta\omega} \quad (19)$$

Therefore, the frequency domain forcing function to be used in Equation 18 is:

$$F(\omega) = (Z-Y) K,$$

or substituting from Equation 19,

$$F(\omega) = (1 - \frac{\omega_1^2}{\omega_1^2 - \omega^2 + j2\eta\omega}) Z_1 K_1 \quad (20)$$

Figure 4 is a typical set of angular power spectral density (PSD) plots for various parameter values, with Z_1 chosen to approximate typical aircraft acceleration data.

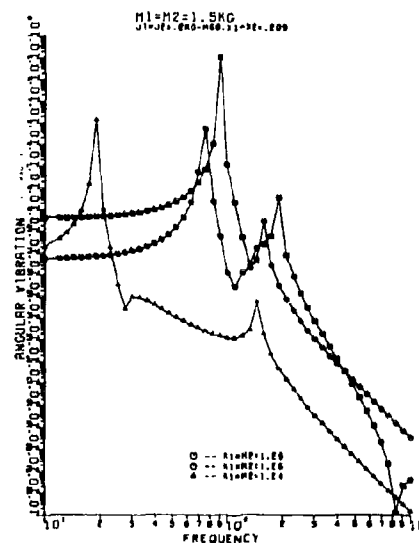


Fig. 4 - Frequency Response for Various k_1, k_2

ATTACHMENT OPTIMIZATION

Numerical Search Procedure

The angular vibration response given by Equation 18 may be used to examine the best positions for the two isolators. The quantity to be extremized is the sum of the mean square responses at the ends.

$$PI = < \left(\frac{\partial y}{\partial x} \right)^2 (0, t) > + < \left(\frac{\partial y}{\partial x} \right)^2 (L, t) > \quad (21)$$

Because of the complexity of the equations given in the previous section, the reader will note that numerical search procedures will likely be time consuming. In addition, the derivatives of Equation 21 are not readily available, and may not even exist. A few trial attempts using a numerical gradient search technique showed no systematic movement towards any fixed number. Exponential overflows and very erratic values for PI suggest that the derivatives of Equation 21 are not well behaved. Gradient search techniques thus are not appropriate.

The Fibonacci search procedure yielded the limited results summarized in Table II [10]. The procedure employed in generating the numbers given in Table II was to fix x_2 and search for the optimum x_1 ; then adjust x_2 to the optimum x_1 , and search for the new optimum x_1 . Since the model of Figure 1 is symmetric, the optimum x_1 should also be optimum for x_2 . The result of Table II is that it appears that variations in x_1 and x_2 have a distinct effect on the mean square angular response of the beam ends.

DISCUSSION

Notice from Table II that the values for k_1 and k_2 also affect the optimum locations x_1 and x_2 . The last three rows of Table II show mean square values almost two orders of magnitude lower than for higher values of k_1 and k_2 . This is also consistent with the general theory of passive isolation where decreasing the spring constants decreases the isolator natural frequency, and thus decreases the higher frequency vibration response. Luckily, Table II indicates that the optimum choice for x_1 and x_2 doesn't change substantially with changes in k_1 and k_2 . If that were not true, the numerical optimization problem would be four-dimensional instead of two-dimensional.

From Table II, $x_1 = x_2 = .209$ is the value converged upon by the numerical search procedure. That general range for x_1 and x_2 was verified by computing angular RMS values of the ends by an independent method. When k_1 and k_2 were changed, then the value for PI also changed, but given a value for k_1 and k_2 , the program converged on an optimum for x_1 and x_2 as summarized by Table II. Although the last three rows of Table II imply that further

TABLE II:

Results of Numerical Search Procedure

$k_1 = k_2$ N/m	x_1 , m (Optimum)	x_2 , m (Fixed)	PI, rad ² (Approximate)
10^{10}	.1571	0.	2.61×10^{-3}
10^{10}	.227	.1571	2.11×10^{-3}
10^{10}	.209	.227	2.23×10^{-1}
10^{10}	.209	.209	1.58×10^{-1}
10^4	.204	.209	6.52×10^{-3}
10^4	.204	.204	5.6×10^{-3}
10^4	.2	.2	4.9×10^{-3}

reduction in PI is possible, those three rows were generated by reducing the searching grid, and therefore represent refinements in the numerical optimization procedure. The last row of Table II represents the last successful refinement using the Fibonacci search; some other numerical search routine might yield even further refinements, but would likely exceed machine tolerances.

CONCLUSIONS

Applying nodalization to airborne electro-optical packages can provide additional vibration reduction of several orders of magnitude for rigid installations. When passive isolators are used nodalization can still supply additional reduction, although not nearly as much as with rigid installations. The optimum isolator attachment locations do not depend significantly upon the isolator spring constants. This means that optimum attachment locations can be chosen independent of choice of isolator.

To provide a rigorous analysis of vibration isolation and control, the use of active control techniques should be considered together with passive isolation and nodalization.

REFERENCES

1. J. Lee and P.W. Whaley, "Prediction of the Angular Vibration of Aircraft Structures," Journal of Sound and Vibration, Vol. 49, No. 4, pp. 541-549, Dec. 1976.
2. P.W. Whaley and M.W. Obal, "Measurement of Angular Vibration Using Conventional Accelerometers," Shock and Vibration Bulletin, Vol. 47, Part 3, pp. 97-106, Sep. 1977.

3. P.W. Whaley and M.W. Obal, "Angular Vibration Measurement Techniques," Shock and Vibration Bulletin, Vol. 48, Part 4, pp. 83-93, Sep. 1978.
4. P.W. Whaley and D.L. Brown, "Prediction of Angular Disturbances From Airframe Members to Airborne Electro-Optical Packages," presented at the National Aerospace & Electronics Conference, Proceedings of the IEEE 1978 National Aerospace and Electronics Conference, Vol. 2, pp. 887-896, May 1978.
5. W.B. Lloyd, D.R. Logan, K.M. Kendall, and J.T. Pritchard, Vibration Control for Airborne Optical Systems, AFFDL-TR-76-145, March 1977.
6. D.P. Shipman, J.A. White and J.D. Crankhite, "Fuselage Nodalization," presented at the 28th Annual National Forum of the American Helicopter Society, Washington, D.C., May 1972.
7. W.T. Thomson, Vibration Theory and Applications, Prentice-Hall, pp. 61-62, 1965.
8. L.S. Shmash and Y.C. Das, "Vibrations of Beams Carrying Mass," Transactions of the ASME (Brief Notes), Vol. 34, Series E, No. 3, 1975.
9. S. Timoshenko, D.H. Young and W. Weaver, Jr., Vibration Problems in Engineering, 4th Edition, 1974.
10. R.L. Fox, "Optimization Methods for Engineering Design, Addison-Wesley, 1971.

DESIGN OF TURBINE BLADES FOR EFFECTIVE SLIP DAMPING
AT HIGH ROTATIONAL SPEEDS (U)

David I.G. Jones
Air Force Materials Laboratory
Wright-Patterson AFB, OH 45433

and

Agnieszka Muszyńska
Institute of Fundamental Technological Research
Polish Academy of Sciences, Warsaw, Poland

(U) The key to designing turbine or compressor blades for high levels of slip damping, at high rotational speeds, lies in ensuring that the root geometry is such that the frictional forces acting on the blade remain as close to optimum as possible over as wide a speed range as possible. Many blade geometries have, in fact, been proposed and are being used but success in achieving high levels of slip damping has not been widespread. In order to look more closely at this problem, this paper will examine the dynamic behavior of a blade having a root geometry compatible with low frictional forces at high rotational speeds, somewhat like a "Christmas Tree" root, but with a gap introduced which will close up only at high speed. Approximate non-linear equations of motion are derived and solved using a method of harmonic balance. Numerical examples are discussed.

INTRODUCTION

Compressor and turbine blade failures caused by excessive vibration can and often do arise in jet engines whenever high flow-induced excitation forces, high static stresses and low modal damping levels occur at the same time. While blade/disk interactions will complicate the response behavior of each individual blade, and cause circumferentially changing peak stress levels around the disk, it is slip at the blade/disk interface which provides a major mechanical source of damping, in addition to the aerodynamic and material sources. Attempts to increase slip damping, by means of mid-span or tip shrouds, or by means of mechanical connections between adjacent blades, have not usually been very successful, perhaps because of the tendency for corresponding points on neighboring blades to vibrate with only relatively small amplitude and phase differences except where extreme efforts are made to mistune adjacent blades relative to each other i.e. the effect is usually to stiffen rather than dissipate energy. Certainly, the analytical difficulties of predicting the response of complete blade/disk systems with slip at each blade/disk interface, or between each blade, are formidable [1,2] and will not be addressed in this paper.

In this paper we shall examine a configuration in which each blade will slip relative to the disk rather than relative to neighboring blades. With proper attention paid to the static and dynamic forces involved, such a configuration can lead to high slip damping even at high rotational speeds. The response behavior of such a system is highly nonlinear, so we shall assume that the impedance of the disk is infinite, as a first approximation, in order to make the analysis more tractable. Figure 1 shows such a blade concept, as compared with a simple dovetail root and a Christmas tree root. The gap between the outer step of the blade root and the disk is very important since it must close only at the selected rotational speed above which some damping is required.

ANALYSIS OF DYNAMIC RESPONSE

In order to model the dynamic response behavior of the blade in a single mode, usually the first, different physical models are required depending on whether slip is or is not occurring at the root or at the sub-platform. The blade is therefore represented for purposes of analysis as shown in Figure 2. The various physical models which represent the

blade under different conditions are shown in Figure 3. The parameter β defines whether slip occurs at the lower dovetail or whether it is locked at this point, whence $X_2 = 0$; and β_1 defines whether the mass m_3 , representing the sub-platform, is slipping against the disk or is locked in place by the frictional forces, for which case $X_3 = 0$. The masses m_1 , m_2 , and m_3 and the stiffnesses k_1 and k_2 must be selected in accordance with the blade geometry. The disk impedance is assumed to be much greater than that of the blade, for simplicity.

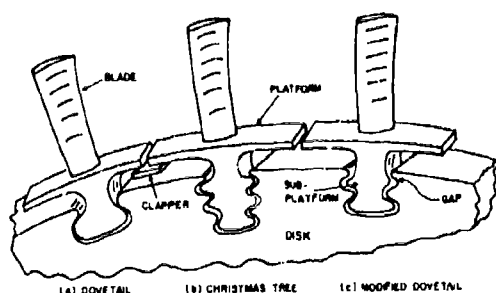


Figure 1. Some Blade Geometries

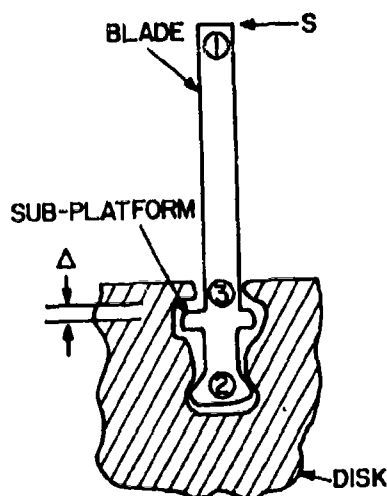


Figure 2. Blade Model

By experimental or analytical (e.g. finite element) methods, one can determine the ratio of the response at any point j to the force applied at any point i , i.e. the compliance $G_{ij}(\omega)$, and this data is then used either directly in a modal analysis or indirectly to determine m_1 , m_2 , m_3 and k_1 , k_2 for the discrete element model. Both methods should give comparable results if the respective assumptions and simplifications are consistent, but the discrete element model is the easiest to analyze.

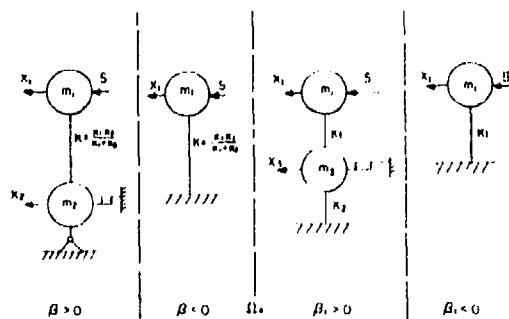


Figure 3. Blade Modelization

For the model, in Figure 3, the equation of motion can be represented for all cases by the equations:

$$m_1 \ddot{X}_1 + k \left(X_1 + \frac{\eta}{\omega} \dot{X}_1 - (X_2 + \frac{\eta}{\omega} \dot{X}_2) \right) \left(\frac{1 - \operatorname{sgn}(\eta - \eta_0)}{2} \right) + k_1 \left(\frac{\operatorname{sgn}(\eta - \eta_0) + 1}{2} \right) \left(\frac{k_2}{k_1 + k_2} (X_1 + \frac{\eta}{\omega} \dot{X}_1) - (X_3 + \frac{\eta}{\omega} \dot{X}_3) \right) = S \cos \omega t \quad (1)$$

$$(m_2 \ddot{X}_2 + \omega N R \operatorname{sgn} \dot{X}_2 + k \left(\frac{\eta}{\omega} (\dot{X}_2 - \dot{X}_1) - \dot{X}_1 \right) (1 + \operatorname{sgn} \beta) \cdot (1 - \operatorname{sgn}(\eta - \eta_0)) + 4k X_2 = 0 \quad (2)$$

$$(m_3 \ddot{X}_3 + \omega N_1 R_1 \operatorname{sgn} \dot{X}_3 + k_1 \left(\frac{\eta}{\omega} (\dot{X}_3 - \dot{X}_1) - \dot{X}_1 \right) + k_2 \frac{\eta}{\omega} \dot{X}_3) (1 + \operatorname{sgn} \beta_1) + 2(k_1 + k_2) X_3 (1 + \operatorname{sgn}(\eta - \eta_0)) = 0 \quad (3)$$

$$\text{where } k = k_1 k_2 / (k_1 + k_2) \quad (4)$$

is the equivalent stiffness, m_1 , m_2 , and m_3 are masses, k_1 and k_2 are sub-stiffnesses, η is the blade loss factor, S and ω are the amplitude and frequency respectively of the exciting force u is the dry friction co-efficient, N and N_1 are the normal loads between the blade root and the disk, R and R_1 are co-efficients depending on the root geometry [3,4] and β , β_1 are co-efficients of the slip thresholds. If we let η_0 be the rotational speed at which the gap $\Delta \rightarrow 0$, then different solutions occur, depending on whether $\eta < \eta_0$ or $\eta \geq \eta_0$.

CASE 1, $\Omega < \Omega_0, \beta > 0$

The analysis is the same, essentially, as that for a blade with a simple dovetail root [3-5]. The equations (1) to (3) reduce to:

$$m_1 \ddot{x}_1 + \frac{kn}{\omega} (\dot{x}_1 - \dot{x}_2) + k(x_1 - x_2) = S \cos \omega t \quad (5)$$

$$m_2 \ddot{x}_2 + \mu NR \operatorname{sgn} \dot{x}_2 + \frac{kn}{\omega} (\dot{x}_2 - \dot{x}_1) - kx_1 + 2kx_2 = 0 \quad (6)$$

We look for an approximate steady state harmonic solution of the non-linear equations (5) and (6) in the form:

$$x_1(t) = D \cos(\omega t + \gamma - \delta) \text{ and } x_2(t) = A \cos(\omega t + \gamma) \quad (7)$$

This is accomplished by expanding the function $\operatorname{sgn} [-A\omega \sin(\omega t + \gamma)]$ in a Fourier series and retaining the first term only [4]. The following results are obtained for the amplitude A and the phase γ .

$$A = \frac{-a\theta_2 + \sqrt{\theta_1^2 S^2 + a^2(\theta_2^2 - \theta_1\theta_3)}}{\theta_1} \quad (8)$$

$$D = \sqrt{[A^2(1 - \nu m_2/m_1)^2 + (An + a/k)^2]/(1 + \eta^2)} \quad (9)$$

$$\gamma = \arctan \frac{A\nu m_2 \eta - a(1 - \nu + \eta^2)}{\lambda \omega^2 [\nu m_2 - (1 + \eta^2)(m_1 + m_2)] - na\omega} \quad (10)$$

$$\delta = \arctan \frac{Anm_2 \omega^2 + a}{Am_2 \omega^2 - Ak(1 + \eta^2) - na} \quad (11)$$

where:

$$\theta_1 = \omega^4 [(m_1 + m_2 - \nu m_2)^2 + \eta^2 (m_1 + m_2)^2]/(1 + \eta^2) \quad (12)$$

$$\theta_2 = nk\nu^2/(1 + \eta^2) \quad (13)$$

$$\theta_3 = [(v - 1)^2 + \eta^2]/(1 + \eta^2) \quad (14)$$

$$a = 4\mu NR/\pi \quad \nu = m_1 \omega^2/k = (\omega/\omega_1)^2$$

The solution (7) with amplitude A, expression (8), exists when $S/\alpha > \sqrt{\theta_3}$. From this we can define the coefficient of the slip threshold as:

$$\beta = S/\alpha - \sqrt{\theta_3} \quad (15)$$

When $\eta = 0$, the non-linear equations (8) and (9) reduce further to the very simple form [1]:

$$|\frac{A}{S}| = \frac{\sqrt{1 - (a/S)^2(1 - \nu)^2}}{k(\omega/\omega_1)^2 [1 + m_2/m_1 - \nu m_2/m_1]} \quad (16)$$

$$|\frac{D}{S}| = \frac{1}{k} \sqrt{\frac{1 - (a/S)^2(1 - \nu)^2(1 - \nu m_2/m_1)^2}{(\omega/\omega_1)^4 (1 + m_2/m_1 - \nu m_2/m_1)^2} + (\frac{a}{S})^2} \quad (17)$$

In these equations R depends on the blade and root geometry. For example, in earlier investigations [3] for a twisted blade of length L, twist angle α' between root and tip, dovetail angle ψ and dovetail radius R_0 , it was

shown that,

$$R = R_0 \cos \psi/L$$

and that S should be replaced by $S \cos \alpha'$.

CASE 2, $\Omega < \Omega_0, \beta \leq 0$

In some range of the parameters, i.e. when $\beta \leq 0$, the solution (7) does not exist. This corresponds to the domain of existence of the linear solution for the one-mass system. In this case, the equations (1) to (3) become:

$$m_1 \ddot{x}_1 + k(x_1 + \frac{n}{\omega} \dot{x}_1) = S \cos \omega t \quad (18)$$

$$x_2 = 0 \quad (19)$$

The solution of (18) is

$$x_1(t) = D^* \cos(\omega t - \delta^*) \quad (20)$$

$$\text{with } D^* = S/k \sqrt{(1 - \nu)^2 + \eta^2} \quad (21)$$

$$\text{and } \delta^* = \arctan \eta/(1 - \nu) \quad (22)$$

CASE 3, $\Omega \geq \Omega_0, \beta_1 > 0$

Slip now occurs at the mass m_3 and ceases to occur at the mass m_2 , which becomes "locked" at high rotation speeds. The slip at the mass m_3 can contribute significant amounts of damping if the term $\mu N_1 R_1$ in equation (3) can be made to remain relatively small through proper control of the blade root geometry.

The equation now takes the form:

$$m_1 \ddot{x}_1 + k_1 (\frac{n}{\omega} \dot{x}_1 + x_1) - k_1 (\frac{n}{\omega} \dot{x}_3 + x_3) = S \cos \omega t \quad (23)$$

$$m_3 \ddot{x}_3 + k_1 (\frac{n}{\omega} \dot{x}_3 - \dot{x}_1) + (x_3 - x_1) + k_2 (\frac{n}{\omega} \dot{x}_3 + x_3) + \mu NR_1 \operatorname{sgn} \dot{x}_3 = 0 \quad (24)$$

The solution of these equations is written in the form:

$$x_1 = D_{II} \cos(\omega t + \gamma_{II} - \delta_{II}) \text{ and } x_3(t) = A_{II} \cos(\omega t + \gamma_{II}) \quad (25)$$

Then again by the method of harmonic balance, it can be shown that:

$$A_{II} = \frac{-a_1\theta_5 + \sqrt{\theta_4 S^2 + a_1^2(\theta_5^2 - \theta_4\theta_5)}}{\theta_4} \quad (26)$$

$$D_{II} = \sqrt{\frac{A_{II}^2(1 + k_2/k_1 - \nu_1 m_3/m_1)^2 + [A_{II}n(1 + k_2/k_1) + a_1/k_1]^2}{(1 + \eta^2)}} \quad (27)$$

$$\gamma_{II} = \arctan \frac{A_{II}\nu_1 m_3 \eta - a_1(1 - \nu_1 + \eta^2)}{A_{II}n[\nu_1 m_3 - (1 + \eta^2)(m_1 + m_3)] - na_1\nu_1} \quad (28)$$

$$\delta_{II} = \arctan \frac{A_{II}m_3 \omega^2 + a_1}{A_{II}m_3 \omega^2 - A_{II}k_1(1 + \eta^2) - na_1} \quad (29)$$

$$\theta_1 = \left(\frac{v_1^2 \omega^2}{1 + v_1^2} - v_1^2 \right) \omega^2 + \left(\frac{v_1^2 \omega^2}{1 + v_1^2} + v_1^2 (1 - v_1) - v_1^2 (v_1 + v_1^2) \right) \omega^2 \quad (30)$$

$$\theta_2 = n v_1^2 v_1 + v_1^2 ((1 - v_1)^2 + v_1^2) / (1 + v_1^2) \quad (31)$$

$$\theta_3 = ((v_1 - 1)^2 + v_1^2) / (1 + v_1^2) \quad (32)$$

$$v_1 = 4 n v_1 v_1 / \omega \quad (33)$$

$$v_1 = v_1^2 / v_1 = (\omega / v_{11})^2 \quad (34)$$

The solution (25) exists when $S/v_1 > \sqrt{\theta_3}$. From this we define the appropriate coefficient B of the slip threshold by:

$$B = S/v_1 - \sqrt{\theta_3} \quad (35)$$

CASE 4, $\Omega > \Omega_0$, $B \leq 0$

In some range of parameters i.e. $B \leq 0$, the solution (25) does not exist. It corresponds to the linear case, for which the relevant solution is:

$$x_1(t) = D_1^* \cos(\omega t - \delta_1^*) \quad (36)$$

$$\text{with } D_1^* = S/k_1 \sqrt{(1 - v_1)^2 + v_1^2} \quad (37)$$

$$\text{and } \delta_1^* = \arctan n/(1 - v_1) \quad (38)$$

Figure 4 illustrates a graphical method for constructing the solution from these equations, for the case $n = 0$. In this figure, note that:

$$\frac{\omega_1^2}{v_{11}^2} = \frac{1}{2} \left\{ \frac{v_1}{v_1} (1 + \frac{v_1^2}{v_1^2}) + 1 \pm \sqrt{\frac{v_1}{v_1} (1 + \frac{v_1^2}{v_1^2})^2 - \frac{v_1^2}{v_1^2}} \right\}^{1/2} \quad (39)$$

Figure 4 illustrates clearly the regions of existence of the non-linear solutions ($|A| \neq 0$) for various values of S/v_1 . When $n = 0$ and $m_3 = 0$, the solution further simplifies to:

$$\frac{\omega_1^2}{v_{11}^2} = \frac{1 - (v_1/v_1)^2 (1 - v_1^2)}{(v_1 + v_1^2) (1 - v_1) - v_1^2 (v_1/v_1) (1 - v_1^2)} \quad (40)$$

$$\frac{\omega_1^2}{v_{11}^2} = \frac{1}{1 + \sqrt{\frac{(1 - v_1/v_1)^2 (v_1/v_1)^2 (1 - v_1^2)^2}{(v_1 + v_1^2) (v_1/v_1) (1 - v_1^2)}}} \cdot \frac{v_1^2}{v_1^2} \quad (41)$$

where it is recognized that $v_1 = \omega^2/\omega_{11}^2$ and $\omega_{11} = \sqrt{k_1/m_1}$. For most practical cases $R_1 = 1$ in these equations and for a twisted blade, as before, we replace S by $S \cos \alpha'$. We now have a formal solution for the cases $\Omega < \Omega_0$ and $\Omega > \Omega_0$, and a numerical example will be discussed after a review of the static blade behavior. Finally, note that the problem addressed here is quite similar to that discussed by Williams and Earles [6].

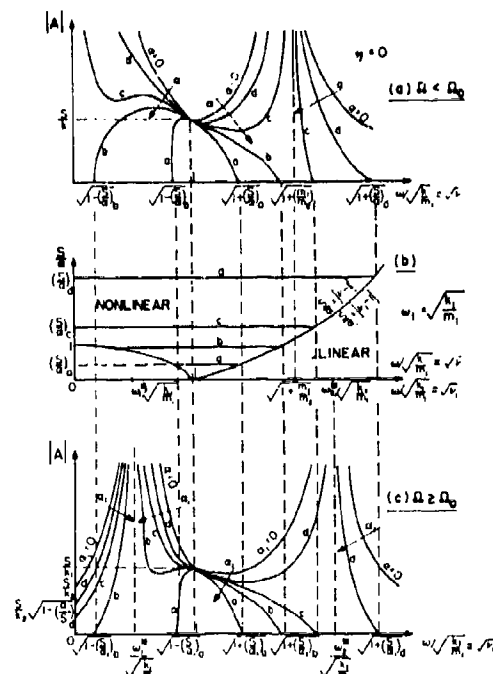


Figure 4. Graphical Construction of Response Solution

ANALYSIS OF QUASI-STATIC BEHAVIOR

Referring to Figure 5, the radial movement γ of the sub-platform under the action of the centrifugal load $W R_D \Omega^2$ due to the outboard part of the blade will be less than the gap Δ up to the speed Ω_0 where:

$$\Omega_0 = \sqrt{k_D \Delta / W R_D} \quad (42)$$

where R_D is the average radius of the blade relative to the rotation axis of the disk. When $\Omega > \Omega_0$, the springs k_D will come into play and provide the normal load N_1 on the mass m_3 . It is easily seen on the basis of static equilibrium that:

$$N_1 = \frac{W R_D (\Omega^2 - \Omega_0^2)}{1 + k_D / 2 k_p} \quad (43)$$

which means that $k_D \gg k_p$ if a significant reduction of the centrifugal loads on the blade is to occur, as is necessary. As an illustration, consider the blade for which the static extensional stiffness k_D of the root below m_3 is provided by a uniform segment of cross sectional area A_D and length l_D . Then:

$$k_D = E A_D / l_D \quad (44)$$

Similarly, if each spring k_p is considered to be represented, as an approximation, by a cantilever beam of length l_p , thickness h_p and breadth b_p , then:

$$k_p = 3 E b_p h_p^3 / 12 l_p^3 \quad (45)$$

For $\Omega \ll \Omega_0$, the normal load N on the mass m_2 is given by:

$$N = W R_D \Omega^2 \quad (46)$$

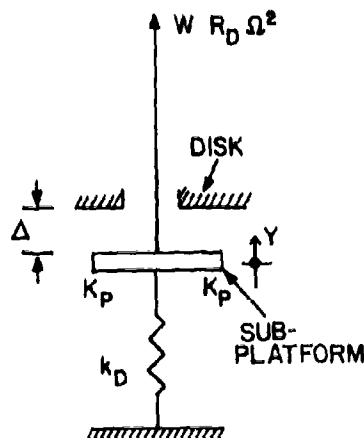


Figure 5. Quasi-Static Model

NUMERICAL ILLUSTRATIONS

The equations derived in this paper permit one to predict the effects of rotational speed on the dynamic response of any blade provided that one knows the modal masses and stiffnesses, and the exciting forces. Unfortunately, in practice, this information is rarely available at the time it is needed. This is especially true of the exciting forces. As an example, the work of Hansen, Meyer and Manson [7] represents a very interesting early investigation of blade damping as a function of rotation speed. The blade geometry data [8] indicates that they used a rectangular section blade of length 50.8mm (2 inches) breadth 15.3mm (0.602 inches), width 1.83mm (0.072 inches) at the tip and 3.05mm (0.120 inches) at the root. The root was cylindrical, of diameter 7.87mm (0.310 inches). In the tests, the blade was attached, alone, in a 33mm (1.3 inch) diameter disk and excited by impacting it with a falling steel ball. While, therefore, the results are very interesting and useful, it is difficult to obtain accurate excitation force data from this source.

Ewins [9] recently described a test system in which air jets were used as a means of exciting the blades. The test results indicate good qualitative agreement between linear analysis and experiment for several tuned and untuned blades in a flexible disk, but no estimate of the exciting forces is given directly. Other investigators [6, 10, 11] are equally uninformative as far as this aspect of the problem is concerned. References [12-14] do seem to address the question to some extent.

The cyclic forces acting on a rotating blade-disk system arise as the blades cut through a quasi-stationary airflow pattern generated by the fixed blades (vanes) ahead of them. The stationary pressure field along a circular path through the center of each stationary vane possesses a minimum between each vane and a maximum at each vane station, as illustrated in Figure 6. If the number of fixed vanes is n , then the rate of repetition of the pressure pulses crossing each rotating blade is $n \Omega / 60$ Hz, if Ω is the rotation speed in rpm. A Fourier expansion of this repeating pulse then gives:

$$S(t) = S(V, \Omega) \sum_{m=1}^{\infty} a_m \cos(m \pi t / 60) \quad (47)$$

where $a_m \approx 1$ if the pulses are sharp. The amplitude $S(V, \Omega)$ depends on the mean velocity V of the airflow through the stage, which in turn depends on the power setting of the engine, as well as the rotation speed Ω . It is not easy to determine $S(V, \Omega)$ analytically and little experimental data from industrial sources seems to have been published. So we shall consider only a few "typical" cases, in the present paper, in order to illustrate the effect of this important parameter on the blade response. Each term of equation (47) gives rise to a possible excitation of a blade mode, and a typical Campbell diagram is constructed by plotting the frequencies $m \Omega / 60$ against Ω for various values of m , along with the blade resonant frequencies f_1 as a function of Ω , as illustrated in Figure 7. As is seen, the fundamental mode is excited by the blade passage excitation when Ω is such that $f_1 = 1 n \Omega / 60$ (n th engine order, point A), by the second harmonic ($2n$ th engine order) when $f_1 = 2 n \Omega / 60$ (point B) and so on. The Campbell diagram is therefore a useful means of estimating where the vibration problems are likely to occur, but again it gives no clue as to excitation force magnitudes.

We shall now examine a specific blade geometry, considered in previous investigations [3, 4] and representing a typical low pressure compressor blade. The main dimensions of this blade are:

$$L = 20 \text{ cm}$$

$$W = 0.20 \text{ kg (0.44 lb)}$$

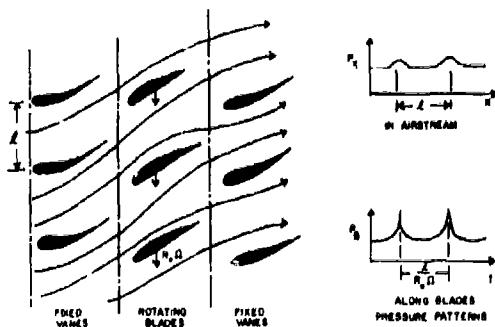


Figure 6. Flow Induced Loads

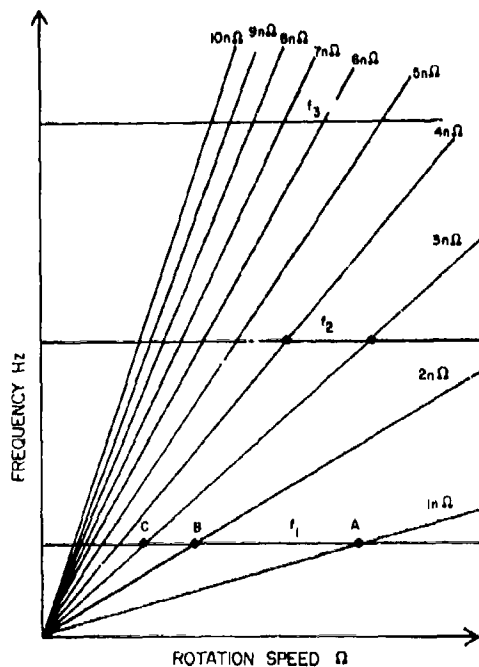


Figure 7. Campbell Diagram

The other relevant magnitudes are given in the nomenclature, as specific numbers associated with the relevant symbols. From these numbers we see from equations (44), (45), (42), (43), and (46) in succession that:

$$k_D = 2.10 \times 10^9 \text{ N/m} (1.2 \times 10^7 \text{ Lb/in})$$

$$k_p = 2.1 \times 10^7 \text{ N/m} (1.2 \times 10^5 \text{ Lb/in})$$

$$A = 0.057 \text{ mm} (0.00225 \text{ in})$$

$$M_1 = 8.342 \times 10^{-6} (\Omega^2 - \Omega_0^2) \text{ Newtons}$$

$$M = 8.342 \times 10^{-4} \Omega^2 \text{ Newton} (1.875 \times 10^{-4} \Omega^2 \text{ Lbf})$$

$$\text{with } \Omega_0 = 12000 \text{ rpm}$$

From equations (18), (19), (40), (41) we can then calculate the response of the blade for the cases $\Omega < \Omega_0$ and $\Omega > \Omega_0$. Results are shown in Figures 8 to 11. From these we can then determine the apparent modal damping η_1' , defined by the "half power bandwidth" method, and plot against α/S (for $\Omega < \Omega_0$) or α_1/S (for $\Omega > \Omega_0$). The results for this particular blade are shown in Figure 12. It is seen that, for $\Omega < \Omega_0$, η_1' increases rapidly as α/S falls and reaches a very high maximum value before finally falling to zero as $\alpha/S \rightarrow 0$ i.e. $\Omega \rightarrow 0$. On the other hand, for $\Omega > \Omega_0$, the damping rapidly increases as α_1/S rises above the threshold level (below which a new peak occurs at lower frequency and with low damping), reaches a peak of about 0.20 and then drops more slowly as α_1/S increases further.

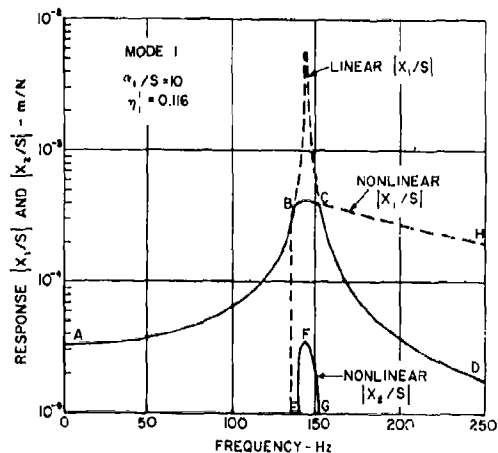


Figure 8. Blade response for $\Omega < \Omega_0$, $\beta > 0$ and $\alpha/S = 10$

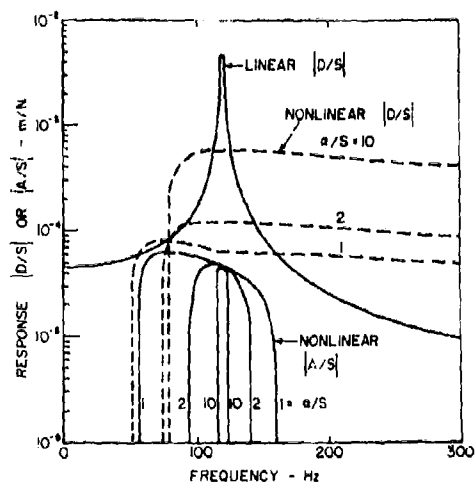


Figure 9. Blade response for $\Omega < \Omega_0$, $\beta > 0$, various α/S

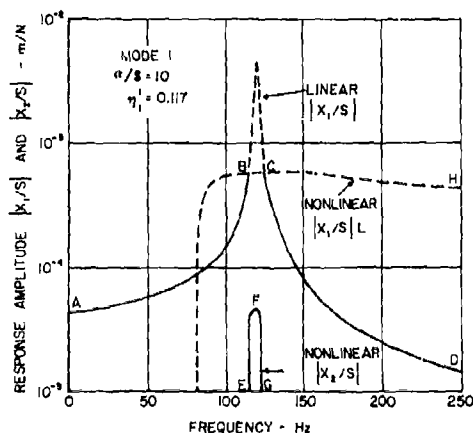


Figure 10. Blade response for $\Omega > \Omega_0$, $\beta_1 > 0$, $\alpha_1/S = 10$

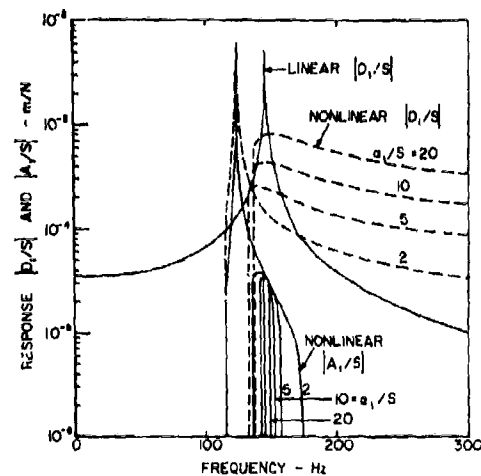


Figure 11. Blade response for $\Omega > \Omega_0$, $\beta_1 > 0$, various α_1/S

From the values of N and N_1 given earlier, we can then calculate α/S and α_1/S for any assumed values of S . We shall consider two cases namely (i) $S = 22.24N$ (5 Lbf) and (ii) $S = 1.69 \times 10^{-5} \Omega^{3/2} N$ ($= 3.8 \times 10^{-6} \Omega^{3/2}$ Lbf) with Ω in rpm. The first represents a constant force, as in Hanson, Meyer, and Manson's experiments [7] and the second represents a more likely situation in which S increases as Ω increases e.g. $S = 12.24N$ (5 Lbf) at 12000 rpm, 31.14N (7.0 Lbf) at 15000 rpm and 5.96N (1.34 Lbf) at 5000 rpm. Tables 1 and 2 show typical calculated values of α/S , α_1/S and η_1 , from Figure 12. The appropriate expressions for α/S and α_1/S are:

$$(i) \quad S = 22.24N \quad (5 \text{ Lbf})$$

$$\frac{\alpha}{S} = \frac{4\pi V R_0}{\pi S L \cos \alpha^* \cos \psi} = \frac{4 \times 0.15 \times 1.875 \times 10^{-4} \Omega^2 \times 1}{20 \pi \times \pi \times 5 \times 0.724 \times 0.5} = 9.89 \times 10^{-7} \Omega^2 \quad (48)$$

$$\frac{\alpha_1}{S} = \frac{4\pi V_1}{\pi S \cos \alpha^*} = \frac{4 \times 0.15 \times 1.856 \times 10^{-6} (\Omega^2 - \Omega_0^2)}{\pi \times 5 \times 0.724} = 9.79 \times 10^{-8} (\Omega^2 - \Omega_0^2) \quad (49)$$

$$(ii) \quad S = 1.69 \times 10^{-5} \Omega^{3/2} \text{ Newton } (3.8 \times 10^{-6} \Omega^{3/2} \text{ lbf})$$

$$\frac{\alpha}{S} = \frac{4\pi V R_0}{\pi S L \cos \alpha^* \cos \psi} = \frac{4 \times 0.15 \times 1.875 \times 10^{-4} \Omega^2 \times 1}{20 \pi \times \pi \times 3.8 \times 10^{-6} \Omega^{3/2} \times 0.724 \times 0.5} = 1.301 \Omega^{1/2} \quad (50)$$

$$\frac{\alpha_1}{S} = \frac{4\pi V_1}{\pi S \cos \alpha^*} = \frac{4 \times 0.15 \times 1.856 \times 10^{-6} (\Omega^2 - \Omega_0^2)}{\pi \times 3.8 \times 10^{-6} \Omega^{3/2} \times 0.724} = 0.1288 (\Omega^2 - \Omega_0^2)^{1/2} \Omega^{1/2} \quad (51)$$

Figure 13 shows the variation of η_1 with Ω for these cases. It is seen that high damping occurs at high speed, as expected. Obviously, the particular numerical values can be changed to represent other conditions, but the approach and general behavior remain the same.

One other possibility can be examined, namely a blade of the type having a hinged root with mating surfaces now parallel to the plane of rotation of the root, and discussed also by Hanson, Meyer and Manson [7]. For this type of blade, N_1 remains just about constant at all speeds, while the force S changes, usually increasing as Ω increases. This would account for the high damping achieved by this type of blade, since α_1 would be nearly constant and α_1/S would change in such a way that η_1 would increase as Ω increases.

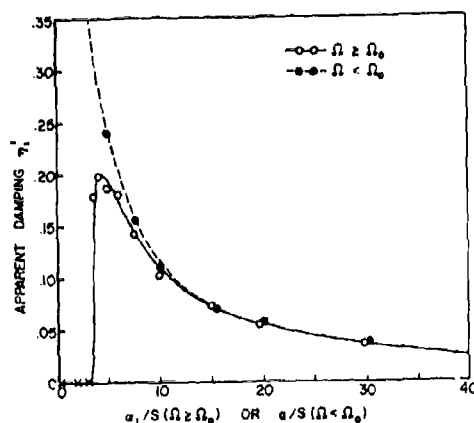


Figure 12. Modal Damping Versus a/S or α_1/S

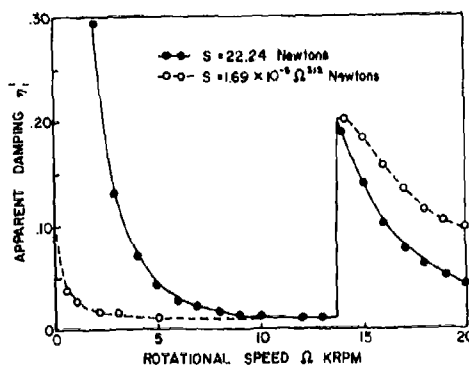


Figure 13. Modal Damping Versus Rotational Speed

CONCLUSIONS

It has been shown that a specific configuration of compressor or turbine blade root geometry, in which part of the root contacts the disk only at high rotational speeds, can provide high levels of slip damping, provided that the relevant stiffnesses are properly selected. The analysis given in this paper can provide the basis for preliminary design investigations, but laboratory and spin pit testing will be necessary to establish the accuracy of the approach and to develop the specific configurations most appropriate for practical application. The changes in blade geometry needed to optimize this type of damping do not represent very large departures from current practice, nor need they represent any weight increases over current blades.

Apart from experimental and spin pit testing, a logical follow on effort would investigate the effects of finite disk compliance, and hence of multiple blade systems, on the dynamic behavior. However, one would expect high levels of slip damping to still be attainable. It is hoped that this paper will stimulate or encourage such investigations, since the need for high damping in rotating blades is becoming ever more urgent.

REFERENCES

1. A.V. Srinivasan (ed.) *Structural Dynamic Aspects of Bladed Disk Assemblies*, ASME Publication, papers presented at Winter Annual Meeting, New York, Dec. 1976.
2. J.S. Rao, "Turbine Blading Excitation and Vibration", *J. Sound and Vibration*, Vol. 9, No. 3, pp 15-22, 1977.
3. D.I.G. Jones and A. Muszyńska, "Vibration Of A Compressor Blade With Slip At The Root", *Shock and Vibration Bulletin* 48, 1978.
4. D.I.G. Jones and A. Muszyńska, "Nonlinear Modelization of Non-Conservative Blade Vibration Response", *Proc. ICNO Conference on Non-Linear Oscillations*, Prague, Czechoslovakia, Sept. 1978.
5. D.I.G. Jones and A. Muszyńska, "Harmonic Response Of A Damped Two-Degree Of Freedom System With Gaps", *Nonlinear Vibration Problems (Zagadnienia Drgan Nieliniowych)*, No. 19, Warsaw, 1978.
6. E.J. Williams and S.W.E. Earles, "Optimization Of The Response Of Frictionally Damped Beam Type Structures With Reference To Gas Turbine Compressor Blading", *ASME Paper 73-DET-108*, *J. Engineering For Industry*, 1973.
7. M.P. Hanson, A.J. Meyer and S.S. Manson, "A Method Of Evaluating Loose-Blade Mounting As A Means of Suppressing Turbine And Compressor

Blade Vibrations", Experimental Stress Analysis, Proc. S.E.S.A., Vol. X, No. 2, 1950.

8. M.P. Hanson, "Vibration Damper For Axial-Flow Compressor Blading", Proc. S.E.S.A., Vol. XIV, No.1, 1955.

9. D.J. Ewins, "An Experimental Investigation Of The Forced Vibration Of Bladed Discs Due To Aerodynamic Excitation", in Structural Dynamic Aspects of Bladed Disk Assemblies, ASME publication of papers presented at ASME Winter Annual Meeting, New York, Dec. 1976.

10. R.B. Kolb, "Measured Vibratory Motions Of Turbine Blades", ASME Paper 67-VIBR-66, presented at ASME Vibrations Conference, Boston, March 1967.

11. S.B. Chubb, "Evaluation Of Wire Lacing For The Control Of Gas Turbine Blade Vibration", ASME Paper 67-VIBR-47, presented at ASME Vibration Conference, Boston, March 1967.

12. B.A. Squires, "Forces On Blades In A Rotor Stage When The Air Flow Is Distorted", Rolls Royce Internal Report, MCR 90157, 1969.

13. T.J. Barber and H.D. Weingold, "Vibratory Forcing Functions Produced By Nonuniform Cascades", J. Engineering for Power, Trans. ASME, 100 (1), pp 82-88, 1978.

14. J.F. Traexler, "Turbomachinery Vibration", Shock and Vibration Digest, Vol. 9, No. 8, Aug. 1977.

NOMENCLATURE

A Amplitude of response of mass m_2 .
 A_{II} Amplitude of response of mass m_3 .
 A_D Cross section area of blade between root mating surfaces and platform (258 mm²/0.4 in²).
 a_m m th Fourier coefficient of excitation force.
 b_p Breadth of platform (50.8 mm/2 ins.).
 D, D_{II} Amplitude of response of mass m_1 (tip of blade).
 D^*, D_{II}^* Amplitude of response of mass m_1 (no slip).
 E Young's modulus of blade material (3 x 10⁷ Lb/in²/ 2.07 x 10¹¹ N/m²).
 f_1 1 th resonant frequency (Hz).
 h_p Thickness of platform (2.54 mm/0.1 ins).
 k_1 Effective stiffness (30000 N/m).

k_2 Effective stiffness (80,000 N/m).
 k Effective stiffness (21,800 N/m).
 k_D Blade root static stiffness
 k_p Platform static stiffness (See Fig. 5).
 L Length of blade (20 cm).
 l_D Length of blade section between root mating surfaces and subplatform (25.4 mm/1 in).
 l_p Length of subplatform (12.7 mm/0.5 ins).
 m_1 Effective mass (0.036 kg).
 m_2 Effective mass (0.0033 kg).
 m_3 Effective mass (0 kg).
 m Integer ($m = 1, 2, \dots$).
 n Number of fixed vanes.
 N Net normal load at dovetail mating surfaces.
 N_1 Net normal load at platform.
 R, R_1 Nondimensional coefficients
 R_0 Radius of dovetail sliding surfaces relative to root rotation center (1 cm).
 R_D Radius of blade relative to disk axis (381 mm/15 ins).
 S Driving force.
 t Time (sec).
 V Average airflow velocity.
 W Weight of blade (0.2 kg/0.44 Lb).
 X_1 Displacement of mass m_1 .
 X_2 Displacement of mass m_2 .
 X_3 Displacement of mass m_3 .
 α, α_1 Friction parameters
 α' Twist of blade tip relative to root (Cos $\alpha' = 0.724$).
 β, β_1 Slip threshold coefficients.
 γ, γ_1 Phase angles.
 $\delta, \delta_1, \delta^*$ Phase angles.
 Δ Gap
 η Loss factor (0.01 for illustration).

- μ Coefficient of friction (0.15 for illustration).
- ν ω/ω_1 - nondimensional frequency parameter.
- ν_1 ω/ω_{11} - nondimensional frequency parameter.
- $\theta_1 - \theta_6$ nondimensional parameters
- ψ Angle of dovetail mating surfaces relative to base of root (Cos $\psi = 0.5$ for illustration).
- ω frequency (rad/sec).
- ω_1 Resonant frequency with $\Delta > 0$ (124 Hz).
- ω_{11} Resonant frequency with no slip at m_3 (146 Hz).
- Ω rotation speed (rpm).
- Ω_0 Critical rotation speed for $\Delta = 0$ (rpm)

TABLE 1 - DAMPING VERSUS Ω FOR $S = 1.69 \times 10^{-5} \Omega^{3/2}$

Ω RPM	$\Omega < \Omega_0$		$\Omega \geq \Omega_0$	
	α/S	η_1'	α/S	η_1'
0	0	-	-	-
100	11.0	0.006	-	-
500	29.1	0.015	-	-
1000	41.1	0.024	-	-
2000	58.1	0.037	-	-
3000	71.2	0.044	-	-
5000	91.9	0.051	-	-
10000	130	0.06	-	-
12000	-	-	0	0.01
13000	-	-	2.18	0.01
14000	-	-	4.04	0.20
15000	-	-	5.68	0.18
16000	-	-	7.13	0.155
17000	-	-	8.43	0.13
18000	-	-	9.60	0.112
19000	-	-	10.67	0.102
20000	-	-	11.66	0.095

TABLE 1 - DAMPING VERSUS Ω FOR $S = 22.24 \Omega$ (5 LBF)

Ω RPM	$\Omega < \Omega_0$		$\Omega \geq \Omega_0$	
	α/S	η_1'	α/S	η_1'
0	0	-	-	-
100	0.0099	-	-	-
500	0.247	-	-	-
1000	0.989	-	-	-
2000	3.96	0.295	-	-
3000	8.90	0.130	-	-
4000	15.83	0.070	-	-
5000	24.7	0.042	-	-
6000	35.6	0.028	-	-
7000	48.5	0.021	-	-
8000	63.3	0.016	-	-
9000	80.1	0.012	-	-
10000	98.9	0.010	-	-
12000	142.5	0.010	0	0
13000	-	-	2.45	0.010
14000	-	-	5.09	0.187
15000	-	-	7.93	0.140
16000	-	-	10.96	0.100
17000	-	-	14.2	0.076
18000	-	-	17.6	0.062
19000	-	-	21.2	0.050
20000	-	-	25.1	0.042

ACKNOWLEDGMENT

The authors wish to thank Marsha Oppy, AFML/LLN, for typing the manuscript.

A SIMPLE LOW-COST TECHNIQUE FOR MEASURING MATERIAL DAMPING BEHAVIOR

by

David I.G. Jones
Air Force Materials Laboratory
Wright-Patterson AFB, Ohio 45433

(U) Many methods have been developed for measuring the damping behavior of elastomeric and other materials, including resonance, mechanical impedance and vibrating beam methods. One feature all of these methods have in common is the expense and inconvenience of preparing appropriate test specimens and the considerable time needed to conduct the tests. A need appears to exist for a simple method to quickly obtain data, even if only approximately accurate, as for example in evaluating samples for quality control. This paper will describe a simple test procedure in which a cylindrical specimen of damping material supporting an added mass is impacted by a small "hammer". The force transmitted through the specimen is measured by a force gage and the acceleration experienced by the hammer is measured by an accelerometer. The transient signals so generated are displayed on a storage oscilloscope, and the modulus and loss factor of the material are derived from comparisons with a simple transient analysis of a single degree of freedom system having a complex stiffness for the spring element. Examples and test data are discussed and comparisons are made with results of other methods of measurement.

1. INTRODUCTION

The various methods currently used to measure damping properties of elastomeric materials require some effort to prepare specimens and to conduct and analyze tests. If one wishes to completely characterize a specific material over a wide range of frequencies and temperatures, there is little chance of avoiding this, so that typically one or two days are needed to prepare specimens, mostly waiting for adhesives to cure, and at least one day to conduct the tests. This is no way to proceed if one wishes merely to screen material samples, as in production control, or to select a few candidate materials, for further evaluation, out of a large number of possibilities. For such purposes, it is often sufficient to use data at a few temperatures and at one frequency.

The test technique discussed in this paper is not only extremely simple to set up, to prepare specimens for and to use, but it also requires only standard vibration laboratory equipment.

Absolutely no new ideas or concepts are involved; however, it is time that simple methods were used to perform simple tasks. The method is essentially that of observing and analyzing the transient response of a damped single degree of freedom system. The particular geometric configuration used consists of a large metal block supported at each end by soft foam rubber "springs" and joined through the specimen, at the center, to a force gage. As the block is impacted by a small hammer, the mass-specimen system will exhibit decaying free vibrations and the period and the amplitude ratio of successive maxima of response can be measured from the oscilloscope trace. The use of a storage oscilloscope allows one to conveniently record the response trace as many times as desired. Temperature control, where needed, was obtained using an environmental chamber. Test results for two materials were compared with those obtained by resonant beam and simple resonance tests, and the agreement was generally found to be good.

2. ANALYSIS

The single degree of freedom system shown in Figure 1 is subjected to an impulsive load $S\delta(t)$. The spring stiffness is represented by a block model:

$$F = kx + (k\eta/|\omega|)(dx/dt) \quad (1)$$

which reduces to a complex modulus $k(1 + i\eta)$ if the displacement $x(t)$ is given by $x = X \exp(i\omega t)$. The complex modulus representation is quite a close approximation to the behavior of real elastomeric materials provided that the true variation of k and η with temperature and frequency is allowed for. However, for this representation, the transient response can be determined only through utilization of a Fourier Transform, because the model (1) contains the frequency ω directly. If $S\delta(t)$ is the applied load, then the Fourier transform of the load is given by:

$$\bar{S}(\omega) = (1/2\pi) \int_{-\infty}^{\infty} S\delta(t) e^{-i\omega t} dt = S/2\pi$$

For each element $\bar{S} d\omega$ of the transformed excitation, the response is:

$$\bar{x} = \frac{\bar{S}(\omega)}{-m\omega^2 + k(1 + i\eta\omega/|\omega|)} \quad (2)$$

Therefore, applying the inverse Fourier Transform:

$$x(t) = \frac{S}{2\pi} \int_{-\infty}^{\infty} \frac{e^{i\omega t} d\omega}{-m\omega^2 + k(1 + i\eta\omega/|\omega|)} \quad (3)$$

For the ideal case considered here, where k and η are independent of frequency, it is instructive to evaluate the integral in equation (3) by contour integration in the complex frequency plane. The poles are the frequencies for which:

$$\omega^2 m/k = 1 + i\eta\omega/|\omega| \quad (4)$$

The roots of this equation are complex. If we therefore write $\omega = \omega_r + i\omega_i$, equation (4) becomes:

$$(\omega_r^2 - \omega_i^2 + 2i\omega_r\omega_i)(m/k) = 1 + \frac{i\eta(\omega_r + i\omega_i)}{\sqrt{\omega_r^2 + \omega_i^2}} \quad (5)$$

Equating real and imaginary parts gives:

$$(\omega_r^2 - \omega_i^2)(m/k) = 1 - \eta\omega_i/\sqrt{\omega_r^2 + \omega_i^2} \quad (6)$$

and

$$(2\omega_r\omega_i)(m/k) = \eta\omega_r/\sqrt{\omega_r^2 + \omega_i^2} \quad (7)$$

If we now substitute for $\sqrt{\omega_r^2 + \omega_i^2}$ from equation (7) into equation (6), we have,

$$(\omega_r^2 - \omega_i^2)(m/k) = 1 - 2\omega_i^2(m/k) \quad (8)$$

$$\therefore \omega_r^2 + \omega_i^2 = k/m$$

From equations (7) and (8) we now have:

$$2\omega_i(m/k) = \eta\sqrt{k/m}$$

$$\therefore \omega_i = (\eta/2)\sqrt{k/m} \quad (9)$$

$$\therefore \omega_r = \pm\sqrt{(k/m)(1 - \eta^2/4)} \quad (10)$$

We have therefore found the values of ω_r and ω_i provided that $\eta \leq 2$. The poles and the path of integration are shown in Figure 2. The response $x(t)$ is equal to $2\pi i$ times the sum of the residues at the poles. The residue R_1 at the pole $\omega = \omega_r + i\omega_i$ is:

$$R_1 = \lim_{\omega \rightarrow \omega_r + i\omega_i} \frac{S e^{i\omega t} (\omega_r - i\omega_i - \omega)}{2\pi m (\omega_r - i\omega_i - \omega) (\omega_r + i\omega_i - \omega)} \quad (11)$$

$$= -S e^{i(\omega_r + i\omega_i)t} / 4\pi m \omega_r \quad (12)$$

$$\text{and } R_2 = S e^{i(-\omega_r + i\omega_i)t} / 4\pi m \omega_r \quad (13)$$

in a similar way. Finally, therefore:

$$x(t) = \frac{S e^{-(\eta t/2)\sqrt{k/m}} \sin\left(t\sqrt{(k/m)(1 - \eta^2/4)}\right)}{m\sqrt{(k/m)(1 - \eta^2/4)}} \quad (14)$$

This solution represents the information needed to deduce k and η from experimental data. The ratio of successive maxima is given by:

$$x_1/x_0 = e^{-\pi\eta/2}$$

$$\therefore \eta = (2/\pi) \ln(x_1/x_0) \quad (15)$$

and the time T between successive zero crossings is:

$$T \sqrt{(k/m)(1-\eta^2/4)} = \pi$$

$$\omega_D = \sqrt{k/m} = \pi/T \sqrt{1-\eta^2/4} \quad (16)$$

$$\text{and} \quad k = m\omega_D^2/T^2(1-\eta^2/4) \quad (17)$$

From the experimental traces representing $x(t)$ as a function of time t , one can read off x_1/x_0 and T and hence deduce the loss factor η and the stiffness k at the frequency ω_D . Typical predicted response traces are shown in Figure 3.

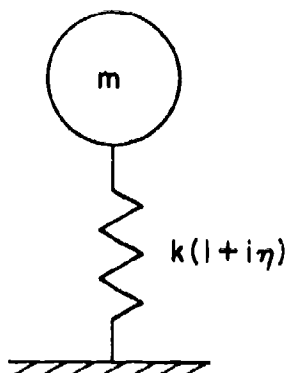


Figure 1. Mass - Complex spring system

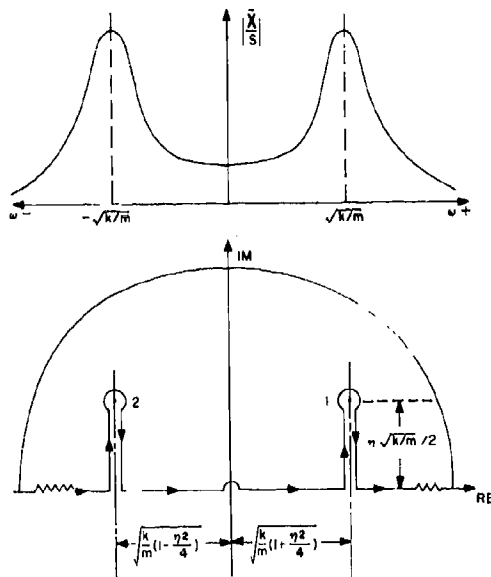


Figure 2. Poles of System, integration Path and Modulus of Integrand versus frequency

3. EXPERIMENTAL INVESTIGATION

The test system used is illustrated in Figures 4 and 5. The mass m rested on the specimen, which was a cylinder of cross sectional area A and thickness h , and was impacted by the hammer with accelerometer attached. Several different elastomeric material specimens were evaluated, as summarized in Tables 1 and 2. These included an acrylic adhesive (3M-467, 3M Co.) and a silicone elastomer (BTR, Lord Mfg. Co.) at several different temperatures. Typical oscilloscope traces for these materials are shown in Figures 6 to 14. From each of these traces, T and x_1/x_0 were read off. The first half cycle was not used because of the finite duration of the actual loading, but succeeding half cycles were usable. Then E was calculated using the usual equations relating stiffness to modulus:

$$m\omega^2 = (EA/h)[1 + \beta(A/A')^2]$$

where $1 + \beta(A/A')^2$ is a shape factor which corrects for the finite length to breadth ratio of the specimen [1]. Typically $\beta \approx 2$ for an unfilled elastomer (e.g. 3M-467) and $\beta \approx 1.5$ for a filled elastomer (e.g. BTR). The results are summarized in Table 2.

In order to compare the measured data obtained by this method with results from other methods, graphs of E and η versus reduced frequency ω_r were used, with construction lines superimposed to directly display temperature and frequency i.e. a reduced temperature nomogram. This method of data reduction and presentation is described in an earlier report [2]. The results are shown in Figures 15 and 16. It is seen that agreement between the various methods is quite good. Some scatter is evident though not much more than for other test methods. It is certainly possible to distinguish between high and low loss factors, and high and low stiffnesses.

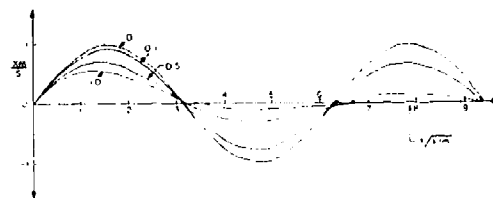


Figure 3. Response versus $t\sqrt{k/m}$

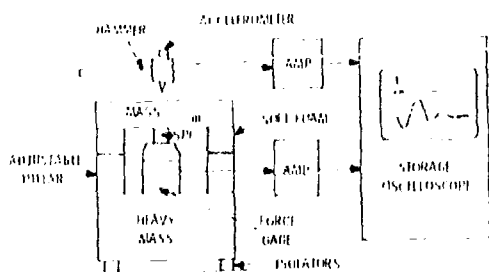


Figure 4. Test System

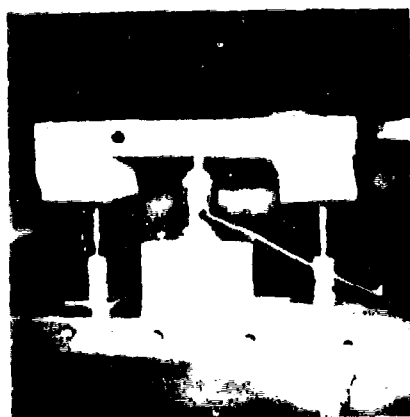


Figure 5. Test System

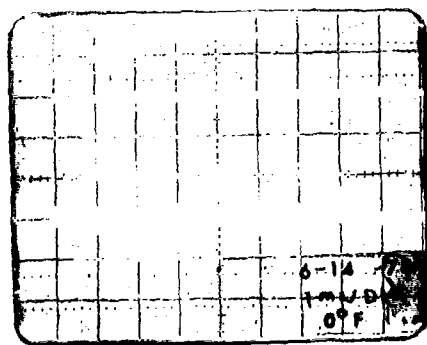


Figure 6. Measured Response at 0°F (-18°C) for 3M - 467

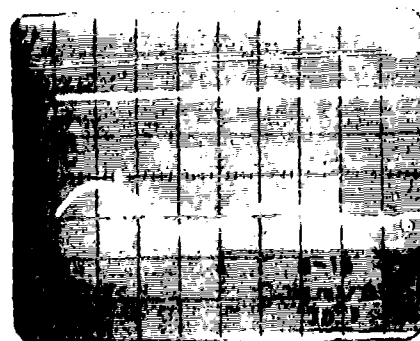


Figure 7. Measured Response at 30°F (-1°C) for 3M - 467

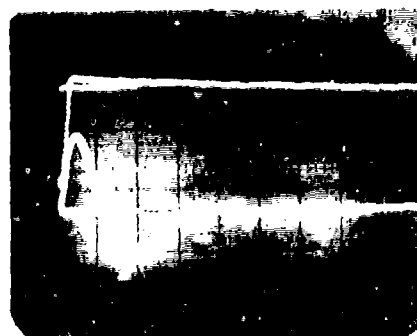


Figure 8. Measured Response at 75°F (24°C) for 3M - 467

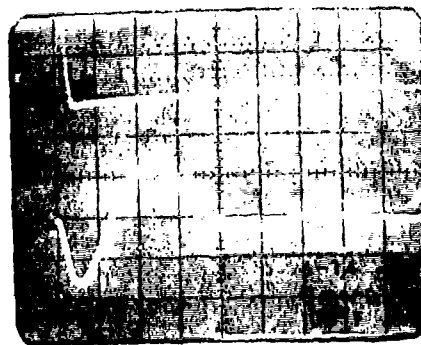


Figure 9. Measured Response at 100°F (38°C) for 3M - 467

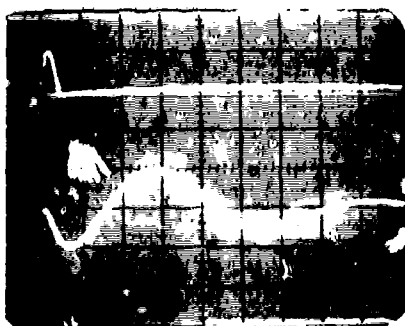


Figure 10. Measured Response at 122°F (50°C) for 3M-467

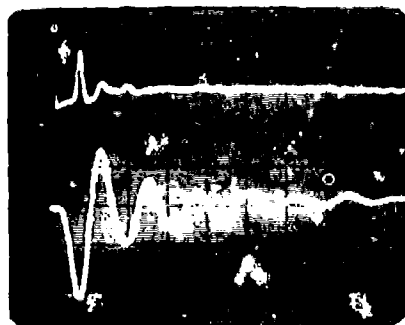


Figure 11. Measured Response at -90°F (-68°C) for BTR



Figure 12. Measured Response at 0°F (-18°C) for BTR

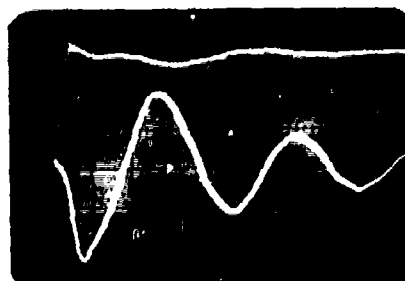


Figure 13. Measured Response at 150°F (66°C) for BTR

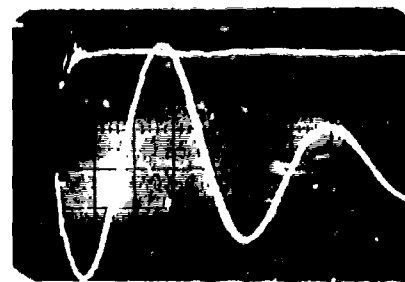


Figure 14. Measured Response at 240°F (116°C) for BTR

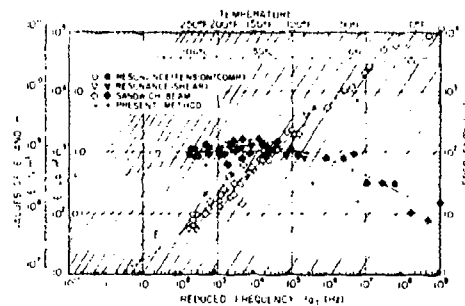


Figure 15. Graphs of E and γ versus Reduced Frequency (3M-467)

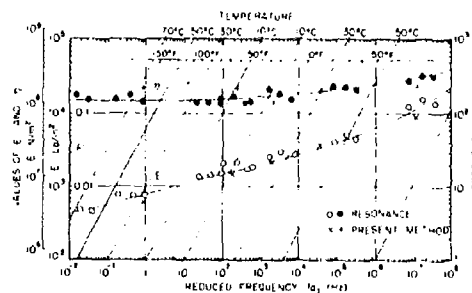


Figure 16. Graphs of E and γ versus Reduced Frequency (BTR)

TABLE 1
MEASURED DATA FOR 3M-467 ADHESIVE
Circular Cylindrical Specimen

$m = 743 \text{ gm}$, $A = 1.61 \text{ cm}^2 (0.249 \text{ in}^2)$, $A' = 2.85 \text{ cm}^2 (0.442 \text{ in}^2)$, $h = 0.64 \text{ cm} (0.25 \text{ in})$

Temperature		$\frac{X_1}{X_2}$	T sec	ω_D Hz	E lb/in ²	η
°F	°C					
0	-18	1.24	0.0018	278	7970	0.14
30	-1	1.40	0.0020	250	6500	0.21
75	24	6.00	0.010	50	381	1.14
100	38	3.00	0.012	40	202	0.69
122	50	1.67	0.015	36	117	0.33

TABLE 2
MEASURED DATA FOR BTR SILICONE
Rectangular Cylindrical Specimen

$m = 743 \text{ gm}$, $A = 1.61 \text{ cm}^2 (0.25 \text{ in}^2)$, $A' = 7.23 \text{ cm}^2 (1.12 \text{ in}^2)$, $h = 1.42 \text{ cm} (0.56 \text{ in})$

Temperature		$\frac{X_1}{X_2}$	T sec	ω_D Hz	E lb/in ²	η
°F	°C					
-90	-68	1.40	0.003	167	9580	0.214
-25	-32	1.35	0.005	100	3440	0.191
0	-18	1.25	0.006	83	2380	0.142
75	24	1.49	0.008	63	1354	0.254
150	66	1.67	0.010	50	876	0.326
240	116	1.50	0.012	42	602	0.258

4. DISCUSSION AND CONCLUSIONS

Crandall [3,4] has noted the existence of analytical problems arising from the complex modulus model for transient oscillatory motions, especially when the Fourier integrals are evaluated numerically, and several investigators have sought alternatives to the complex modulus approach [5-7]. These discrepancies, while indicating that we certainly have not yet achieved complete resolution of all aspects of linear damping material behavior, are not large numerically, and do not seriously affect the solution, equation (14). As far as analyzing experimental data to a modest degree of accuracy is concerned, therefore, it is

of little consequence. Furthermore, the contour integration solution seems to be quite well behaved.

For sure, therefore, we have described a very simple and effective method for very quickly determining the complex modulus properties of samples of soft damping materials, at a single frequency. The specimens can be changed quite readily by raising the mass, putting the specimen in place, and restoring the mass on the foam supports. Obviously, some further improvement of the configuration can be anticipated before extensive use of the approach is made. The important thing is that it is a simple method and should not be looked upon as anything

else. If measurements are to be made on stiff materials, shapes other than cylindrical should be considered in order to reduce the stiffness of the specimen to an acceptable level. One possibility is to make a vertically oriented ring shaped specimen.

We have used this system to evaluate the qualitative and quantitative damping behavior of many materials, ranging from soft foams to stiff elastomers, and results have generally been acceptable and readily obtained. One point to remember at all times is that the stiffness of the specimen should always be much greater than that of the foam supports, unless of course one allows for that in the calculations by subtracting the support stiffness from the total stiffness to determine the specimen stiffness.

ACKNOWLEDGEMENT

This investigation was conducted at the Air Force Materials Laboratory under Work Unit Number 24180302. The assistance of David B. Signor of Michigan State University, assigned to AFML as a Co-op student, is gratefully acknowledged, in conducting many of the tests. Discussions with A. Różycki and several other industry and research personnel concerning the need for a simple screening test to evaluate damping properties of materials led to this particular effort.

REFERENCES

1. J.C. Snowdon, Vibration and Shock in Damped Mechanical Systems, John Wiley and Sons Inc., New York, 1968.
2. D.I.G. Jones, "A Reduced-Temperature Nomogram for Characterization of Damping Material Behavior", Shock and Vibration Bull., 48, Part 2, pp 13-22, 1978
3. S.H. Crandall, "Dynamic Response of Systems With Structural Damping", Air, Space and Instruments, Draper Anniversary Volume, ed. H.S. Lees, McGraw Hill, pp 183-193, 1976.
4. S.H. Crandall, "The Role of Damping in Vibration Theory", Journal of Sound and Vibration, 11(1), pp 3-18, 1970.
5. R.E.D. Bishop, "The Treatment of Damping Forces in Vibration Theory", J. Royal Aero. Society, Vol. 59, pp 738-742, 1955.
6. M. Caputo, "Vibrations of an Infinite Plate With a Frequency Independent Q", J. Acoust. Soc. Am., Vol. 60, No. 3 pp 634-639, 1976.

7. R.L. Bagley and P.J. Torvik, "A Generalized Derivative Model for an Elastomer Damper", Shock and Vibration Bulletin 49, 1979.

NOMENCLATURE

A	Cross-sectional area of specimen
A'	Free-surface area of specimen
E	Young's modulus of specimen material
f	Frequency (Hz)
F	Force
h	Height of specimen
i	$\sqrt{-1}$
k	Stiffness of specimen
m	Mass
R ₁ , R ₂	Residues
S	Load
S	Fourier transform of load
t	Time
T	Time between successive zero crossings
x	Displacement
X	Fourier transform of displacement
x ₀ , x ₁	Amplitudes at successive maxima
a _T	Shift factor
β	Non-dimensional factor
n	Loss factor
ω	Frequency (rad/sec)
ω_r	Real part of complex frequency
ω_i	Imaginary part of complex frequency
ω_D	Resonant frequency

THE EFFECTS OF FREQUENCY, AMPLITUDE, AND LOAD ON
THE DYNAMIC PROPERTIES OF ELASTOMERS

John E. Cole, III
Cambridge Acoustical Associates, Inc.
1033 Massachusetts Avenue
Cambridge, Massachusetts 02138

The dynamic-mechanical properties of elastomers are known to depend upon the nature of the loading of the material. While many aspects of the dependence of the dynamic properties on frequency and temperature are well known and customarily accounted for, these properties are also known to vary significantly with other aspects of the loading such as strain amplitude and static load. Furthermore, not all of these aspects of the loading act independently. To a fair degree of approximation the effects of frequency and strain amplitude are separable. The effects of hydrostatic loading are weakly coupled with frequency. The implications of these results on designs using elastomers is discussed.

INTRODUCTION

Many types of natural and synthetic rubber compounds, generally referred to as elastomers, find wide use in anti-vibration mounts. These materials have a microscopic structure consisting of small molecular units arranged into long-chain molecules. The basic structure of an elastomer is often altered by the addition of "fillers" such as carbon black particles which are known to strengthen the material by inhibiting relative molecular movement [1]. When an external load is applied, such as in a stress-relaxation test, these polymer chains undergo various types of mechanical deformation. The deformation processes of these polymer chains each require time to take place; consequently a time-dependent response of the material to an applied load is observed. In fact, the response of a particular elastomer material is known to depend on several aspects of the loading, as well as on the temperature of the material.

The behavior of the mechanical properties of elastomers under conditions of dynamic loading (i.e., when the applied load varies with time) is of particular interest for the design of anti-vibration mounts. These dynamic properties may be determined as a function of frequency in a vibration test by applying a

periodic load and measuring the resulting deformation. In such a test, the material may be loaded dynamically in either shear, tension, or compression. The dynamic properties corresponding to small applied loads may also be determined from acoustic measurements of sound speed and attenuation [2]. For either type of test there is found to be a phase difference between the response of the elastomer and the applied dynamic load. This viscoelastic behavior is described by considering the modulus of the material to be a complex quantity. For example, the dynamic Young's modulus may be written

$$E^* = E' + iE''$$

where the single and double primed components describe the relationship of the applied stress, respectively, to the in-phase and the out-of-phase strain. The ratio of the imaginary to real parts of the dynamic modulus (e.g., E''/E') is referred to as the loss or damping factor (η_E or $\tan \delta_E$). The reciprocal of the dynamic modulus is defined as the compliance. For instance, the shear compliance is related to the shear modulus (G^*) as follows:

$$J^* = 1/G^* = J' - iJ''$$

and therefore

* The work presented here was supported by the Office of Naval Research, Structural Mechanics Program, under Contract N00014-69-C-0056.

$$\delta' = (1/G') \cos^2 \delta_G$$

and

$$\delta'' = (1/G'') \sin^2 \delta_G,$$

where

$$\delta_G = \tan^{-1}(G''/G').$$

The dependence of the dynamic properties of viscoelastic materials on temperature and frequency (or time) is well known under conditions of no static deformation and small strain amplitudes [4]. The empirical relationship between temperature and frequency effects may be obtained from experimental data using the method of reduced variables [4]. In this manner data giving the dependence of a dynamic property on temperature may be "transformed" to give the dependence on frequency, and vice versa. Since the temperature-frequency "equivalence" of the dynamic properties of simple elastomers is discussed in detail in standard texts (see for example [4], [29] and [30]), it will not be elaborated upon here. Only the frequency dependence will be reviewed. It should be noted however, that in terms of temperature dependence, a designer of anti-vibration mounts is often interested in the "rubbery" temperature region of the material (i.e., well above the "glass transition" temperature). In this region the dynamic properties typically vary slowly with both temperature and frequency.

Under conditions of small strain, the dynamic properties of elastomers are found to be independent of strain amplitude. This is the regime of linear viscoelasticity within which the dependence of the dynamic properties on frequency is related to the dependence on time via an integral transform (either Fourier or Laplace). That is, the behavior of the dynamic property obtained at long time from a relaxation test corresponds with the behavior during a dynamic test at low frequency. Within the confines of linear viscoelastic behavior, either a relaxation test or a dynamic test provides the same information on the variation of the dynamic property with either frequency or time [5]. Furthermore, the properties obtained from either a dynamic tension or shear test are simply related. In particular, many elastomeric materials are nearly incompressible having a Poisson's ratio of 0.5. For such materials [3]

$$E' = 3G',$$

and

$$\delta_E = \delta_G.$$

In addition to frequency and temperature variations, elastomer compounds used in anti-vibration mounts may be subject to large strain amplitudes and to significant static loads. It

is therefore of interest to explore the variation of the dynamic properties of an elastomer with three of the parameters that are important to the design of an anti-vibration mount, namely, frequency, dynamic strain amplitude, and static load. It has been suggested that the effects of frequency, strain amplitude, and static load on the dynamic properties of elastomers are separable [6], in particular, that the dynamic Young's modulus may be written:

$$E^* = E_0^* \lambda_f \lambda_{\epsilon_d} \lambda_\sigma,$$

where λ_f is a function of frequency (f) only, λ_{ϵ_d} is a function of dynamic strain amplitude (ϵ_d), λ_σ is a function of static load (σ), and E_0^* is the dynamic modulus measured under conditions of small strain amplitude ($\epsilon_d < 10^{-4}$) at a given frequency and at zero static load. If this separation were possible, the task of the designer in choosing the material properties for an acceptable anti-vibration mount would be greatly simplified. Based upon the data that exist, however, it does not appear that a complete separation of effects is reasonable. In the following sections the variation of the dynamic properties with each of these effects and their interaction is discussed. This discussion is in the form of a survey of related literature rather than of a detailed study.

VARIATION OF DYNAMIC PROPERTIES INDEPENDENTLY WITH FREQUENCY, STRAIN AMPLITUDE, AND STATIC LOAD

Variation with Frequency

The dependence of the dynamic modulus on frequency is reasonably well known for a variety of elastomer compounds under conditions of no static load. As an example, the shear modulus and damping factor at small strain amplitudes for a filled natural rubber is shown in Fig. 1 [3]. For a specified temperature the shear modulus is seen to exhibit a monotone increase with frequency above a certain "critical frequency," which is characteristic of the particular elastomer. The damping factor increases rapidly and is found to peak in the region of maximum increase in shear modulus.

The fact that the dynamic modulus is an increasing function of frequency is a direct consequence of the temporal behavior of viscoelastic materials observed during either a creep test or a stress-relaxation test. From either test of a viscoelastic material, the modulus is found to be a monotone decreasing function of time. This behavior reflects the molecular relaxation processes, each being characterized by its own relaxation time. The frequency dependence of the dynamic properties is formally given by an integral transform of this observed time dependence [5]. The behavior

at low frequency therefore corresponds with the long-time behavior, the long period providing sufficient time for substantial relaxation to occur. Similarly, the high-frequency and the short-time behavior correspond with each other.

The effect of varying frequency at higher values of strain amplitude for a filled natural rubber is shown in Fig. 2. The difference from one frequency to another of both shear modulus and loss factor is seen to be about the same for all values of strain amplitude. More will be said about the implications of this observation later.

Variation with Strain Amplitude

The dependence of the dynamic modulus of elastomers on strain amplitude has been examined by several investigators [7-15]. Several types of tests have been used to explore this dependence with the same basic results. The dynamic shear modulus and the phase angle (i.e., δ_G) measured by Payne [11,12] at a frequency of 0.1 Hertz for a carbon-black filled butyl rubber is shown in Fig. 3. The parameter of each curve is the amount of filler present. For compounds with little filler content there is little change of either modulus or phase angle with strain. For larger filler content, however, the dynamic modulus decreases dramatically with increasing strain amplitude. Correspondingly, the phase angle is found to peak in the region where the modulus is decreasing most rapidly.

While for a particular elastomer and temperature the sensitivity to strain amplitude is a function of the amount of filler present, the detailed variation of the dynamic properties of a particular filler varies with the type and composition of the elastomer and with the average size, shape and chemical properties of the dispersed filler particles [16,17,18].

Two conclusions are drawn from these and similar data. First, there is little dependence of the modulus and loss factor on strain for small values of strain amplitude (i.e., less than 10^{-4}). This is the region of linear viscoelastic behavior. Secondly, the sensitivity of the dynamic properties of elastomer compounds to strain amplitude increases with the filler content. The dynamic properties of some unfilled elastomers that exhibit little dependence on strain amplitude at room temperatures have been observed to exhibit some strain dependence at lower temperatures [19].

One mechanism has been discussed to describe the sensitivity of the dynamic properties of filled elastomers to strain amplitude. The fillers that produce this sensitivity are forms of carbon black [11], certain silicas [11] and salts [10] existing as particles or chains of particles embedded in the elastomer matrix. There are interaction forces of either chemical or surface-active origin which bond the

particles to the elastomer matrix under equilibrium conditions. Payne [12] refers to this situation as a "wetting" of the particles by the matrix. Since for the materials under discussion the elastic moduli of the filler materials are much greater than the equilibrium (or zero frequency) modulus of the elastomer matrix, the effect of filling is to enhance the modulus by increasing the resistance to deformation. When such a filled elastomer is strained in a periodic manner at low amplitude, the enhanced equilibrium modulus is observed (see Fig. 3). At larger values of strain amplitude, a process of "dewetting" is thought to occur. Owing to the large strain amplitudes, the filler particles "separate" somewhat from the elastomer matrix. This process results in a loss in the magnitude of the dynamic modulus and an increased loss factor. A simple theoretical model of this effect has been proposed by Freudenthal [17]. This mechanism however, does not account for the observed strain dependence of unfilled elastomers at low temperature [19].

Variation with Compressive Static Loading

There has been a considerable interest in evaluating the effect of static load on the dynamic properties of polymeric compounds. A variety of loading conditions and experimental methods have been employed [2,15,20-25]; however, the concern of this discussion is those studies using compressive static loadings (i.e., hydrostatic or uniaxial).

The effect of hydrostatic pressure on the bulk compressibility (B^*) of rubber-sulfur vulcanizate over a frequency range of 50 to 1000 Hz has been investigated by McKinney, et al. [25]. The real and imaginary parts of the bulk compressibility at 1000 Hz as a function of temperature are shown in Fig. 4 for gauge pressures from 0 to 9.81×10^7 Pascals. For a given temperature, the real part of the compliance is a monotone decreasing function of pressure. The imaginary part of the compressibility shows even greater sensitivity to pressure in the temperature range of -10° to 10° C. For low temperatures there is a monotone decrease of B^* with increasing pressure. At higher temperatures, this is no longer the case. The data of Fig. 4 can be used to calculate the bulk modulus and loss factor as functions of pressure for several temperatures. The modulus (i.e., $(1/B^*) \cos^2 \delta_B$) is found to increase slightly with pressure while the behavior of the loss factor depends strongly on temperature. The results of an acoustic transmission test on "rubber-like" resins under hydrostatic pressure are discussed by Boiko [2]. In the ranges of frequency and pressure from 10 to 100 kHz and 0 to 1.5×10^7 Pascals, both the real and imaginary parts of the elastic modulus are observed to increase with pressure.

The dynamic Young's modulus obtained using a vibration test by de Mey and van Amerongen [15] for cylindrical samples of an unfilled natural rubber compound under uniaxial compression is shown in Fig. 5. The modulus is shown as a function of static compressive strain for different values of the shape factor ($D_0/4h_0$) where D_0 is the cylinder diameter and h_0 the height. The modulus is obtained for frequencies of 30-35 Hertz and a dynamic strain amplitude of 5×10^{-3} . These data show the modulus increasing with static load.

These data provide an indication of the dependence of the dynamic properties of elastomers on compressive static load. A mechanism for explaining such a dependence for materials subjected to volume compression has been discussed by Ferry [4]. This mechanism uses the concept of the "free volume" of a material that is present in the form of voids on either a molecular or macromolecular scale. When a material is loaded compressively, there is a tendency to decrease its free volume, thereby inhibiting molecular motions. Such a process results in a decrease in the compressibility of the material (and hence an increase in the modulus). The effect of decreasing the free volume of a material is more directly observed under hydrostatic loading. As suggested in [2], it would be expected that this mechanism would only manifest itself for very large uniaxial loadings which decrease the macroscopic volume (and hence decrease Poisson's ratio) of the material.

INTERDEPENDENCE OF THE EFFECTS ON THE DYNAMIC PROPERTIES OF FREQUENCY STRAIN AMPLITUDE AND STATIC LOAD

Dependence of the Effects of Frequency and Strain Amplitude

The discussion thus far has shown that the dynamic properties of elastomer compounds are observed to vary significantly as changes are made to either one of the three factors: frequency, dynamic strain amplitude, and static loading. In addition, mechanisms thought to give rise to these variations have been briefly described. A complete description of the dependence of the dynamic properties of any elastomer material on these factors requires that all three be allowed to vary independently. Such an experimental program for any material is not easy to fulfill. There do exist however, results of experimental programs in which two of the three factors have been varied. By "piecing" these results together, some insight into the dependence on all three factors can be obtained.

The relationship between the effects of frequency (or time) and dynamic strain amplitude on the dynamic properties has been discussed for a variety of elastomer compounds by Freudenthal [16], Smith [8], Landel and

Stedry [9], and Warnaka and Miller [10]. The conclusions drawn in [8], [9], and [16] is that to a fair degree of approximation the effects of dynamic strain amplitude and frequency (or time) are separable (i.e., act independently). This conclusion has also been drawn by Vashchuk and Rosin [6].

The independence of these two effects is consistent with the "dewetting" mechanism used to describe the strain amplitude dependence of filled elastomers. It would be expected that to a first approximation this mechanism would occur at any frequency. The primary cause of the "dewetting" is the relative motion between filler particles and elastomer matrix; hence, frequency effects would not be expected to be dominant.

Since the effects of frequency and dynamic strain amplitude are approximately separable, the dependence of any dynamic property (H^*) on frequency (f), strain amplitude (ϵ_d), and static load (σ) may be expressed

$$H^*(f, \epsilon_d, \sigma) = H_f^*(f, \sigma) H_{\epsilon_d}^*(\epsilon_d, \sigma)$$

It remains to examine the dependence of the dynamic properties on static load and frequency effects and on static load and strain amplitude effects.

Relationship of the Effects of Frequency and Static Load

The dependence of frequency and hydrostatic pressure effects has been discussed by Ferry [4] and Marvin and McKinney [26] in terms of the free-volume concept. This concept can be used to explain the dependence of the relaxation times, which characterize the material behavior, on the pressure. When there is a relatively large free volume in the material (for example, at high temperatures), reorientation of molecular chains owing to deformation can be achieved relatively easily with correspondingly short relaxation times. The effect of a hydrostatic load is to decrease the free volume of the material. This means that the molecular reorientation takes longer to achieve owing to an increase "viscosity" or resistance to molecular motion. Hence, relaxation times are increased with hydrostatic pressure. In general, the effect of any static load that alters the free volume of the material also changes the relaxation times.

Experimental investigations into the effects of hydrostatic pressure on dynamic properties have been made among others by McKinney, et al. [25] and Bartenev and Kuznetsova [20]. The effect of increased hydrostatic pressure is to reduce the free volume of an elastomer in the same way as that produced by a reduction in temperature. Based on such reasoning the method of reduced variables is extended by McKinney et al. to include

the effects of pressure as well as frequency and temperature [25]. A reasonable collapse of the data of Fig. 4 is obtained in [25] with this extension. These results have been used to obtain the variation of the bulk compressibility with frequency at 0° C for several pressures shown in Fig. 6. The frequency dependence is not significantly altered for hydrostatic pressure less than approximately 10^7 Pascals (1500 Psi). There do not appear to be low frequency studies of the effect of frequency and uniaxial compressive stress on the dynamic properties of elastomers.

Dependence on the Effects of Dynamic Strain Amplitude and Static Load

This dependence does not appear to have been the source of significant study to date. In fact, one can only offer speculation based on the preceding discussions. If the "dewetting" process described in [16] is the dominant mechanism of the strain dependence of filled elastomers, it would be reasonable to assume that this strain dependence would depend upon the static loading. The effect of hydrostatic pressure, for instance, would be expected to delay the process to larger strain amplitudes by retarding the filler-matrix dewetting. Such reasoning, however, must remain purely speculative awaiting experimental evaluation.

INFLUENCE OF THE DYNAMIC PROPERTIES OF ELASTOMERS ON THE PERFORMANCE OF ANTI-VIBRATION MOUNTS

The frequency variation of the storage modulus of elastomers indicated in Fig. 1, results in a stiffening of an anti-vibration mount with frequency. In the region of increase in modulus, the transmissibility of an anti-vibration mount increases. Several calculations have been made by Snowdon [3] that display this effect for models of simple mounts. When the storage modulus is constant for all frequencies of interest, the transmissibility decreases at a rate of 12 dB per octave above the natural frequency of the "mount". This rate is reduced when the storage modulus of the elastomer increases in the frequency range of interest. As expected the maximum value of transmissibility decreases as the damping factor of the respective material increases.

For a more general approach to estimating the effects of the stiffness and damping of a mount on the mount effectiveness (E_M), reference is made to the result of Sykes [27]:

$$E_M = 1 + \left| \frac{Y_1}{Y_F + Y_M} \right|^2$$

where Y_1 is the mobility (i.e., reciprocal impedance) of the mount, and Y_F , Y_M are the respective mobilities of the foundation and

machine. An increase in mount stiffness therefore in general reduces the mount effectiveness.

The strain dependent behavior of filled elastomers might be expected to be important near a resonance of an anti-vibration mount. Since the storage modulus (i.e., stiffness) decreases and the damping factor increases with increasing strain amplitude, the resonant response is diminished. Another effect of the stiffness is to decrease the "natural" frequency of the vibrating system. It is difficult to quantify the effects of strain sensitivity further since the differential equation that governs the forced motion of a simple vibratory system with strain dependent stiffness is nonlinear. Many aspects of the general nature of the response of simple systems with non-linear "springs" is discussed by Stoker [28]. As expected the maximum response of a single-degree-of-freedom vibration system with a soft spring (i.e., one whose stiffness decreases with extension) and with constant damping is shifted to lower frequencies. In addition the response displays a "jump" in traversing the frequency range (see [28] for a more detailed discussion).

For elastomers in static compression, the existing data at low frequencies (see Figs. 5 and 6) indicate a slight stiffening with increasing static loading. No single trend is indicated for the damping factor. The increased stiffening tends to increase the transmissibility of a mount.

The separability of frequency and strain amplitude effects on the dynamic properties of elastomers permits these two effects to be estimated independently. The effects on the dynamic properties of frequency and hydrostatic pressure however, are not separable. With the exception of large static pressures (e.g., $> 10^7$ Pascals), there does not appear to be a significant coupling of these effects (see Fig. 6). There is little information available to establish similar guidelines in the case of uniaxial compression. In addition, the dependence of the effects of dynamic strain amplitude and static load appears to require further investigation.

SUMMARY OF CONCLUSIONS

In summary the major conclusions of this study are the following:

1. The dynamic properties of elastomers can vary with frequency (and temperature) as well as with compressive static load.
2. The dynamic properties of certain filled elastomers exhibit a strong dependence on strain amplitude.
3. The effects of frequency and strain amplitude act independently.

4. There appears to be a weak dependence of the effects of frequency and hydrostatic (compressional) loads.
5. There is little information available concerning the combined effects of strain amplitude and static compression load.
6. The stiffness of elastomers tends to increase with frequency (decrease with temperature), decrease with dynamic strain amplitude (for strain-sensitive filled elastomers), and increase with hydrostatic load.

REFERENCES

1. L. H. Van Vlack, Elements of Materials Science, p. 253, Addison-Wesley Publishing Co., Inc., Reading, MA, 1960.
2. L. M. Boiko, V. G. Kozubov, and V. V. Ostudin, "Acoustic Measurements on Rubber-like Polymers During Compressive Deformation", Polymer Mech. **10**, 1, pp. 123-128 (English Trans., Aug. 1975).
3. J. C. Snowdon, Vibration and Shock on Damped Mechanical Systems, pp. 1-9, 27-31, 39-43, John Wiley & Sons, Inc., NY, 1968.
4. J. D. Ferry, Viscoelastic Properties of Polymers, pp. 203-244, John Wiley & Sons, Inc., NY, 1961.
5. A. C. Pipkin, Lectures on Viscoelasticity Theory, Applied Mathematical Science Semrs., Vol. 7, Springer-Verlag, NY, 1972.
6. D. B. Vashchuk and G. S. Rosin, "Dynamic Properties of Rubber," Sov. Phys. Acoust. **19**, 2, pp. 101-102, 1973.
7. G. E. Warnaka, "Dynamic Strain Effects in Elastomers," Rubber Chem. & Tech. **XXXVI**, 2, pp. 407-421, 1963.
8. T. L. Smith, "Nonlinear Viscoelastic Response of Amorphous Elastomers to Constant Strain Rates," Trans. Soc. Rheology **VI**, pp. 61-80, 1962.
9. R. F. Landel and P. J. Stedry, "Stress as a Reduced Variable: Stress Relaxation of SBR Rubber at Large Strains," J. Appl. Phys. **31**, 11, pp. 1885-1891, 1960.
10. T. Nicholas and A. M. Freudenthal, "The Mechanical Behavior of a Filled Elastomer at High Strain Rates," Trans. Soc. Rheology, **12:3**, pp. 323-333, 1969.
11. A. R. Payne, "The Dynamic Properties of Carbon Black-Loaded Natural Rubber Vulcanizates, Part I," J. Appl. Polymer Science **VI**, 19, pp. 57-63, 1962.
12. A. R. Payne, "The Dynamic Properties of Carbon Black Loaded Natural Rubber Vulcanizates, Part II," J. Appl. Polymer Science **VI**, 21, pp. 368-372, 1962.
13. A. R. Payne, "Dynamic Properties of Heat-Treated Butyl Vulcanizates," J. Appl. Polymer Science **7**, pp. 873-885, 1963.
14. A. K. Sircar and T. G. Lamond, "Strain-Dependent Dynamic Properties of Carbon Black Reinforced Vulcanizates. II. Elastomer Blends," Rubber Chem. & Tech. **48**, pp. 89-96, 1975.
15. S. de Mey and G. J. van Amerongen, "Dynamic-Mechanical Characteristics of Rubber Compounds," Rubber Chem. & Tech. **29**, pp. 1215-1232, 1956.
16. A. M. Freudenthal, "Stress Sensitive Response of Filled Elastomers," AAIA J. **5**, pp. 917-922, 1970.
17. T. B. Lewis and L. E. Nielsen, "Dynamic Mechanical Properties of Particulate-Filled Composites," J. Appl. Polymer Science **14**, pp. 1444-1471, 1970.
18. L. E. Nielsen, "Dynamic Mechanical Properties of Filled Polymers," Appl. Polymer Symposia **12**, pp. 249-265, 1969.
19. G. E. Warnaka and H. T. Miller, "Strain-Frequency-Temperature Relationships on Polymers," Paper No. 67-RP-A, J. of Engineering for Industry, pp. 1-8, 1967.
20. G. M. Bartenev and I. A. Kuznetsova, "Influence of Pressure on the Relaxation Properties of Elastomers," Polymer Mech. **10**, 3, pp. 381-388, 1974 (English Trans. Nov. 1975).
21. A. M. Lokoshchenko, et al., "Allowance for the Effect of Hydrostatic Pressure in Describing the Nonlinear Viscoelastic Properties of High-Density Polyethylene," Polymer Mech. **10**, 6, pp. 859-863, 1974 (Eng. Trans., March 1976).
22. W. Goldberg and G. Lianis, "Behavior of Viscoelastic Media Under Small Sinusoidal Oscillations Superimposed on Finite Strain," J. Appl. Mech. **35**, 3, pp. 443-449, 1968.
23. K. L. DeVries and D. K. Backman, "Rheology of Polyethylene at High Pressures," Polymer Letters **9**, pp. 717-721, 1971.
24. W. Kuhl, et al., "Sound Absorption and Sound Absorbers on Water, Volume I" (translated by C. E. Mongan), NavShips Rpt. 900, 164, pp. 230-233, June 1947.

25. J. E. McKinney, H. V. Belcher and R. S. Marvin, "The Dynamic Compressibility of a Rubber-Sulfur Vulcanizate and its Relation to Free Volume," Trans. Soc. Rheology IV, pp. 347-362, 1960.
26. R. S. Marvin and J. E. McKinney, "Volume Relaxation in Amorphous Polymers," Physical Acoustics, Vol. 2B (W. P. Mason, Ed.) pp. 165-229, Academic Press, NY, 1965.
27. A. O. Sykes, "The Effects of Machine and Foundation Resilience and of Wave Propagation on the Isolation Provided by Vibration Mounts," SAE Transactions 66, pp. 533-548, 1958.
28. J. J. Stoker, Nonlinear Vibrations in Mechanical and Electrical Systems, pp. 81-117, Interscience Publishers, Inc., NY, 1950.
29. R. M. Christensen, Theory of Viscoelasticity, Academic Press, NY, 1971.
30. A. V. Tobolsky, Structure and Properties of Polymers, John Wiley & Sons, Inc., NY 1960.

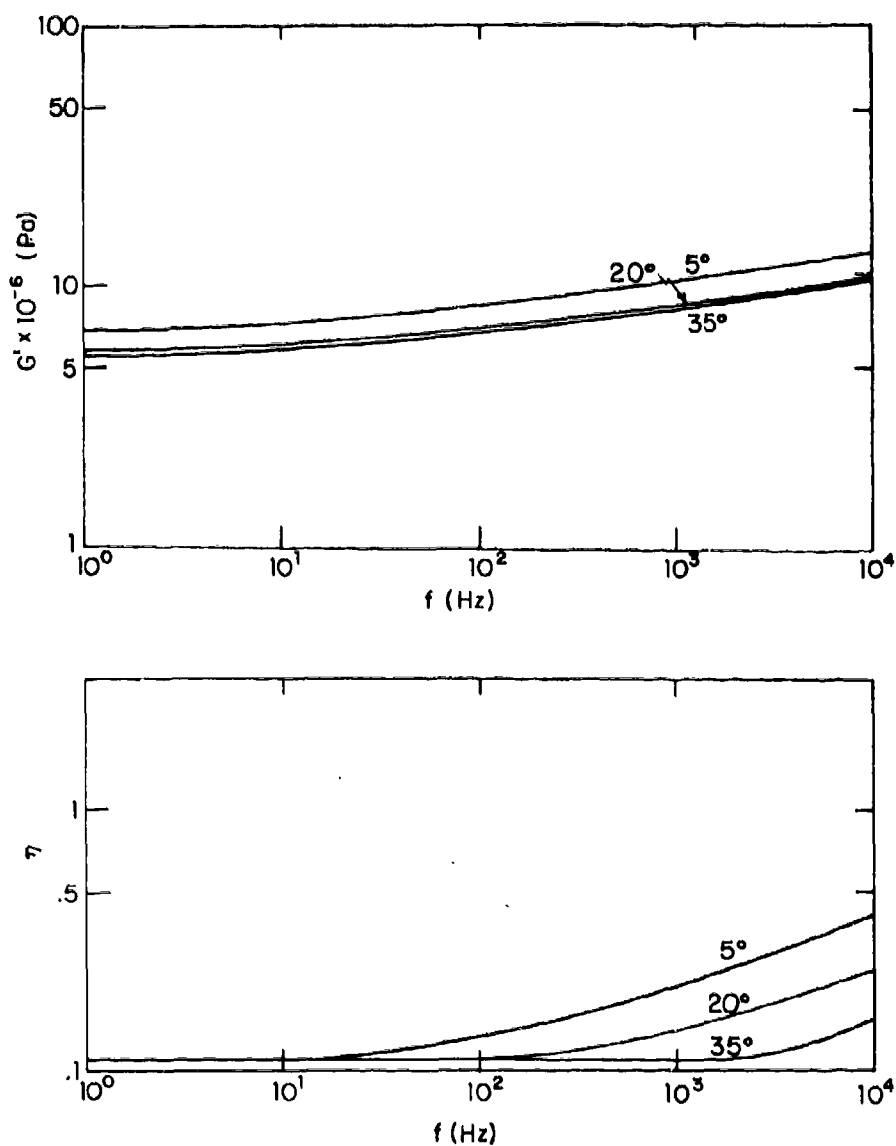


Fig. 1 - Frequency dependence of the dynamic shear modulus and the damping factor of natural rubber filled with 50 parts by weight of HAF carbon black per 100 parts rubber. Temperatures are in degrees Celsius [3].

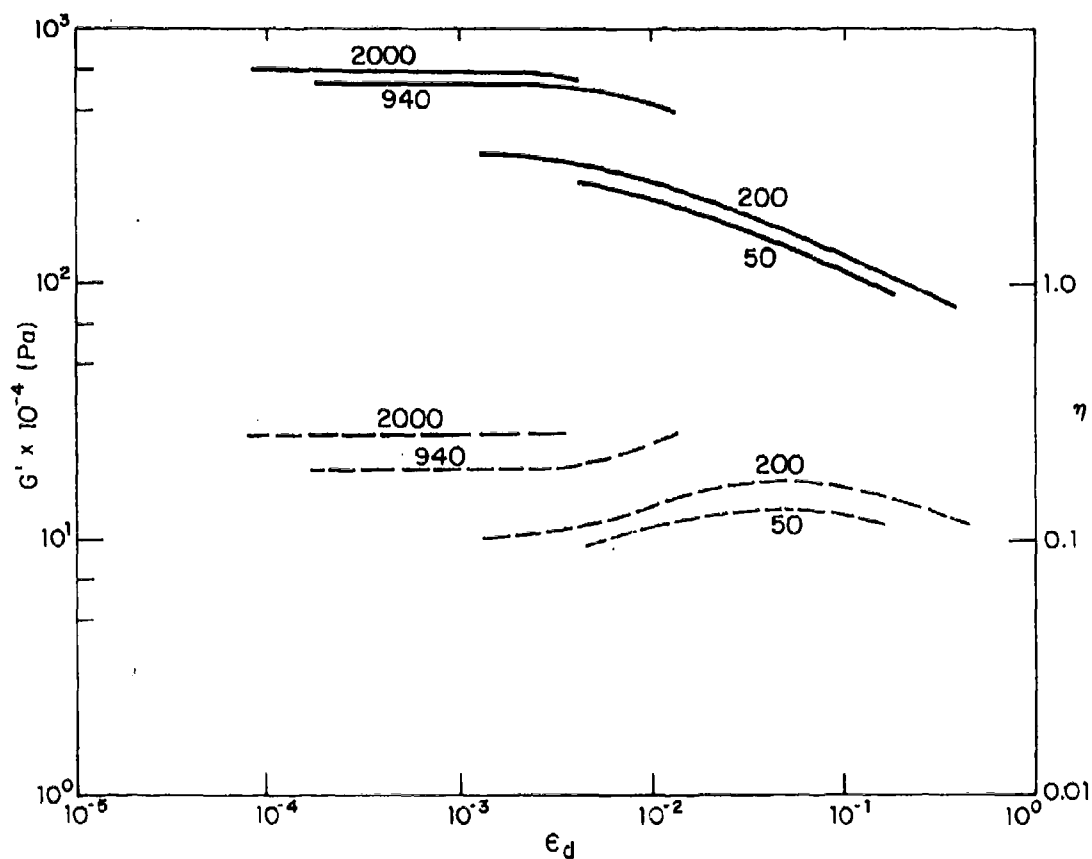


Fig. 2 - Effect of dyanmic shear strain on the dynamic-mechanical properties of a natural rubber compound containing 50 parts of carbon black per 100 parts rubber by weight. The parameter is frequency in Hz. (—, G' ; ---, η) [7].

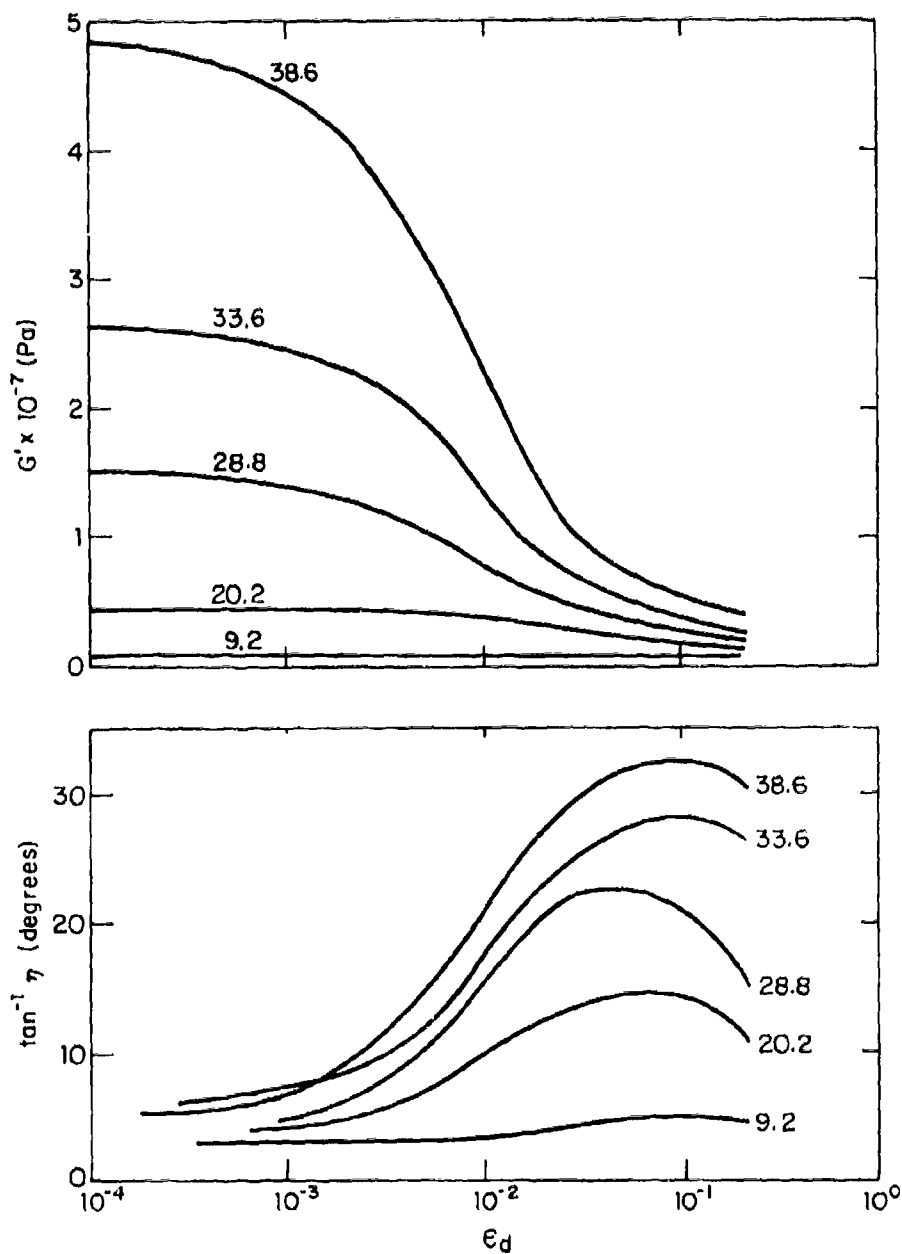


Fig. 3 - Strain amplitude dependence of carbon black filled butyl rubber at 0.1 Hz and different filler content in parts of filler per 100 parts of rubber by weight [4, 12].

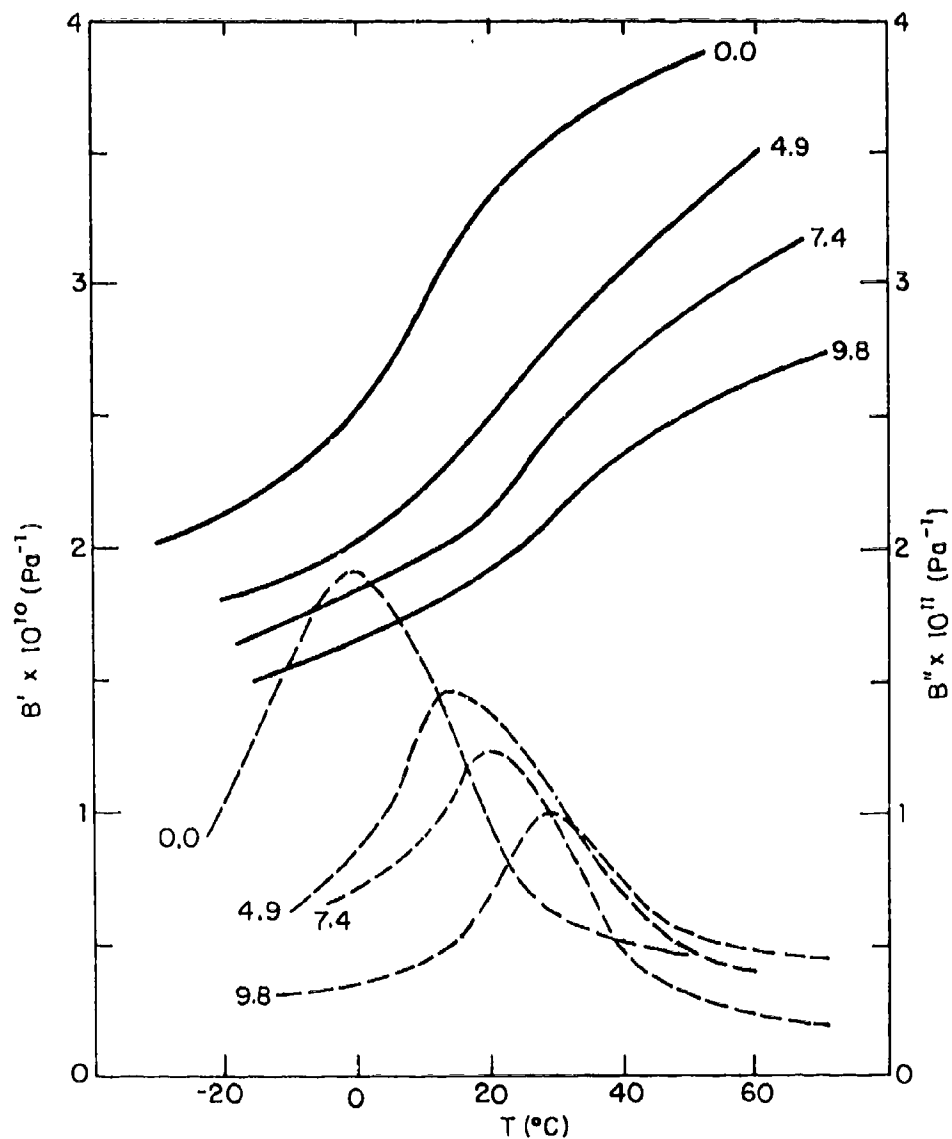


Fig. 4 - Storage and loss compliances of natural rubber (12% sulfur) versus temperature at 1000 Hz for several values of static pressure (in $\text{Pa} \times 10^{-7}$) [26].

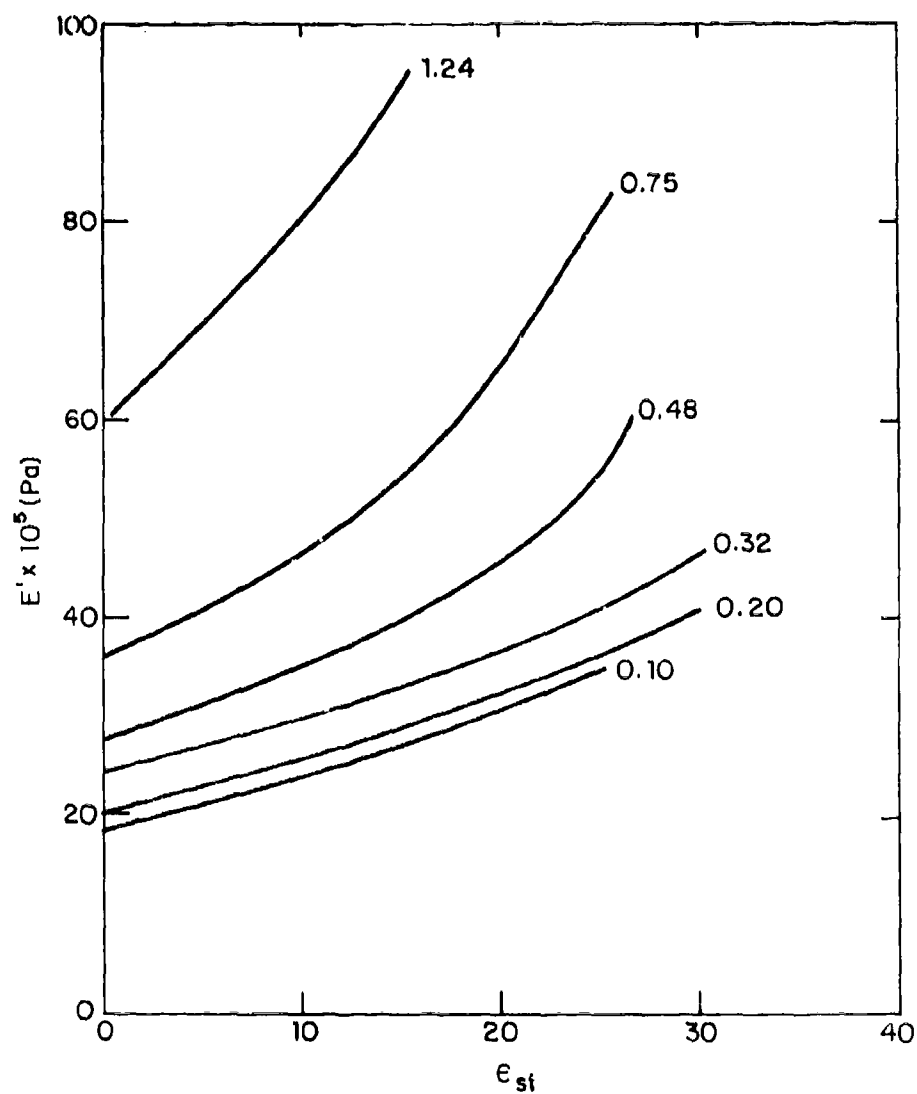


Fig. 5 - Elastic storage modulus of cylindrical samples of an unfilled natural rubber compound for several shape factors ($f = 30-35$ Hz; dynamic strain amplitude = 0.005; $T = 25^\circ\text{C}$) [15].

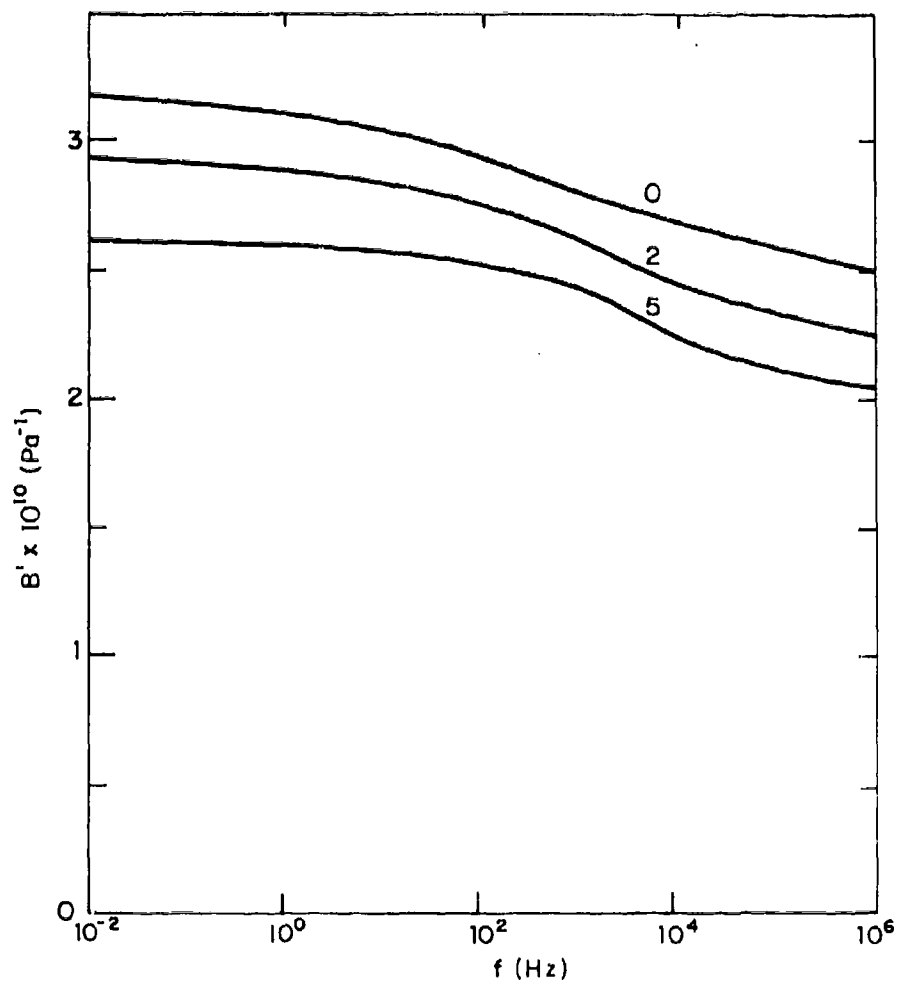


Fig. 6 - Storage compliance of natural rubber (12% sulfur) versus frequency at 0°C for several values of static pressure (in $\text{Pa} \times 10^{-7}$) [25].

LIQUID SPRING SHOCK ISOLATOR MODELING BY SYSTEM IDENTIFICATION

P. N. Gonnemburg, B. H. Wendler, and W. E. Fisher
The U.S. Army Corps of Engineers
Construction Engineering Research Laboratory
Champaign, Illinois

1. INTRODUCTION

Background

Liquid springs can be designed for near optimal performance. However, there is limited documentation by manufacturers relating isolator mathematical models to hardware design parameters. Hence, the liquid spring design methods have yet to reach the state of the art whereby optimum elastic and damping qualities can be specified and subsequently transformed into predictable hardware performance. Furthermore, in practice it is found that pneumatic or liquid-filled isolators require continuous maintenance, and the conceived optimum performance is subject to degradation between servicing operations.

If open-parameter mathematical models of isolators with common design features were available, the model parameters could be optimized directly for the expected environmental and isolation system physical properties. To this end, a feasibility study was undertaken to determine if a reasonably accurate model of an off-the-shelf liquid-spring isolator could be found, using data from a few simple and inexpensive tests. A liquid spring was selected for its design versatility and potential use in high-performance shock isolation systems. General acceptance of a system identification approach ultimately will depend on the simplicity and cost of testing and the ability to represent installed operating conditions by the mathematical formulation.

Purpose

The purpose of this report is to present the results of a study to determine the feasibility of establishing mathematical models of high-performance liquid-spring shock isolators from performance test data.

Approach

Several general nonlinear formulations were attempted when modeling the isolator. The isolator's model was included in an overall model of the test configuration. Terms representing the test configuration could be changed as required to model any suitable configuration. For example, the manufacturer's test entailed dropping a weight from

various heights onto a plate supported by the isolator. However, for this study, a hydraulic shaketable was used whereby the isolator formed the spring and damping elements of a simple horizontal oscillator. Generally, the test configuration must be able to provide the same range of motion variables (displacement, velocity, and acceleration) to the isolator as expected under actual field conditions.

For the horizontal oscillator configuration, three tests were performed, using approximated displacement box functions. Two of these tests were similar and provided confidence in repeatability and consistency. The third test, which was performed at an elevated fluid temperature, provided information regarding the variability of the optimized coefficients.

2. EQUIPMENT AND TEST CONFIGURATION

Selection of the Isolator

Isolator performance can be defined in terms of dissipated energy—that is, force-displacement relationships. For example, equipment fragility dictates that to insure functional survival, imposed accelerations must be limited, thus controlling the maximum force transmitted to the equipment through the isolator. Either overall or internal displacements can impair functional survival, so both types of displacement must be constrained. The dotted horizontal and vertical lines in Fig. 1 indicate the performance of an ideal isolator: one that dissipates as much energy as possible.

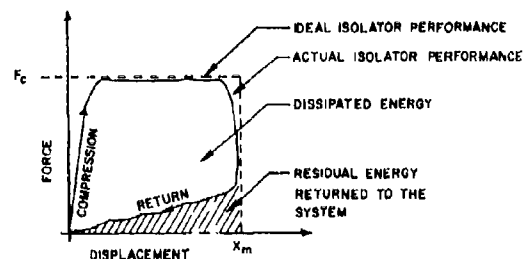


Fig. 1 — Force-displacement relationship for high performance isolators

The fluid compressibility and viscosity, and the mechanical and fluid friction determine the response of liquid-spring isolators. Compression of the silicone fluid with a variable diameter piston rod provides the spring effect (Fig. 2a); fluid flow around the piston provides the major source of damping (Fig. 2b). The spring effect, as illustrated, acts only for rod motion from left to right. The actual liquid spring used was double-acting, giving a spring effect in both directions.

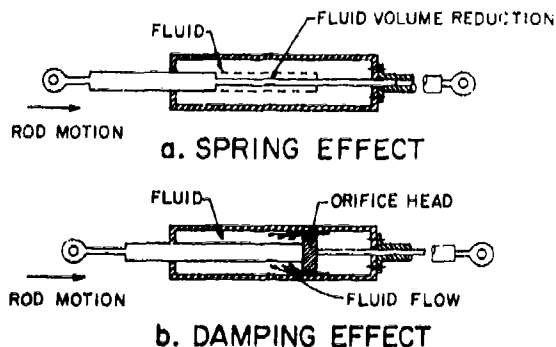


Fig. 2 — Characteristics of a liquid-spring shock isolator

A liquid-spring shock isolator was used in a simple test to provide data for optimizing the coefficients of the mathematical model. The isolator met performance specifications requiring a spring rate of 70 051 N/m (400 lb/in.), an effective linear viscous damping ratio of 0.3, and a 0.305-m (12-in.) stroke. Static tests by the manufacturer indicated a spring rate of 55 165 N/m (315 lb/in.) for small displacements and 95 619 N/m (546 lb/in.) at full stroke (Fig. 3). Section 3 further discusses the hardening property of this static spring rate.

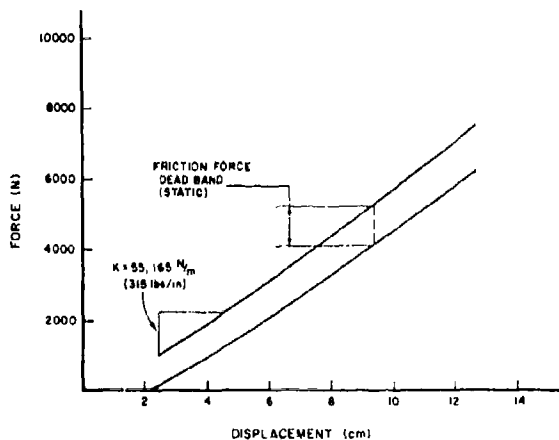


Fig. 3 — Static spring-rate curve for the test isolator

The manufacturer's tests indicated an equivalent viscous damping coefficient of 0.28 to 0.43, varying with velocity. Thus, damping was expected to be nonlinear.

The manufacturer suggested that the dynamic spring rate and damping coefficient would exhibit *softening* (see Section 3), even though static tests showed *hardening*. This statement simply implies, however, that the dynamic properties were generally different from those the manufacturer had equipment to measure.

Test Configuration

The least-squares system-identification technique requires measured input motion (base displacement), measured output response (mass displacement), and an open-parameter differential equation as a trial mathematical model of the isolator.

The test configuration, shown in Fig. 4, provides the maximum relative displacement and velocity using available test fixtures. One end of the liquid spring was attached to a rigid base mounted on the CERL Biaxial Shock Test Machine (BSTM) test platform and the other end was attached to a 2722-kg (6000-lb) mass. Rollers supported the mass and allowed it to move only in the horizontal plane. Rolling friction was not significant. Base displacement was applied to the isolator through the rigid base mounted on the test platform.

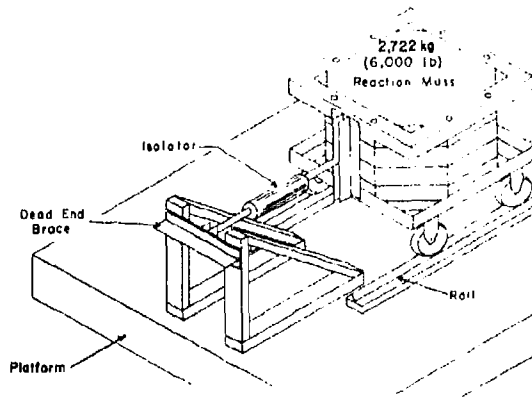


Fig. 4 — Test carriage on liquid-spring mounting frame

Six uniaxial electrohydraulic actuators, with a total capacity of 2 001 700 N (450,000 lb) provided the horizontal motion. The actuators drive the 3.658-m square (12-ft square) all-welded aluminum test platform. A pressurized hydraulic fluid provided the excitation energy, and a 0.0208 m³/s (330-gpm) servo valve on each actuator controlled it.

Optical-electronic equipment provided the excitation and mass response displacement data. Differentiating the displacement data yielded the velocity and acceleration. All data were recorded on analog tape, then digitized and filtered for reduction.

Base Excitation Motions

A series of preliminary sinusoidal tests to determine adequate mass response showed a gradual increase in relative response amplitude, caused by a rapid rise in isolator fluid temperature and a decrease in fluid viscosity. These results caused the steady-state testing to be abandoned.

Three transient tests, labeled runs A, B, and C, were then performed. Figure 5 shows the platform displacement for these runs. Run A input motion was an initial step to 0.140 m (5.50 in.) displacement with a rise time of 0.20 sec. This displacement was held for approximately 2.00 sec, followed by a return to the original platform position in 0.12 sec. Platform displacement for run B was opposite in direction but equal in size and duration to run A. Run C had an initial rise to 0.140 m (5.5 in.) displacement in 0.12 sec, followed by an immediate return to the original position in 0.12 sec.

3. FORMULATION OF THE MATHEMATICAL MODEL

Physical and Mathematical Properties

Liquid springs behave like automotive shock absorbers. Figure 6a. shows a simplified, single-acting liquid spring. Motion of the rod to the right will cause a spring effect by fluid compression, and a damping effect by flow of fluid through or around the orifice head. This isolator can (1) dissipate energy efficiently by fluid damping, and (2) return to original length after distortion. The latter property causes some loss of efficiency from energy dissipation, but it is a practical necessity. This energy is conserved and is shown as the hatched area in Fig. 1.

Figure 6b shows a free-body model of the isolator. $F(t)$ represents the action and reaction forces applied externally

to the isolator. The internal force causing the compressed isolator to return to its original position is shown as a spring, and is depicted mathematically as $f_1(z)$. The internal force causing damping is shown as a dashpot, and is depicted mathematically as $f_2(\dot{z})$. The mathematical model for the general test configuration is:

$$F(t) + f_1(z) + f_2(\dot{z}) = 0 \quad (\text{Eq. 1})$$

Either the spring or the fluid damping can exhibit hardening or softening properties, as illustrated in Fig. 7 [1,2]. Hardening occurs when the internal force increases more rapidly than the displacement or velocity. Softening occurs when the internal force increases less rapidly than the displacement or velocity. By requiring both $f_1(z)$ and $f_2(\dot{z})$ to soften as in Fig. 1, one can cause energy to be dissipated efficiently. Optimizing the precise shape of the softening curves for each of these functions and for each isolation system allows one to maximize the energy dissipation efficiency.

Several practical design features such as displacement dead space, fluid preloading, and static friction, can influence the shape of the curves for $f_1(z)$ and $f_2(\dot{z})$. Displacement dead space results from little or no resistance to motion in the vicinity of $z = 0$, and is not directly associated with the frictional dead space shown in Fig. 3. Under dynamic operating conditions, frictional dead space will appear as a constant friction damping term in $f_2(\dot{z})$. An air bubble or void in the fluid chamber can cause a dead space in displacement. Preloading a liquid spring can slightly modify the shapes of $f_1(z)$ and $f_2(\dot{z})$ in addition to modifying the spring's response at small displacement velocities. However, preloading is impossible if there is a void in the fluid chamber, and static friction will create a minimum applied force before the relative motion of the isolator starts. The mathematical aspects of these features will be discussed below.

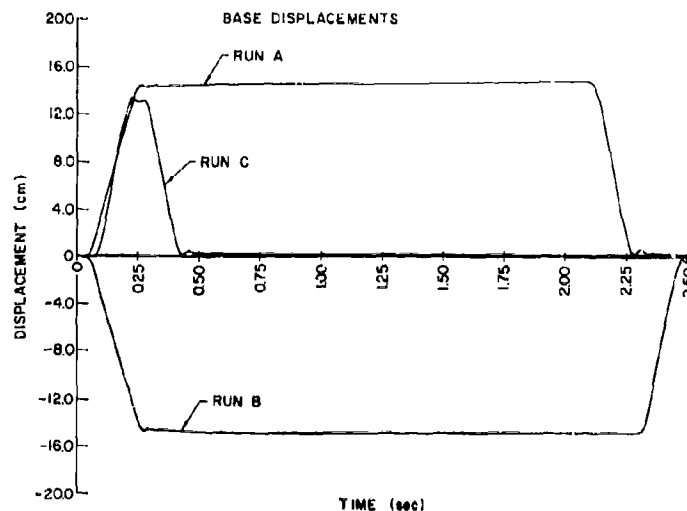
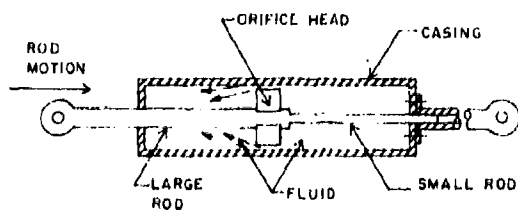
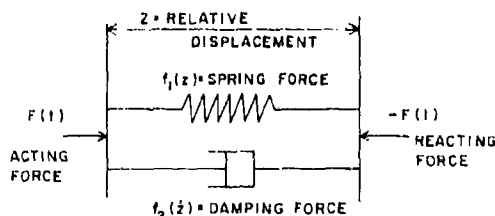


Fig. 5 — Base displacements



A. DIAGRAM OF A SINGLE ACTING LIQUID SPRING SHOCK ISOLATOR



B. FREE BODY DIAGRAM OF ISOLATOR

Fig. 6 — Simplified diagrams of liquid-spring shock isolator

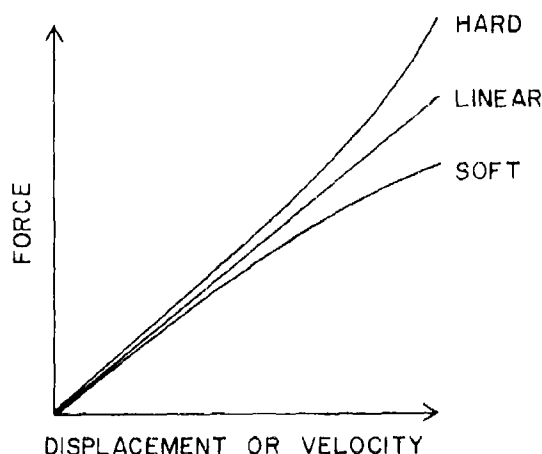


Fig. 7 — Hardening and softening properties

General Formulation of the Model

Figure 8 shows a simplified model of the test configuration. The coordinate, x , is the absolute displacement of the mass, m : absolute table displacement, u , causes the forces applied to the mass. The relative displacement between the mass and the table is $z = x - u$. Likewise, the relative velocity is $\dot{z} = \dot{x} - \dot{u}$, where the superimposed dot means differentiation with respect to time.

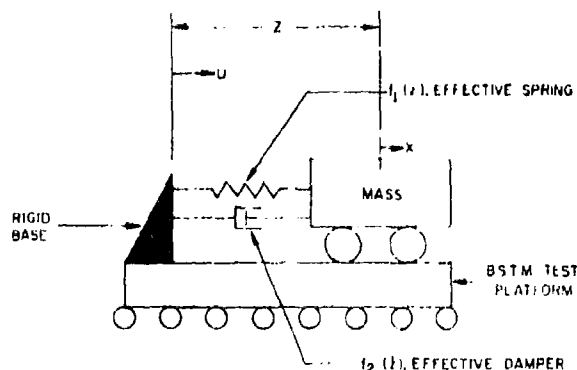


Fig. 8 — Simplified test configuration

The spring and damper effects represent the isolator's behavior. Spring forces that restore the mass to equilibrium are represented by $f_1(z)$, which is a nonlinear function of z . Forces that dissipate energy are represented by $f_2(\dot{z})$, which is a nonlinear function of \dot{z} . The forces applied to the isolator, which constitute the $F(t)$ term in Eq. (1), are caused by the table motion and the inertia of the mass.

Identification of Applied Forces

For an oscillator with linear elasticity and damping, the mathematical model is [3]:

$$m\ddot{z} + kz + c\dot{z} = -m\ddot{u} \quad (\text{Eq. 2})$$

where m is the mass, and k and c are constants, i.e., $f_1(z) = kz$ and $f_2(\dot{z}) = c\dot{z}$. Thus, $-m\ddot{u}$ appears on the right side as a forcing function. The same form of the differential equation is applicable when $f_1(z)$ and $f_2(\dot{z})$ are nonlinear, whereby:

$$m\ddot{z} + f_1(z) + f_2(\dot{z}) = -m\ddot{u}. \quad (\text{Eq. 3})$$

Substituting $\ddot{x} = \ddot{z} + \ddot{u}$ yields

$$m\ddot{x} + f_1(\dot{x}) + f_2(\dot{z}) = 0. \quad (\text{Eq. 4})$$

Equation (4) is the general equation governing the test configuration shown in Fig. 8. At rest initial conditions were assumed.

In passing, it is considered worthwhile to derive the form of the governing equation which would be applicable for a more versatile test configuration. A drop test, for example, may enable one to achieve a broad range of motion variables which cannot be achieved with the horizontal oscillator configuration discussed above. Figure 9 shows the notation of such a test. A mass of weight, w , is dropped vertically from a height, h , onto a flat supported by the isolator, which acts in the vertical direction. Summing forces at the mass yields the relation

$$m\ddot{z} + f_1(z) + f_2(\dot{z}) = 0 \quad (\text{Eq. 5})$$

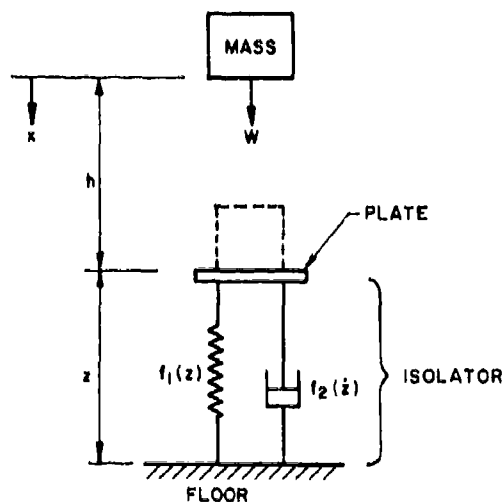


Fig. 9 - Drop test notation

where $m = w/g$. Note that $F(t)$ from Eq. (1) is now equal to $m\ddot{z}$, instead of $m\ddot{x}$, as for the horizontal oscillator configuration. Also in this case, initial conditions are:

$$\begin{aligned} z(0) &= 0 \\ \dot{z}(0) &= \sqrt{2gh} \end{aligned} \quad (\text{Eq. 6})$$

Nonlinear Spring and Damping Effects

The nonlinear terms $f_1(z)$ and $f_2(\dot{z})$ can be expressed to any desired degree of accuracy by expanding orthogonal functions. For example, for a sufficiently large number of terms, N , the following expansion can represent either a hardening or softening spring:

$$f_1(z) = \sum_{n=1}^N k_n z^n \quad (\text{Eq. 7})$$

where n is an integer, and k_n is a constant. Accumulating more than a few terms for either $f_1(z)$ or $f_2(\dot{z})$, however, would result in awkward and time-consuming calculations. Although in theory, short power-series expansions can model either softening or hardening, in practice, for softening, unstable solutions result when large motions are modeled.

The hyperbolic tangent provides an appropriate representation for softening [4]:

$$f_1(z) = k_1 z + k_2 \tanh(\alpha z). \quad (\text{Eq. 8})$$

A similar expression can represent damping, except that the equation includes a term for coulomb friction:

$$f_2(\dot{z}) = c_1 \dot{z} + c_2 \tanh(\beta \dot{z}) + c_3 \text{sgn}(\dot{z}). \quad (\text{Eq. 9})$$

In Eqs. (8) and (9) α and β are constants, while $\text{sgn}(\dot{z}) = \pm 1$, according to the algebraic sign of \dot{z} .

Discussions with the manufacturer indicated that response results might reflect the effects of displacement dead space and preloading. These conditions affect the form of either $f_1(z)$ or $f_2(\dot{z})$ in the neighborhood of $z = 0$. Figure 10a shows the effect of dead space—no resistive force—for $z = \pm \delta$. Figure 10b shows the effect of preloading—an instantaneous positive or negative force—for $f_1(z) = \pm \gamma$ at $z = 0$. It is conceivable (but not likely) that these two conditions could exist simultaneously, as shown in Figure 10c. Dead space is usually caused by a fluid void or air bubble, while preloading is effected when the fluid is injected under pressure. Hence, the two conditions might exist if an air bubble was trapped under pressure within the casing. The computer model was adjusted to account for this effect.

Final Model and Supporting Rationale

All the mathematical forms mentioned in the previous subsection were tried. The least-squares method of system identification was used to find optimum values of k_1 , k_2 , c_1 , c_2 and c_3 . These constants, which constitute the unknowns in a set of simultaneous linear algebraic equations, are optimized using the techniques described in Appendix A. The constants α , β , γ , δ , and ϵ , which appear within the nonlinear expressions of z and \dot{z} , were independent values obtained from the experimental data, and were thus optimized by trial and error. Because the least-squares method yields an overall variance and a covariance matrix (see Appendix A), the Greek constants could be optimized quickly in several iterations by selecting values which would minimize the variance while permitting good conditioning of the covariance matrix. Good conditioning of the covariance matrix, in turn, implies that the form of the mathematical model was appropriate, since the nonlinear terms would be relatively independent of each other.

Analysis of the least-squares results yielded the following observations about the form of the mathematical model of the isolator:

1. Softening effects for both $f_1(z)$ and $f_2(\dot{z})$ were clear, so hyperbolic tangents were used as in Eqs. (8) and (9).

2. There appeared to be no constant friction force. Inclusion of coulomb friction for all velocities invariably increased the variance and decreased the conditioning of the covariance matrix. This result does not imply that friction was not present, but rather that it was most likely not independent of velocity. If friction depended on velocity, it would be accounted for in the hyperbolic tangent term of $f_2(\dot{z})$. It was finally decided to set $c_3 = 0$ to allow the $\tanh(\beta \dot{z})$ term to account for frictional effects other than static friction.

3. The combination of displacement dead space, and preloading (as shown in Fig. 10c) applied to both the linear and the hyperbolic tangent terms for $f_1(\dot{z})$, but only to the hyperbolic tangent term for $f_2(\dot{z})$. In other words, linear damping appeared active in the dead space, while the remaining terms provided no resistance to motion. Furthermore,

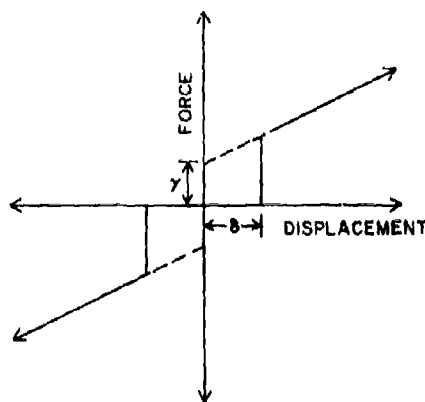
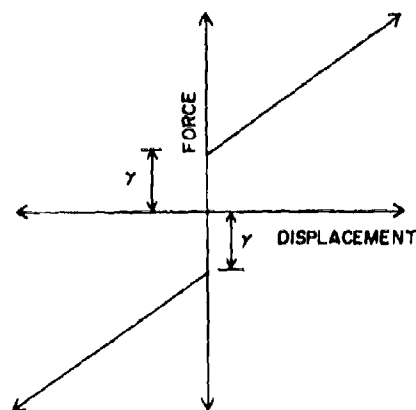
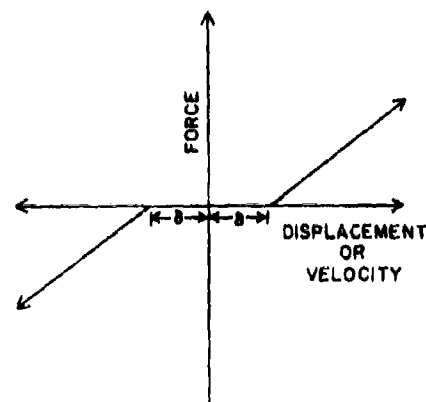


Fig. 10 — Dead space and preload effects on spring rate

the value of γ associated with preloading was found to be negligible—a result verified as likely by the manufacturer—for two reasons. First, the initial preloading fluid pressure provided by the manufacturer was relatively low. Second,

because the isolator had been operating for extended periods at high fluid temperatures, it had leaked some fluid. In either case, a void in the fluid chamber could be expected.

The observations led to a definition of the best mathematical model for the isolator in the form of Eq. (1) as

$$F(t) + k_1 z + k_2 \tanh(\alpha z) + c_1 \dot{z} + c_2 \tanh(\beta \dot{z}) = 0. \quad (\text{Eq. 10})$$

Equation (10) shows that

$$f_1(z) = k_1 z + k_2 \tanh(\alpha z) \quad (\text{Eq. 11})$$

$$f_2(\dot{z}) = c_1 \dot{z} + c_2 \tanh(\beta \dot{z}). \quad (\text{Eq. 12})$$

The results of applying Eq. (10) to the physical model for the test configuration (replacing $F(t)$ with $m\ddot{x}$) are presented in the following section. The actual table displacement was used as the base motion excitation for both models. Appendices A and B discuss techniques for treating the special effects of dead space and static friction.

4. RESULTS

Average Parameter Values

The coefficient parameters k_1 , k_2 , c_1 , and c_2 (with $c_3 = 0$) in Eq. (10) were calculated and optimized by the least-squares method. Nonlinear parameters (those denoted by lower-case Greek letters) could not be optimized in this manner. Although it would have been desirable to optimize the nonlinear parameters automatically, more programming time would have been needed, so these parameters were adjusted by trial and error, using the overall variance and the covariance matrix conditioning as indicators of improvement (see Appendix A). Solutions were always highly stable [6] in that small changes in constant parameters yielded small changes in response.

Table 1 gives the optimized constants for all three tests; averages are in the far right column of the table. The constants for tests A and B appear to agree fairly closely, although k_2 and c_2 for run C are somewhat high. Table 1 allows comparison of the experimental response variables of relative displacement and velocity and absolute mass acceleration, with the corresponding theoretical values of the same variables calculated using the average constants. Such a comparison should demonstrate the stability of the theoretical solution of the mathematical model.

The figures in Section 2 show the table motions, $u(t)$, for the three tests selected for analysis. Changes in the viscous properties for run C are explainable, given the sensitivity of liquid springs to changes in fluid temperature [6]. Test C was run after about ten previous tests in close succession, which raised the temperature of the fluid enough to render the isolator casing warm to the touch.

Comparison of Model Solutions With Experimental Data

A comparison of some preliminary model predictions with experimental data demonstrates that the least-squares

Table 1

Optimized Constants

Constant	Run A	Run B	Run C	Average
k_1 N/m	76 900	68 000	68 100	70 900
k_2 N	543	685	1 630	952
c_1 N/m/s	6 440	7 620	4 010	6 020
c_2 N	1 600	1 300	4 050	2 310
c_3 N	0	0	0	0
α 1/m	78.7	78.7	78.7	78.7
β s/m	78.7	78.7	78.7	78.7
γ N	0	0	0	0
δ cm	1.96	1.96	1.96	1.96
ϵ cm/s	1.52	1.52	1.52	1.52

technique can generate optimum constants for the mathematical model. Figures 11a, b, and c show the comparison of the variables (relative displacement and velocity and absolute mass acceleration) for test A, using the optimum constants generated for test A.

Agreement is sufficiently accurate in Figs. 11a, b, and c to conclude that the mathematical model depicts the behavior of the isolator for test A. The large oscillations in the acceleration trace of the real data in Fig. 11c are attributable to experimental noise, since the measured displacement trace is differentiated twice to obtain acceleration. The pulse at point A in Fig. 11c is the sudden actuation of the $\tanh(\beta\dot{z})$ term (nonlinear damping) in Eq. (10) when motion is somewhat mild and the relative displacement has exceeded the dead band. Only linear viscous forces have been observed to be active in the dead band, where $|z| \leq \delta$. The model would be more accurate if this pulse (point A) had occurred slightly earlier, to match the real data at about point B in the figure. Although no time was spent matching the slow motion of the isolator near the dead band with any greater accuracy, it should not be difficult to adjust the model for better agreement. For high-performance shock isolation, accurate prediction of terminal motion around the dead band is unnecessary.

In Table 1, the average values of the constants (the far right column of values) are somewhat different than the optimum values found for test A. In particular, k_2 is 75 percent higher, and c_2 is 45 percent higher. As previously discussed, the rather large changes in these constants are attributable to the weighting effect of those values optimal for test C for which the fluid temperature was elevated. Figs. 12a, b, and c show the effect of using the average constants, using test A again for the comparison. The effect is slightly less agreement than in the optimal plots for test A (Figs. 11a, b, and c). Thus, the theoretical solutions are stable.

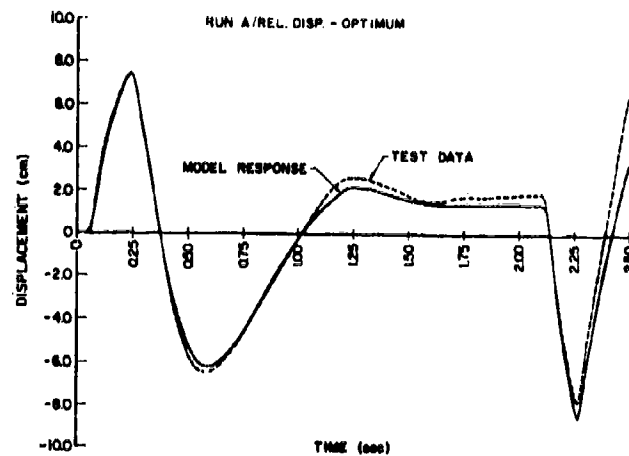
The significant conclusion from Figs. 11 and 12 is that the constant parameters do not have to be specified precisely in order to obtain reasonably accurate predictions of response-properties. This is a highly desirable result, since minor design-tolerance differences between nominally identical isolators in practical applications will cause the constants for optimal models to be slightly different. Therefore, average values for these constants should predict response properties that reasonably approximate actual response properties.

Figures 13a, b, and c compare the response variables for test B, using the average constants from Table 1. Figures 14a, b, and c show the same type of results for test C, again using the average constants instead of the optimal constants for that test.

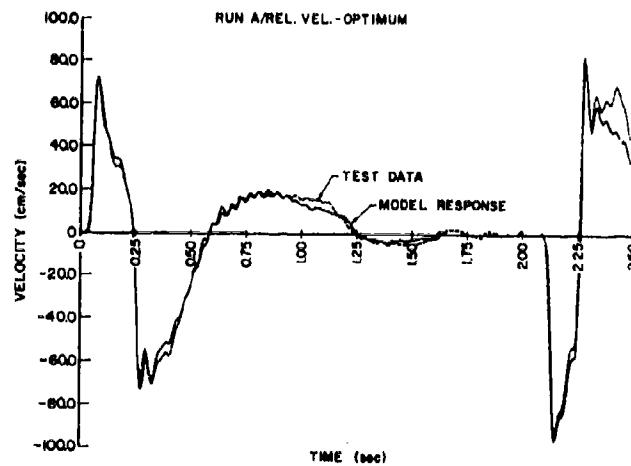
Finally, Figs. 15 and 16 show the nonlinear spring and damping curves calculated from Eqs. (11) and (12) for $f_1(z)$ and $f_2(\dot{z})$, using the averaged constants from Table 1. These figures will be discussed in detail separately to interpret the nonlinear properties and their effects on the form of Eq. (10).

The dynamic spring rate shown in Fig. 15 was found to be almost linear (i.e., it had a slight softening property) for values of $|z|$ greater than the dead band. The softening term $k_2 \tanh(\alpha z)$ was retained (even though the spring rate was nearly linear) because its presence yielded a smaller error variance than when (a) the linear term, $k_1 z$, alone was used, and (b) the superposition of a constant term (for example, k_0 , shown in Fig. 15) and a linear term was used, such as $k_0 \operatorname{sgn}(z) + k_1 z$. The value of k_0 was taken as the extended intercept of the elastic line to the force axis, and is analogous to a force which might be caused by preloading. However, it is not likely that preloading could exist if a bubble were present in the fluid, as evidenced by the existence of the dead band. Instead, it is theorized that the $k_2 \tanh(\alpha z)$ term served to shift the linear curve $k_1 z$ (shown by line OA in Fig. 15) upward and almost parallel to it by a force approximately equal to k_0 . In this case, large changes in α caused very little change in error variance, because the influence of α was almost eliminated by the existence of the dead band. The value of $\alpha = 78.7 \text{ m}^{-1}$ (2.0 in.^{-1}) was selected from trial and error more for convenience than as an optimal value, since it could have ranged from $39.3 \leq \alpha \leq 157.4$ ($1 \leq \alpha \leq 4$ in English units) without significantly changing the error variance.

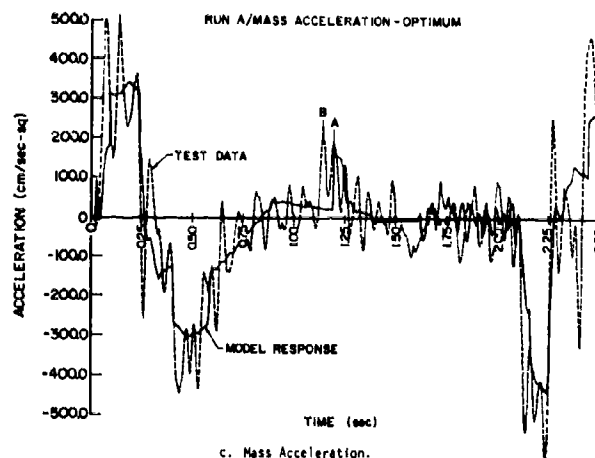
To some extent, the above comments are applicable in a similar manner to the viscous damping curve shown in Fig. 16. For example, this curve is nearly linear for $|\dot{z}| > 25 \text{ cm/s}$ (10 in./sec). The value of $\beta = 78.7 \text{ s/m}$ (2.0 sec/in.) is analogous to α , but in this case, the error variance was somewhat more sensitive to changes in β because of the requirement to fit the data in the velocity range below $|\dot{z}| = 25 \text{ cm/s}$ (10 in./sec). Again the hyperbolic tangent term yielded a smaller error variance than the superposition of a constant (c_0 in the figure) and a linear term, such as $c_0 \operatorname{sgn}(\dot{z}) + c_1 \dot{z}$. Here $c_0 \operatorname{sgn}(\dot{z})$ is identified as coulomb friction. It is recalled that the inclusion of a coulomb friction term with the linear and hyperbolic terms, as given in Eq. (9), yielded an increase in error variance. This was probably because the coulomb friction effect was largely accounted for in the hyperbolic tangent term, except in the range



a. Relative Displacement.

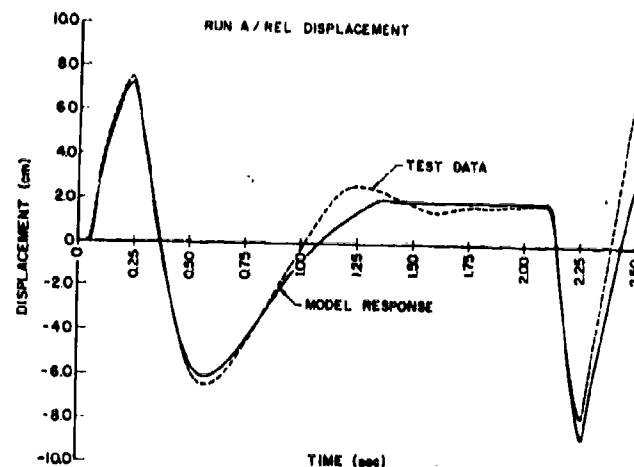


b. Relative Velocity.

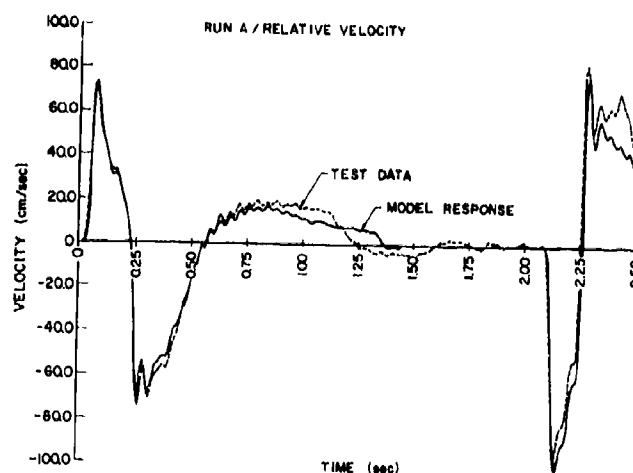


c. Mass Acceleration.

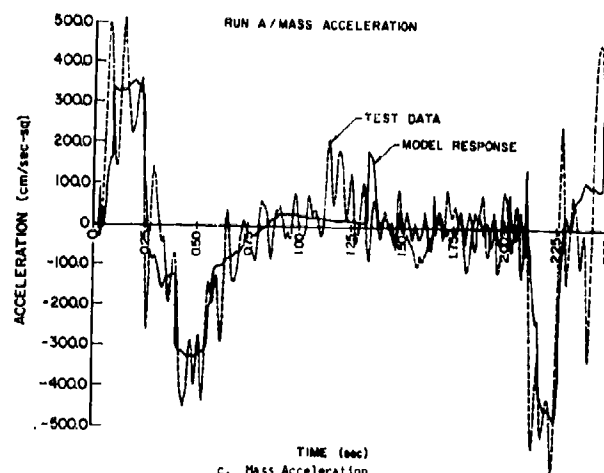
Fig. 11 — Run A—optimum constants



a. Relative Displacement.

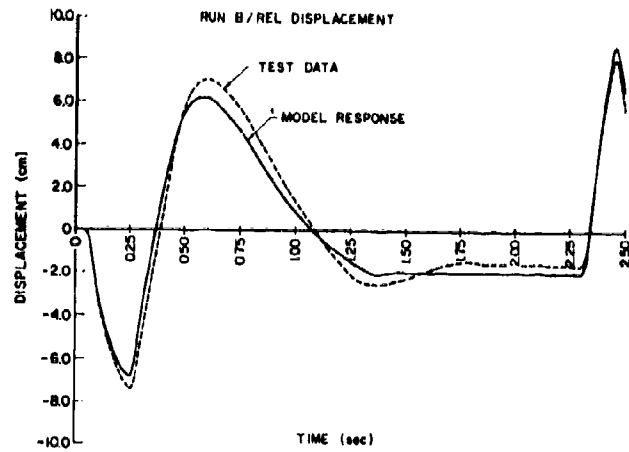


b. Relative Velocity.

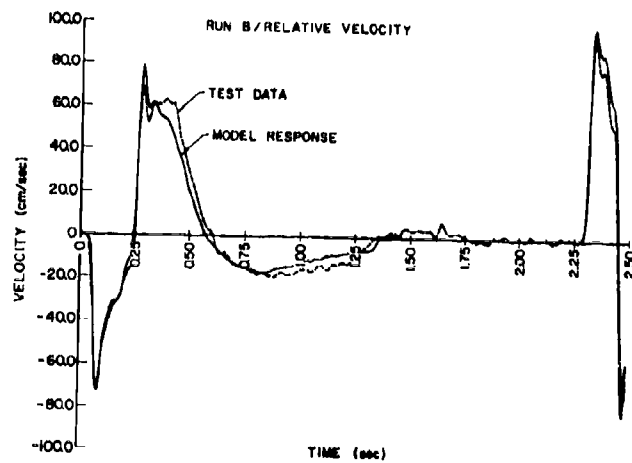


c. Mass Acceleration.

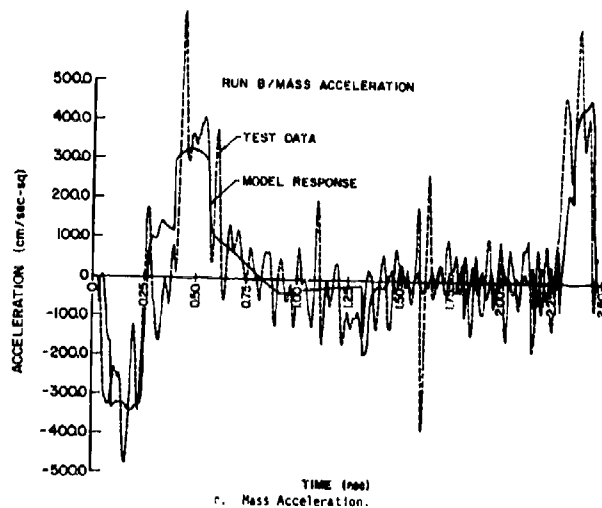
Fig. 12—Run A—averaged constants



a. Relative Displacement.



b. Relative Velocity.



c. Mass Acceleration.

Fig. 13 - Run B-averaged constants

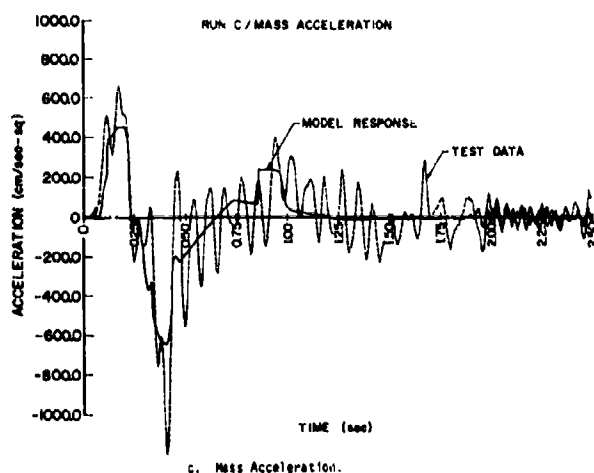
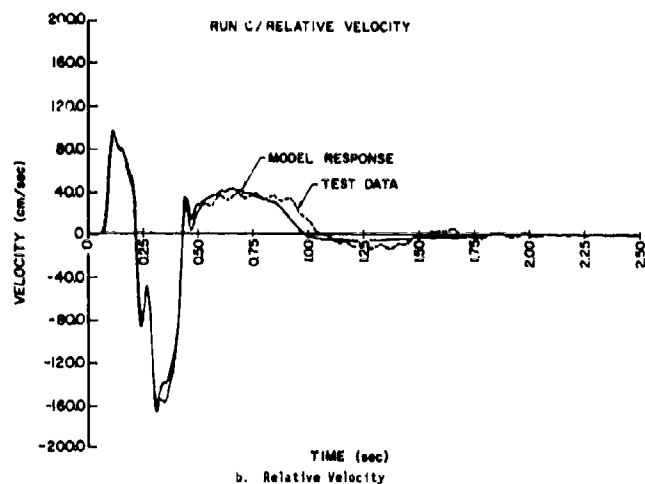
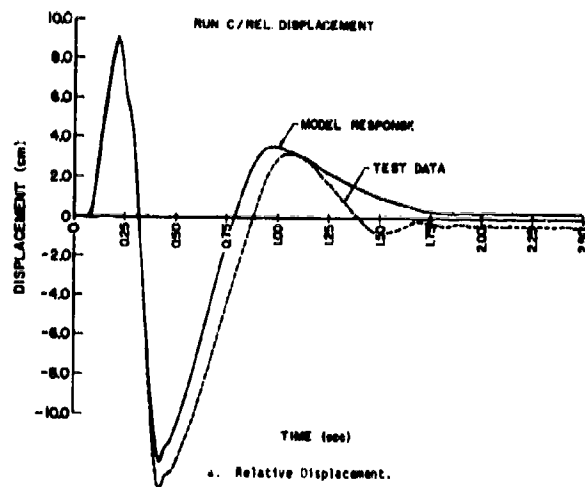


Fig. 14 - Run C-averaged constants

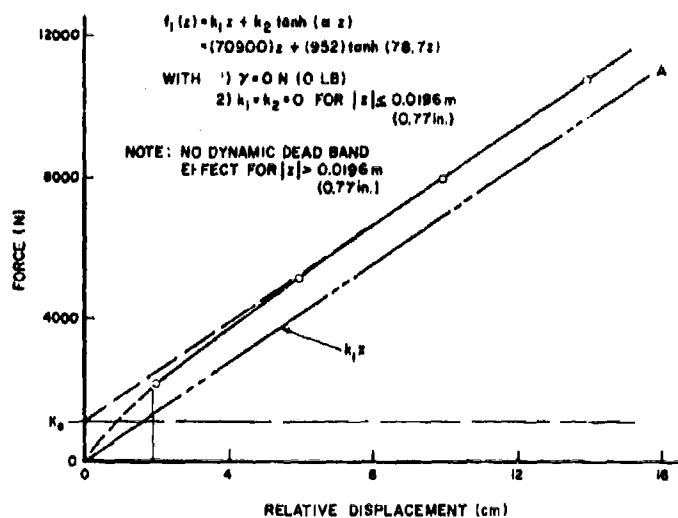


Fig. 15 — Dynamic spring rate

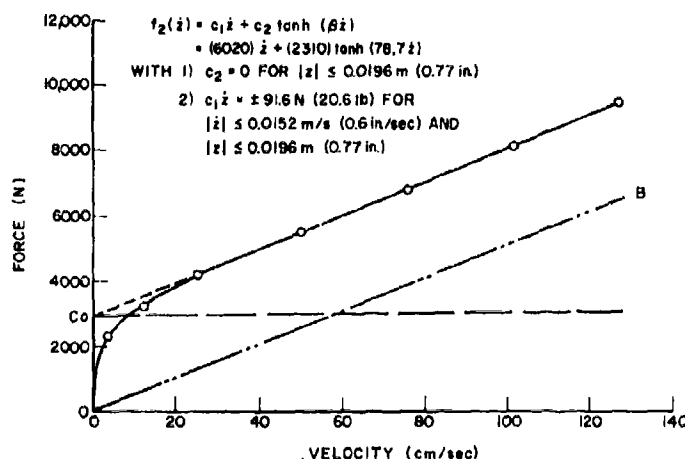


Fig. 16 — Viscous damping force vs. velocity

below $|\dot{z}| \sim 51$ cm/s (10 in./sec). Hence the two terms may not have been sufficiently independent. Nevertheless, the hyperbolic tangent term yielded the smallest error variance, and was therefore retained.

These results were obtained from only three tests, one of which was held with elevated fluid temperature. For the purposes of this work, establishing mathematical models for high-performance isolators from experimental data is considered feasible.

5. CONCLUSIONS

The lack of reasonably accurate open-parameter mathematical models of typical classes of isolators makes it

difficult to predict isolator performance. System-identification methods can produce mathematical models from experimental test data on individual isolators. The least-squares method of system identification was used to obtain a mathematical model of a liquid spring isolator, which was selected because it provides near-optimum performance for shock isolation.

Because preloading and dead-band properties affected peak response values, some time was devoted to modeling these effects accurately enough to duplicate large motions. The only significant forces opposing motion in the dead band were linear viscosity and static friction.

Equation 10 gives the open parameter mathematical model developed for the isolator. Table 1 gives the optimum

values of the parameters for each of the three tests, together with average values.

Agreement of the actual and computed responses (using the optimized constants for each test separately) ranged from very good to excellent. The two similar tests yielded similar parameters, with the largest single parameter difference being approximately 26 percent. Using the optimized parameters from one test to compute the response of the other caused the agreement to deteriorate slightly. The test held at elevated fluid temperature caused large changes in the optimized constants, although average constants from all three runs still yielded good agreement with the test results.

APPENDIX A

LEAST-SQUARES SOLUTION FOR COEFFICIENT PARAMETERS

In Eq. (10), the Arabic parameters (k_1 , k_2 , c_1 , and c_2) may be treated as the unknown quantities to be optimized using the least-squares method of system identification. Although other methods might prove more profitable, the least-squares method was basic and could be applied directly.

The constants denoted by lower-case Greek letters (α and β) appear in nonlinear factors that form the known coefficients (from experimental-response data) of the unknown constants to be optimized. The Greek constants modify the nonlinear form of the known values in the matrix of equations to be solved, and therefore they modify the form of the mathematical model. Thus the Greek constants had to be adjusted by trial and error in this work. The Arabic constants are the unknowns to be calculated.

The derivation for optimizing the Arabic constants by the least-squares method begins by rewriting Eq. (10) as

$$m\ddot{x}_i + z_{ij}k_j = 0, \quad (Eq. A1)$$

$$i = 1, 2, \dots, I; j = 1, 2, \dots, J$$

where standard summation notation is used. Subscript i denotes the i^{th} time step of the digitized experimental data, while subscript j indicates the term in the equation containing the j^{th} unknown constant. Total time steps I are considered, with J total unknown constants to be optimized. The j^{th} unknown constant is k_j . In any test configuration such as that described in Section 2, m denotes the mass to be isolated, and \ddot{x}_i is the acceleration of the mass with respect to coordinates fixed in space (that is, absolute acceleration, as opposed to acceleration relative to the table motion). The values of x_i ($i = 1, 2, \dots, I$) come from measured displacement data that have been differentiated twice, and that therefore contain some experimental noise. The z_{ij} values come from the nonlinear products of relative displacement, z , and relative velocity, \dot{z} . They also include the lower-case Greek constants as modifying factors, so to know the z_{ij} values, one must know the Greek constants formed from experimental data.

The major conclusion of the study was that a reasonably accurate mathematical model of an isolator can be found from a few simple tests, using system identification methods. Design features which affect maintenance (such as fluid leakage) can also be modeled. Substantial changes in optimized constants yielded small changes in computed response, indicating some degree of insensitivity to production hardware tolerances as well as mathematical stability of the model. The practical application of system identification methods in the design of shock isolation systems appears plausible. This approach could replace the in-place testing of entire isolation systems with simplified tests of single isolators, and therefore should be significantly more economical.

For simplicity and clarity, let

$$y_i = m\ddot{x}_i \quad (Eq. A2)$$

and

$$\xi_i = -z_{ij}k_j \quad (Eq. A3)$$

In the least-squares method, minimizing the squared difference, or error, between y_i and ξ_i for all i yields the optimum values of the k_j . Therefore, let

$$2S = \sum_{i=1}^I (y_i - \xi_i)^2 \quad (Eq. A4)$$

where S is a constant. Setting the partial derivative of Eq. (A4) with respect to each k_j equal to zero minimizes S with respect to each k_j and produces a system of J simultaneous linear algebraic equations of the form

$$\frac{\partial S}{\partial k_j} = \sum_{i=1}^I (y_i - \xi_i) \frac{\partial \xi_i}{\partial k_j} = 0 \quad (Eq. A5)$$

Substituting Eq. (A3) into Eq. (A5) gives

$$\sum_{i=1}^I (y_i + z_{ij}k_j)(z_{ij}) = 0 \quad (Eq. A6)$$

For matrix computational purposes, Eq. (A6) is rewritten as

$$\sum_{i=1}^I z_{ij}z_{ij}k_j = - \sum_{i=1}^I z_{ij}y_i \quad (Eq. A7)$$

where z_j is the transpose of z_{ij} . In matrix notation, Eq. (A7) is

$$[z^T][z]\{k\} = -[z^T]\{y\} \quad (Eq. A8)$$

where $[z]$ is a $J \times I$ rectangular matrix and $[z^T]$ is its transpose. Then $\{k\}$ is a $J \times 1$ column matrix of the unknown constants, and $\{y\}$ is an $I \times 1$ column matrix.

Now denoting

$$[A] = [z^T][z] \quad (Eq. A9)$$

as a $J \times J$ matrix of known values from experimental data, and

$$\{b\} = \{z^T\} \{y\} \quad (\text{Eq. A10})$$

as a $J \times 1$ column matrix of known values from the data, the final form of the matrix equation to be solved is

$$\{A\} \{k\} = \{b\} \quad (\text{Eq. A11})$$

Equation (A11) is a well-known problem in matrix algebra. A suitable subroutine for solving Equation A11 for the column of constants $\{k\}$ can be found in programming literature and need not be discussed here. Using such a subroutine, one can find the optimum Arabic constants for a given mathematical model of an isolator.

The overall variance and the covariance matrix are highly useful for analyzing goodness of fit of a model to data. The overall variance, σ^2 , is obtained by averaging the mean square error corrected for bias. The error, e_i , at each time step was used in Eq. (A4) and may be written in matrix form as

$$\{e\} = \{y\} - \{z\} \quad (\text{Eq. A12})$$

where all three terms are 1×1 column matrices. Averaging the squared errors for all i provides a biased estimate of the variance, $\bar{\sigma}^2$:

$$\bar{\sigma}^2 = \frac{1}{I} \langle e \rangle \langle e \rangle \quad (\text{Eq. A13})$$

where $\langle e \rangle$ is the transpose of e , or a $1 \times I$ row matrix. Reducing I by the number of unknown constants, J , to be estimated renders the variance unbiased (σ^2):

$$\sigma^2 = \frac{1}{I - J} \langle e \rangle \langle e \rangle \quad (\text{Eq. A14})$$

If N is much larger than J , the biasing influence will be negligible.

The covariance matrix, $\{V\}$, is $J \times J$ and indicates the accuracy and independence of the individual estimators (the unknown constants to be optimized). This matrix is calculated from the relation:

$$\{A\} \{V\} = \sigma^2 \{I\} \quad (\text{Eq. A15})$$

where all matrices are $J \times J$, and $\{I\}$ is unit diagonal. Here $\{A\}$, σ^2 , and $\{I\}$ are known quantities, and $\{V\}$ is the unknown matrix to be calculated. $\{V\}$ can be solved using the same subroutine as used for obtaining $\{k\}$ in Eq. (A11).

The numerical value of σ^2 and the conditioning of the $\{V\}$ matrix were continuously monitored through the trial-and-error process of varying the form of the mathematical model and the lower-case Greek constants. As the model's fit improves, the value of σ^2 decreases, and the principal diagonal elements of $\{V\}$ grow significantly larger than the off-diagonal elements. These changes indicate good conditioning and imply that the individual terms of the equation are independent.

Accounting for displacements, dead-band, and static-friction effects requires minor condition statements in the computer program. Usually relative motion was assumed (or forced) to be zero whenever $|z| < \delta$ and $|\dot{z}| < \epsilon$, but eliminating many of the points where the relative motion was zero produced a better-fitting curve. For example, in Fig. 14a, relative motion essentially ceased between 1.50 sec and 2.12 sec. If this portion of the test were included in the least-squares solution, a good fit in this region would be obtained at the expense of less accurate fits of the more significant portions of the curves. Since getting a good fit of the data for no relative motion was trivial, the majority of these points were eliminated.

Preloading was accounted for originally by adding the term $\gamma \text{sgn}(z)$ to Eq. (10). In this case, γ was a constant coefficient, so the least-squares analysis ought to optimize it automatically. The relatively small influence of this term in the $\{A\}$ matrix (for this particular isolator) caused poor conditioning of the corresponding diagonal element in the $\{V\}$ matrix. Therefore, the value of $\gamma = 0$ was verified by trial and error instead.

APPENDIX B

TIME DOMAIN SOLUTION OF THE DIFFERENTIAL EQUATION

Comparison of the analytical and experimental results made it necessary to superimpose the solution of the optimized differential equation on the real data, as done in Chapter 4. Since computer storage and speed of solution were not serious problems, a fourth-order Runge-Kutta algorithm [7] was used to solve the equation. This algorithm was selected for its simplicity and common usage.

In the least-squares solution for the optimized coefficients, the response behavior in the dead-band and static friction had to be accounted for by special programming. Both of these effects occur in regions of small relative displacement and low relative velocity, so they should be of trivial concern for high performance shock isolation systems

It became apparent, however, that distinct changes in the peak values of the response variables might be directly associated with changes in dead-band and static friction. The solutions remained stable, in that small changes to the dead-band or static friction parameters yielded small changes in peak values of the response variables. Since anything that affects the peak response values should interest designers of isolation systems, the dead-band and static friction modifications were retained as special properties in the Runge-Kutta solution.

In Eq. 10, both the linear and hyperbolic tangent terms ($k_1 + k_2 \tanh cz$) for spring forces and the hyperbolic tangent term ($c_2 \tanh cz$) for damping forces were inactive in

the dead band, where $|z| \leq \delta$. Hence linear viscosity ($c\dot{z}$) was the only dynamic force that opposed motion in this band.

Static friction effects were treated differently for initial and terminal motion. Relative motion did not begin until the magnitude of the force applied to the isolator (in this experiment, $F(t) = m\ddot{x}$ was the applied force) exceeded a small static force of $F(t) = 91.6 \text{ N}$ (20.6 lb). For terminal motion, when $|\dot{u}|$ decreased to zero, the motion of the mass was allowed to continue until $|\dot{z}|$ dropped below $\epsilon = 0.0152 \text{ m/s}$ (0.6 in./sec). The static friction force in each case was the same, and the average value of $c_1 = 6023 \text{ N/m/s}$ (34.4 lb/in./sec) from Table 1 was used.

Again, the only reason for considering dead-band and static friction effects was because of their noticeable influence on peak response motions. This study made no attempt to model the motion near the rest condition in the dead band with high accuracy. The intent was to model effective conditions for those properties that would yield consistent results and better accuracy for the peak values.

The average constants from Table 1 repeated below reflected the modifications made to the solution programming to account for displacement dead-band, static friction, and preloading effects.

$$k_1 \begin{cases} = 70900 \text{ N/m} & |z| > \delta \\ (405 \text{ lbs/in.}) & \\ = 0 & \text{for } |z| \leq \delta \end{cases}$$

$$k_2 \begin{cases} = 952 \text{ N} & \text{for } |z| > \delta \\ (214 \text{ lbs}) & \\ = 0 & \text{for } |z| \leq \delta \end{cases}$$

$$c_1 = 6023 \text{ N/m/s} \quad \text{for all } z \text{ and } \dot{z} \\ (34.4 \text{ lbs/in./sec})$$

$$c_2 \begin{cases} = 2313 \text{ N} & \text{for } |z| > \delta \\ (520 \text{ lbs}) & \\ = 0 & \text{for } |z| \leq \delta \end{cases}$$

$$\gamma = 0.0 \text{ N (preloading) (0.0 lb)}$$

$$\delta = 0.0196 \text{ m (0.77 in.) (displacement dead space)}$$

$$z = \dot{z} = 0 \text{ for } c_1 \dot{z} \leq 91.6 \text{ N (20.6 lb) (initial motion)} \\ \text{or } \dot{z} \leq 0.0152 \text{ m/s (0.6 in./sec) (terminal motion) (static friction)}$$

SYMBOLS

- a Constant
- b Substitution column vector
- c Constants, subscripted, for damping coefficients
- d Differential symbol
- f Nonlinear function, subscripted, for spring and damping effects

- i Summation index for time
- j Summation index for unknown parameters
- k Constants, subscripted, for spring coefficients; also used for general coefficients
- m Mass
- n Summation index for series expansion terms
- t Time
- u Table displacement (absolute)
- x Mass displacement (absolute)
- y Substitution variable
- z Relative displacement
- A Substitution matrix
- F Applied forces
- l Maximum number of digitized time points; also used for unit diagonal matrix
- J Maximum number of unknown parameters
- N Maximum number of series expansion terms
- S Constant
- T Transpose matrix symbol
- V Covariance matrix
- Z Known variable matrix

- α
 - β
 - γ
 - δ
 - ϵ
- } Known constants used in nonlinear factors

- ξ Substitution variable
- σ Standard deviation ($\sigma^2 = \text{variance}$)
- Σ Summation symbol
- ∂ Partial derivative symbol
- { } Rectangular matrix
- { } Column matrix
- $\langle \rangle$ Row matrix

REFERENCES

1. Cunningham, W. J., Introduction to Nonlinear Analysis (McGraw-Hill, 1958), p 76.
2. Timoshenko, S., D. H. Young, and W. Weaver, Vibration Problems in Engineering (John Wiley and Sons, 1974), pp 163, 167.
3. Crandall, S. H. and W. D. Mark, Random Vibration in Mechanical Systems (Academic Press, 1963), p 62.
4. Timoshenko, S., D. H. Young, and W. Weaver, Vibration Problems in Engineering (John Wiley and Sons, 1974), pp 163, 167.
5. Courant, R. and D. Hilbert, "Methods of Mathematical Physics," Vol II, Partial Differential Equations (John Wiley and Sons, 1962), p 227.
6. Crawford, R. E., C. J. Higgins, and E. H. Baltman, A Guide for the Design of Shock Isolation Systems for Ballistic Missile Defense Facilities, Technical Report S-23 (Construction Engineering Research Laboratory, 1973), p 247.
7. Carnahan, B., H. A. Luther, and J. O. Wilke, Applied Numerical Methods (John Wiley and Sons, 1969).

BIBLIOGRAPHY

Brandt, R. J., Considerations on the Selection of Shock Isolation Systems for the SAFEGUARD Program, Memorandum No. 6820-1186 (Aghabian-Jacobsen Associates, April 20, 1970).

Collins, J. D., et al., "Methods and Applications of System Identification in Shock and Vibration," System Identification of Vibrating Structures (American Society of Mechanical Engineers [ASME], 1972).

Crawford, R. E., et al., The Air Force Manual for Design and Analysis of Hardened Structures, AFWL-TR-74-102 (Air Force Weapons Laboratory, October 1974).

Harris, C. M., and C. E. Crede, Shock and Vibration Handbook, 3 Vols (McGraw-Hill, 1961).

Investigation of Optimum Passive Shock Isolation Systems, Technical Report No. AFWL-TR-72-148 (Air Force Weapons Laboratory, 1973), p 154.

Kendall, M. G. and A. Stuart, The Advanced Theory of Statistics, 3 Vols (Hafner Publishing Company, 1969).

Mood, A. M. and F. A. Graybill, Introduction to the Theory of Statistics (McGraw-Hill, 1968).

Pilkey, W. and B. Pilkey, Shock and Vibration Computer Programs—Reviews and Summaries (Naval Research Laboratory, 1975).

Safford, A. A. and R. E. Walker, Hardness Program Non-EMP In-Place Testing of Shock Isolation Systems for SAFEGUARD TSE Ground Facilities, R-7317-3757, Contract No. DACA 87-73-0035 (U.S. Army Corps of Engineers, 1975).

Sevin, E., et al., Computer-Aided Design of Optimum Shock Isolation Systems, Shock and Vibration Bulletin 39-4 (Naval Research Laboratory, 1969), pp 185-188.

Shock Isolation Design Manual, HNDSP-73-98-ED-R (USACE, August 1973).

Study of Shock Isolation for Hardened Structures, AD 639303, Contract No. DA-49-120-ENG-532 (Office of the Chief of Engineers, June 1966).

A GENERALIZED DERIVATIVE MODEL FOR AN ELASTOMER DAMPER

Ronald L. Bagley and Peter J. Torvik

Air Force Institute of Technology
Wright-Patterson AFB, Ohio

A generalized derivative (fractional order) is used to construct a dynamic stress-strain constitutive relation for the elastomer 3M-467. The desirable features of this constitutive relation are demonstrated and the constitutive relation is used to determine vibration time histories of a single degree of freedom oscillator having an elastomer damper.

NOMENCLATURE

- D : Energy dissipated in a unit volume of material undergoing uniform, sinusoidal strain
- D^z : The operator notation for a generalized derivative of fractional order z
- $F(\omega)$: The Fourier transform of the applied force
- G_0, G_j : Parameters in the generalized derivative constitutive relation
- k : stiffness
- k_0, k_j : Resulting stiffnesses from the generalized derivative constitutive relation
- L : The operator notation for a Laplace transform
- m : mass
- U : The maximum strain, energy stored in a unit volume of material undergoing uniform, sinusoidal strain
- $x(t), X(s)$: A displacement time history and its Laplace transform
- $x_I(t), X_I(s)$: The displacement time history for impulsive loading and its Laplace transform
- $X(\omega)$: The Fourier transform of a displacement time history
- z_j : A parameter of the generalized derivative constitutive relation
- $\epsilon(t)$: a strain history
- $\sigma(t)$: a stress history

INTRODUCTION

The damping and stiffness properties encountered in elastomers undergoing steady-state, sinusoidal motion are generally described by a complex modulus with real and imaginary parts that are functions of frequency and temperature [1]. For a given temperature a typical elastomer exhibits distinctly different damping and stiffness properties as the frequency of sinusoidal motion is varied, Fig. 1 [2]. At low frequencies (the rubbery region), an elastomer has relatively low and frequency independent stiffness, and has relatively small damping that increases with frequency. At high frequencies (the glassy region), an elastomer has relatively high stiffness that is again frequency independent and has relatively small damping that decreases as frequency increases. At intermediate frequencies (the transition region), the elastomer has stiffness that increases with frequency and has relatively high damping.

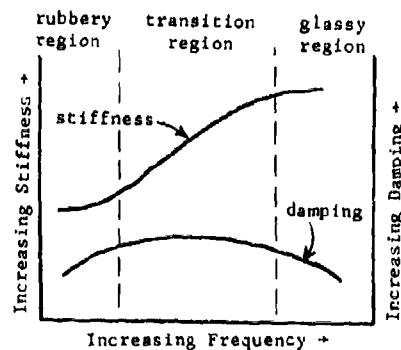


Fig. 1. Typical Elastomer Properties

The typical current practice is to incorporate the properties of an elastomeric material into the equation of motion in the complex frequency domain

$$m(i\omega)^2 X(\omega) + kX(\omega) = F(\omega) \quad (1)$$

by substituting for k the complex number that represents the material properties at ambient temperature and at the frequency of greatest interest, typically, a resonant frequency.

$$m(i\omega)^2 X(\omega) + (ik_1 \operatorname{sgn}(\omega) + k_0)X(\omega) = F(\omega) \quad (2)$$

$$\operatorname{sgn}(\omega) = +1, \quad \omega > 0 \quad (3)$$

$$\operatorname{sgn}(\omega) = -1, \quad \omega < 0 \quad (4)$$

This method of constructing the equation of motion is known as the "complex modulus method." Notice that the resulting equation of motion has exactly the same form as the equation for a single degree-of-freedom (DOF) oscillator with "structural damping" [3].

Unfortunately, this approach contains several inadequacies, from a mathematical point of view. The first of these is that the equation of motion has a non-causal response to impulsive loading, which erodes the credibility of any solution for a broad band input [4]. The second problem area arises if one attempts to express in the time domain the equation of motion having Eq. (2) as its transform [5].

$$m\ddot{x}(t) + [i\omega \frac{k_1}{\omega} \operatorname{sgn}(\omega) + k_0]x(t) = f(t) \quad (5)$$

The inverse Fourier transform of the Fourier transform of the above equation will, in general, not return the original equation. The equation mixes time and frequency parameters; hence, any solution obtained with integral transforms using frequency as a parameter has no precise mathematical meaning.

In spite of these mathematical weaknesses the complex modulus method yields acceptable results in some cases. The method predicts steady-state, sinusoidal responses that are in many cases in good agreement with experimental observations. In addition some transient responses can be closely approximated [6].

It cannot be denied that the complex modulus method is a valuable engineering tool; however, a mathematical model for elastomeric materials with frequency dependent stiffness and damping properties that is free of mathematical contradictions is desired. It is the objective of the authors to present such an entity; the generalized derivative model of an elastomer damper.

GENERALIZED DERIVATIVES AS CONSTITUTIVE RELATIONS

The generalized (or fractional) derivative is a linear operator that will be used to model

linear, frequency dependent damping and stiffness. The generalized derivative of real order z , $0 < z < 1$, of the function $c(t)$ is defined to be [7]

$$\frac{d^z c(t)}{dt^z} = D^z c(t) = \frac{1}{\Gamma(1-z)} \frac{d}{dt} \int_0^t \frac{c(t-\tau)}{\tau^z} d\tau \quad (6)$$

$$\Gamma(1-z) = \int_0^\infty e^{-x} x^{-z} dx \quad (7)$$

The utility of this definition becomes more apparent when one examines the Laplace transform of the generalized derivative.

$$\mathcal{L}\{D^z c(t)\} = s^z \mathcal{L}\{c(t)\} \quad (8)$$

$$\mathcal{L}\left\{\frac{dc(t)}{dt}\right\} = s \mathcal{L}\{c(t)\} - c(0) \quad (9)$$

Notice that the Laplace transform of a generalized derivative of order z yields a coefficient s^z instead of the s that results when the Laplace transform of the first derivative is taken.

Generalized derivatives have been used by Caputo to model frequency dependent damping observed in geological strata. Caputo was successful in obtaining approximate solutions to the equations of motion for an infinite, viscoelastic layer with uniform, prescribed motion on one surface [8]. Caputo has also solved a modified one-dimensional, viscoelastic wave equation for unbounded regions where dissipation was modeled with generalized derivatives [9]. In addition, Caputo investigated the nature of hysteresis resulting from a sawtooth strain history in a material where the damping and stiffness were modeled with a generalized derivative [10].

Caputo chose to use a slightly different definition for the generalized derivative.

$$\frac{d^z c(t)}{dt^z} = \frac{1}{\Gamma(1-z)} \int_0^t \frac{dc(\tau)}{d\tau} \frac{1}{(t-\tau)^z} d\tau \quad (10)$$

This definition, Eq. (10), and the definition stated earlier, Eq. (6), are equivalent if $c(0) = 0$. The following investigations deal with mechanical systems excited from a state of rest. Hence, the assumption that $c(0) = 0$ will be made in all cases.

Caputo suggested a general constitutive relation for one dimensional deformation, of the form

$$\sigma(t) = \mu c(t) + \frac{n}{\Gamma(1-z)} \int_0^t \frac{d^n c(\tau)}{d\tau^n} \frac{1}{(t-\tau)^z} d\tau \quad (11)$$

$$0 < z < 1 \quad n = 1, 2, 3, \dots$$

Here $\sigma(t)$ is the stress, $c(t)$ is the strain and μ and n are parameters describing the material.

For n equal 2 and greater this constitutive relation models material properties that are strongly frequency dependent, $O(\omega^{1/2})$ and higher. Such a strong frequency dependence is not characteristic of the elastomer of interest here, thus a constitutive relation corresponding to a much weaker frequency dependence is adopted, using a superposition of generalized derivatives of the type presented in Eq. (6).

$$\sigma(t) = G_0 \epsilon(t) + \sum_{j=1}^J \frac{G_j}{\Gamma(1-z_j)} \frac{d}{dt} \int_0^t \frac{\epsilon(t-\tau)}{\tau^{z_j}} d\tau, \quad (12)$$

$$0 < z_j < 1$$

or

$$\sigma(t) = G_0 \epsilon(t) + \sum_{j=1}^J G_j D^{z_j} \{\epsilon(t)\} \quad (13)$$

This constitutive relation will be used to model the behavior of an elastomer undergoing shear strain in the rubbery region and into the transition region, and will hereafter be referred to as the RT model.

Before introducing the RT model into the equation of motion of a single degree of freedom oscillator with elastomeric damping, the hysteresis behavior of the RT model will be examined. To accomplish this, a sinusoidal strain history, $\epsilon(t)$, starting at $t = 0$, will be assumed and $\sigma(t)$, the resulting stress history, is calculated. First it must be shown that the RT model produces a hysteresis loop, and second it must be demonstrated that the stress required to attain this hysteresis loop, starting from rest, is physically realizable. The first requirement on $\sigma(t)$ is assumed to be met if $\sigma(t)$ becomes sinusoidal in the limit as t becomes very large. The second requirement on $\sigma(t)$ will be assumed to be satisfied if it can be shown that the stress history is a bounded, continuous function of time.

We begin by letting

$$\epsilon(t) = \epsilon_0 \sin \omega_0 t, \quad t \geq 0; \quad (14)$$

$$\epsilon(t) = 0, \quad t < 0$$

$$\sigma(t) = G_0 \epsilon_0 \sin \omega_0 t + \sum_{j=1}^J \frac{G_j \epsilon_0}{\Gamma(1-z_j)} \frac{d}{dt} \int_0^t \frac{\sin \omega_0(t-\tau)}{\tau^{z_j}} d\tau \quad (15)$$

and note that

$$\frac{1}{\Gamma(1-z_j)} \frac{d}{dt} \int_0^t \frac{\sin \omega_0(t-\tau)}{\tau^{z_j}} d\tau$$

$$= \frac{\omega_0}{\Gamma(1-z_j)} \int_0^t \frac{\cos \omega_0(t-\tau)}{\tau^{z_j}} d\tau \quad (16)$$

and

$$\cos \omega_0(t-\tau) = \cos \omega_0 t \cos \omega_0 \tau + \sin \omega_0 t \sin \omega_0 \tau \quad (17)$$

Then

$$\lim_{t \rightarrow \infty} D^{z_j} \{\epsilon_0 \sin \omega_0 t\} = \frac{\omega_0 \cos \omega_0 t}{\Gamma(1-z_j)} \int_0^\infty \frac{\cos \omega_0 \tau}{\tau^{z_j}} d\tau + \frac{\omega_0 \sin \omega_0 t}{\Gamma(1-z_j)} \int_0^\infty \frac{\sin \omega_0 \tau}{\tau^{z_j}} d\tau. \quad (18)$$

The two integrals in Eq. (18) are in fact the Fourier cosine and sine transformations of τ^{-z_j} . Evaluating these integrals and supplying some trigonometric manipulation yields

$$\lim_{t \rightarrow \infty} D^{z_j} \{\epsilon_0 \sin \omega_0 t\} = \omega_0^{z_j} \epsilon_0 \sin(\omega_0 t + \frac{z_j \pi}{2}). \quad (19)$$

Thus, in the limit as t becomes large, we have

$$\lim_{t \rightarrow \infty} \sigma(t) = G_0 \epsilon_0 \sin \omega_0 t + \sum_{j=1}^J G_j \omega_0^{z_j} \epsilon_0 \sin(\omega_0 t + \frac{z_j \pi}{2}). \quad (20)$$

Since the superposition of any number of out of phase sine waves can be expressed as a single sine wave, the existence of a hysteresis loop is established, and that loop is elliptical. For positive G_j and z_j , the stress does lead the strain, as one would expect.

To demonstrate that $\sigma(t)$ is a continuous function, Laplace transforms are used. Taking the Laplace transform of Eq. (15) produces

$$\mathcal{L}\{\sigma(t)\} = \frac{G_0 \epsilon_0 \omega_0}{s^2 + \omega_0^2} + \sum_{j=1}^J \frac{G_j \epsilon_0 \omega_0 s^{z_j}}{s^2 + \omega_0^2}. \quad (21)$$

Using a theorem (stated in full in Appendix A) that deals with existence of the inverse Laplace transform, one can show that the inverse transform, $\sigma(t)$, exists and that $\sigma(t)$ is a continuous function for all time and that $\sigma(t) = 0$, $t \leq 0$. Since we have already indicated that $\sigma(t)$ is sinusoidal for t large, and we now know that $\sigma(t)$ is continuous and $\sigma(t) = 0$, $t \leq 0$, it may be concluded that $\sigma(t)$ is bounded for all time.

Several parameters useful in the evaluation of the damping, or energy dissipation, may be computed. The total energy dissipated by a unit volume of material undergoing a homogeneous strain given by Eq. (14) is

$$D = \int_0^{2\pi/\omega_0} \sigma d\epsilon = \int_0^{2\pi/\omega_0} \sigma \epsilon' dt \quad (22)$$

Substitution of Eq. (14) and (20) yields

$$D = \pi \epsilon_0^2 \sum_{j=1}^J G_j \omega_0^{z_j} \sin \frac{z_j \pi}{2} \quad (23)$$

The maximum energy stored at any point in the cycle is

$$U = \int_{\epsilon=0}^{\epsilon=\epsilon_0 \cos \frac{z_1 \pi}{2}} \sigma_1(\epsilon) d\epsilon \quad (24)$$

where $\sigma_1(\epsilon)$ is the portion of the total stress given by Eq. (20) which is in phase with the strain. For $\epsilon = \epsilon_0 \sin \omega_0 t$,

$$U = (G_0 + \sum_{j=1}^J G_j \omega_0^{z_j} \cos \frac{z_j \pi}{2}) \frac{\epsilon_0^2}{2} \quad (25)$$

Finally, the loss factor, η , can be computed by dividing the energy dissipation per unit volume by the peak energy stored per unit volume, and introducing the customary factor of 2π .

$$\eta = \frac{D}{2\pi U} = \left(\sum_{j=1}^J G_j \omega_0^{z_j} \sin \frac{z_j \pi}{2} \right) \cdot (G_0 + \sum_{j=1}^J G_j \omega_0^{z_j} \cos \frac{z_j \pi}{2})^{-1} \quad (26)$$

We note that the energy dissipated, the energy stored, and the loss factor all display a frequency dependence. For a material which can be modeled by a single term, i.e.,

$$\sigma(t) = G_1 \frac{d}{dt} \frac{z_1}{z_1} \epsilon(t), \quad (27)$$

the loss factor is seen to be

$$\eta = \tan \pi z_1 / 2, \quad (28)$$

which is independent of frequency, as was noted by Caputo [11].

THE RT MODEL AND DAMPING

The RT model will now be used to construct the force-displacement relation of a spring mass system containing an elastomer damper, where the elastomer experiences a one-dimensional shear strain, Fig. 2. The force-displacement relation for the elastomer damper takes the form

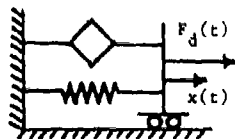


Fig. 2. A Damper Employing an Elastomer Undergoing Pure Shear Strain

$$F_d(t) = k_0 x(t) + \sum_{j=1}^J k_j D^{z_j} \{x(t)\}. \quad (29)$$

Using this damper to dampen the motion of single DOF oscillator with external force $f(t)$ produces the equation of motion

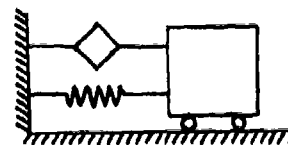


Fig. 3. A Single DOF Oscillator Using an Elastomer Damper

$$m\ddot{x}(t) + \sum_{j=1}^J k_j D^{z_j} \{x(t)\} + kx(t) = f(t) \quad (30)$$

for the system shown in Fig. 3 where

$$k = k_0 + K \quad (31)$$

The solution to the equation of motion for the damped oscillator is dependent on the particular choices of J and z_j . For the purpose of demonstrating that a solution to the equation of motion can be obtained, and in order to investigate the properties of such a solution, we will consider a particular case* $J = 1$, and $z_1 = \frac{1}{2}$, or

$$m\ddot{x}(t) + k_1 D^{\frac{1}{2}} \{x(t)\} + kx(t) = f(t) \quad (32)$$

We apply the method of Laplace transforms to determine the response $x_1(t)$, to an impulsive loading, $f(t) = \delta(t)$. Taking

$$x(0^-) = \dot{x}(0^-) = 0 \quad (33)$$

we find

$$X_1(s) = (ms^2 + k_1 s^{\frac{1}{2}} + k)^{-1} \quad (34)$$

where [12]

$$x_1(t) = \mathcal{L}^{-1}\{X_1(s)\} = ce^{i\omega_1 t} + \bar{c}e^{-i\omega_1 t} + \frac{1}{\pi} \int_0^\infty \frac{e^{-rt} k_1 \sqrt{r}}{(mr^2 + k)^2 + k_1^2 r} dr. \quad (35)$$

Since $i\omega_1$ is complex with a negative real part, the first two terms in the solution are exponentially decaying sinusoids. For t large the integral in the solution takes the form [13]

*The solution technique for the more general case, Eq. (30), is demonstrated in Appendix A.

$$t \gg M, \quad \int_0^\infty \frac{e^{-rt} k_1 \sqrt{r}}{(mr^2 + k)^2 + k_1^2 r} dr \quad (36)$$

$$\approx \int_0^\infty \frac{e^{-rt} k_1 \sqrt{r}}{k^2} dr.$$

$$\int_0^\infty \frac{e^{-rt} k_1 \sqrt{r}}{k^2} dr = \frac{k_1}{k^2} \frac{\Gamma(3/2)}{t^{3/2}} \quad (37)$$

Since the integral decays as $t^{-3/2}$ for large t and the other terms in the solution decay exponentially, the integral dominates the impulse response for large t [14].

$$t \gg M, \quad x_1(t) \sim t^{-3/2} \quad (38)$$

Although not readily apparent, $x_1(t)$ is a continuous, real function where $x_1(t) = 0$ for $t < 0^*$.

It has already been shown that sinusoidal strain in the RT model produces sinusoidal stress. It remains to be shown that a sinusoidal force acting on the system in Fig. 3 produces sinusoidal displacements after transients have died out. To obtain the displacement time history of the elastomer damped oscillator for sinusoidal loading applied at $t = 0$, one can convolve the forcing function with the impulse response given by Eq. (35).

$$x(t) = \int_0^t f(t-\tau) x_1(\tau) d\tau \quad (39)$$

$$x_s(t) = \int_0^t f_0 \sin \omega_0(t-\tau) x_1(\tau) d\tau \quad (40)$$

Performing the integration in Eq. (40) and retaining only those terms in the solution, $x_s(t)$, which do not go to zero as t becomes large yields

$$t \gg M, \quad x_s(t) \approx \text{Re} \left(\frac{ce^{i\omega_0 t} f_0}{(\omega_1 - \omega_0)} \right) + \text{Re} \left(\frac{-ce^{i\omega_0 t} f_0}{(\omega_1 + \omega_0)} \right) \quad (41)$$

$$+ \text{Re} \left(\frac{e^{-i\omega_0 t} f_0}{\pi i} \int_0^\infty \frac{k_1 r^{1/2}}{[(mr^2 + k)^2 + k_1^2 r](r + i\omega_0)} dr \right)$$

For t large, i.e., after the transients have died out, a sinusoidal load is seen to produce a sinusoidal response in the structure. This prediction is, of course, essential if the RT model is to be used to describe real materials since sinusoidal loadings in experiments conducted to determine the material properties lead to an observed sinusoidal response.

*These properties of $x_1(t)$ are proven in Appendix A.

We have now demonstrated that the RT model leads to predictions which are correct in several respects. The response is causal, a sinusoidal input leads to a sinusoidal response, and the stiffness (or modulus) and damping are frequency dependent. It remains to be demonstrated that the frequency dependence is characteristic of materials of interest.

THE RT MODEL FOR 3M-467

The data given in Fig. 4 are the observed properties [15] of 3M-467 [16]. The material properties are those for 23.9°C, however, not all of the data given was measured at 23.9°C. Experimental measurements of the properties of 3M-467 were performed at numerous frequencies between 320 Hz and 6100 Hz and at temperatures ranging from -31.6°C to 93.3°C. It was then assumed that 3M-467 was a "thermo-rheologically simple" material and the "temperature-frequency equivalence" principle was invoked to reduce the data to the single temperature of 23.9°C. The resulting range of equivalent frequencies was from 10^0 Hz to 10^5 Hz [17].

The data from the first three decades, 10^0 Hz to 10^3 Hz, were used to construct a three parameter model for 3M-467 in the upper part of the rubbery region and the lower part of the transition region. Let

$$\sigma(t) = 2(G_0 + G_1 D^{z_1}) \epsilon(t) \quad (42)$$

The values of the parameters, G_0 , G_1 , and z_1 , were determined by choosing initial values to match asymptotes and slopes and then making iterative changes to parameters until an acceptable fit was obtained. The final values for the material parameters describing 3M-467 were found to be

$$G_0 = 5.5 \times 10^4 \text{ Newtons/(meter)}^2 \quad (43)$$

$$G_1 = 4.1 \times 10^4 \text{ Newtons-(sec)}^{.56}/(\text{meter})^2 \quad (44)$$

$$z_1 = .56 \quad (45)$$

For a sinusoid strain history

$$\epsilon(t) = \epsilon_0 e^{i\omega t} \quad (46)$$

the stress time history at large time takes the form

$$\sigma(t) = G^* \epsilon_0 e^{i\omega t} \quad (47)$$

where

$$G^* = G_0 + G_1 (i\omega)^{z_1} \quad (48)$$

The frequency dependent shear modulus, G , is the real part of the frequency dependent complex modulus, G^* , or

$$G = \text{Re} \{ (5.5 \times 10^4) + (4.1 \times 10^4) (i\omega)^{.56} \} \quad (49)$$

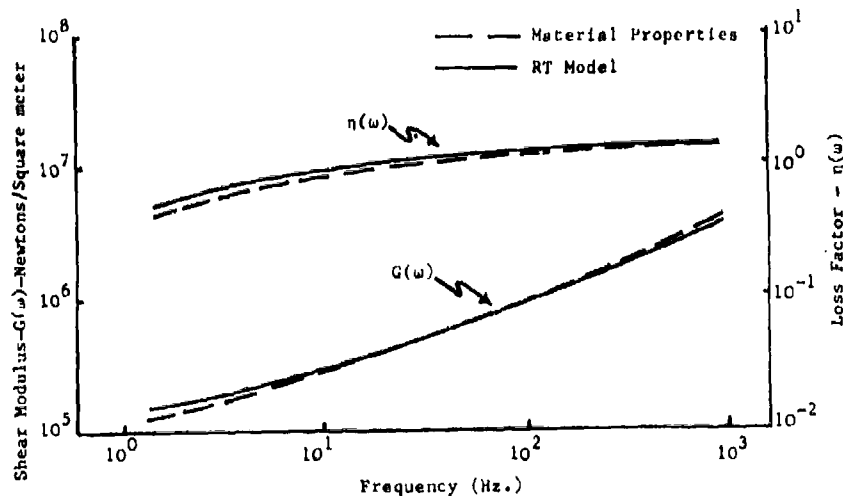


Fig. 4. Material Properties of 3M467 at 23.9°C
(USAF Materials Lab Test - December 77)
With Generalized Derivative Model
Superimposed

The loss factor, η , is calculated by dividing the real part of the modulus into the imaginary part of the modulus, or

$$\eta = \frac{\text{Im}(G_1(i\omega)^{z_1})}{\text{Re}(G_0 + G_1(i\omega)^{z_1})} \quad (50)$$

The same result is found using Eq. (26). The predicted frequency dependent modulus, and frequency dependent damping, (solid lines) are compared to the initial data in Fig. 4. The agreement is seen to be acceptable, both qualitatively and quantitatively.

The generalized derivative model for 3M-467 uses frequency independent parameters, G_0 , G_1 , and z_1 , determined from data taken in the time domain, to correctly model the frequency dependence of the shear modulus, G_1 , and loss factor, η , over three decades of frequency. Since the frequency dependence of G and η is correctly modeled, the generalized derivative model can be employed to determine the response of 3M-467 under broad-band loading and response.

If the properties of 3M-467 were modeled by a single frequency independent complex number as is the case for "structural damping" or the "complex modulus method," the observed frequency dependence of the shear modulus, G , and loss factor, η , would not be well modeled. While the loss factor of 3M-467 is seen to be quite insensitive to frequency, as in the complex modulus method, the significant frequency dependence of the modulus is not well modeled.

A standard linear viscoelastic model

$$\sigma(t) = 2G'\epsilon(t) + 2G''\dot{\epsilon}(t) \quad (51)$$

is even less successful in approximating the properties of 3M-467. The linear viscoelastic model predicts a frequency independent modulus,

$$G = G' \quad (52)$$

rather than the observed frequency dependent modulus, and predicts a loss factor proportional to frequency,

$$\eta = \frac{\omega G''}{G'} \quad (53)$$

rather than the (essentially) frequency independent loss factor which was observed.

CONCLUSIONS

The generalized derivative is a linear operator that has been shown to be capable of modelling the frequency dependent stiffness and damping properties in the rubbery region and into the transition region of 3M-467. In addition, the generalized derivative was found to lead to an appropriate stress-strain law or constitutive relation in that the stress time history is well behaved (continuous and bounded) for sinusoidal strain. In addition the stress time response to an induced sinusoidal strain was found to become sinusoidal for large times.

When the model is used to portray an elastomer damper in a single DOF oscillator, a sinusoidal loading was shown to produce (at large time) a sinusoidal time history. Moreover, the impulse response of the elastomer damper was

shown to be causal, as is necessary if responses to arbitrary loadings are to be computed. In this respect, the generalized derivative leads to models of elastomer responses which are superior to "structural damping" models for which impulse response is non-causal. The essential mathematical feature of the generalized derivative model is that it is a time domain model which properly predicts a frequency dependence, rather than a model which mixes time and the frequency parameter, as do the "structural damping model" or the "complex modulus method."

In summary, the generalized derivative model describes the linear, frequency dependent stiffness and damping of 3M-467. When used to model the motion of a single DOF oscillator with elastomeric damping, the mathematical inadequacies of the "structural damping" model or the "complex modulus method" are avoided.

APPENDIX A

In this section, we present the method used to obtain the response, $x_1(t)$, to an impulse loading. The Laplace transform of Eq. (30) for impulse loading is

$$ms^2 X_1(s) + \sum_{j=1}^J k_j s^{z_j} X_1(s) + k X_1(s) = 1 \quad (A-1)$$

Let

$$d(s) = \sum_{j=1}^J k_j s^{z_j} \quad (A-2)$$

(z_j are assumed rational)

Then the Laplace transform of the impulse response is

$$X_1(s) = (ms^2 + d(s) + k)^{-1} \quad (A-3)$$

At this point we wish to establish the existence and the properties of the inverse Laplace transform of $X_1(s)$. To this end we quote a theorem on the inverse Laplace transform [18].

"Let F be [a Laplace transform and] any function of the complex variable s that is analytic and order s^{-k} for all s ($s = x + iy$) over a half plane $x \geq \alpha$, where $k > 1$; also let $F(x)$ be real when $x > \alpha$. Then for all real t the [inverse transform is] a real-valued function, f, \dots Furthermore $f(t)$ is a continuous function of exponential order and $f(t) = 0$ when $t \leq 0$."

$X_1(s)$ is a Laplace transform that is a function of the complex variable s ($s = x + iy$). The term $d(s)$ in $X_1(s)$ contains functions s^{z_j} , $0 < z_j < 1$, that are analytic everywhere except along branch cuts, which are chosen by conven-

tion to lie on the negative real axis of the s plane. Thus, the functions, s^{z_j} , are analytic in the half plane defined by $x > 0$ and $X_1(s)$ is analytic for $x > 0$. Since $X_1(s)$ is also real for real and positive s , one can conclude that $X_1(s)$ satisfies the conditions stipulated in the above theorem. As a result, the impulse response $x_1(t)$ is a continuous function of exponential order and $x_1(t) = 0$ for $t \leq 0$. Consequently, $x_1(t)$ is causal.

Contour integration is employed to evaluate the inverse Laplace transform

$$x_1(t) = \frac{1}{2\pi i} \int_{\gamma-i\infty}^{\gamma+i\infty} \frac{e^{st}}{ms^2 + d(s) + k} ds \quad (A-4)$$

The inversion integral is evaluated by using the "residue theorem" [19] and the integration contour given in Fig. 5.

Fig. 5. Integration Contour to Evaluate the Inverse Transform of the Impulse Response

$$\oint_c g(s) ds = 2\pi i \sum_n B_n \quad (A-5)$$

B_n are the residues of the poles of $g(s)$ enclosed by the closed contour, c . The contour c is comprised of six segments.

$$\oint_c g(s) ds = \sum_{k=1}^6 \int_k g(s) ds \quad (A-6)$$

The integral along contour 1 becomes the inversion integral as $R \rightarrow \infty$ and can be expressed as

$$\begin{aligned} x_1(t) &= \lim_{R \rightarrow \infty} \frac{1}{2\pi i} \int_1 g(s) ds \\ &= - \lim_{R \rightarrow \infty} \frac{1}{2\pi i} \sum_{k=2}^6 \int_k g(s) ds + \sum_n B_n \end{aligned} \quad (A-7)$$

where

$$g(s) = e^{st} X_1(s) = (ms^2 + d(s) + k)^{-1} e^{st} \quad (A-8)$$

To determine the inverse, we must evaluate the integrals along contours 2 through 6 and the residues B_n .

The residues are generated by two poles of the transform at $s = i\omega_1$ and $s = -i\omega_1$. The locations of these poles, $i\omega_1$ and $-i\omega_1$, are solutions of the equation

$$ms^2 + d(s) + k = 0. \quad (A-9)$$

where $d(s)$ is evaluated by using the principal branch of $s^{1/2}$. The residues of the poles are evaluated using the limiting process

$$B_1 = \lim_{s \rightarrow i\omega_1} (s - i\omega_1)(s^2 m + d(s) + k)^{-1} e^{st} \quad (A-10)$$

$$= c e^{i\omega_1 t}$$

Similarly

$$B_2 = \lim_{s \rightarrow -i\omega_1} (s + i\omega_1)(s^2 m + d(s) + k)^{-1} e^{st} \quad (A-11)$$

$$= \bar{c} e^{-i\omega_1 t}.$$

Contribution from the segment of the contour labeled "2" may be shown to go to zero in the limit as $R \rightarrow \infty$.

$$\int_2 g(s) ds = \int_{-\pi}^{\pi} \frac{\exp[R(\cos\theta + i\sin\theta)t] Re^{i\theta} i d\theta}{[R^2 e^{i2\theta} m + d(Re^{i\theta}) + k]} \quad (A-12)$$

$$s = Re^{i\theta} = R(\cos\theta + i\sin\theta) \quad (A-13)$$

$$\left| \int_2 g(s) ds \right| \leq \int_{-\pi}^{\pi} \left| \frac{\exp[R(\cos\theta + i\sin\theta)t] Re^{i\theta} i d\theta}{[R^2 e^{i2\theta} m + d(Re^{i\theta}) + k]} \right| d\theta$$

$$\leq \int_{-\pi}^{\pi} \frac{e^{Yt} R}{R^2 m - (|d(Re^{i\theta})| + k)} d\theta \quad (A-14)$$

$$\text{for } R > R^* \text{ where}$$

$$R^{*2} m - (|d(R^* e^{i\theta})| + k) = 0$$

$$\leq \frac{e^{Yt} R}{R^2 m - (|d(Re^{i\theta})| + k)} (\pi - \alpha)$$

$$\lim_{R \rightarrow \infty} \frac{e^{Yt} R}{R^2 m - (|d(Re^{i\theta})| + k)} (\pi - \alpha) = 0 \quad (A-15)$$

$$\lim_{R \rightarrow \infty} \int_{-\pi}^{\pi} \frac{\exp[R(\cos\theta + i\sin\theta)t] Re^{i\theta} i d\theta}{[R^2 e^{i2\theta} m + d(Re^{i\theta}) + k]} d\theta = 0 + i0 \quad (A-16)$$

Similarly, the integral along contour 6 can be shown to be zero.

The contribution from the contour labeled 4 can be shown to be zero, in the limit as $\rho \rightarrow 0$.

$$\int_4 g(s) ds = \int_{-\pi}^{\pi} \frac{\exp[\rho(\cos\theta + i\sin\theta)t] \rho e^{i\theta} i d\theta}{[\rho^2 e^{i2\theta} m + d(\rho e^{i\theta}) + k]} \quad (A-17)$$

$$s = \rho e^{i\theta} = \rho(\cos\theta + i\sin\theta) \quad (A-18)$$

$$\left| \int_4 g(s) ds \right| \leq \int_{-\pi}^{\pi} \left| \frac{\exp[\rho(\cos\theta + i\sin\theta)t] \rho e^{i\theta} i d\theta}{[\rho^2 e^{i2\theta} m + d(\rho e^{i\theta}) + k]} \right| d\theta$$

$$\leq \int_{-\pi}^{\pi} \left| \frac{\exp[\rho(\cos\theta + i\sin\theta)t] \rho e^{i\theta} i d\theta}{[\rho^2 e^{i2\theta} m + d(\rho e^{i\theta}) + k]} \right| d\theta$$

$$\leq \int_{-\pi}^{\pi} \frac{e^{\rho \cos\theta t}}{k - (|d(\rho e^{i\theta})| + \rho^2 m)} d\theta; \quad (A-19)$$

$$\text{for } \rho < \rho^* \text{ where}$$

$$k - (|d(\rho^* e^{i\theta})| + \rho^{*2} m) = 0$$

$$\leq \frac{e^{\rho t 2\pi}}{k - (|d(\rho e^{i\theta})| + \rho^2 m)}$$

$$\lim_{\rho \rightarrow 0} \frac{e^{\rho t 2\pi}}{k - (|d(\rho e^{i\theta})| + \rho^2 m)} = 0 \quad (A-20)$$

$$\lim_{\rho \rightarrow 0} \int_{-\pi}^{\pi} \frac{\exp[\rho(\cos\theta + i\sin\theta)t] \rho e^{i\theta} i d\theta}{[\rho^2 e^{i2\theta} m + d(\rho e^{i\theta}) + k]} d\theta = 0 + i0 \quad (A-21)$$

Hence, the contribution of the integration on contour 4 is zero.

The evaluation of the contribution from segments labeled 3 and 5 are given below. On contour 3, $s = re^{i\pi}$ and on contour 5, $s = re^{-i\pi}$. Thus

$$\int_3 g(s) ds + \int_5 g(s) ds \quad (A-22)$$

$$= - \int_0^{\infty} \frac{e^{-rt}}{mr^2 + d(re^{i\pi}) + k} dr$$

$$- \int_0^{\infty} \frac{e^{-rt}}{mr^2 + d(re^{-i\pi}) + k} dr$$

It should be noted that

$$d(re^{i\pi}) \neq d(re^{-i\pi}) \quad (A-23)$$

but rather, that

$$d(re^{i\pi}) = \overline{d(re^{-i\pi})} \quad (A-24)$$

and the sum of the two integrals will not vanish.

Combining the contribution from the

residues with that from the last pair of contours, the impulse response can be expressed as

$$x_1(t) = \frac{1}{2\pi i} \int_0^{\infty} e^{-rt} \frac{1}{mr^2 + d(re^{-i\pi}) + k} dr \quad (A-25)$$

$$+ \frac{1}{mr^2 + d(re^{i\pi}) + k} dr$$

$$+ \frac{i\omega_1 t}{ce} + \frac{\overline{i\omega_1 t}}{ce}$$

This integral may be evaluated for any operator $d(s)$ of the form given earlier. From this, convolution may be used to determine the response of the single degree of freedom system to any broad-band excitation for which a Laplace transform may be evaluated.

REFERENCES

1. Lazan, B. J., Damping of Materials and Members in Structural Mechanics, Pergamon Press, London, p. 54, 1968.
2. Ref. 1, p. 49.
3. Hurty, W. C., Rubinstein, M. F., Dynamics of Structures, Prentice-Hall, Englewood Cliffs, New Jersey, p. 257, 1964.
4. Crandall, S. H., "Dynamic Response of Systems with Structural Damping," Air, Space, and Instruments, Draper Anniversary Volume, ed. H.S. Lees, McGraw-Hill, pp. 183-193, 1963.
5. Crandall, S. H., "The Role of Damping in Vibratory Theory," J. Sound and Vibration, Vol. 11, pp. 3-18, 1970.
6. Milne, R. D., "A Constructive Theory of Linear Damping," Proceedings of Symposium on Structural Dynamics, 23-25 March 1970, Loughborough University of Technology, Loughborough, England.
7. Ross, B., "A Brief History and Exposition of the Fundamental Theory of Fraction Calculus," Lecture Notes in Mathematics, Vol. 457, Springer-Verlag, Heidelberg, FRG, p. 18, 1974.
8. Caputo, M., "Vibrations of an Infinite Viscoelastic Layer With a Dissipative Memory," J. Acoustical Society of America, Vol. 56, No. 3, pp. 897-904, 1974.
9. Caputo, M., Elasticita e Dissipazione, Zanichelli, Bologna, pp. 51-55, 1969.
10. Caputo, M., "Vibrations of an Infinite Plate with a Frequency Independent Q ," J. Acoustical Society of America, Vol. 60, No. 3, pp. 636-638, 1976.
11. Ref. 10, p. 634-639.
12. Ref. 9, p. 54-55.
13. Erdelyi, A., Asymptotic Expansions, Dover Publications, New York, pp. 29-33, 1956.
14. Ref. 9, p. 55.
15. 3M-467 Material properties provided by USAF Materials Laboratory.
16. 3M-467 is produced by Minnesota Mining and Manufacturing, Minneapolis, Minnesota.
17. Jones, D. I. G., "Temperature-Frequency Dependence of Dynamic Properties of Damping Materials," J. of Sound and Vibration, 33(4), pp. 451-470, 1974.
18. Churchill, R. V., Operational Mathematics, 3 ed., McGraw-Hill, New York, N.Y., p. 195, 1970.
19. Churchill, R. V., Complex Variables and Applications, 3 ed., McGraw-Hill, New York, N.Y., p. 172, 1973.

SHOCK RESPONSE OF NON-LINEAR SYSTEMS

Kalman Peleg, Associate Professor
School of Packaging, Michigan State University
East Lansing, Michigan
on leave of absence from
Technion Israel Institute of Technology

The response of many practical systems to shock excitation resulting from a drop on a hard surface can not be predicted adequately by simple linear elasticity and damping models. A more realistic model consisting of a mass between two preloaded non-linear (cubic elasticity) springs and restrained by a Coulomb and viscous damper is proposed. An approximate quasi-harmonic solution of the non-linear differential equation of motion of the model whereby both amplitude and phase are time dependent, enables a study of the motion during the first half cycle (pulse) after collision. Formulae are developed for calculating peak acceleration, rise time, pulse duration and maximum deflection. These are compared with corresponding formulae of special cases for which exact solutions are known. Acceleration versus time pulses are classified in accordance to pulse shape, e.g. sawtooth, halfsine and trapezoidal, as a function of system damping. Although the model is intended mainly for quantitative design in packaging engineering problems it is suitable for studying general shock isolation problems as well.

INTRODUCTION

The response of many practical systems to shock excitation resulting from a drop on a relatively hard surface (substrate) cannot be predicted adequately by simple linear elasticity and damping models. Mindlin [1] investigated extensively the response of undamped spring mass systems with different elasticity functions to shocks resulting from free fall drops. He also investigated the response of a Kelvin model (viscously damped linear spring mass system) to drop shocks. Comparing the shock acceleration time pulses of an undamped linear mass spring system to the pulse of a Kelvin model, Mindlin found that the addition of viscous damping changes the undamped sinusoid of the simple linear spring mass system into a damped sinusoid with shorter pulse duration time and increased initial phase. Mustin [2] describes a procedure for calculating the peak acceleration and maximum strain of a cushioned item resulting from a free fall drop for different cushion elasticity functions in terms of a "Cushion Factor" due to Jansen [3]. This cushion factor is a ratio of the peak stress developed in the cushion to the energy stored per unit volume of the cushion. Practical application of this procedure requires the ability to measure the instantaneous energy stored in the cushion which is not an easy task.

It is well known that damage sensitivity (fragility) of many products is a function of peak acceleration, duration and shape of the first (first half cycle) acceleration time pulse from the instant of contact with the substrate [4,5]. The influence of preloading [6] the system is, however, less recognized. The popularity of linear elasticity and viscous damping models is due to the simplicity of the mathematics required for solving the equations of motion of such models. Unfortunately, many practical products exhibit non-linear elasticity as well as combined viscous and dry friction (Coulomb) damping characteristics. The application of linear models in such cases may lead to significant discrepancies between the model and reality. In this article we shall endeavor to analyze a preloaded single degree of freedom system with non-linear elasticity and combined Coulomb and viscous damping. In particular, we shall develop formulae for calculating peak acceleration, pulse duration, and maximum deflection of such systems resulting from a free fall and impact with a hard substrate. The system to be considered is schematically illustrated in Fig. 1. The mechanical model consists of a mass M contained in an infinitely rigid frame and restrained by two massless non-linear ("hardening") springs, a dashpot and a dry friction damper. Shock excitation is achieved by

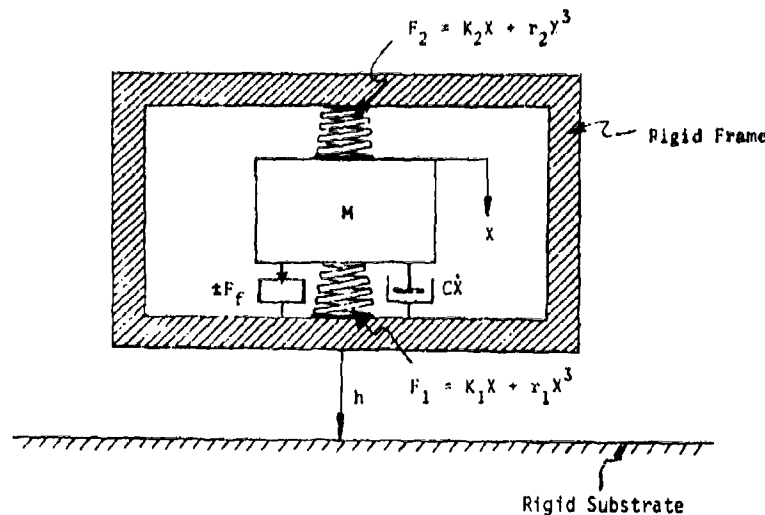


Fig. 1 - Mechanical model of a preloaded single degree of freedom system with cubic elasticity and combined Coulomb and viscous damping.

letting the rigid frame free fall through a distance h whereby it hits the substrate in a perfectly flat drop.

The main practical applications of the model are intended for packaging engineering design problems. However, the model is general enough for other applications as well. In packaging problems the model may represent a cushioned item in a rigid container or a dropped pallet-load of shipping containers. The lower spring would represent the lower cushion or the most heavily loaded containers in the bottom of the stack, the mass represents the dead weight of the stack of containers on top of the bottom containers or the cushioned item, while the upper spring represents strapping forces and elasticity of the upper containers in the stack or an upper cushion on top of the cushioned item. The dashpot and friction damper represent the combined energy dissipation capabilities of the system. For the force deflection characteristics of the springs we choose cubic elasticity of the form:

$$F = K_0 X + r X^3, \quad (1)$$

where K_0 represents the initial spring rate,

$\frac{dF}{dX}$ when $X = 0$ and r is the hardening spring

coefficient. It can be shown that no generality is lost by such a choice since by proper choice of K_0 and r it is possible to obtain an adequate fit to most practical force deflection curves. It can also be shown that the combined

initial spring rate and hardening coefficients of the system are equal to the sums of the respective values of the two springs:

$K_0 = K_1 + K_2$ and $r = r_1 + r_2$ provided that both springs are never unstressed. Thus, the influence of preloading is imbedded in the parameters K_0 and the system may be analyzed as a single degree of freedom system.

EQUATION OF MOTION

Suppose that now the rigid frame is dropped from a height h , free falls and hits the (substrate) in a perfectly flat drop. We want to examine the response of the system from the instant of contact with the substrate onwards. As long as the frame remains in contact with the substrate, i.e. there is no rebound, we have the following equation of motion for the relative motion of the mass M with respect to the frame:

$$M\ddot{X} + K_0 X + r X^3 + C\dot{X} + F_f \operatorname{sgn}(\dot{X}) = 0. \quad (2)$$

The conventional single and double dot notation will be used for the first and second time derivatives of the relative displacement of the mass M with respect to the frame. The other symbols are described in the notation list. There is no exact analytical solution for equation (2); however, an approximate solution can be obtained by using the "Linearization Principle" due to N. Kryloff and N. Bogoliuboff [7] whereby a quasi-harmonic solution of the

form $X = A \cos(\omega_0 t + \psi)$ satisfies equation (2) to within accuracy of r^2 . Thus, for small values of r , the approximate solution is very near the exact solution, while the results for relatively large values of r^2 are well within the accuracy required for engineering problems. The quasi-harmonic motion is periodic, but unlike in true harmonic motion, both the amplitude A and phase ψ are functions of time rather than constants. The Kryloff-Bogoliuboff method of linearization consists essentially of transforming a non-linear equation of the form:

$$M\ddot{X} + K_0 X + r f(X, \dot{X}) = 0 \quad (3)$$

into an equivalent linear equation (4):

$$M\ddot{X} + \lambda \dot{X} + KX = 0 \quad (4)$$

where $f(X, \dot{X})$ must be an odd function and the parameters λ and K are defined by equation (5) and (6) as:

$$\lambda = \frac{-r}{\pi A \omega_0} \int_0^{2\pi} f(A \cos \phi, -A \omega_0 \sin \phi) \sin \phi d\phi \quad (5)$$

$$K = K_0 + \frac{r}{\pi A} \int_0^{2\pi} f(A \cos \phi, -A \omega_0 \sin \phi) \cos \phi d\phi \quad (6)$$

Here ϕ is a dummy variable of integration. The quasi-harmonic solution then takes the form:

$$X = A \cos(\omega_c t + \psi) = A \cos \psi \quad (7)$$

where:

$$\frac{dA}{dt} = -\frac{\lambda A}{2M} \quad (8)$$

$$\frac{d\psi}{dt} = \omega = \sqrt{\frac{K}{M}} \quad (9)$$

It can be seen from equations (8) and (9) that both the amplitude A and frequency of oscillation ω are functions of time. In our case, we have, from equation (2):

$$f(X, \dot{X}) = X^3 + \frac{C}{r} \dot{X} + \frac{F_f}{r} \operatorname{sgn}(\dot{X}). \quad (10)$$

Inserting equation (10) into the integrals in equations (5) and (6) and performing the integration we have:

$$\lambda = \frac{-r}{\pi A \omega_0} \int_0^{2\pi} \left(A^3 \cos^3 \phi \sin \phi - \frac{CA \omega_0}{r} \sin^2 \phi + \frac{F_f}{r} \operatorname{sgn}(\dot{X}) \sin \phi \right) d\phi = C + \frac{4F_f}{\pi A \omega_0} \quad (11)$$

$$K = K_0 + \frac{r}{\pi A} \int_0^{2\pi} \left(A^3 \cos^4 \phi - \frac{CA \omega_0}{r} \sin \phi \cos \phi + \frac{F_f}{r} \operatorname{sgn}(\dot{X}) \cos \phi \right) d\phi = K_0 + \frac{3}{4} r A^2 \quad (12)$$

By introducing the notations (13) through (18) we can write equations (7), (8), (9), (11) and (12) in a dimensionless form to enhance the analysis of the system.

$$\Delta = A/X_b \quad (13)$$

$$\mu = r X_b^2 / K_0 \quad (14)$$

$$D = C / 2M \omega_0 \quad (15)$$

$$\alpha = F_f / K_0 X_b \quad (16)$$

$$\eta = \omega / \omega_0 \quad (17)$$

$$\epsilon = X / X_b \quad (18)$$

Here X_b is the maximal permissible relative displacement of the mass M with respect to the frame, say bottoming deflection of a cushion or a container deflection causing unacceptable damage to the product inside. Equations (7), (8), (9), (11) and (12) are then respectively:

$$\epsilon = \Delta \cos \psi \quad (19)$$

$$\frac{d\Delta}{dt} = -\omega_0 \left(D\Delta + \frac{2\alpha}{\pi} \right) \quad (20)$$

$$\frac{d\psi}{dt} = \omega = \sqrt{\frac{K_0}{M} \left(1 + \frac{3}{4} \mu \Delta^2 \right)} \quad (21)$$

$$\lambda = \omega_0 M \left(2D + \frac{4\alpha}{\pi \Delta} \right) \quad (22)$$

$$K = K_0 \left(1 + \frac{3}{4} \mu \Delta^2 \right) \quad (23)$$

The parameter λ may be considered as the energy dissipation coefficient of the system while K is the equivalent spring constant in the linearized system. The dimensionless frequency ratio η is readily derived from equation (21):

$$\eta = \frac{\omega}{\omega_0} = \sqrt{1 + \frac{3}{4} \mu \Delta^2} \quad (24)$$

Equation (20) may be rewritten:

$$\int dt = -\frac{1}{\omega_0} \int \frac{d\Delta}{D\Delta + \frac{2\alpha}{\pi}} \quad (25)$$

Performing the integration we have:

$$t = -\frac{1}{D\omega_0} \ln \left(D\Delta + \frac{2\alpha}{\pi} \right) + C_1 \quad (26)$$

Denoting the undamped amplitude ratio (when $t = 0$) by Δ_0 , we find the constant of

integration C_1 :

$$C_1 = \frac{1}{D\omega_0} \ln(D\Delta_0 + \frac{2\alpha}{\pi}) . \quad (27)$$

After some algebraic manipulations, equations (26) and (27) lead to:

$$\Delta = \Delta_0 e^{-D\omega_0 t} - \frac{2\alpha}{\pi D} (1 - e^{-D\omega_0 t}) . \quad (28)$$

Equation (28) indicates an exponential reduction of the undamped amplitude Δ_0 as a function of time t , viscous damping ratio D and natural initial frequency ω_0 of an equivalent simple spring mass system with spring ratio K_0 . The damped amplitude Δ is further reduced by the Coulomb friction parameter α . Note that when $\alpha = 0$, equation (28) is reduced to the familiar expression for the logarithmic decrement of a Kelvin model (viscously damped linear spring). To find the initial undamped amplitude ratio Δ_0 , we take the first time derivative of equation (7) to obtain the velocity \dot{x} :

$$\dot{x} = \frac{dA}{dt} \cos \psi - A \frac{d\psi}{dt} \sin \psi . \quad (29)$$

At the instant of collision with the substrate, after the free fall from a height h , we have:

$$t = X = 0, \psi = \theta = \frac{\pi}{2}, A = A_0, \dot{x}_0 = \sqrt{2gh}.$$

Inserting these initial values in equation (29) and making use of equation (21), we obtain:

$$\sqrt{2gh} = -A_0 \omega_0 \sqrt{1 + \frac{3}{4} \mu \Delta_0^2} . \quad (30)$$

This may be transformed into a dimensionless form by dividing both sides of (30) by x_b :

$$E_s^2 = \Delta_0^2 (1 + \frac{3}{4} \mu \Delta_0^2) . \quad (31)$$

Now E_s is a dimensionless shock excitation parameter defined as:

$$E_s = \frac{\sqrt{2gh}}{x_b \omega_0} \quad (32)$$

Solving the quartic equation (31) for Δ_0 , we obtain the expression for the undamped dimensionless amplitude ratio:

$$\Delta_0 = \sqrt{\frac{2}{3\mu} [\sqrt{1 + 3\mu E_s^2} - 1]} . \quad (33)$$

Notice that Δ_0 in equation (33) is undefined at $\mu = 0$, however, it can be seen from equation (31) that in the linear case we have the

familiar expression

$$\Delta_0 = E_s, \text{ or } A_0 = \sqrt{2Wh/K_0}.$$

SOLUTION OF THE LINEARIZED SYSTEM

The displacement, velocity and acceleration solutions of the linearized system represented by equation (4) with the initial conditions, $t = 0, X = 0, \dot{X} = \sqrt{2gh}$ considering λ and K as constants, are well known from elementary shock and vibration theory, namely:

$$X = \frac{\sqrt{2gh}}{\omega \sqrt{1 - \beta^2}} e^{-\beta \omega t} \sin(\sqrt{1 - \beta^2} \omega t) \quad (34)$$

$$\dot{X} = \frac{\sqrt{2gh}}{\sqrt{1 - \beta^2}} e^{-\beta \omega t} \cos(\sqrt{1 - \beta^2} \omega t + \delta) \quad (35)$$

$$\ddot{X} = \frac{\omega \sqrt{2gh}}{\sqrt{1 - \beta^2}} e^{-\beta \omega t} \cos(\sqrt{1 - \beta^2} \omega t + \gamma) \quad (36)$$

Here β is the combined viscous and Coulomb damping ratio (equation (37)) while δ and γ are the phase angles of the velocity and acceleration (equations (38) and (39)).

$$\beta = \frac{\lambda}{2M\omega} = \frac{D + \frac{2\alpha}{\pi\lambda}}{\sqrt{1 + \frac{3}{4}\mu\Delta^2}} = (D + \frac{2\alpha}{\pi\lambda}) \frac{1}{\eta} \quad (37)$$

$$\tan \delta = \frac{-\beta}{\sqrt{1 - \beta^2}} \quad (38)$$

$$\tan \gamma = \frac{2\beta^2 - 1}{2\beta \sqrt{1 - \beta^2}} \quad (39)$$

Using the definitions of equations (18), (24), (32) and (33), we can rewrite equations (34) and (36) in the nondimensional form:

$$\epsilon = \frac{\Delta_0}{\sqrt{1 - \beta^2}} e^{-\beta \eta \omega_0 t} \sin(\eta \sqrt{1 - \beta^2} \omega_0 t) \quad (40)$$

$$\ddot{\epsilon} = \frac{\eta^2 \omega_0^2 \Delta_0 e^{-\beta \eta \omega_0 t}}{\sqrt{1 - \beta^2}} \cos(\eta \sqrt{1 - \beta^2} \omega_0 t + \gamma) \quad (41)$$

Here, ω_0 and Δ_0 are independent of time and given by $\omega_0 = \sqrt{\frac{K_0}{M}}$ and equation (33) respectively, while η and β are time dependent

quantities given by equations (24), (28) and (37) respectively for any time t . For heavily damped systems, the motion is non-oscillatory and the maximum value of $\dot{\epsilon}$ occurs at $t = 0$ decaying with time to zero. The value of this initial relative acceleration $\ddot{\epsilon}_0$ is obtained by setting $t = 0$ in equation (41):

$$\ddot{\epsilon}_0 = \frac{\eta_0^2 \omega_0^2 \Delta_0}{\sqrt{1 - \beta^2}} \cos y = 2\beta E_s \omega_0^2 \eta_0 \quad (42)$$

$$= 2E_s \omega_0^2 (D + \frac{2\alpha}{\pi \Delta_0}) .$$

In lightly damped systems the motion is oscillatory and the maximum values of relative accelerations $\ddot{\epsilon}_m$ occur at times greater than zero. These times may be found by setting $\dot{\epsilon} = 0$ as well as the third time derivative $\ddot{\epsilon}' = 0$, respectively. These rise times, t_{m1} , for maximum displacement and t_{m2} , for maximum acceleration, are given by:

$$tg(\eta_{m1} \sqrt{1 - \beta_{m1}^2} \omega_0 t_{m1}) = \frac{\sqrt{1 - \beta_{m1}^2}}{\beta_{m1}} \quad (43)$$

$$tg(\eta_{m2} \sqrt{1 - \beta_{m2}^2} \omega_0 t_{m2}) = \frac{(1 - 4\beta_{m2}^2) \sqrt{1 - \beta_{m2}^2}}{\beta_{m2}(3 - 4\beta_{m2}^2)} \quad (44)$$

These times, together with their corresponding values of Δ_m , η_m and β_m , must simultaneously satisfy equations (24), (28) and (37) as well as (43) or (44). Thus, we have in each case four simultaneous independent equations and four unknowns t_m , Δ_m , η_m and β_m , which may be found by simultaneous solving equations (24), (28), and (37) with (43) or (44) as may be the case.

For computerized calculations, a solution of any desired accuracy is possible by an iterative process of successive approximations with the initial value of

$\omega_0 t = \frac{\pi}{2}$. The maximum values of the relative displacement, ϵ_m , and relative acceleration are then given by equations (45) and (46) respectively:

$$\epsilon_m = \Delta_0 e^{-\beta_{m1} \eta_{m1} \omega_0 t_{m1}} \quad (45)$$

$$\ddot{\epsilon}_m = \eta_{m2}^2 \omega_0^2 \Delta_0 e^{-\beta_{m2} \eta_{m2} \omega_0 t_{m2}} \quad (46)$$

An alternative method is to assume that during the first half cycle $\Delta = \Delta_m = \Delta$, $\eta = \eta_m = \eta_0$, $\beta = \beta_{m1} = \beta_0$, remain constant. Substitution of

these values in equations (37) through (41) and (43) through (46) enables straight-forward calculations, albeit of somewhat lesser accuracy.

COMPARISON OF RESULTS WITH EXACT SOLUTIONS FOR SPECIAL CASES

Mindlin [1] obtained exact solutions for the following special cases:

- Undamped linear spring ($D = \alpha = \mu = 0$)
- Kelvin model ($\mu = \alpha \neq 0$)
- Linear spring with Coulomb damping ($\mu = D \neq 0$)
- Undamped spring with cubic elasticity ($D = \alpha \neq 0$)

For the assessment of the viability of our approximate solution, in the general case, when $D \neq 0$, $\alpha \neq 0$ and $\mu \neq 0$, we shall compare our results of maximum displacement and acceleration for the above four special cases, with the exact solutions of Mindlin.

Case a. $D = \alpha = \mu = 0$

We have $\beta = 0$, $\eta = 1$. Equations (45) and (46) reduce to: $\epsilon_m = \Delta_0 = E_s$ and

$\ddot{\epsilon}_m = \omega_0^2 \Delta_0 = \omega_0^2 E_s$. Using Mindlin's notation:

$d_0 = E_s x_b$ and $G_0 = \omega_0^2 E_s x_b / g$, we obtain the

familiar exact solution:

$$d_0 = \sqrt{\frac{2Wh}{k_0}} \quad (47)$$

$$G_0 = \sqrt{\frac{2hK_0}{W}} \quad (48)$$

Here, $W = Mg$, d_0 is the maximum deflection of an undamped linear spring mass system dropped from a height h and G_0 is the corresponding maximum acceleration in number of g 's on the mass M .

Case b. $\mu = \alpha = 0$

$\beta = D$, $\eta = 1$. Equations (45), (46) and (42) reduce to:

$$\epsilon_m = E_s e^{-D \omega_0 t_{m1}} \quad (49)$$

$$\ddot{\epsilon}_m = \omega_0^2 E_s e^{-D \omega_0 t_{m2}} \quad (50)$$

$$\ddot{\epsilon}_0 = 2DE_s \omega_0^2 \quad (51)$$

Here, the times t_{m1} and t_{m2} are obtained from equations (43) and (44) by setting $\beta = D$ and $\eta = 1$. Using Mindlin's notation once again:

$G_m = \xi_m X_b / g$ when $t \neq 0$, and $G_m = \xi_0 X_b / g$ when $t = 0$, while $d_m = c_m X_b$. Thus.

$$\frac{d_m}{d_c} = e^{-D\omega_0 t_{m1}} \quad (52)$$

$$\text{when } t = 0: \frac{G_m}{G_0} = 2D \quad (53)$$

$$\text{when } t = t_{m2}: \frac{G_m}{G_0} = e^{-D\omega_0 t_{m2}} \quad (54)$$

Equation (52) is the familiar expression for the logarithmic decrement of the amplitude of a viscously damped spring mass system while (53) and (54) are identical with Mindlin's results.

Case c. $\mu = D = 0$

$\eta = 1$, $\Delta_0 = E_s$, $\beta = \frac{2\alpha}{\pi E_s}$. From equation (20) for $D = 0$ we have: $d\Delta/dt = -\frac{2\alpha}{\pi}\omega_0$, which by direct integration leads to:

$$\Delta = E_s - \frac{2\alpha}{\pi}\omega_0 t \quad (55)$$

In this case, equations (45), (46) and (42) reduce respectively to:

$$e_m = E_s e^{-(\frac{2\alpha}{\pi}\omega_0 t_{m1})} / (E_s - \frac{2\alpha}{\pi}\omega_0 t_{m1}) \quad (56)$$

$$\ddot{e}_m = \omega_0^2 E_s e^{-(\frac{2\alpha}{\pi}\omega_0 t_{m2})} (E_s - \frac{2\alpha}{\pi}\omega_0 t_{m2}) \quad (57)$$

$$\ddot{e}_0 = \frac{4\alpha}{\pi}\omega_0^2 \quad (58)$$

The times t_{m1} and t_{m2} in equations (56) and (57) may be obtained by simultaneous solution of equations (56) and (43) or (57) and (44) respectively. A solution is possible by an iterative process of successive approximations. However, for lightly damped system an approximation is feasible, whereby a direct analytical solution is obtained. During the first half cycle $\frac{2\alpha}{\pi}\omega_0 t \ll E_s$, $\Delta \approx E_s$ (if α is small),

and $\beta = \frac{2\alpha}{\pi E_s} \ll 1$, permitting equations (43)

and (44) to be approximated by (59) and (60) respectively:

$$\text{tg}(\omega_0 t_{m1}) \approx \frac{\pi E_s}{2\alpha} \quad (59)$$

$$\text{tg}(\omega_0 t_{m2}) \approx \frac{\pi E_s}{6\alpha} \quad (60)$$

Similarly, equations (56) and (57) may be approximated by (61) and (62):

$$e_m \approx E_s e^{-\frac{2\alpha}{\pi E_s}\omega_0 t_{m1}} = E_s e^{-\frac{2\alpha}{\pi E_s} \text{arctg}(\frac{\pi E_s}{2\alpha})} \quad (61)$$

$$\begin{aligned} \ddot{e}_m &\approx \omega_0^2 E_s e^{-\frac{2\alpha}{\pi E_s}\omega_0 t_{m2}} \\ &= \omega_0^2 E_s e^{-\frac{2\alpha}{\pi E_s} \text{arctg}(\frac{\pi E_s}{6\alpha})} \end{aligned} \quad (62)$$

The corresponding exact expressions developed by Mindlin are:

$$e_m = \sqrt{E_s^2 + \alpha^2} - \alpha \quad (63)$$

$$\ddot{e}_m = \omega_0^2 E_s - \omega_0 \alpha \quad (64)$$

The graphs in Figures 2 and 3 compare equations (61) with (63) and (62) with (64). It can be seen from the graphs that good agreement exists between the approximate solution and Mindlin's exact solution.

Case d. $D = \alpha = 0$

When $\beta = 0$, and $\eta = \eta_0$, equations (45) and (46) reduce to:

$$e_m = \Delta_0 = \frac{E_s}{\eta_0} \quad (65)$$

$$\ddot{e}_m = \eta_0^2 \omega_c^2 \Delta_0 = \omega_0^2 \eta_0 E_s \quad (66)$$

Using Mindlin's notation:

$$B = \frac{4Whr}{K_0^2} = 2\mu E_s^2 \quad (67)$$

We may transform equations (65) and (66) into the form:

$$\frac{d_m}{d_0} = \frac{1}{\eta_0} = \sqrt{\frac{4}{3B}} [\sqrt{1 + \frac{3}{2}B} - 1] = \sqrt{\frac{4}{3B}} \quad (68)$$

$$\frac{G_m}{G_0} = \eta_0 = \sqrt{\frac{1}{2}} [\sqrt{1 + \frac{3}{2}B} + 1] = \sqrt{\frac{3B}{8}} \quad (69)$$

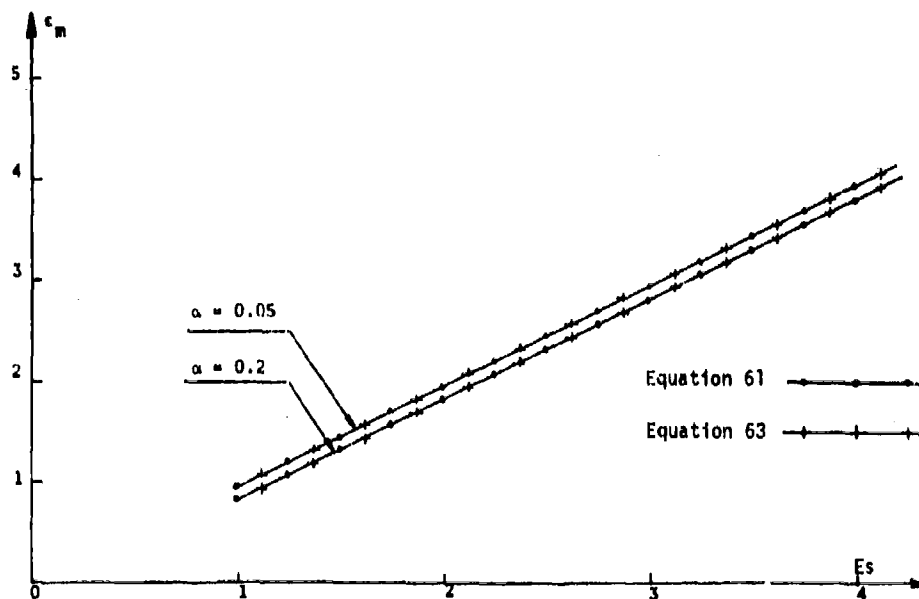


Fig. 2 - Maximum relative displacement of a friction damped linear spring.

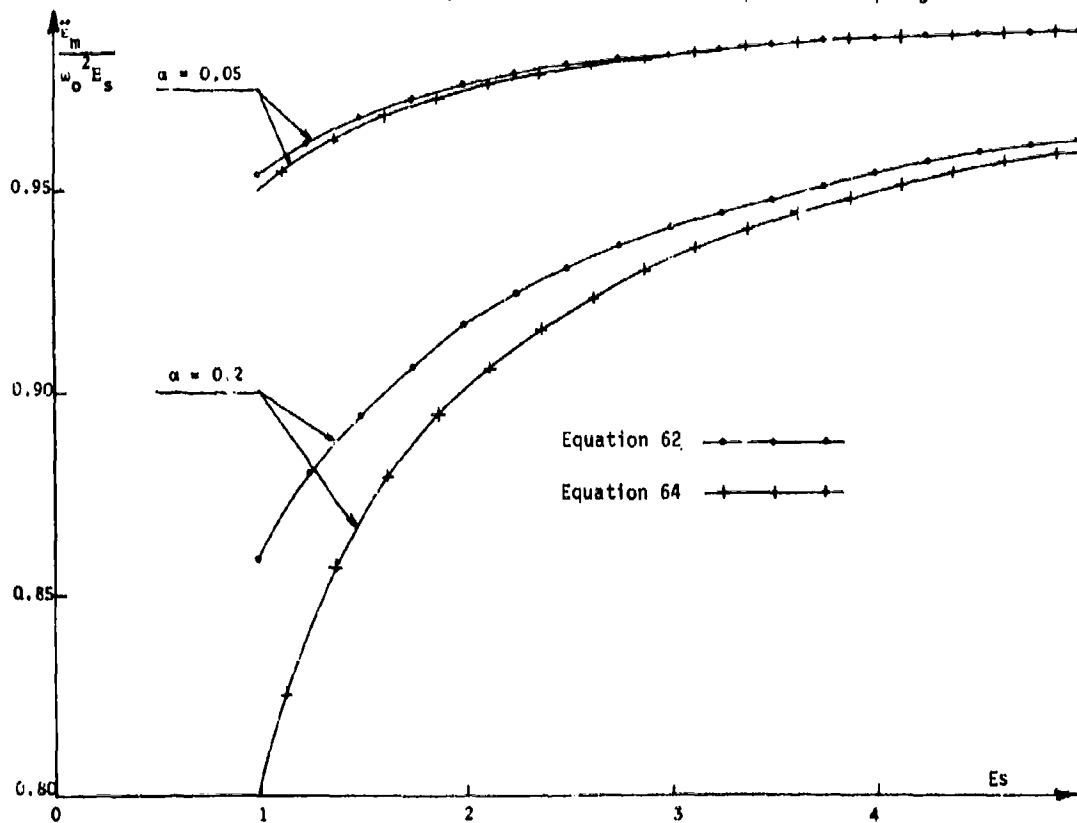


Fig. 3 - Maximum relative acceleration of a friction damped linear spring.

These can be compared to Mindlin's solutions for this case:

$$\frac{d_m}{d_0} = \sqrt{\frac{2}{B} (\sqrt{1+B} - 1)} = \sqrt{4 \frac{4}{B}} \quad (70)$$

$$\frac{G_m}{G_0} = \sqrt{\frac{2}{B} (\sqrt{1+B} - 1) (1+B)} = \sqrt{4B} \quad (71)$$

The approximations in equations (68) through (71) are justified when the dimensionless parameter B is much greater than unity ($1 \ll B$). Comparing equations (68) with (70) and (69) with (71) we find that our approximate solution underestimates the maximum displacement, and acceleration ratios, by a factor of approximately 0.903 and 0.553 respectively for very large values of the parameter B . The underestimation is only 0.967 and 0.883 when $B = 1$. Both results approach identity with further decrease in the parameter B . This is consistent with the basic limitation of the Kryloff-Bogoliuboff solution of the differential equation, whereby the accuracy is proportional to $r = \frac{BK_0^2}{4Wh}$.

Simplified Formulae for Lightly Damped Systems

When the damping ratios D and α are small, say smaller than 0.2 ($\beta^2 \ll 1$), we may approximate $\Delta \approx \Delta_0$ and equations (40) and (41) as well as (43) through (46) may be reduced into simplified forms respectively:

$$e = \Delta_0 e^{-\beta_0 \eta_0 \omega_0 t} \sin(\eta_0 \omega_0 t) \quad (72)$$

$$\ddot{e} = \omega_0^2 \eta_0^2 \Delta_0 e^{-\beta_0 \eta_0 \omega_0 t} \cos(\eta_0 \omega_0 t + \gamma) \quad (73)$$

$$t_{m1} = \frac{1}{\eta_0 \omega_0} \arctg\left(\frac{1}{\beta_0}\right) \quad (74)$$

$$t_{m2} = \frac{1}{\eta_0 \omega_0} \arctg\left(\frac{1}{3\beta_0}\right) \quad (75)$$

$$e_m = \Delta_0 e^{-\beta_0 \arctg(1/\beta_0)} \quad (76)$$

$$\ddot{e}_m = \omega_0^2 \eta_0^2 \Delta_0 e^{-\beta_0 \arctg(1/3\beta_0)} \quad (77)$$

Here, γ , β_0 , and Δ_0 are given by:

$$\tg \gamma = -\frac{1}{2\beta_0} \quad (78)$$

$$\beta_0 = \frac{D + \frac{2\alpha}{\pi \Delta_0}}{\sqrt{1 + \frac{3\mu \Delta_0^2}{4}}} = \left(D + \frac{2\alpha}{\pi \Delta_0}\right) \frac{1}{\eta_0} \quad (79)$$

$$\Delta_0 = \sqrt{\frac{2}{3\mu} [\sqrt{1 + 3\mu E_s^2} - 1]} \quad (80)$$

$$\eta_0 = \sqrt{1 + \frac{3}{4} \mu \Delta_0^2} \quad (81)$$

Since most of the mechanical systems (including packaging systems), are usually lightly damped, the set of simplified equations (72) through (81) may serve as a handy tool for the designer.

We are interested mostly in the first half cycle of the motion, i.e. the relative displacement and acceleration pulses of the system immediately after contact with the substrate. Note that t_{m1} and t_{m2} are the rise times of these pulses. Comparing equation (74) and (75) we find that the acceleration pulse rise time is shorter than the rise time of the displacement pulse. The difference vanishes for undamped systems when $\beta = 0$. Both rise times are decreased by increasing damping. To find the total duration time of the displacement pulse τ_d and acceleration pulse τ_a , we set in equation (72) and (73) $t = \tau_d$, $t = \tau_a$ respectively. Since $e = 0$ when $\eta_0 \omega_0 \tau_d = \pi$ and $\ddot{e} = 0$ when $\eta_0 \omega_0 \tau_d + \gamma = \frac{\pi}{2}$ we have for lightly damped systems:

$$\tau_d = \frac{\pi}{\eta_0 \omega_0} \quad (82)$$

$$\tau_a = \frac{\frac{\pi}{2} - \arctg\left(-\frac{1}{2\beta_0}\right)}{\eta_0 \omega_0} \quad (83)$$

As $\beta \geq 0$ and $\tau_a < \tau_d$, we find again that the acceleration pulse duration time is shorter than the displacement pulse. The difference is proportional to the combined damping ratio β_0 and vanishes when the system is undamped ($\beta_0 = 0$). Notice also that both τ_d and τ_a are shorter for non-linear systems than for linear systems by a factor:

$$1/\eta_0 = \sqrt{\frac{8}{3B}} = \sqrt{\frac{4}{3\mu E_s^2}}$$

Thus, the pulse duration time is reduced both by increasing the non-linearity of the spring and drop height.

CONCLUSION

A mechanical model simulating drops of cushioned items in containers, consisting of a mass contained in an infinitely rigid frame and restrained by two preloaded massless non-linear springs, a dashpot and a dry friction damper, was introduced. The differential equation of motion of the system from the instant of collision onto a hard surface after a free fall from a height h onwards was solved by the "linearization principle" due to Kryloff and Bogoliuboff [7]. This method affords an approximate quasi-harmonic solution of the non-linear differential equation of motion with accuracy proportional to the deviation of the spring force-deformation curve from linearity. The study of the quasi-harmonic motion whereby both the amplitude and phase are functions of time, was facilitated by solving the "linearized" equation of motion as if it were an ordinary linear differential equation. Particular attention was directed to the study of the motion during the first half cycle, e.g. displacement and acceleration versus time pulses. To assess the accuracy of the solution, a comparison of results with special cases for which exact solutions are known was conducted. It was found that the general equations of our approximate solution converge to the corresponding exact expressions found by Mindlin [1], for undamped and viscously damped linear springs, while deviation from the exact solutions for friction damped linear springs and undamped springs with cubic elasticity is well within requirements for practical engineering problems. For expediency of calculations in practical problems, simplified approximate formulae were developed separately for lightly, medium and heavily damped systems. These provide a ready to use tool for conservative design. It was found that for heavily damped systems maximum acceleration is reached at the instant of collision, falling off to zero with time. Such systems are characterized by sawtooth acceleration versus time pulses, with the initial maximum acceleration directly proportional to system damping, (β) , shock excitation (E_s) and ω_0^2 , i.e. inversely proportional to the mass. Pulse A in Figure 4 is a representative example. For lightly damped systems, most common in practice, maximum acceleration is reached during the first half cycle period while the initial acceleration is comparatively small. Such systems are characterized by half sine acceleration versus time pulses. Pulse B in Figure 4 is a representative example. The graphs in Figures 5 and 6 comprise examples of equations (76) and (77) respectively for representative values of E_s , α and D . From these we may conclude that for lightly damped systems, increasing the non-linearity of the springs (μ) increases maximum acceleration \ddot{e}_m and decreases maximum displacement e_m , for a certain set of values of E_s , α and D . Increasing shock excitation E_s increases both e_m and \ddot{e}_m while increasing damping (α , D) decreases both e_m and \ddot{e}_m . It

was shown by equations (82) and (83) that the acceleration pulse duration time τ_a is shorter than the corresponding displacement pulse time τ_d , the difference is proportional to the damping ratio β_0 and vanishes when $\beta_0 = 0$. From equations (74) and (75) we conclude that the same is true for acceleration and displacement pulse rise times. It can be shown also (from equations (82), (74) and (83), (75)) that $\tau_d - t_{m1} \geq t_{m1}$ and $\tau_a - t_{m2} \leq t_{m2}$, i.e. both pulses are not symmetrical as rise times are shorter than decay times. The difference is proportional to the damping ratio β_0 . Thus, we have symmetrical and equal duration displacement and acceleration pulses only when damping is absent. Finally, it was shown that both pulse duration times are shorter in non-linear (hardening spring) systems than in linear systems.

For medium damped systems, the initial acceleration and maximum acceleration during the pulse period are approximately equal; thus, such systems are characterized by trapezoidal acceleration versus time pulse shapes. Pulse C in Figure 4 is a representative example. To find the damping ratio β_0 when $\ddot{e}_0 = \ddot{e}_m$, we recall that during the first half cycle equations (44) and (46) may be approximated by:

$$\begin{aligned} & \operatorname{tg}(n_0 \sqrt{1 - \beta_0^2} \omega_0 t_{m2}) \\ &= \frac{(1 - 4\beta_0^2) \sqrt{1 - \beta_0^2}}{\beta_0(3 - 4\beta_0^2)} \end{aligned} \quad (84)$$

$$\ddot{e}_m = n_0^2 \omega_0^2 \Delta_0 e^{-\beta_0 n_0 \omega_0 t_{m2}} \quad (85)$$

Introducing $\omega_0 t_{m2}$ from equation (84) into equation (85) and equating equations (85) and (42) yields:

$$\ln(2\beta_0) = \frac{-\beta_0}{\sqrt{1 - \beta_0^2}} \operatorname{arctg} \left[\frac{(1 - 4\beta_0^2) \sqrt{1 - \beta_0^2}}{\beta_0(3 - 4\beta_0^2)} \right] \quad (86)$$

The value of β_0 satisfying equation (86) is $\beta_0 = 0.475$. Curve D in Figure 4 is a representative example of an acceleration pulse when the system is damped by this trade-off value of β_0 .

Increasing the preload of the system by increasing precompression of the springs decreases the values of X_b , μ , α and D , while K_0 , r and the product $K_0 X_b$ are increased. Rigorous mathematical treatment of the influence of varying precompression is outside the scope of this article. It can be shown, however, that the net effect of increasing precompression is a "harder" spring with reduced nonlinearity.

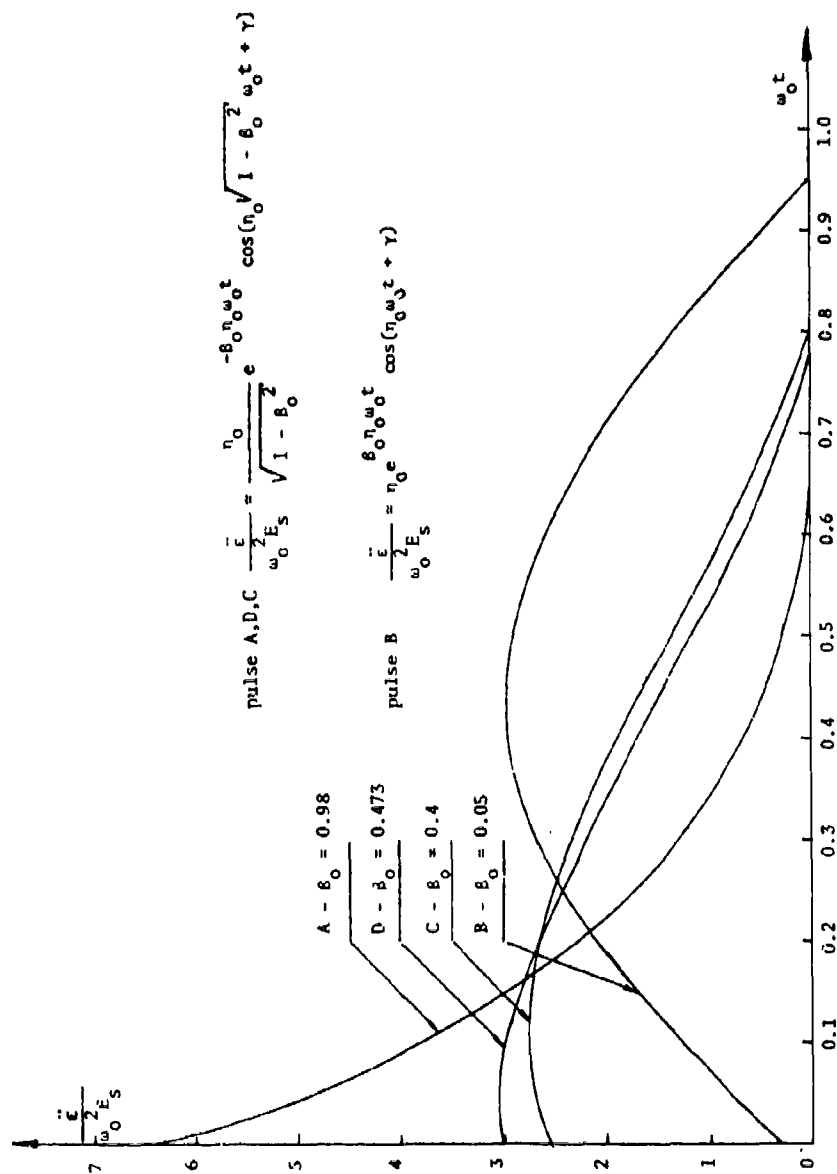


Fig. 4 - Acceleration versus time pulses for various damping ratios. Pulse A, D, C by Equation (41). Pulse B by Equation (73).

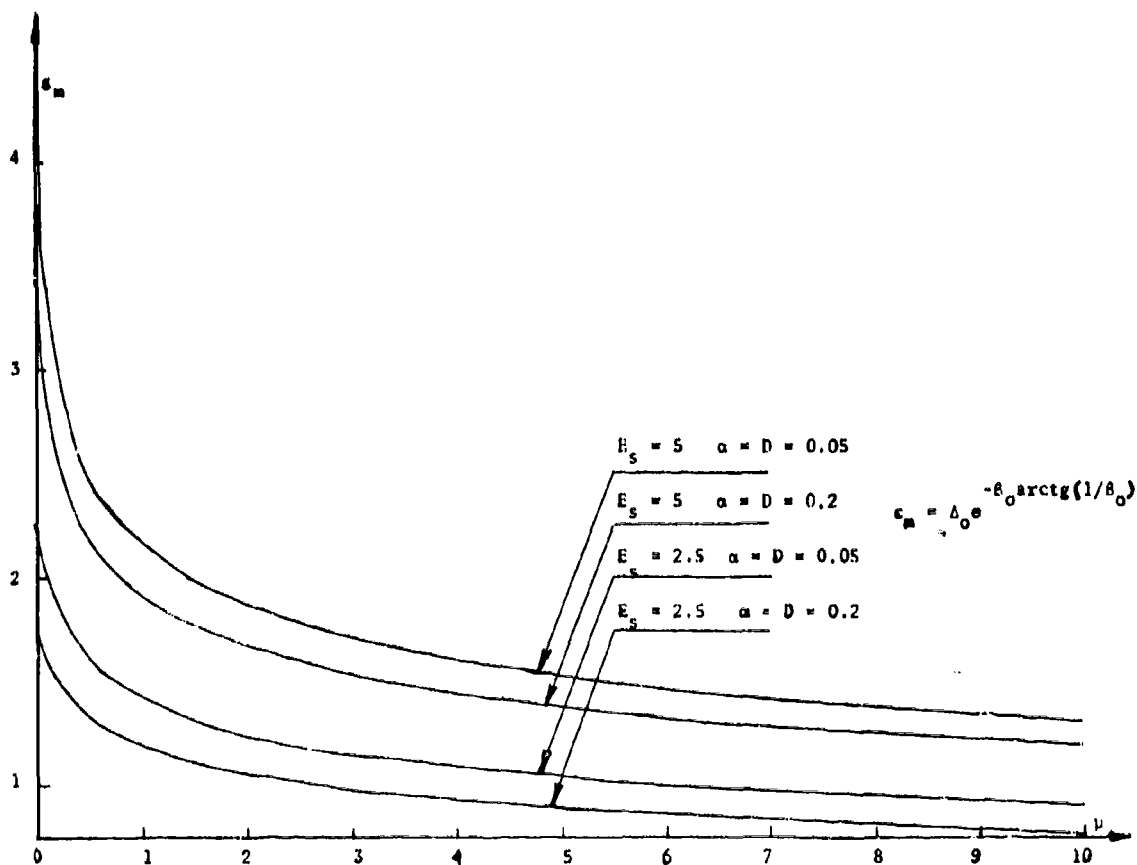


Fig. 5 - Maximum relative displacement versus spring hardening ratio (Equation 76).

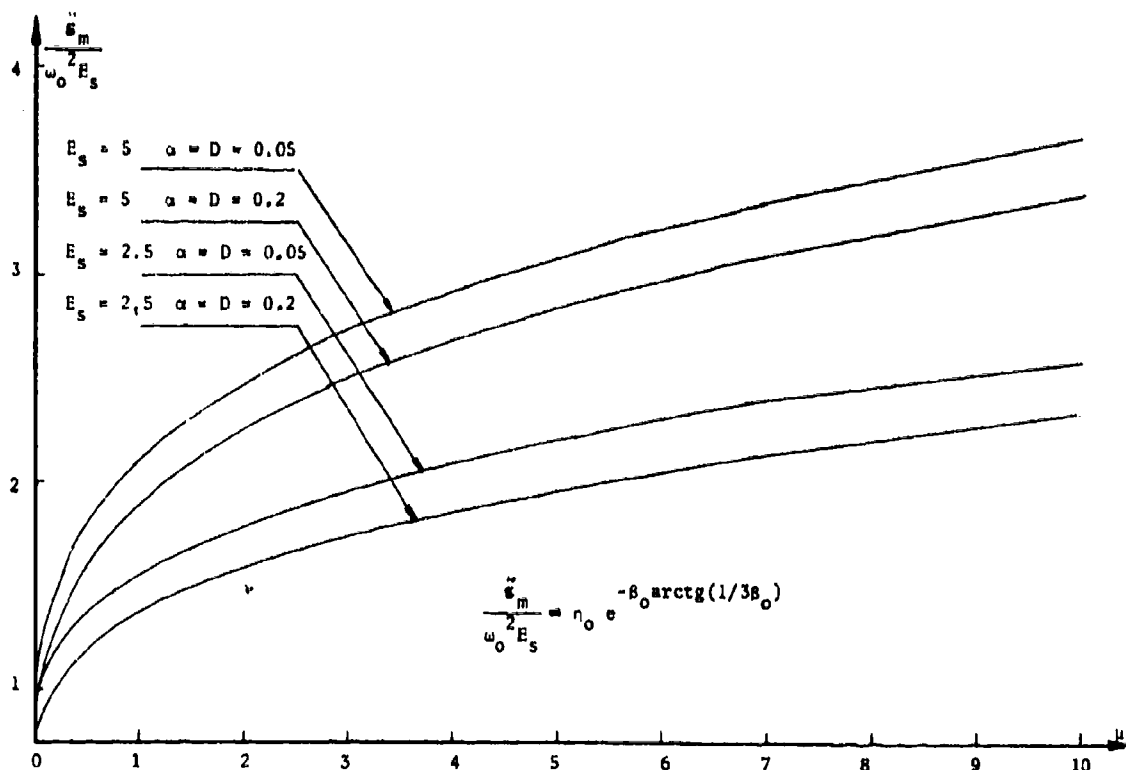


Fig. 6 - Maximum relative acceleration versus spring hardening ratio (Equation 77).

Usually this results in shorter pulse duration times and increased values for maximum acceleration and displacement (\ddot{e}_m, e_m). Thus, increasing precompression is usually harmful in shock isolation problems while the inverse problem of assuring activation of inertia mechanisms may benefit by increased precompression. Note also that excessive precompression, on its own, may have a damaging effect on the product.

DEFINITION OF SYMBOLS*

- A - relative displacement amplitude, or maximum spring deflection
- B - Mindlin's dimensionless parameter for undamped cubic elasticity systems
- C - viscous damping coefficient
- D - viscous damping ratio
- d_0 - maximum deflection of an undamped linear spring mass system

*Unless otherwise stated, symbols in the text subscripted by 0 indicate initial undamped values of the variables, at the instant of collision ($t = 0$).

- d_m - maximum deflection of a viscously damped linear spring mass system
- E_s - dimensionless shock excitation parameter
- F - combined spring force of the system
- F_f - friction (Coulomb) damping force
- g - acceleration of gravity
- G_0 - maximum acceleration in g's of an undamped linear spring mass system
- G_m - maximum acceleration in g's of a viscously damped linear spring mass system
- h - drop height
- K_1, K_2 - initial spring constants of lower and upper springs respectively
- K_0 - combined initial spring rate constant of the system
- K - equivalent spring constant of the linearized system
- M - mass
- r - combined spring hardening coefficient of the system

r_1, r_2 - spring hardening coefficients of lower and upper springs respectively

t - time

t_{m1} - displacement pulse rise time

t_{m2} - acceleration pulse rise time

W - weight

X - relative displacement of mass M with respect to the frame

X_b - maximal permissible relative displacement of the mass M with respect to the frame

α - Coulomb friction parameter (dimensionless friction damping ratio)

β - combined viscous and coulomb damping ratio

β_{m1} - combined viscous and Coulomb damping ratio at the instant of maximum displacement

β_{m2} - combined viscous and Coulomb damping ratio at the instant of maximum acceleration

γ - acceleration phase angle

δ - velocity phase angle

Δ - dimensionless relative displacement amplitude ratio

Δ_0 - undamped relative displacement amplitude ratio

Δ_m - maximal relative displacement amplitude ratio

ϵ - dimensionless relative displacement ratio

$\ddot{\epsilon}$ - dimensionless relative acceleration

$\ddot{\epsilon}_m$ - maximum dimensionless relative acceleration

$\ddot{\epsilon}_0$ - initial relative acceleration at collision ($t = 0$)

θ - phase angle

λ - energy dissipating coefficient of the linearized system

μ - dimensionless spring hardening ratio

τ_a - acceleration pulse duration time

τ_d - displacement pulse duration time

ϕ - dummy variable of integration

ψ - total phase angle

η - dimensionless frequency ratio

η_{m1} - dimensionless frequency ratio at the instant of maximum displacement

η_{m2} - dimensionless frequency ratio at the instant of maximum acceleration

ω - angular velocity

ω_0 - natural angular velocity of an equivalent linear spring with spring ratio K_0

$$(\omega_0 = \sqrt{K_0/M})$$

REFERENCES

1. Mindlin, R. D., "Dynamics of Package Cushioning", Bell System Technical Journal, 24, pp. 353-467, July-October 1945.
2. Mustin, G. S., Theory and Practice of Cushion Design, The Shock and Vibration Information Center, U. S. Dept. of Defense SVM-2, 1968.
3. Janssen, R. R., Packaging Review, Vol. 73, No. 79, p. 38, March 1953.
4. Kornhauser, M., "Prediction and Evaluation of Sensitivity to Transient Accelerations", J. Of Applied Mechanics, pp. 371-380, December 1954.
5. Newton, R. E., Fragility Assessment Theory and Test Procedure, A publication of MTS Systems Corporation, Box 24012, Minneapolis, Minnesota.
6. Zell, G., "Vibration Testing of Resilient Package Cushioning Materials", Picatinny Arsenal Technical Report 3160, August 1964.
7. Kryloff, N. and Bogoliuboff, N., Introduction to Non-Linear Mechanics, Princeton University Press, 1947 (Fifth printing 1959)

DYNAMICS ANALYSIS

STABILITY ANALYSIS AND RESPONSE CHARACTERISTICS OF TWO-DEGREE OF FREEDOM NONLINEAR SYSTEMS*

M. Subudhi and J. R. Curreri
Brookhaven National Laboratory
Upton, New York

Understanding the behavior of nonlinear systems is important in laboratory testing. Sine sweep-up and sweep-down tests are routinely done to reveal all of the stable roots in this type of system. There are, however, certain types of softening-hardening restoring force characteristics for which sine sweep testing, whether up or down, will not reveal all of the stable roots. In such cases, it is important that the stable roots be identified so that proper testing procedures are used and the test results are correctly evaluated.

The stability of a nonlinear two degree-of-freedom spring-mass system subjected to a sinusoidal exciting force is examined. The solution is perturbed to arrive at a set of coupled variational linear differential equations with periodic coefficients. Floquet theory is used to obtain a characteristic equation. The Routh-Hurwitz stability criterion is adopted to study the stable and unstable regions of the response curves. A computer program is developed to carry out the entire analysis. Extensive information regarding stable zones of the system response is described by means of nondimensional frequency-amplitude diagrams. The results are examined in terms of inferring dynamic response characteristics for sine sweep tests.

INTRODUCTION

In recent years, problems involving nonlinear characteristics have received much attention. Many designs require an understanding of the effects of nonlinear restoring elements in multi-degree-of-freedom systems. It is characteristic of such systems that some of the roots are stable while others are unstable. In addition, it may be desirable to know the proximity of the stable roots to the unstable regions.

The behavior of nonlinear systems is especially important in laboratory testing. Sine sweep-up and sweep-down tests are routinely done to reveal all of the stable roots in this type of system. There are, however, certain types of softening-hardening restoring force characteristics for which sine sweep testing, whether up or down, will not reveal all of the stable roots [1,2]†. In such cases, it is important that the stable roots be identified so that proper testing procedures are used and the test results

are correctly evaluated. This paper shows the results for some cases of softening-hardening spring characteristics (such as the HTGR nuclear core) for which it is necessary to identify the stable regions in order to correctly interpret the results of a testing program.

Several investigators [3,4,5, and 6] have studied the stability of nonlinear systems using different analytical approaches. Atkinson [4] has reported on an analog computer solution of two degree-of-freedom systems. He compares these analog results with what he calls suspected stability regions, as inferred by an extension of the one degree-of-freedom stability criterion of Klotter and Pinney [7]. However, the present method is found to be very general for multi-degree-of-freedom systems.

The question of stability may be defined by determining whether or not a system, once disturbed, returns to its equilibrium state. Given an equilibrium state of a physical system, whose stability we wish to study, we consider a state near equilibrium and ask whether in the course of time the system will tend towards the given equilibrium state.

* Work performed under the auspices of the United States Nuclear Regulatory Commission.

† Numbers in brackets designate references at end of paper.

In the stability study, the system is described by the two nonlinear differential equations. The procedure follows the often used definition for infinitesimal stability as described by Stoker [3]. A perturbed solution is introduced. This results in the perturbed linear "variational" differential equations for $\delta X_1(t)$. Floquet theory is used to solve the above variational equations with periodic coefficients. This suggests that there is a solution to these equations of the form $e^{at} \phi_1(t)$ which are periodic functions and regular enough to be expanded in a Fourier series. Equating the coefficients of like independent functions gives a set of algebraic equations in the Fourier coefficients from which, for a nontrivial solution, a characteristic polynomial in the exponent a is obtained. The Routh-Hurwitz stability criterion is employed to find the unstable roots of the characteristic equation.

Several cases with nonlinearity in either or both springs have been considered. Results are compared with those obtained by Atkinson [4] with an analog computer. Some differences are discussed. The special case of the dynamic absorber is also investigated to compare with the general response results obtained earlier by Robertson [8] and the Frahm-type dynamic absorber that was studied graphically by Carter and Liu [9]. The paper also shows that much more complex jump phenomena can occur in some kinds of nonlinear systems.

The results are displayed via plots between the nondimensional frequency versus the amplitude of each mass. This analysis is found to be very useful in solving stability problems without any prior knowledge of the stability of any problem in the field of nonlinear mechanics. In addition, a more complete understanding can be obtained of the response of multi-degree-of-freedom nonlinear systems.

THE SYSTEM UNDER INVESTIGATION

The schematic diagram for the more general system being investigated is illustrated in Figure 1. The governing equation of motion for each mass is obtained in nondimensional form and they are given as:

$$X_1'' + C_1 X_1' + (X_1 \pm \alpha_1 X_1^3) - C_2 X_3' - K (X_3 \pm \alpha_2 X_3^3) = F \sin \omega t \quad (1)$$

$$X_2'' + \frac{C_2}{M} X_3' + \frac{K}{M} (X_3 \pm \alpha_2 X_3^3) = 0$$

where $X' = \frac{dX}{dt}$

$X_1, i=1, 2$ represents nondimensional absolute motion of masses

$$X_3 = X_2 - X_1$$

$$C_1 = \text{nondimensional viscous damping coefficient} = \frac{c_1}{(k_1 m_1)^{1/2}}$$

$$\alpha_1 = \text{nondimensional nonlinear spring constant}$$

$$K = k_2/k_1$$

$$M = m_2/m_1$$

$$F, \omega, t = \text{nondimensional forcing amplitude, frequency and time variables, respectively}$$

The Ritz average method [10] is used to obtain an approximate solution to equation (1). As the initial approximating functions for the steady-state response of the nonlinear system shown in Figure 1, the following relations will be used:

$$\begin{aligned} X_1 &= A_1 \sin \omega t + A_2 \cos \omega t \\ X_2 &= D_1 \sin \omega t + D_2 \cos \omega t \end{aligned} \quad (2)$$

Using the Ritz averaging procedure, the final form of the algebraic equations in terms of the unknowns A_1 and D_1 are given as:

$$\begin{aligned} -\omega^2 A_1 - C_1 \omega A_2 + A_1 (1 \pm \beta_1 A^2) + C_2 \omega G_2 - \\ K G_1 (1 \pm \beta_2 G^2) = F \end{aligned}$$

$$\begin{aligned} -\omega^2 A_2 + C_1 \omega A_1 + A_2 (1 \pm \beta_1 A^2) - C_2 \omega G_1 - \\ K G_2 (1 \pm \beta_2 G^2) = 0 \end{aligned} \quad (3)$$

$$-\omega^2 D_1 - \frac{C_1}{M} \omega G_2 + \frac{K}{M} G_1 (1 \pm \beta_2 G^2) = 0$$

$$-\omega^2 D_2 + \frac{C_2}{M} \omega G_1 + \frac{K}{M} G_2 (1 \pm \beta_2 G^2) = 0$$

where

$$A^2 = A_1^2 + A_2^2$$

$$G_1 = D_1 - A_1$$

$$G^2 = G_1^2 + G_2^2$$

$$\beta_1 = 3/4 \alpha_1$$

The solution to these equations were carried out by numerical methods.

For the stability study, the damping terms are neglected since these terms add complexities without materially affecting the nature of the stability conclusion. The exact solution is perturbed to investigate the nature of the solutions near equilibrium. The variational equations in terms of the perturbation δX_1 are obtained. These equations are:

$$\delta \ddot{X}_1 + (1 \pm 3\alpha_1 X_1^2) \delta X_1 - K (1 \pm 3\alpha_2 X_2^2) \delta X_3 = 0$$

$$(4)$$

$$\delta \ddot{X}_2 + \frac{K}{M} (1 \pm 3\alpha_2 X_2^2) \delta X_3 = 0$$

If all solutions of δX_i are bounded, then X_i are said to be stable, otherwise they are unstable.

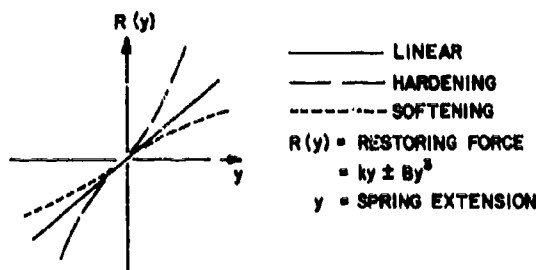
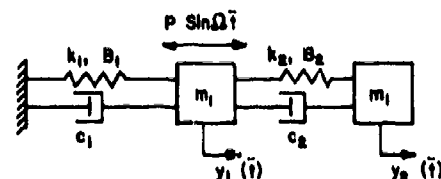


Fig. 1 - Schematic model of mechanical system and generalized spring force versus spring extension characteristics

The above are known as coupled Hill's equations. The terms X_i are the actual solutions. Since we do not have any such solutions, we use the approximate solutions indicated by solving equation (3). Now substituting (2) into (4), we arrive at two coupled linear equations with Mathieu-type coefficients as given below:

$$\delta \ddot{X}_1 + (\delta_1 + \epsilon_1 \cos \tau) \delta X_1 - (\delta_2 + \epsilon_2 \cos \tau) \delta X_2 = 0$$

$$(5)$$

$$\delta \ddot{X}_2 + (\delta_3 + \epsilon_3 \cos \tau) \delta X_2 - (\delta_4 + \epsilon_4 \cos \tau) \delta X_1 = 0$$

where $\delta \ddot{X}_1 = \frac{d^2 \delta X_1}{d\tau^2}$
 $\tau = 2\omega t$

$$\delta_1 = (1 \pm 2\beta_1 A_1^2 \pm 2K\beta_2 G_1^2) / (4\omega^2)$$

$$\delta_2 = (K \pm 2K\beta_2 G_1^2) / (4\omega^2)$$

$$\delta_3 = \delta_4 = \frac{K}{M} (1 \pm 2\beta_2 G_1^2) / (4\omega^2)$$

$$\epsilon_1 = \mp (2\beta_1 A_1^2 + 2K\beta_2 G_1^2) / (4\omega^2)$$

$$\epsilon_2 = \mp (2K\beta_2 G_1^2) / (4\omega^2)$$

$$\epsilon_3 = \epsilon_4 = \mp \frac{K}{M} (2\beta_2 G_1^2) / (4\omega^2)$$

From Floquet theory, the Mathieu equation always possesses a fundamental set of solutions in which one solution is an even and the other is an odd function of τ . Since the above equations have periodic solutions and they are regular for all values of τ , the solutions of (5) can be expressed in Fourier series such as:

$$\delta X_1(\tau) = e^{i\omega\tau} \left[\sum_{n=0}^{\infty} (a_{n1} \cos n\tau + b_{n1} \sin n\tau) \right] \quad (6)$$

Insertion of these series solutions in (5) leads to a set of recurrence relations for a_{n1} and b_{n1} by equating the coefficients of identical terms $e^{i\omega\tau} \cos n\tau$ and $e^{i\omega\tau} \sin n\tau$. These relations are linear homogeneous algebraic equations. For nontrivial solutions, the coefficient determinant must vanish. This results in a characteristic equation in α , which must have either zero or negative real parts to stable solution.

DISCUSSION

In the field of stability, Klotter and Pinney [7] have established a comprehensive stability criterion for a single degree-of-freedom system. This states that the maximum amplitude of the response must increase with the increase of the exciting force for a stable system and decrease for one which is unstable. Atkinson [4] used the above principle for a two degree-of-freedom system for suspected stable regions; but he used the one degree-of-freedom stability criterion in his investigation. The present analysis confirms most of the stable regions suspected by him.

Figure 2 and 3 show the results for a case with the auxiliary spring being nonlinear. The positive (+) and negative (-) signs on the plots indicate the in-phase and out-of-phase responses of the two masses respectively. For the softening case, the results agree with the suspected regions of Atkinson except for the positive loop

at low frequencies. According to Atkinson, both sides of the loop are stable while in the present investigation, it is found that the inner branch of the loop is unstable. However, from the plots of Atkinson it is clear that no computer solution was obtained for this unstable branch. Double absorber effects have been noticed, but one of them is found to be unstable. In fact, all of these cases of double absorber action have shown only one of them to be stable.

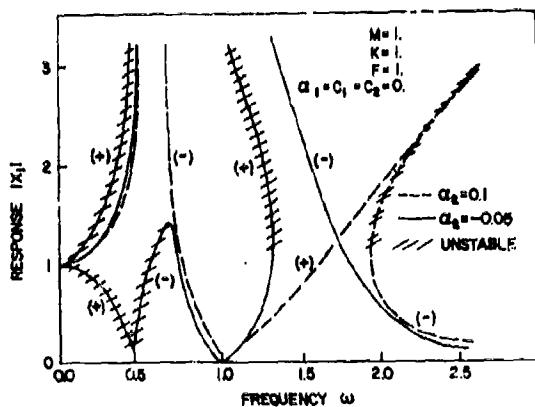


Fig. 2 - Response of main mass with auxiliary spring nonlinear

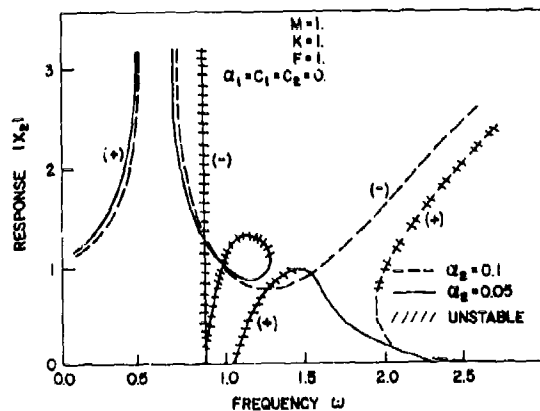


Fig. 3 - Response of auxiliary mass with auxiliary spring nonlinear

The dynamic absorber results are compared with the previous work of Roberson [8] and Carter and Liu [9] as shown in Figure 4. Roberson has defined the "forbidden region" as the regions where the auxiliary spring extension

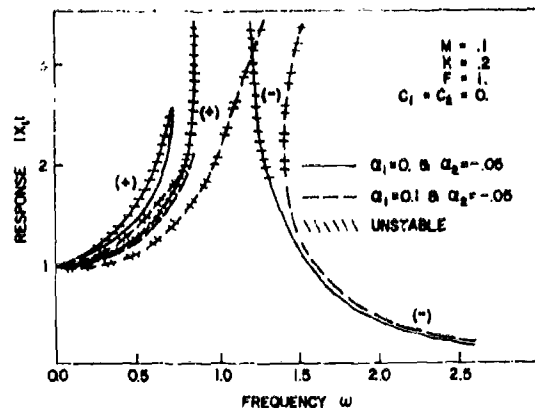


Fig. 4 - Response of main mass of dynamic absorbers

or compression exceeds the critical deflection of the spring at which the slope of the load-deflection curve becomes zero. It is implied that this is an unstable region. The present investigation has determined that the forbidden region for a Roberson-type system is $0.7 < \omega < 1.4$ and $\omega < 0.2$. For the system considered by Carter and Liu, the present results determine the forbidden region to be $0.8 < \omega < 1.5$. Thus it is found that the dynamic absorber with the hardening main spring together with the softening absorber spring has a better suppression band, as claimed by Carter and Liu.

Moreover, Roberson has defined the forbidden region at such amplitudes where the slope of the softening spring characteristics goes to zero. Arnold [10] has extended this to the point of zero restoring force. Therefore, for a case with $\alpha_2 = -0.05$, this critical amplitude is 4.47 for Arnold and 2.58 for Roberson. However, the present analysis determines that the forbidden region can allow this critical amplitude up to 3.36. Comparing this with the above two cases, it is found that Roberson is more conservative and the corresponding forbidden region is closer than Arnold. Atkinson has also noticed similar kinds of results in his analog computer analysis.

Figure 5 shows a block of the HTGR core which can translate and rotate. The equations for this system are equivalent to the in-line arrangement shown in Figure 1. This type of system shows that much more complex jump phenomena could occur. Unless their characteristics are understood, the physical testing of such systems may not reveal all of the stable roots that are possible. For the case of rocking with two degrees of freedom, as in the response of the HTGR nuclear core, a softening-hardening characteristic shows a first mode response which is an

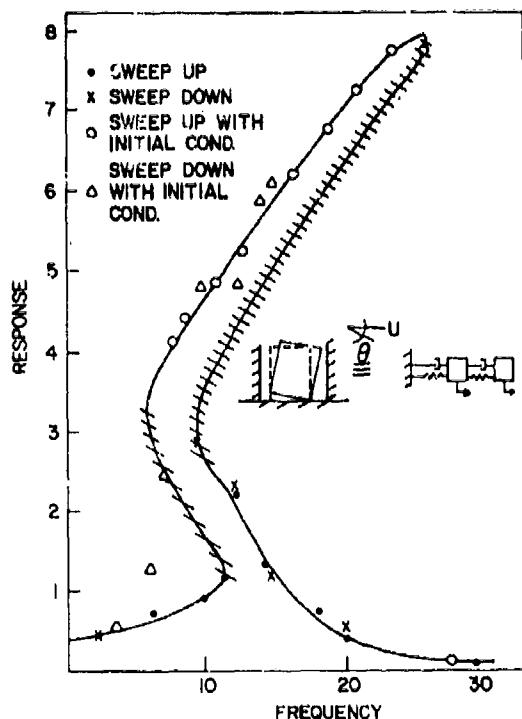


Fig. 5 - First mode response of a two degree-of-freedom system with softening-hardening main spring characteristic

"S" curve. Of the five roots that are possible, three are stable and two are unstable. However, the upper stable root can never be attained in any simple sine wave test, either by sweeping up or down. On the other hand, the upper root is attainable with the sine test in conjunction with the proper transient excitation, as might be induced by seismic disturbances.

For the hardening absorber spring, sine sweep tests show a jump down at high frequencies and a jump up at low frequencies. This is in accordance with ordinary one degree-of-freedom thinking. By simply changing mass ratio, or forcing function amplitude, only jump down characteristics can be revealed as shown in Figure 6, whether sweep up or down testing is done.

REFERENCES

- [1] P. Bezler, J. R. Curreri, "Subharmonic Excitation in an HTGR Core," 4th SMIRT Conf., San Francisco, CA, Aug. 15-19, 1977.
- [2] J. R. Curreri, "Multiple Sine Wave Excitation of a Hard Spring Oscillator," 47th

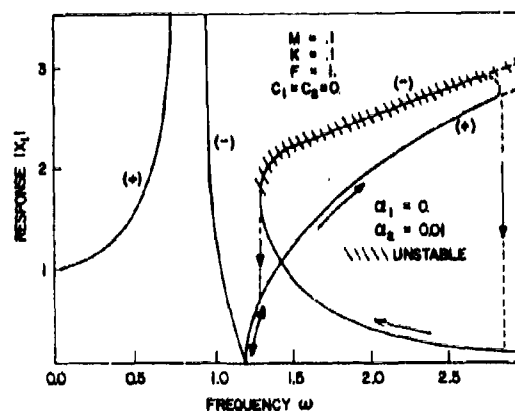


Fig. 6 - Response of main mass of a two degree-of-freedom system with hardening auxiliary spring

Shock and Vibration Symposium, 1976.

- [3] J. J. Stoker, *Nonlinear Vibrations in Mechanical and Electrical Systems*, Interscience, New York, 1950.
- [4] C. P. Atkinson, "Electronic Analog Computer Solutions of Nonlinear Vibrating Systems of Two Degree-of-Freedom," *J. Applied Mechanics*, pp. 629-634, Trans. ASME, Dec., 1956.
- [5] V. V. Bolotin, *The Dynamic Stability of Elastic Systems*, Holdenday, New York, 1964.
- [6] C. S. Hsu, "On the Stability of Periodic Solutions of Nonlinear Dynamical Systems Under Forcing," *Colloques Internationaux, Marseille*, pp. 125-144, 1964.
- [7] K. Klotter, E. Finney, "A Comprehensive Stability Criterion for Forced Vibrations in Nonlinear Systems," *J. Applied Mechanics*, pp. 9-12, Trans. ASME, March, 1953.
- [8] R. E. Roberson, "Synthesis of a Nonlinear Dynamic Vibration Absorber," *J. Franklin Institute*, Vol. 254, No. 3, pp. 205-220, 1952.
- [9] W. J. Catter, F. G. Liu, "Steady-State Behavior of Nonlinear Dynamic Absorber," *J. Applied Mechanics*, pp. 67-70, Trans. ASME, March, 1961.
- [10] F. R. Arnold, "Steady-State Behaviour of Systems Provided with Nonlinear Dynamic Vibration Absorbers," *J. Applied Mechanics*, pp. 487-492, Trans. ASME, Vol. 77, 1955.

APPLICATION OF RANDOM TIME DOMAIN* ANALYSIS TO DYNAMIC FLIGHT MEASUREMENTS

S. R. Ibrahim
Department of Mechanical Engineering and Mechanics
Old Dominion University
Norfolk, VA 23508

In this paper, an approach is presented for modal identification of aerospace structures from flight measurements. This approach is the result of combining the "time domain" modal identification technique and the multiple channel random decrement technique. Also, a new technique is presented to determine relative levels of excitation for identified modes. These techniques are applied to flight data taken from the B-1 bomber. Results are extremely encouraging.

INTRODUCTION

The solution of a variety of flight vehicle dynamic response problems including flutter, pogo, control/structure interactions, and payload dynamic loads requires an accurate knowledge of the dynamic characteristics of vehicles under actual flight conditions. Analytical models which are verified by ground tests and later by flight tests are used to treat these problems. However, the degree to which flight data can be used to determine the actual flight responses and, hence, verify the quality of modeling techniques has been limited, heretofore, by the inability to extract good quality modal information from the flight data. Although natural frequencies can be obtained by spectral analysis, good quality mode shapes are not normally available because their determination using ordinary methods requires comparison of responses with carefully-controlled and measured input forces--a luxury not available in flight. More importantly, damping cannot be readily determined for assessing stability margins except in transient loading cases, and then only for a limited number of modes.

The work reported in this paper discusses the application of a potentially powerful new technique to the analysis of random flight data. The method, called the "randomdec-time-domain" technique, overcomes the above difficulties to provide frequencies, damping, and with a sufficient number of sensors, mode shapes for vehicles

under random flight loads. Furthermore, it determines automatically the number of modes in the data through the use of a modal confidence factor.

The "randomdec-time-domain" technique is based upon the combination of two recently developed techniques. The first is the random decrement method developed by Cole, [1], for obtaining equivalent free responses from random forced responses. This method was initially developed for single-channel, single-mode data and later extended by Ibrahim, [2], to retain phase relations for multiple-channel correlation. The second technique, used in combination with the multiple-channel random-decrement analysis for obtaining free responses, is a time-domain dynamic data analysis method developed by Ibrahim, [3-6].

The other important feature in this paper is the development of an algorithm to determine the relative modal contribution constant for modes identified by the time-domain technique. Since the time-domain technique identifies modal vectors as eigenvectors, this information does not indicate how strongly modes are excited relative to each other. The algorithm developed in this paper fits the identified modes to the measured free-decay response. The response is assumed to be a linear combination of these modes. A set of constants results from this fitting procedure. Each constant is associated with one mode, thus, indicates the level of excitation of this specific mode.

The procedure (random-decrement analysis, time domain identification and determination of the relative model contribution constants) is applied to two channels of flight data from the prototype B-1 bomber. Although

*This work is part of a research project supported by NASA's Langley Research Center. Grant NSG 1459

the method is applied here to single-channel, the procedure will be the same for multiple channels.

THEORY (Relative Modal Contribution Constant)

Starting with the random response vector $y(t)$, and using the random decrement technique [2], the free-decay response vector for n stations $x(t)$ can be determined. From this free-decay response, using time domain identification [3-4], the modal parameters are identified. These parameters are characteristic roots $\lambda_j = a_j + ib_j$ and modal vectors ψ_j where j is an index for identified modes ($j = 1, 2, \dots, m$). Modal vectors occur in complex conjugate pairs with an amplitude vector p_j and phase angle vector α_j .

The free-decay responses can be expressed as linear summation of these modes as:

$$\underline{x}(t) = [\underline{R} \quad \underline{Q}] \begin{bmatrix} \underline{c} \\ \underline{d} \end{bmatrix} \quad (1)$$

$$(n \times 1) \quad (n \times 2m) \quad (2m \times 1)$$

where x_i is response of the i th station at time t ,

$$R_{ij} = p_{ij} \cos(b_j t + \alpha_{ij}),$$

$$Q_{ij} = p_{ij} \sin(b_j t + \alpha_{ij}),$$

$\underline{c}, \underline{d}$ are constants.

Equation (1) is n equations in $2m$ unknowns. Repeating equation (1) a number of times at different time intervals t_1, t_2, \dots, t_ℓ such that $(n \times \ell)$ is greater than $2m$.

$$\begin{bmatrix} \underline{x}_1 \\ \underline{x}_2 \\ \underline{x}_3 \\ \vdots \\ \underline{x}_\ell \end{bmatrix} = \begin{bmatrix} \underline{R}_1 & \underline{Q}_1 \\ \underline{R}_2 & \underline{Q}_2 \\ \vdots & \vdots \\ \underline{R}_\ell & \underline{Q}_\ell \end{bmatrix} \begin{bmatrix} \underline{c} \\ \underline{d} \end{bmatrix} \quad (2)$$

$$(n\ell \times 1) \quad (n\ell \times 2m) \quad (2m \times 1)$$

Equation (2) can be written as:

$$\underline{r} = \underline{S} \begin{bmatrix} \underline{c} \\ \underline{d} \end{bmatrix}$$

$$\begin{bmatrix} \underline{c} \\ \underline{d} \end{bmatrix} = (\underline{S}^T \underline{S})^{-1} (\underline{S}^T \underline{r})$$

and the relative modal contribution constant for the j th mode will be:

$$''(\text{RMCC})_j'' = \frac{\sqrt{c_j^2 + d_j^2}}{\sqrt{\max_{1 \leq j \leq m} (c_j^2 + d_j^2)}}$$

and the physical amplitudes of the j th mode at all its n stations will be equal to $''(\text{RMCC})_j'' \times p_j$.

EXPERIMENTAL RESULTS

Figures 1-a and 1-b show the free-decay responses of the horizontal and vertical tail accelerometers. These free-decay signals were obtained by applying the random decrement technique [1,2], to the random responses recorded during a test flight of a prototype of the B-1 bomber. Sampling frequency was 300 cps. The free-decay signal for the horizontal table was about 0.85 seconds (256 time samples). For the vertical tail signal, the record length was about 1.7 seconds (512 time samples). Each set of data was used as input to the time domain identification program. A math model of 10 modes was used for the horizontal tail. For the vertical tail 15 modes math model was used. In each case the number of modes in the math model was intentionally larger than the number of modes excited in each signal. This is to allow exits for noise. The concept of modal confidence factor, MCF, [6], which indicates the purity of the mode, was used to separate good modes from noise modes.

The procedure for the analysis is shown in the block diagram of Figure 2.

Table 1. summarizes results obtained. Four modes were identified for the horizontal tail, and eight modes for the vertical tail. The relative modal contribution constants "RMCC" were calculated using the algorithm previously discussed. Under the column designated notes, frequencies and damping factors identified, by other researchers who preferred not to be referred to, using frequency domain and special flutter testing techniques are listed. Evidences of having more than one made in the horizontal tail response are, blips on figure 1, unequal time periods, and a beating like phenomena. From the relative modal contribution factors listed in table 1, it is evident that the time domain identification technique can

identify modes that have very low response level, because this technique does not depend on manual observation and judgment during identification process.

6. S. R. Ibrahim, "Modal Confidence Factor in Vibration Testing," *AIAA Journal of Spacecrafts and Rockets*, Vol. 15, September-October 1978, pp. 313-316.

VERIFICATION OF RESULTS

Figures 3 and 4 show comparison between the test response and response made up by linear combination of identified modes using the calculated relative modal contribution constants. The fitted response was calculated using equation (1). Agreement is extremely good.

CONCLUSIONS

The combination of time domain identification, random decrement technique and the concept of relative modal contribution constant present a very powerful tool that can be very effective in modal analysis of structures from flight measurement. The relative modal contribution constant gives information on the level of excitation of each individual mode. Further work needs to be done on transient and random flight measurements with varying mean, amplitude and structural properties.

REFERENCES

1. Henry A. Cole, Jr., "On-Line Failure Detection and Damping Measurement of Aerospace Structures by Random Decrement Signatures," NASA CR-2205, 1973.
2. S. R. Ibrahim, "Random Decrement Technique for Identification of Structures," *The AIAA Journal of Spacecrafts and Rockets*, Vol. 14, No. 11, November 1977, pp. 696-700.
3. S. R. Ibrahim and E. C. Mikulcik, "A Time Domain Modal Vibration Test Technique," *Shock and Vibration Bulletin*, Bulletin 43, Part 4, 1973.
4. S. R. Ibrahim and E. C. Mikulcik, "The Experimental Determination of Vibration Parameters from Time Responses," *Shock and Vibration Bulletin*, Bulletin 46, Part 5, August 1976.
5. S. R. Ibrahim and E. C. Mikulcik, "A Method for the Direct Identification of Vibration Parameters from Time Responses," *Shock and Vibration Bulletin*, Bulletin 47, Part 4, September 1977.

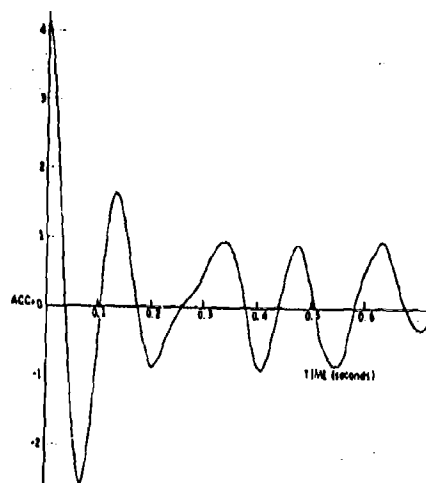


Fig. 1-A - Horizontal tail free decay response.

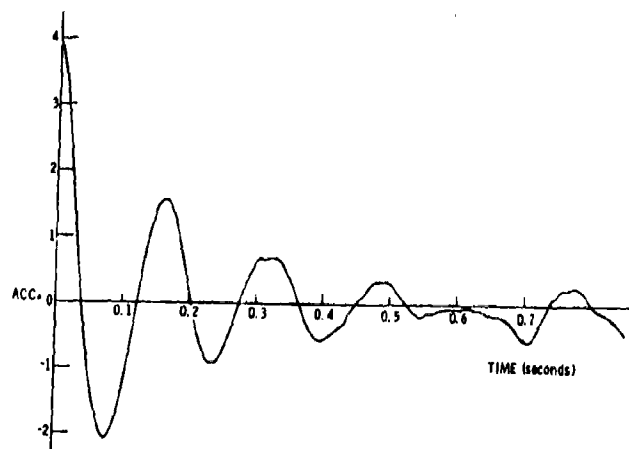


Figure 1-B - Vertical tail free decay response.

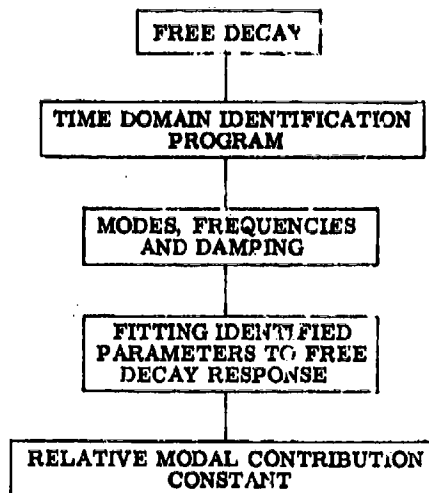


Fig. 2 - Analysis procedure.

TABLE 1
Identified Parameters

Structural Component	Frequency Hz	Damping Factor	"RMCC"	"MCF"	Notes
Horizontal tail	4.31	0.068	6.4	99.5	6.67, 0.102
	6.21	0.140	100.0	100.0	
	10.89	0.223	12.0	98.3	
	11.47	0.031	1.5	99.7	
Vertical tail	4.05	0.062	3.0	99.6	3.9, 0.044
	5.12	0.102	4.4	99.8	
	7.77	0.109	62.2	99.7	
	8.22	0.112	100.0	99.8	
	10.70	0.030	16.0	100.0	8.4, 0.058
	12.07	0.032	6.2	99.7	
	14.46	0.015	1.5	99.5	
	22.60	0.147	4.0	99.4	

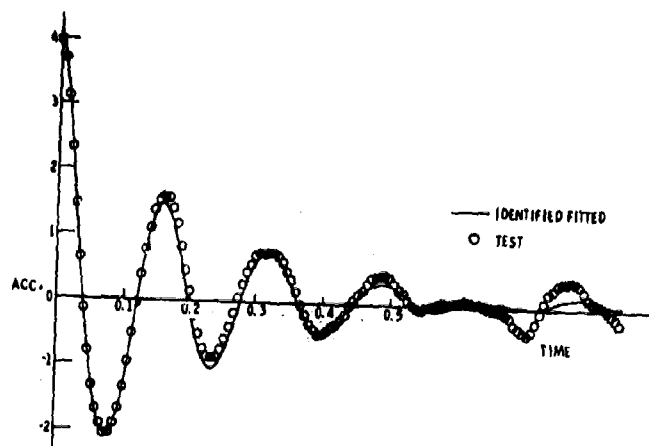


Fig. 3 - Test and identified responses for horizontal tail.

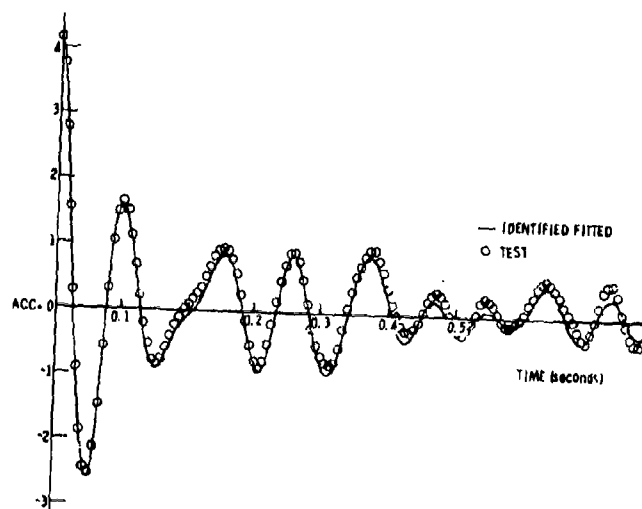


Fig. 4 - Test and identified responses for vertical tail.

SHOCK SPECTRA DESIGN METHODS FOR EQUIPMENT-STRUCTURE SYSTEMS

James M. Kelly

Professor of Civil Engineering
Department of Civil Engineering
Division of Structural Engineering & Structural Mechanics
University of California, Berkeley

Jerome L. Sackman

Professor of Engineering Science
Department of Civil Engineering
Division of Structural Engineering & Structural Mechanics
University of California, Berkeley

ABSTRACT

An analytical method is developed whereby a simple estimate can be obtained of the maximum dynamic response of light equipment attached to a structure subjected to ground motion. The natural frequency of the equipment, modeled as an undamped single-degree-of-freedom system, is considered to be close or equal to one of the natural frequencies of the undamped N -degree-of-freedom structure. This estimate provides a convenient, rational basis for the structural design of the equipment and its installation.

The approach is based on the transient analysis of tuned or slightly detuned equipment-structure systems in which the mass of the equipment is much smaller than that of the structure. It is assumed that the information available to the designer is a design spectrum for the ground motion, fixed-base modal properties of the structure, and fixed-base properties of the equipment. The results obtained are simple estimates of the maximum acceleration and displacement of the equipment. The method can also be used to treat closely spaced modes in structural systems, where the square root of the sum of the squares is known to be invalid.

INTRODUCTION

The design of equipment to withstand dynamic loading is a neglected feature of structural design. Equipment is rarely designed with the same care as the building within which it is housed. A rational approach to one aspect of equipment design, that of relatively light equipment, is presented here. The model considered is an undamped N -degree of freedom structure to which is attached an undamped single-degree-of-freedom component. The frequency of the latter can be higher than the fundamental frequency of the structure. In previous work [1], we have described the response of such a system to steady-state ground shaking. Significant interaction effects were shown to occur in the case of tuning, the situation in which the equipment frequency is close or equal to one of the natural frequencies of the structure. If the equipment frequency is not tuned to a structural frequency, the response is roughly the superposition of the structural response and the equipment response with

little interaction, in which case the conventional floor spectrum method should be valid for transient problems. If, on the other hand, the equipment frequency is tuned to a structural frequency, it was found that for the combined system there are two closely spaced frequencies on either side of the tuning frequency around which a band of high amplification appears, offering a substantial target for sympathetic oscillation. The significant equipment-structure interaction in this case means that the conventional floor spectrum method, which ignores that interaction, will not be valid for the transient analysis problem.

In this paper the previous research is extended to transient analysis of the equipment-structure interaction problem. The peak response of the equipment is estimated by utilizing a design spectrum for a specified input to the structure, and fixed-base dynamic properties of the structure alone and of the equipment alone. By taking advantage of the mathematical structure of the equations and of asymptotic methods made possible by

the smallness of the equipment mass in comparison with the structure mass, we obtain simple results that are valid for tuned and nearly tuned systems.

The rationale for using design spectrum methods is that they are inexpensive and to a certain extent incorporate the probabilistic nature of the problem, i.e., the uncertainty involved in specifying the structural parameters and the ground shock input. These uncertainties are accounted for in constructing a design spectrum and also in the way that the maximum values in each mode are combined to predict the maximum for the entire system.

For light equipment, the results obtained can be implemented easily and efficiently by a designer. A surprising feature of the analysis is its extreme simplicity; namely, if the response spectrum for the ground motion is available, the response spectrum for the equipment can be calculated merely by multiplying the former by an amplification factor.

ANALYSIS OF EQUIPMENT-STRUCTURE SYSTEMS

In this section we formulate the equations of motion governing the response of a general undamped N -degree-of-freedom structure to which is attached equipment modeled as an undamped single-degree-of-freedom oscillator (Figure 1).

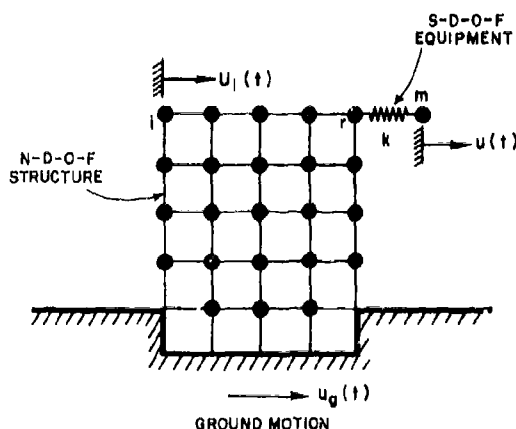


FIGURE 1 EQUIPMENT-STRUCTURE SYSTEM

The equations of motion of the N -degree-of-freedom structural system take the form

$$\sum_{j=1}^N (M_{ij} \ddot{U}_j + K_{ij} U_j) = \sum_{j=1}^N K_{ij} R_j u_x + F e_i \quad (1)$$

where $i=1, 2, \dots, N$ and M_{ij} and K_{ij} are the mass and stiffness matrices, respectively. The vector R_i is a vector of influence coefficients introduced to couple the actual ground motion $u_x(t)$ to the structure, and e_i a vector whose components are zero at every degree of freedom except the one to which the equipment is attached, denoted by the index r , where it takes unit value. The term F is the interaction force between the equipment and the structure.

The natural frequency Ω_n and mode shape Φ_n^i of the n^{th} mode ($n=1, 2, \dots, N$) are obtained from the equations

$$\Omega_n^2 \sum_{j=1}^N M_{ij} \Phi_j^n = \sum_{j=1}^N K_{ij} \Phi_j^n \quad (2)$$

where $i=1, 2, \dots, N$. Equation (1) in modal coordinates is

$$\ddot{q}_k + \Omega_k^2 q_k = \sum_{i=1}^N \Phi_i^k F_i / M_k \quad (3)$$

where $k=1, 2, \dots, N$ and

$$M_k = \sum_{i=1}^N \sum_{j=1}^N \Phi_i^k \Phi_j^k M_{ij}$$

$$F_i = \sum_{j=1}^N K_{ij} R_j u_x + F e_i$$

with M_k the generalized mass. The Laplace transform of the structural response $U_i(t)$ is given by

$$\bar{U}_i = \sum_{k=1}^N \frac{\sum_{j=1}^N \Phi_j^k \Phi_i^k \bar{F}_j}{M_k (p^2 + \Omega_k^2)} \quad (4)$$

where

$$\bar{F}_i = \sum_{j=1}^N K_{ij} R_j \bar{u}_x + \bar{F} e_i$$

where p is the Laplace transform parameter and a bar above a function denotes its Laplace transform. The corresponding equation of motion for the equipment displacement u is

$$-m\ddot{u} = F = k(u - U_r) \quad (5)$$

or, in Laplace transforms,

$$-p^2 \bar{u} = \frac{\bar{F}}{m} = \omega^2 (\bar{u} - \bar{U}_r) \quad (6)$$

where m and k are the mass and stiffness of the equipment, respectively. A relationship between u and U_r is obtained from Eq. (6) in the form

$$(p^2 + \omega^2) \bar{u} = \omega^2 \bar{U}_r \quad (7)$$

which, from Eq. (4), can be written as

$$\bar{u} (p^2 + \omega^2) = \omega^2 \sum_{k=1}^N \frac{\sum_{i=1}^N \Phi_i^k \Phi_r^k [\bar{F}_i + \sum_{j=1}^N K_{ij} R_j \bar{u}_x]}{M_k (p^2 + \Omega_k^2)}$$

Since $\bar{F} = -mp^2 \bar{u}$, \bar{F} can be eliminated. The final transformed equation for the equipment response is then

$$\bar{u} \left[(p^2 + \omega^2) + \sum_{k=1}^N \frac{mp^2 \omega^2 \Phi_r^k \Phi_i^k}{M_k (p^2 + \Omega_k^2)} \right] = \omega^2 \sum_{k=1}^N \frac{\Phi_r^k \sum_{i=1}^N \Phi_i^k \sum_{j=1}^N K_{ij} R_j}{M_k (p^2 + \Omega_k^2)} \bar{u}_x \quad (8)$$

The expression $\sum_{i=1}^N K_{ij} \Phi_i^k$ can be written as $\Omega_k^2 \sum_{i=1}^N M_{ij} \Phi_i^k$; thus the solution for \bar{u} for the multi-degree-of-freedom system takes the form

$$\bar{u} \left[(p^2 + \omega^2) + p^2 \sum_{i=1}^N \frac{m \Phi_i^2 \omega^2}{M_i (p^2 + \Omega_i^2)} \right] = - \omega^2 \sum_{i=1}^N \frac{\Omega_i^2 \Phi_i^2 \sum_{j=1}^N \Phi_j^2 M_j R_j}{M_i (p^2 + \Omega_i^2)} \bar{u}_k \quad (9)$$

The zeroes of the term in brackets on the left-hand side of the equation must be determined to invert the Laplace transform by residue theory. These zeroes are the poles of the transfer function for the equipment response. The case considered here is that illustrated in Fig. 2, where the equipment frequency is close to a structural frequency, say Ω_n . The two expressions in the brackets on the left-hand side of Eq. (9) have been plotted separately; p was replaced by $i\Omega$ and the graph of the second function and the negative of the first function in the bracketed expression were then drawn. The plot for the first function is a simple quadratic in Ω , zero when $\Omega = \omega$, the natural frequency of the equipment. The plot for the summation is a complicated curve that reaches $\pm \infty$ when $\Omega = \Omega_k$ and $k=1, 2, \dots, N$, the natural frequencies of the structure. Two such curves have been plotted, one for equipment of small mass, and another for equipment of larger mass.

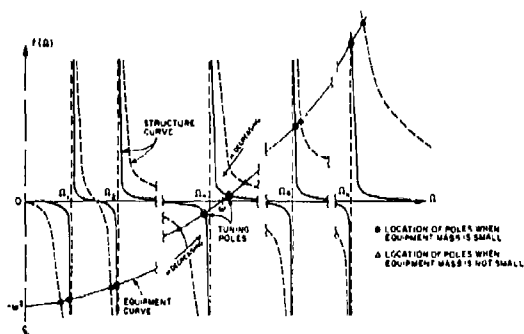


FIGURE 2 LOCATION OF POLES OF EQUIPMENT RESPONSE TRANSFER FUNCTION

The values of Ω at the intersections of these two curves locate the zeroes in the bracketed expression, where equipment-structure interaction is considered. When the equipment mass is small, these poles, all of which are simple, appear near the natural frequencies of the structure. Two closely spaced poles, referred to herein as tuning poles, are located near the equipment frequency and the frequency of the structure to which the equipment is nearly tuned, one below these frequencies and one above them as shown in the figure. These two poles coalesce into a double pole when $\omega = \Omega_n$ and $m \rightarrow 0$. Thus, the contribution to the sum of the residues at all poles is dominated by the residues associated with the two tuning poles. The contribution of the summation term to the residues at these two poles is dominated by the term where $k=n$ since the denominator of that term is nearly zero. Hence, in the region of $p = i\omega$, Eq. (9) can be approximated by

$$\bar{u} \left[(p^2 + \omega^2) + p^2 \frac{m}{M_n / (\Phi_n^2)} \cdot \frac{\omega^2}{p^2 + \Omega_n^2} \right] = - \frac{\omega^2 \Omega_n^2}{p^2 + \Omega_n^2} \left[\sum_{i=1}^N \Phi_i^2 \Phi_n^2 M_i R_i / M_n \right] \bar{u}_k \quad (10)$$

This expression is identical to that for a two-degree-of-freedom system, as shown in Fig. 3. The equivalent expression for the system shown in that figure is

$$\bar{u} \left[(p^2 + \omega^2) + p^2 \gamma \frac{\omega^2}{p^2 + \Omega^2} \right] = \left[\frac{\omega^2 \Omega^2}{p^2 + \Omega^2} \right] \bar{u}_k \quad (11)$$

where $\gamma = m/M$ is the mass ratio. When we compare this expression to Eq. (10), we see that the effective mass ratio is

$$\gamma^{eff} = \frac{m}{M_n / (\Phi_n^2)} \quad (12)$$

and the effective ground motion

$$u_k^{eff} = C_k^* u_k \quad (13)$$

where

$$C_k^* = \Phi_k^2 \sum_{i=1}^N \sum_{j=1}^N \Phi_i^2 M_i R_j / M_n \quad (14)$$

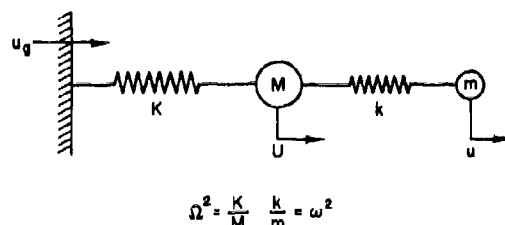


FIGURE 3 TWO-DEGREE-OF-FREEDOM SYSTEM

In the subsequent development, the contribution of the residues from the tuning poles (which are near $p = i\omega$) will be obtained from an analysis of the equivalent two-degree-of-freedom system defined by the above equations. The contributions at the other $(N-1)$ poles are straightforward and will be considered after the two-degree-of-freedom analysis has been completed. Although it is not essential that an equivalent two-degree-of-freedom system be considered, since it is only conceptual and introduces no further approximations beyond those made in passing from Eq. (9) to Eq. (10), the following development will be for such a system in order to simplify notation. We will use the notation of expression (11). Thus, Ω will refer to Ω_n , and γ and u_k to γ^{eff} and u_k^{eff} , as defined in Eqs. (12) and (13).

The transformed equipment acceleration $\bar{u}(p)$ for the equivalent two-degree-of-freedom system takes, from Eq. (11), the form

$$\bar{u} = [N(p)/D(p)] \bar{u}_k \quad (15)$$

where

$$N(p) = (1 + \xi)^2 \omega^4 \quad (16)$$

and

$$D(p) = p^4 + \omega^2 p^2 [2 + \gamma + 2\xi + \xi^2] + \omega^4 (1 + \xi^2)^2 \quad (17)$$

In the above $\xi = (\Omega - \omega)/\omega$ is the detuning parameter. The following discussion concentrates on equipment acceleration; results for equipment displacement can be easily developed.

The nature of the solution strongly depends on the location of the zeroes of the denominator $D(p)$. These are given by

$$p = \pm i\omega \left(1 + \frac{\gamma}{2} + \xi + \frac{\xi^2}{2} \right) \pm \left(\gamma + \xi^2 + \gamma\xi + \xi^3 + \frac{\gamma^2}{4} + \frac{\xi^4}{4} + \frac{\gamma\xi^2}{2} \right)^{1/2} \quad (18)$$

Since the analysis is concerned with light equipment which is only slightly detuned, we take $\gamma^{1/2}$ and ξ to be of the same order and $\ll 1$. Thus, to dominant order, the four roots are

$$p_{1,2} = i\omega \left[1 + \frac{\xi}{2} \pm \frac{1}{2}(\gamma + \xi^2)^{1/2} \right] \quad (19)$$

and the corresponding complex conjugates of p_1 and p_2 .

The formal inversion of the transform expression (15) is

$$\ddot{u}(t) = \frac{1}{2\pi i} \int_{\Gamma} \frac{N(p)}{D(p)} \ddot{u}_g(p) e^{pt} dp \quad (20)$$

where Γ is a suitable Bromwich path. If $\ddot{u}_g(p)$ is taken to be 1, then the inversion directly yields Green's function $\ddot{u}_G(t)$ for the solution, the essential component of the subsequent analysis. The complete solution for the equipment acceleration for given ground motion $\ddot{u}_g(t)$ will take the form

$$\ddot{u}(t) = \int_0^t \ddot{u}_G(t-\tau) \ddot{u}_g(\tau) d\tau \quad (21)$$

Green's function will be obtained by residue theory, since there are no branch cuts in the p plane. The inversion of the transformed Green's function is obtained by evaluating the residues at each pole, Eq. (19), and collecting complex conjugate terms in pairs. To dominant order,

$$\ddot{u}_G(t) = -\frac{\bar{\omega}}{(\gamma + \xi^2)^{1/2}} \cos \bar{\omega} t \sin \eta t \quad (22)$$

where

$$\bar{\omega} = (1 + \xi/2)\omega = (\omega + \Omega)/2$$

$$\eta = (\gamma + \xi^2)^{1/2}\omega/2$$

This function represents an undamped beat solution with the beat frequency η much smaller than the tuning frequency ω .

APPLICATION TO EQUIPMENT MOUNTING DESIGN

The results given in Eqs. (21) and (22) could in principle be used by a designer of equipment mounting if a specified ground acceleration history were available to estimate the forces that would develop in the equipment or its mounting. However, such information is not readily available and the numerical evaluation of these integrals may be inconvenient during the design process. Commonly, a designer begins with a design spectrum that

may be specified by a code or determined by averaging several possible inputs. We are thus interested in determining the extent to which Eqs. (21) and (22) can be used to obtain estimates of maximum acceleration when the information available is the response spectrum of the ground motion \ddot{u}_g . In a previous paper for the undamped perfectly tuned case [2] we considered a number of alternative approaches. Of these the approach termed the amplified ground motion spectrum method was found to be the only practical procedure. This can be extended readily to the present situation.

When Green's function, Eq. (22), is substituted into Eq. (21), the response is given by

$$\ddot{u}(t) = -\frac{\bar{\omega}}{(\gamma + \xi^2)^{1/2}} \int_0^t \ddot{u}_g(\tau) \sin \eta(t-\tau) \cos \bar{\omega}(t-\tau) d\tau \quad (23)$$

The term $\sin \eta(t-\tau)$ is expanded, leading to

$$\ddot{u}(t) = -\frac{\bar{\omega}}{(\gamma + \xi^2)^{1/2}} \sin(\eta t - \theta) \left\{ \left[\int_0^t \ddot{u}_g(\tau) \cos \eta \tau \cos \bar{\omega}(t-\tau) d\tau \right]^2 + \left[\int_0^t \ddot{u}_g(\tau) \sin \eta \tau \cos \bar{\omega}(t-\tau) d\tau \right]^2 \right\}^{1/2} \quad (24)$$

where

$$\theta = \tan^{-1} \frac{\int_0^t \ddot{u}_g(\tau) \sin \eta \tau \cos \bar{\omega}(t-\tau) d\tau}{\int_0^t \ddot{u}_g(\tau) \cos \eta \tau \cos \bar{\omega}(t-\tau) d\tau} \quad (25)$$

We are interested in situations where the ground motion has prescribed finite duration and for those frequencies ω where the maximum response of a single-degree-of-freedom oscillator, i.e. the response spectrum, is achieved late in or after the termination of the ground motion. These frequencies correspond to peaks in the response spectrum. Design spectra, reflecting the probabilistic motion of the input, correspond closely to the peaks of actual spectra and thus presuppose late-occurring maxima. When ground motion is caused by a blast, which is of short duration, it is likely that the maxima of equipment response will occur long after the ground motion has ended.

Thus, for $\eta t_1 = 2\pi t_1/T \ll 1$, where t_1 is the duration of the ground motion and T is the beat period of the system, the first integral in Eq. (24) can be approximated by

$$\int_0^t \ddot{u}_g(\tau) \cos \bar{\omega}(t-\tau) d\tau \quad (26)$$

and the second neglected since $\sin \eta t$ will be bounded by $\eta t_1 \ll 1$, and $\ddot{u}_g = 0$ for $t > t_1$. For $\eta t_1 \ll 1$, then, we have

$$\ddot{u}(t) = -\frac{\bar{\omega}}{(\gamma + \xi^2)^{1/2}} \sin \eta t \int_0^t \ddot{u}_g(\tau) \cos \bar{\omega}(t-\tau) d\tau \quad (27)$$

The term in the integral is a function that oscillates with frequency $\bar{\omega}$, which is high compared to η , and a maximum of that will nearly coincide with the maximum of $\sin \eta t$. Thus, an estimate of the maximum value of $\ddot{u}(t)$ is

$$|\ddot{u}|_{\max} = \frac{\dot{\omega}}{(\gamma + \xi^2)^{1/2}} \max \left| \int_0^t \ddot{u}_g(\tau) \cos \omega(t-\tau) d\tau \right| \quad (28)$$

We recognize that

$$\max \left| \int_0^t \ddot{u}_g(\tau) \cos \omega(t-\tau) d\tau \right|$$

is the undamped relative velocity response spectrum, which is very nearly the pseudo-velocity response spectrum $S_1(\dot{\omega})$, for a single-degree-of-freedom system with frequency $\dot{\omega}$. Accordingly, we obtain the following estimate of maximum acceleration

$$|\ddot{u}|_{\max} = \frac{\dot{\omega}}{(\gamma + \xi^2)^{1/2}} S_1(\dot{\omega}) \quad (29)$$

If the displacement and pseudo-acceleration undamped response spectra as functions of frequency ω are denoted by $S_D(\omega)$ and $S_A(\omega)$ and since $S_D = S_1/\omega$ and $S_A = \omega S_1$, then alternative estimates are

$$|u|_{\max} = \frac{S_D(\dot{\omega})}{(\gamma + \xi^2)^{1/2}} \quad (30)$$

and

$$|\ddot{u}|_{\max} = \frac{S_A(\dot{\omega})}{(\gamma + \xi^2)^{1/2}} \quad (31)$$

If a designer is given only the response spectrum of the ground motion, the maximum displacement and force in the equipment can be estimated by using these spectra amplified by the factor $(\gamma + \xi^2)^{-1/2}$. These remarks refer to the equivalent two-degree-of-freedom system. Results for the general system are obtained by utilizing the factors in Eqs. (12), (13), and (14).

The simplicity of the result can be explained on physical grounds. In weakly coupled systems with the same frequency, the response of the system involves a perfect energy exchange between each component at a beat frequency much lower than the natural frequency of each component. The same phenomenon -- a classical beat phenomenon -- occurs here. The coupling is weak because the ratio of equipment mass to structure mass is small.

When a structure is subjected to a ground motion, the velocity imparted to the structure is mass-independent and determined only by the ground motion. Thus, if the same ground motion were applied directly to tuned equipment, the same velocity would be transmitted to it. Kinetic energy, on the other hand, is proportional to the mass of the system excited; in equipment, that energy would be much smaller than in a structure. However, if the equipment were attached to a structure and the structure subjected to a ground motion, the kinetic energy imparted to the latter would subsequently be wholly transmitted to the equipment, if tuned, and the velocity imparted would be amplified by the reciprocal of the square root of the mass ratio.

Damping is clearly important in this process because the energy transfer requires many cycles and much of the kinetic energy in a damped system could be dissipated before being transmitted. The transient analysis of damped tuned and nearly tuned systems will be developed in future work.

COMPLETE SOLUTION INCLUDING OTHER POLES

Equations (30) and (31) give the dominant equipment response, corresponding to the contributions from the tuning poles, but contributions from the other poles can be easily computed. To do so, recall that the nontuning poles of Eq. (9) are close to their location for the structure alone, as indicated in Fig. 2. The poles for the m^{th} nontuned mode are nearly

$$p = \pm i\Omega_m \quad (32)$$

If we evaluate the residues and drop negligible terms, we obtain, to dominant order, the contribution from the m^{th} structure poles as

$$\frac{C_r^m}{1 - (\Omega_m/\omega)^2} \Omega_m \sin \Omega_m t \quad (33)$$

where $m \neq n$.

Nondominant contributions of the same order from the tuning poles are

$$\sum_{\substack{m=1 \\ m \neq n}}^N \frac{C_r^m}{1 - (\omega/\Omega_m)^2} \omega \sin \omega t \quad (34)$$

where C_r^m is defined in Eq. (14). The complete solution for the response of the equipment then takes the form

$$\ddot{u}(t) = \int_0^t \ddot{u}_g(\tau) \left\{ \sum_{\substack{m=1 \\ m \neq n}}^N \frac{C_r^m}{1 - (\Omega_m/\omega)^2} \Omega_m \sin \Omega_m(t-\tau) + \sum_{\substack{m=1 \\ m \neq n}}^N \frac{C_r^m}{1 - (\omega/\Omega_m)^2} \omega \sin \omega(t-\tau) + \ddot{u}_g(t-\tau) \right\} d\tau \quad (35)$$

where $\ddot{u}_g(t)$ is given in Eq. (22).

The character of the two parts of the solution in Eq. (35) differs. The contributions from the nontuning poles and the nondominant contributions from the tuning poles are conventional and would attain their peaks during the ground excitation or shortly thereafter. The dominant response from the tuning poles, on the other hand, is controlled by the energy transfer from the structure to the equipment through beating, which takes a relatively long time. The latter contribution achieves its peak value considerably later than the former and they should be treated as separate maxima. The maximum response from the nondominant contributions can be estimated by the conventional square root of the sum of squares method.

Accordingly, the estimate of the maximum acceleration has two parts, namely, an early peak given by

$$|\ddot{u}|_{\max} = \left\{ \sum_{\substack{m=1 \\ m \neq n}}^N \left[\frac{C_r^m}{1 - (\Omega_m/\omega)^2} S_A(\Omega_m) \right]^2 + \left[\sum_{\substack{m=1 \\ m \neq n}}^N \frac{C_r^m}{1 - (\omega/\Omega_m)^2} S_A^2(\omega) \right]^2 \right\}^{1/2} \quad (36)$$

and a later peak, from the dominant contribution of the tuning poles, given by

$$|\ddot{u}|_{\max} = \frac{|C_n''|}{(\gamma'' + \xi^2)^{1/2}} S_n \left(\frac{\omega + \Omega_n}{2} \right) \quad (37)$$

The detuning parameter is $\xi = (\Omega_n - \omega)/\omega$, and γ'' is given by Eq. (12). For light equipment and closely tuned systems, the second peak is likely to be more important. However, the early peak may be the larger and both should therefore be evaluated.

The methods developed here can also be used to estimate the peak response of grossly detuned systems, i.e., where the equipment frequency is far from all structural frequencies, and will be given in future work. The advantages of this approach are its simplicity and adaptability for practical application. A great deal of computational effort is avoided since time history analyses need not be performed. The equipment-structure system need not be analyzed as an $N+1$ -degree-of-freedom system either by modal or matrix-time-marching methods, and errors in estimates of peak response due to the possible unreliability of numerical time-integration schemes, or to uncertainty as to the appropriate procedure for summing the contributions of the two closely spaced modes, are thereby avoided. For tuned and nearly tuned systems the method accounts for the important effect, neglected in the floor spectrum method, of equipment-structure

interaction. The method advanced here does not require new information to be generated. Data available from the building design alone, the equipment alone, and the ground shock spectra are used.

ACKNOWLEDGMENT

This research was partially supported by the National Science Foundation under Grant No. ENG 77-05197, and by the Defense Nuclear Agency of the United States Department of Defense under Contract DNA001-C-0233 with Weidlinger Associates, Menlo Park, California, which support is gratefully acknowledged.

REFERENCES

- [1] J. M. Kelly and J. L. Sackman, Equipment-structure interaction at high frequencies, *Report No. DNA 42987*, Weidlinger Associates, Menlo Park, California (1977).
- [2] J. M. Kelly and J. L. Sackman, Response spectra design methods for tuned equipment-structure systems, *Journal of Sound and Vibration*, Vol. 59, 171-181 (1978).

A COMPUTATIONAL MODEL DESCRIBING THE INITIATION OF
SILVER ACETYLIDE-SILVER NITRATE EXPLOSIVE BY AN INTENSE LIGHT SOURCE*

Floyd H. Mathews †
Sandia Laboratories †
Albuquerque, New Mexico 87185

The surface initiation of Silver Acetylide-Silver Nitrate explosive is studied. Initiation occurs when the explosive is exposed to irradiation produced by an electrical discharge through an array of tungsten wires, each surrounded by an air-filled Pyrex tube. The initiation process is modeled by first calculating the wire heating and subsequent arc breakdown. Then the arc energy is allowed to reradiate toward the explosive surface using a characteristic relaxation time. Finally the thermal initiation of the explosive surface is modeled as the conductive transfer of heat through a surface layer of inert explosive which had previously been darkened by exposure to the sun. Initiation occurs when active explosive reaches a critical temperature. A number of unknown parameters are accommodated by normalizing the calculation to agree with the time delay before firing which was measured during a single experiment.

Reasonable agreement is obtained between calculated and measured values of the current time history during the electrical discharge, and a similar agreement is obtained between measured and calculated irradiance time histories. Calculated explosive initiation times are also reasonably close to measured values over a range of test conditions. Parametric studies indicate that the initiated area may be increased by a factor of 3.5 by modifications to the electrical circuit while maintaining present initiation conditions.

INTRODUCTION

Laboratory nuclear effects testing allows the study of weapon response to simulated exoatmospheric x-ray encounters. Coatings of the primary explosive Silver Acetylide-Silver Nitrate (SASN) are employed in our laboratory to study the mechanical response of structures to externally applied impulsive loads [1-4]. This process involves spray painting the surface to be loaded with carefully controlled thin layers of explosive.

The explosive is then exposed to sunlight (suntanning) causing a surface darkening of the outer layer of the explosive. When exposed to an intense flash of light the explosive is detonated nearly simultaneously on its surface, and an impulse load is imparted to the structure within a few microseconds. The suntanned explosive exhibits a more uniform initiation

pattern than exhibited by untreated white explosive. The local impulse value can be varied over a wide range by appropriate local variations of the explosive mass. Typical values of explosive areal density are 300g/m^2 to yield an impulse of $\sim 200\text{ Pa}\cdot\text{s}$.

Depending upon the expected damage modes of the structure, initiation

*The submitted manuscript has been authored by a contractor of the United States Government under contract. Accordingly the United States Government retains a nonexclusive, royalty-free license to publish or reproduce the published form of this contribution, or allow others to do so, for United States Government purposes.

†A U.S. Department of Energy Facility.

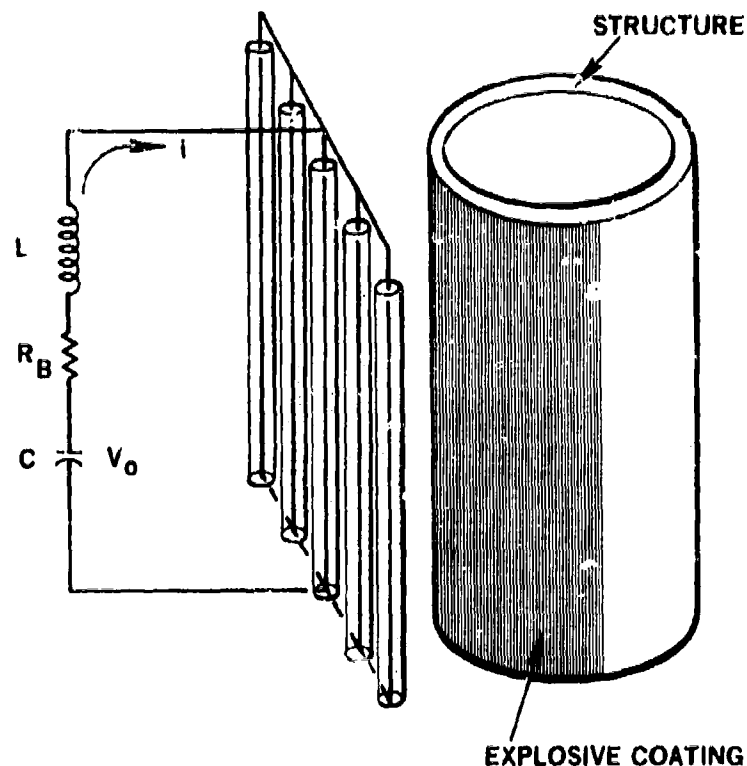


Fig. 1 - Light source and explosive coated structure

simultaneity over widely separated locations on the explosive surface may be permitted to scatter over a range from 1.0 to about 10 μ s. However, in a small local area it is desirable to produce initiation within a scatter of 0.1 to 1.0 μ sec.

In this paper the initiation process is studied. First an analytical model is constructed describing the electrical discharge light source and then this computation is coupled to a model of the process which heats the explosive to its initiation temperature. This model is then made to agree with a single experimental point in order to normalize for physical parameters which are not accurately known. Useful, though not exact, agreement is obtained when comparison is made with additional experimental measurements made for different conditions. Finally, studies are made of various parameters which can be altered through design of the light source. Conclusions resulting from these studies have proven useful during

the design of light sources applied to testing of various structures.

INITIATION PROCESS

One of five units in the modular light source and its capacitor discharge power supply is illustrated schematically in Figure 1 and has been described elsewhere [5]. A typical experiment involves discharging the capacitor which is initially charged to 40 kV through an array of five 0.076 mm diameter tungsten wires 609 mm long and spaced 90 mm apart. The tungsten wires are surrounded by heavy wall Pyrex tubes of 12.7 mm bor. Depending upon test requirements many parameters may be varied. These include wire spacing, wire length, number of capacitor modules, curvature of the light array and the use of white paper reflectors. The setup shown in Figure 1 is typical of all experiments described in this paper and is fairly typical of a structural testing arrangement. The explosive

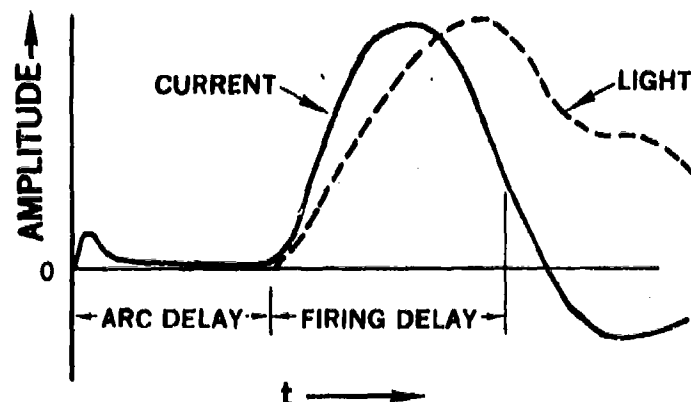


Fig. 2 - Current and light waveforms

surface is ordinarily placed within approximately one wire spacing from the light source in order to realize a reasonably uniform light flux and acceptably small radiant loss at the edges.

When the capacitor bank is triggered, the current waveform follows the time history illustrated schematically in Figure 2. During the arc delay, all current passes through the tungsten wire, causing it to heat from the solid state up through the onset of vaporization. Corresponding nearly to the instant of wire surface vaporization, the current transfers from the high resistance wire to an arc which forms in the surrounding air and grows to fill the entire Pyrex envelope. During the period of arc growth the circuit resistance drops to a low value resulting in a current waveform characteristic of an underdamped discharge. Even with the rapidly decreasing resistance as current transfers from the wire to the arc, current is shared approximately uniformly between the different parallel arcs which form within a jitter of 1 μ s. Glass tubes serve to confine the arc, thus increasing circuit resistance in comparison to an unconfined discharge. Shattering is avoided if peak currents are below 30 k amps in each arc.

Energy is radiated in all directions at a rate dependent upon the arc energy density and the arc size. The resulting radiated light energy follows the current waveform illustrated in Figure 2, lagging somewhat behind as a result of energy storage in the heated gas. Radiated energy is lost through

absorption in the Pyrex envelopes, and is lost to the sides and to the rear of the fixture. Quartz envelopes improve the efficiency; however, the tubes are frequently damaged by the explosive blast and better economy is achieved by using Pyrex. We have assumed that 40% of the energy emitted by the arc is absorbed in the explosive and that this energy is distributed uniformly over an area equal to the planar area of the light source.

The thermal process believed to cause initiation of the explosive is illustrated in Figure 3. The energy flux radiated by the light source is incident upon the outer surface of darkened explosive. Because of a photo reaction which occurred during exposure to sunlight, this "suntanned" layer is inert to an unknown small depth h . Since most of the energy is deposited on the outer surface, with a small reflective and radiative loss, only those losses associated with geometry, i.e., edge and rear losses, significantly reduce the energy flux. During the small interval while energy is incident upon the receiver surface, but before the explosive has detonated, energy is conducted thermally from the surface through the inert layer toward the active explosive. Eventually the active explosive is heated until a sufficiently high temperature is reached to cause initiation. Somewhat arbitrarily a temperature rise of 200°C above ambient is selected to represent the value causing thermal initiation [6] rather than the higher values suggested for thermally induced cookoff [1] (250°C) or the value suggested by Roth [7] for pulse heating reactions (~600°C) of

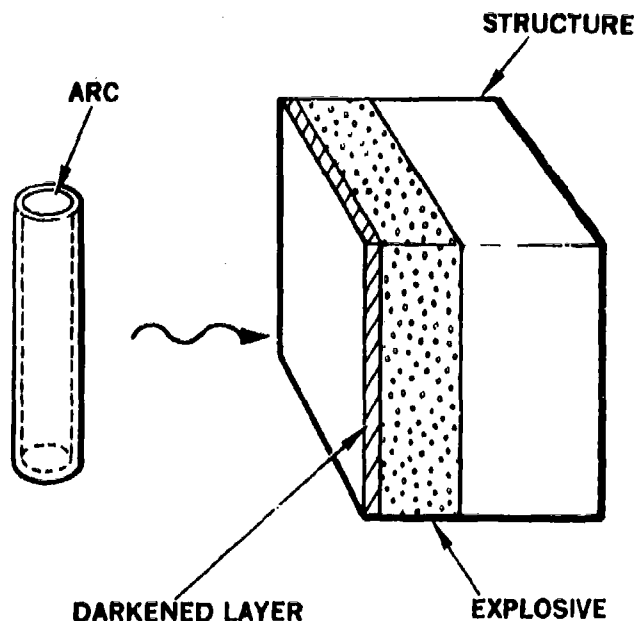


Fig. 3 - Explosive initiation model

lead azide. Normalization of computed results to an experimentally measured firing delay which will be discussed later is intended to compensate for a lack of detailed knowledge of this important parameter.

In the past section, the physical processes which cause explosive initiation have been described. In the next section details of a computational model of this process will be discussed. In formulating this model the goal is to provide a means for investigating the influence of various physical parameters upon the time delay between arc formation and explosive output. With this limited goal, the difficult task of accurately confirming details of the theory is avoided. Instead, estimated values for many of the required physical variables are used and the computed results are normalized to agree with a particular measurement. Thus by adjusting a single parameter, i.e., the unknown thickness of the inert layer of untanned explosive, agreement is forced by using a single experimental measurement. The adequacy of the normalized theory may then be checked by comparison with other experimental measurements. This type of empirical theory is formulated in the next section.

COMPUTATIONAL MODEL

The resistance behavior of wire heated to explosion by a rapid electrical discharge has been extensively studied by Tucker [8,9]. Although his vacuum conditions are not exactly duplicated in our arrangement, the requirement of short time scales, i.e., a few 10's of μ seconds are met and the requirement of adiabatic heating during the electrical discharge is approximately correct. Therefore, the analytical formulation in which the resistivity of tungsten wire $\rho(t)$ varies during the electrical discharge is used in accordance with the value of specific action $g(t)$ as the discharge occurs. Specific action is defined by

$$g(t) = \frac{\int i^2 dt}{A^2} \quad (1)$$

where i is the current, A is the wire area and t is the time. Tucker gives approximate analytical expressions for tungsten in [9] which allow calculation of the resistivity of the wire throughout the discharge. This process includes (1) a solid heating phase, (2) a solid to liquid transition, (3) a liquid heating phase, and (4) a liquid

vapor transition. Thus the variable resistance offered by the wire during the arc delay period is calculated directly as a function of action. In functional form

$$R_w(t) = \frac{\rho(t)l}{A} = \frac{\rho(g(t))}{A} \quad (2)$$

where $R_w(t)$ is the time dependent wire resistance, and l is the wire length. With this information and the circuit equation,

$$L \frac{di}{dt} + (R_B + R_w(t))i + \frac{\int_0^t i dt}{C} = V_0 \quad (3)$$

where L , R_B , C , V_0 are the circuit inductance, bank resistance, capacitance, and initial voltage respectively. Numerical solution of these equations yields the result of Figure 4 for a typical case. When these conditions are repeated experimentally, we find that the current waveforms agree until formation of the arc at 6.3 μ s, which corresponds to the instant when the tungsten wire is just vaporizing on its surface. We conclude that arc formation starts at a specific action of 42500 amp² s/mm².

Once an arc has formed in the gas surrounding the tungsten wire, the resistance afforded by the ionized air is much less than that of the partially vaporized wire. Therefore wire resistance is dropped from the calculation and replaced by the arc resistance.

An appropriate theory for air resistance during arc formation was not found. Instead, in order to continue the calculation, data from [10] was employed which applies specifically for xenon. With this approximation, the resistance of each arc path is given by

$$R_A = \frac{0.127l}{D^2} \quad (4)$$

where l is the arc length in mm, D is the arc diameter in mm, and R_A is the resistance of a single arc in ohms.

The arc growth was observed as a function of time using a streaking camera to obtain the data illustrated in Figure 5. Arc growth rate was found to be a function of initial charge voltage as illustrated in Figure 6. This data approximated a straight line with the equation

$$\frac{dD}{dt} = 2(110000 + 10.89 V_0) \text{ mm/s} \quad (5)$$

where $14,000 \leq V_0 \leq 45,000$ volts,

$D \leq 12.7$ mm and $l = 610$ mm and dD/dt is the rate of arc growth. We assume further that after the arc expands to the tube wall, then the arc remains at the tube diameter. Note that injection of this empirical equation severely restricts the theory since the desirable cause and effect relationship between current and arc size is not permitted.

The arc radiation process is

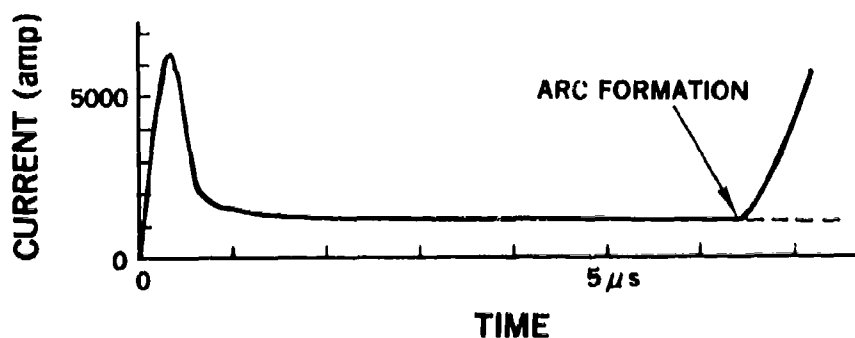


Fig. 4 - Computed current time waveform during arc delay

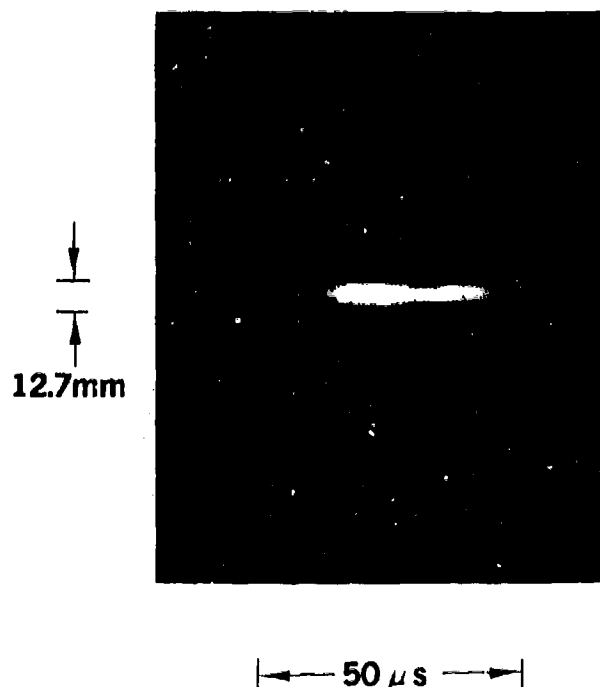


Fig. 5 - Arc size as a function of time

modeled after the methods given in [11] by Hug et. al., who found that a characteristic relaxation time t_r could be defined for various gases radiating energy during an arc discharge. For our tube geometry using air at 85 kPa their results suggest that the relaxation time t_r is given in terms of the arc diameter by

$$t_r = 0.97 \times 10^{-6} D \quad (6)$$

The rate of energy increase E in the arc is given by

$$\frac{dE}{dt} = i^2 R_A - \frac{E(t)}{t_r} \quad (7)$$

where the singularity at $D = 0$ is avoided because the arc must begin at the finite tungsten wire diameter. The term $E(t)/t_r$ represents the time dependent power leaving the arc through radiation. Integration of Equation 7 from the initial zero energy state in the arc allows computation of the time history of the radiated energy. The energy flux $F(t)$ reaching the target

explosive surface is given by

$$F(t) = \eta \frac{E(t)}{t_r A_s} \quad (8)$$

where η is the source efficiency and A_s is source area. Values of η were estimated to be 0.4 when no reflector is used behind the light array and a flat target equal in area to the light source was placed one tube spacing in front of the array. This estimate, which accounts only for geometrical losses, was justified by the very high electrical to optical efficiency measured in [12].

This flux may now be employed to calculate the internal temperature rise resulting from conduction of heat through the inerted explosive layer to the interface between inactive and active explosive. This calculation is made by superposition of the solution given in [13] for the step application of a heat flux to a conducting half space. Then

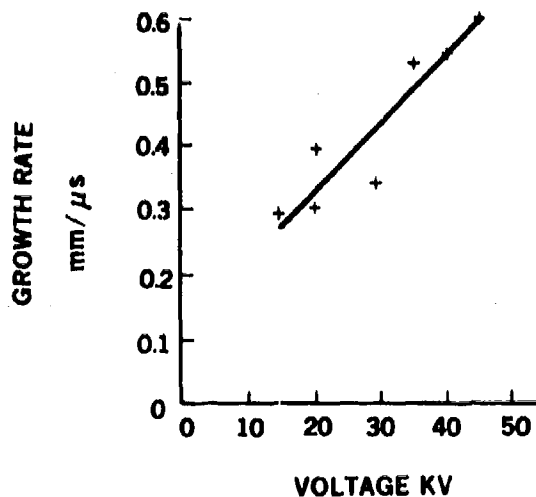


Fig. 6 - Arc growth rate as a function of initial voltage

$$T(h,t) = \frac{2F\sqrt{\alpha t}}{K} \operatorname{ierf} \frac{h}{2\sqrt{\alpha t}} \quad (9)$$

where $T(h,t)$ is the temperature increase at interior location h , α is the thermal diffusivity of the inerted explosive and K is the thermal conductivity. Representative values of $168 \text{ mm}^2/\text{s}$ for diffusivity and $0.02 \text{ J}/(\text{s}^\circ\text{K mm})$ for conductivity were assumed.

Only one parameter remains unknown, the thickness of inert material h . The delay period from arc formation until explosive firing was measured by spraying a 300 g/m^2 coating $\sim 0.55 \text{ mm}$ thick over a quartz pressure gage and measuring both the time of pressure output and the discharge current waveform. With a charge voltage of 40 kV and a test setup similar to Figure 1 using suntanned explosive, a delay period of $20 \mu\text{s}$ was measured between arc formation and explosive pressure output. Agreement between calculated and measured values was obtained when an inert thickness of 0.0095 mm was assumed in the calculation. Thus the theory was normalized to agree with experimental values by selecting a specific value for the unknown inert layer thickness.

Forcing agreement of the calculation and the experiment by selecting a value of one parameter may mask the possibility that values for other important parameters are not accurately

known. In order for the theory to be useful, though only approximately correct, agreement must be demonstrated between calculated and experimental values for other conditions. The next section illustrates the adequacy of this agreement.

COMPARISON TO EXPERIMENT

The ability of the theory to predict the current waveform is illustrated in Figure 7. The current was measured by integrating the signal from a Rigowsky coil placed on the current return path common to all five wires. Measured values of R_E , L , and C were used in the calculation and the value of action representing arc formation was adjusted to force agreement between observed and computed delay time before arc formation. This relatively good agreement between computed and observed waveshapes was repeated for similar comparisons as the initial bank voltage was varied between 14 kV and 45 kV .

A comparison between measured and computed optical irradiance time histories both normalized to a peak value of 1 is shown in Figure 8. Again the relatively good agreement in waveshape is encouraging. The optical instrument, a bhargmeter of a type specialized for nuclear effects testing, was located 30 meters from the source. Almost an order of magnitude lower peak

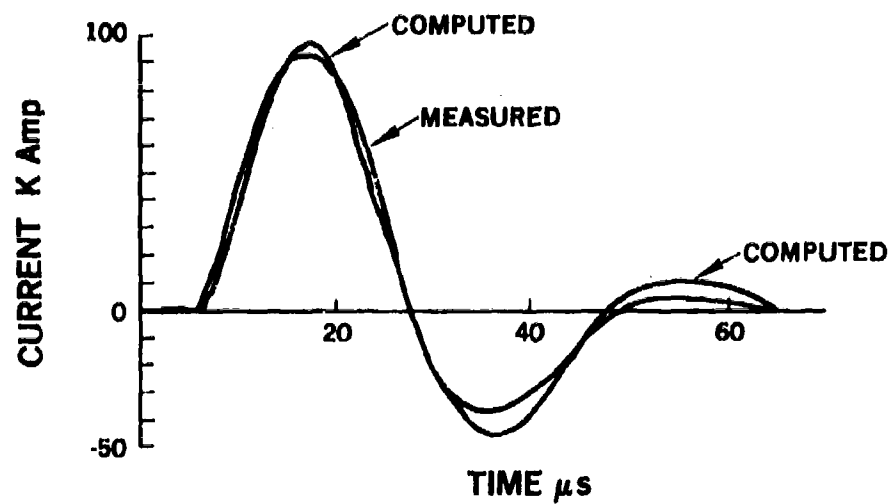


Fig. 7 - Comparison between measured and computed total current waveforms

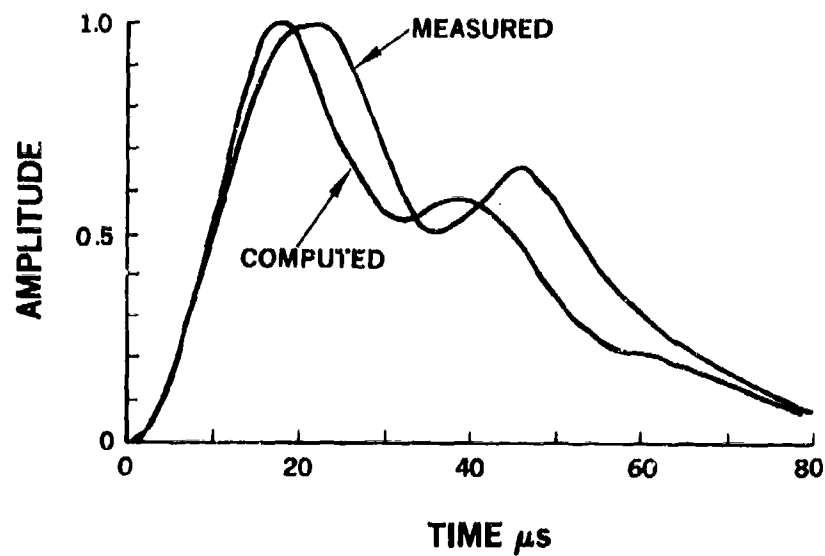


Fig. 8 - Comparison of computed and measured normalized light flux waveforms

Table I
Measured and Computed Arc Delay Time

Charge Voltage (kV)	Delay Time (μ s)		
	Measured	Computed	Ratio
45	5.4	5.2	0.96
40	6.6	6.6	1.00
28	12.4	13.8	1.12
20	23.9	27.8	1.16
14	50.6	60.5	1.20

power was indicated by this instrument than the computed value. Unfortunately, the bhangmeter was available only for a single day, hence, resolution of this important difficulty must await future testing. With this uncertainty and the observation that use of quartz rather than Pyrex has little effect upon the observed initiation density, a 100% efficiency was assumed for the transformations between electrical energy and radiated energy.

The computed delay time for arc formation is compared to the measured time for 0.076 mm diameter wires 609.7 mm long in Table I for a range of initial capacitor voltages. Clearly a time dependent phenomenon which is not included in this theory favors shorter arc delays in those cases where the wire heating is relatively slow.

The most important comparison between computed and measured values is given in Table II where values for the

Table II
Comparison of Computed and Measured Firing Delays

Bank Voltage (kV)	$\frac{E_0}{A^{(1)}}$ (kJ/m ²)	Computed		Measured
		$\frac{dT}{dt}$ (°C/ μ s)	Firing Delay ⁽²⁾ (μ s)	Firing Delay ⁽³⁾ (μ s)
45	85.0	28	18.5	16.0
40	67.1	26	19.8	20.0
28	32.9	15	25.8	24.4
20	16.8	4	41.8	No-Fire
18.2	13.9	0	No-Fire	

- (1) A is the mid plane area of the light source.
- (2) The firing delay time is measured from the instant of arc formation until the instant of explosive initiation.
- (3) Same as 2 above except that explosive initiation corresponds to measured pressure output from a quartz gage covered by explosive.

Table III

Observed Detonation Pattern Spot Densities

Charge Voltage	Computed Temperature Rise Rate	Detonation (1) Spot Density
(kV)	(°C/μs)	(Points/cm ²)
45	28	336
40	26	136
28	15	54
(1) Approximate value		

time delay from arc formation to explosive output are given as a function of voltage. Also, values for the rate of temperature rise, and stored electrical energy per unit of light source area computed at the light source mid plane have been included. The reasonably good comparison between observed and computed firing delay is justification for further use of this model. The observation of a no-fire point measured at 20 kV with no reflector was repeated with a reflector and again a no-fire situation was observed. It is estimated that for these experimental conditions a no-fire threshold would be expected at about 25 kJ/m² initial stored energy. The theory predicts a value of 13.9 kJ/m². No further adjustment of assumed explosive properties, i.e., the diffusivity, was attempted in order to improve agreement.

A further experimental observation is that a pattern of markings is left on the structural surface after explosive firing. These markings result from discrete points of initiation occurring at the interface between active and inert sintered explosive. Hence, when the most favorably situated explosive points are heated to firing conditions, an explosive reaction is started which detonates adjacent explosive by shock wave excitation before a thermally induced reaction takes place. Interaction between detonations radiating from one initiation point with those radiating from an adjacent initiation point cause a pattern of uneven pressure on the target surface which leaves a "detonation spot pattern." Counting this spot pattern is

a somewhat subjective exercise; however, representative data using the setup of Figure 1 is given above in Table III.

The spot pattern is indicative of surface firing simultaneity. For instance, consider a spot pattern where spots are located uniformly about 2.4 mm apart or at 17 points/cm². Then, with the known detonation velocity of 1.2 mm/μs [1], initiation simultaneity cannot be better than 1 μs on the surface. Simultaneity is probably less due to lower detonation rates associated with transition from thermal initiation to full detonation. A specification for acceptable initiation can be derived from these observations. We adopt the results from the 40 kV observations of Table II and Table III as the desired initiation condition where a computed temperature rise rate of 25.9°C/μs at an initiation temperature of 200°C produces a spot density of 136 per cm² and the similar values obtained at 28 kV are adopted as minimum which must be maintained in order to avoid any possibility of initiation failure.

PARAMETER STUDIES

Parametric studies were conducted in order to identify those design variables which might be altered in order to increase the area which could be fired without increasing the capacitor bank size. In all cases the experimental arrangement described in Figure 1 was used as the nominal value

Table IV
Variation of Lamp Diameter

Lamp Diameter (mm)	Area (m ²)	Firing Delay (μs)	$\frac{dT}{dt}$ (°C/μs)	i_{max} (k amp)	i_{min} (k amp)	$\frac{E_0}{A}$ (kJ/m ²)
15.90	0.239	19.5	25.9	98.2	52.0	77.0
12.70 ⁽¹⁾	0.274	20.5	25.9	98.1	43.4	67.2
9.52	0.366	21.1	25.9	95.7	37.0	50.3
6.35	0.527	21.5	25.9	86.0	10.3	34.9

(1) Nominal circuit

Table V
Variation of Wire Number

Number	Area (m ²)	Firing Delay (μs)	$\frac{dT}{dt}$ (°C/μs)	i_{max} (k amp)	i_{min} (k amp)	$\frac{E_0}{A}$ (kJ/m ²)
9	0.222	18.9	25.8	104.9	58.1	82.8
7	0.347	20.4	25.9	102.0	58.1	74.5
5 ⁽¹⁾	0.274	20.5	25.9	98.1	43.4	67.2
3	0.300	20.5	26.0	90.8	29.4	61.3

(1) Nominal circuit

over which improvements are sought. ‡ Usually several iterations were required in order to select the appropriate area which would just reproduce the nominal value of temperature rise rate at the instant of explosive initiation. Results of these iterations are summarized in Tables IV through X.

Reducing the lamp diameter reduces the lamp's characteristic relaxation time resulting in an increased area. Numerical verification is given in Table IV. This improvement is limited by the ability of the tube to withstand arc pressure, a parameter which was not investigated. Heavy wall Pyrex tubes

12.7 mm in diameter will sometimes burst at maximum currents above 30 k amps. A

‡ Nominal values are; Capacitor bank: R = 0.076 ohms, L = 1.59 μH, C = 23. μF, V₀ = 40 kV; Wire: D = 609.6 mm, diameter = 0.076 mm, Number = 5, Arc

action $g = 42500 \frac{\text{amp}^2 \text{s}}{\text{mm}^4}$, Source: Area 0.274 m², Efficiency 0.40, Explosive diffusivity = 168 mm²/S, Conductivity = 0.02 J/(s °C m), Inert layer h = 0.0095 mm.

Table VI
Variation of Wire Length

Length	Illuminated Area (m ²)	Arc Delay (μs)	Firing Delay (μs)	$\frac{dT}{dt}$ (°C/μs)	$\frac{E_0}{A}$ (kJ/m ²)
457.2	0.239	3.8	19.2	25.9	77.0
609.7 ⁽¹⁾	0.274	6.6	20.5	25.9	67.2
812.8	0.290	12.5	20.4	25.8	63.4
(1) Nominal circuit					

Table VII
Variation of Bank Resistance

R (ohms)	Illuminated Area (m ²)	Firing Delay (μs)	$\frac{dT}{dt}$ (°C/μs)
0	.274	19.5	25.8
.0176 ⁽¹⁾	.274	20.5	25.9
.0352	.261	19.7	25.9
(1) Nominal circuit			

second important result is that the negative current, which occurs after explosive initiation, is reduced by smaller tube diameters. Reducing this current amplitude will exhibit the added advantage of reducing instrumentation noise [14] since any current flowing after explosive initiation is likely to cause noise.

Changing the number of wires produced the results of Table V. Only a limited gain is possible since peak currents above 30 k amp/Tube exist when 3 wires are used. Changing the wire length (Table VI) changed the arc delay time but had a small effect upon the firing delay. Increasing the tube length allowed a modest increase in the area. Similarly, variation in the bank resistance, R_B (Table VII) had little effect.

Increasing the speed of the discharge by reducing the inductance (Table VIII) had a significant influence upon the maximum area. This is an important finding of the study because major inductance reduction is possible through carefully executed modifications to the light fixture.

The illuminated area increased with higher charge voltage (Table IX) while the energy per unit area remained relatively constant. The area increase is therefore a result of increased stored energy.

The results shown in Table X indicate the changes in firing time and temperature rise rate which would result from decreasing the spacing of the tubes and thereby decreasing the illuminated area with no other changes in the nominal setup. As the area is reduced,

Table VIII
Variation of Inductance

(μH)	Illuminated Area (m^2)	Firing Delay (μs)	($^{\circ}\text{C}/\mu\text{s}$)	$\frac{E_0}{A}$ (kJ/m^2)
.40	0.432	17.1	25.9	42.6
.80	0.360	18.3	25.9	51.1
1.59 ⁽¹⁾	0.274	20.5	25.9	67.2
4.00	0.147	21.6	25.9	125.2
8.00	0.080	22.9	26.0	1230.0

(1) Nominal circuit

Table IX
Variation of Charge Voltage

V_0	Illuminated Area (m^2)	Firing Delay (μs)	($^{\circ}\text{C}/\mu\text{s}$)	$\frac{E_0}{A}$ (kJ/m^2)
50	.400	20.2	25.8	71.9
45	.336	20.1	25.8	69.3
40 ⁽¹⁾	.274	20.4	25.9	67.2
35	.212	19.4	25.9	66.5

(1) Nominal circuit

significant improvements in temperature rise rate and reduced firing delays are realized. The effect on the stored energy requirement is dramatic and leads to excessively large capacitor banks. An indication of the importance of light intensity variations can also be derived from this table. Thus, if the light intensity were half the nominal value, firing would be delayed 6.6 μs and if light intensity were twice the nominal value firing would be premature by 5.1 μs .

An investigation into an optimized light source is given in Table XI. Here the length to width ratio was held at 1.33, the 9.4 mm tube diameter was selected, the source efficiency was improved to 0.6 by a reflector, and an inductance value of 0.4 μH was used. This type of improvement with a 45 kv initial voltage could potentially increase the illuminated area by a factor of 3.5 while preserving the firing simultaneity typical of existing test experience. These improvements could also be employed to increase the

Table X
Variation of Firing Time and Temperature Rise Rate with Area

Area (m ²)	Firing Delay (μs)	$\frac{dT}{dt}$ (°C/μs)	$\frac{E_0}{A}$ (kJ/m ²)
.0635	12.1	57.47	279.8
.1370	15.3	37.48	134.3
.2740 ⁽¹⁾	20.4	25.88	67.2
.5480	27.0	13.65	33.6
(1) Nominal circuit			

Table XI
Performance of Optimized Light Source

Voltage V ₀ (kV)	Area (m ²)	Delay (μs)	$\frac{dT}{dt}$ (°C/μs)	$\frac{E_0}{A}$ (kJ/m ²)	i _{max} (k amp)
40 ⁽¹⁾	.2740	20.4	25.88	67.2	98.1
40 ⁽²⁾	.7300	19.0	26.18	25.2	94.8
40 ⁽²⁾	.2740	12.2	52.89	67.2	94.8
45 ⁽²⁾	.9640	19.3	25.33	24.2	107.0
45 ⁽²⁾	.2740	11.6	59.56	85.0	107.0
(1) Nominal circuit					
(2) The following changes were made from the nominal circuit -- L = 0.4 μH, N = 0.6, d = 9.52 mm					

temperature rise rate by a factor of 2.0 and thereby reduce the firing delay. Note that these improvements yield maximum currents in each of five lamps of only 21 k amps.

CONCLUSION

An analytical model has been formulated of the processes occurring during the firing of SASN explosive by the discharge of a capacitor bank

through an arc light source. This model is shown to agree reasonably with experiments over a limited range of important variables. When this model is used to study improvements which could be made to the light source, significant improvements to the firing process are predicted. It is concluded that the most significant variables are the circuit inductance and the tube diameter.

ACKNOWLEDGEMENTS

The assistance of B. D. Duggins in Computer Programming and P. B. Higgins and D. Shirey who conducted experiments is gratefully acknowledged.

REFERENCES

1. A. B. Wenzel and W. E. Baker, "The Use of Light-Initiated Explosives for the Impulse Loading of Structures," Institute of Environmental Sciences. Proceedings 1970, pp. 142-150.
2. R. A. Benham and F. H. Mathews, "X-Ray Simulation with Light-Initiated Explosive," The Shock and Vibration Bulletin, No. 45, Part 4, p. 88, June 1975.
3. R. A. Benham, "Simulation of X-Ray Blowoff Impulse Loading on a Reentry Vehicle Aft End Using Light Initiated High Explosive," The Shock and Vibration Bulletin, No. 46, Part 3, p. 183, August 1976.
4. R. A. Benham, F. H. Mathews and P. B. Higgins, "Application of Light-Initiated Explosive for Simulating X-Ray Blowoff Impulse Effects on a Full Scale Reentry Vehicle," The Shock and Vibration Bulletin, No. 47, 1977, Supplement.
5. P. B. Higgins, "An Arc Source for Initiating Light-Sensitive Explosives," The Shock and Vibration Bulletin, No. 46, Part 3, p. 191, 1977.
6. M. A. Cook, The Science of High Explosive, Reinhold, 1958.
7. J. Roth, "Initiation of Lead Azide by High Intensity Light," The Journal of Chemical Physics, Vol. 41, No. 7, October 1964, pp. 1929-1936.
8. T. J. Tucker, "A Theoretical Model of the Resistance Behavior of Exploding Wires," SC-RR-71 0739, January 1972, Sandia Laboratories Research Report.
9. T. J. Tucker and T. J. Toth, "EBW1 - Computer Code for Predicting the Behavior of Electrical Circuits Containing Exploding Wire Elements," SAND75-0041.
10. J. H. Goncz, "Resistivity of Xenon Plasma," Journal of Applied Physics 36: 742-743, March 1965.
11. W. F. Hug, J. F. Shaw and R. D. Buhler, "Nonsteady Model for Pulsed Arc Discharge Radiation Sources," Applied Optics, June 1973.
12. H. K. Aslin, "Measurement of Radiant Energy Emitted by Xenon Flashlamps," Rev. Sc. Instrum., Vol. 38, No. 3.
13. H. S. Carslaw, J. C. Yeager, Conduction of Heat in Solids, Oxford Press, Second Edition, 1969.
14. P. B. Higgins, "A Convenient Method of Increasing the Circuit Damping Produced by an Exploding Foil," Rev. Sc. Instrum., Vol. 45, No. 4, April 1974, p. 602.

TERMINAL VELOCITY AND ROTATION RATE OF A FLYER PLATE PROPELLED

BY A TUBE-CONTAINED EXPLOSIVE CHARGE*

R. A. Benham
Sandia Laboratories
Albuquerque, New Mexico 87185

A method for predicting the terminal velocity and rotation rate of a flyer plate propelled by an open-ended, tube-contained explosive charge has been developed. A procedure for calculating the fraction of the explosive that is effective in accelerating the plate leads to a very simple set of equations for predicting the performance of the explosive system. Calculations using this theory are compared with results from numerous experiments. Measured values of flyer velocity are predicted within $\pm 5\%$ and rotation rates with $\pm 10\%$.

INTRODUCTION

Experiments employing open-ended, tube-contained explosive charges to propel intact flyer plates to high terminal velocity are currently being employed to study weapon fuzing under conditions simulating high velocity impact into hard earth targets. The moving plates are used to impact stationary ballistic missile warhead fuzes at impact velocities of up to 3650 m/s. This turnaround method produces representative impact stresses while avoiding the high cost of flight test. Previous papers [1,2,3] have described the basic experimental concepts and have developed an analytical approach useful in predicting the behavior of explosively accelerated flyer plates. The approach in these papers relies on the empirical development of an explosive mass "discount factor"*** which is then used to analytically predict the behavior of similar systems. Recently, a simple analytical model of the explosive process was developed by modifying one initial basic assumption of the previous work. This achievement is significant in that it eliminates the need for new empirical data in the design of different open-ended, tube confined explosive systems. The new model comes from a concept developed by Baum [4] and reiterated by Kennedy [5] of estimating the mass of explosive that is useful in accelerating a plate

for an unconfined explosive charge. This paper extends the concept to allow estimating the flyer plate terminal velocity for tube-contained explosive systems. The model allows prediction of flyer plate terminal velocity and rotation rate within a few percent. The system performance is calculated using only the explosive, the tube and the flyer masses, the explosive diameter and length, along with explosive properties of detonation velocity and Gurney [6] constant.†

This paper presents the theory used in the development of the model of the open-ended, tube-contained explosively propelled flyer plate. The theory has been applied to 25 tests conducted during the previous development work [1,2,3]. The theoretical-experimental correlation which indicates excellent agreement between theory and measured results is included.

DEVELOPMENT OF THE THEORY

Figure 1 shows the configuration of the explosive system. The explosive is housed in a cylindrical tube container and is detonated at a single point at the open end. The tube provides lateral confinement to the explosive expansion process, thus containing the explosive gas pressure behind the flyer for long enough to accelerate the plate to a high

*This work was supported by the U.S. Energy and Research Development Administration.

***The explosive mass "discount factor" represents the fraction of the explosive that is effective in accelerating a plate for a particular explosive system.

†The Gurney constant, or velocity, relates the quantity of chemical energy (E) of an explosive that is converted to kinetic energy by the detonation process and is denoted as $\sqrt{2E}$.

terminal velocity. The cushion attenuates the shock pressure into the flyer plate, therefore decreasing the probability of its breakup due to spallation. The flyer plate consists of an impact plate and a guard ring. The pressure exerted across the back face of the flyer plate is not exactly uniform; i.e., it is lower at the edges because of lateral rarefaction waves. The guard ring is included to isolate the impact plate from the edge pressure gradient, as well as to separate the plate from any interactions that might occur between the guard ring and the tube walls. The interface between the guard ring and the impact plate is spherical which prevents angular moments, as well as shear stresses, from affecting the impact plate motion. The flyer plate may be tapered across a diameter to cause plate rotation which allows impact with the test item at a predetermined angular orientation. The explosive mass (C), flyer mass (M) and effective tube-confinement mass (N) will be used in the theory later in this report.

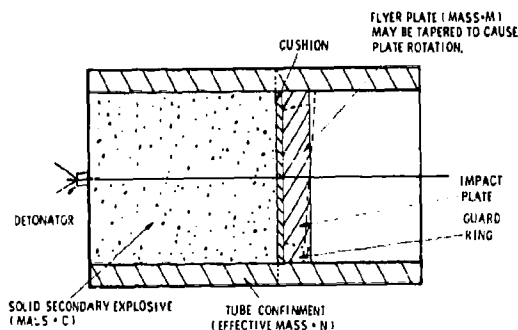


Fig. 1 - Experimental Configuration

The new theory extends a Gurney concept, of discounting explosive mass [6], which has been used extensively to predict the velocity of fragments in the design of explosive systems such as bombs, shells, and grenades. The Gurney model has been reviewed by J. E. Kennedy [5] who presented applications that illustrated its range of applicability. Kennedy concurs with Baum [4] that for explosive systems with significant losses due to lateral rarefaction waves, i.e., no tube confinement, "that the explosive material within 30° of the normal at an edge of the charge cannot contribute to metal acceleration." Baum [4] determined the magnitude of the discount angle by assuming that the explosive that had experienced an "average or characteristic rarefaction wave" by the time the explosive had just completely detonated, could not contribute to driving the flyer plate mass. He estimated that the

magnitude of the "average rarefaction wave" velocity, radially inward (for explosives with $\gamma = 3$), is approximately one-half of the detonation velocity (D), which leads to the calculation of a discount angle of θ ($\theta = \tan D / (2 \cdot D)$). Figure 2 shows how the discount angle process works for a lossy system (no lateral confinement).

If the explosive length (L) is less than the charge diameter divided by the tangent of the discount angle, then the explosive in the volume of a truncated cone of half angle 30° and height (L) is the effective mass used for driving the flyer plate.

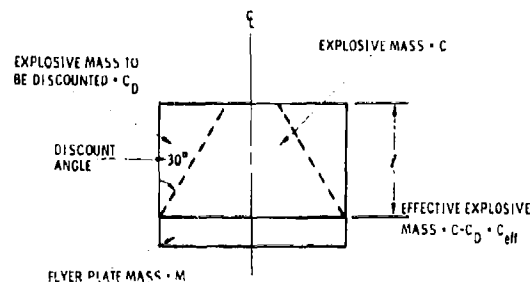


Fig. 2 - Mass Discount Method for Lossy Configurations

The explosive mass discounting method can now be extended to systems that are laterally confined by a cylindrical tube since it is established that an unconfined explosive charge requires a 30° discount angle for use in predicting the flyer terminal velocity. The discount angle for a tube-confined system is assumed to be dependent upon the velocity of the characteristic rarefaction waves moving laterally inward toward the system axis. The velocity of the characteristic rarefaction wave is controlled by the escape velocity of the detonation products from the lateral surface of the explosive. The maximum escape velocity is equal to the terminal radial velocity of the confining tube wall. The tube terminal velocity can be calculated using the Gurney [5] relation shown in Equation 1. This equation predicts the terminal radial velocity of a long cylindrical tube packed with explosive. The effect of the gas losses at the end of the tube is not addressed by Equation 1. Since the flyer plate is generally far away from the open end of the tube, then the effect of the gas losses out the end of the tube upon the radial terminal velocity near the flyer is not critically important.

$$\frac{V_T}{\sqrt{2E}} = \left(\frac{N}{C} + 0.5 \right)^{1/2} \quad (1)$$

V_T = tube terminal radial velocity

$\sqrt{2E}$ = Gurney velocity of the explosive

N/C = ratio of the tube mass that is contact with the explosive* to explosive mass per unit length of tube

For simplicity, the discount angle for the tube-confined system is assumed to be linear** in the tube terminal radial velocity between the limits of θ (discount angle) = 0° for a very thick confining wall ($N = \infty$ in Equation 1, $V_T = 0$) and $\theta = 30^\circ$ for an unconfined explosive ($N = 0$ in Equation 1, $V_T = 2\sqrt{2E}$). This linear relation is shown in Equation 2 relating discount angle to tube terminal velocity.

$$\theta = \frac{30^\circ}{V_{T0}} V_T \quad (2)$$

V_{T0} is the maximum velocity of the confinement wall (for a very thin wall)

$$V_{T0} = \sqrt{2} \cdot \sqrt{2E} \quad (3)$$

and is found by putting $N = 0$ in Equation 1, as seen above. Putting Equations 1 and 3 into Equation 2 gives the formula for the tube-confined discount angle, θ :

$$\theta = 30^\circ / \left(\sqrt{2} \left(\frac{N}{C} + 0.5 \right)^{1/2} \right) \quad (4)$$

Figure 3 shows the process of the lateral confining tube expansion where V_F is the flyer plate terminal velocity. In the figure the detonation wave front has just reached the back of the flyer plate.

*Only that portion of the tube which is in radial contact with the explosive is used in calculating N . The portion of tube that houses the flyer plate and that acts as a barrel is not used in calculating the effective tube mass (N).

**The linear assumption does fit experimental data as seen in a later section.

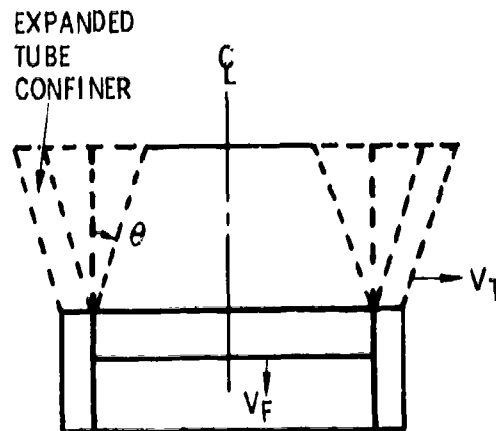


Fig. 3 - Discount angle for the Tube-Confined Explosive Charge

The discount angle of Equation 4 defining a truncated or full cone, can be used to determine the effective mass (C_{eff}) of explosive for driving the flyer plate. The effective explosive mass is assumed to act in a one-dimensional manner and, therefore, can be used directly in the one-dimensional gas dynamics solution for the motion of a plate with detonation loading [7]. Equation 5 is the relation for the final average velocity of the plate using the one-dimensional gas dynamics solution with the explosive mass C replaced by the effective explosive mass C_{eff} .

$$V_F = D \sqrt{\frac{8}{\gamma^2 - 1}} \left(\frac{Z - 1}{Z + 1} \right) \quad \text{where} \quad (5)$$

$$Z = \left(1 + \frac{32 C_{eff}}{27 M} \right)$$

D = Detonation velocity
 M = Mass of the flyer plate
 C_{eff} = Effective explosive mass

In Kennedy's paper [5] the gas dynamic solution ($\gamma = 3$) was compared to the Gurney solution with very good results. The author chose $\gamma = 3$ for the explosives used in the experimental series (Comp. C-4, PBX-9404) based on Kennedy's work and upon calculated average values of γ from the JWL Equation of State [8] (see Appendix).

One limit that comes from the discount angle concept is that if the length of the explosive charge is greater than a critical length l (the radius divided by the tangent of the discount angle), then the effective explosive mass is that of a cone with the base equal to the charge radius and length equal l .

No additional velocity is achieved by adding explosive beyond this length l .

Equations 4 and 5 can be used to predict the average velocity (V_a) of a flyer plate from an explosive assembly like that in Fig. 1. The values for N (mass of the effective tube confinement) and C (total mass of the explosive) are used to calculate θ (Eq. 4). The values of explosive diameter and length are used with θ to calculate the effective mass of the explosive (C_{eff}). The explosive detonation velocity (D) and flyer mass (M) are used with C_{eff} and γ to calculate the flyer terminal velocity using Eq. 5.

In some cases, it is desired to cause the flyer plate to rotate slowly so that oblique impacts with targets may be obtained. The flyer plate thickness is varied linearly across a diameter and since, for a constant thickness of explosive, the local flyer plate velocity is inversely proportional to plate thickness, then a velocity gradient is developed across the tapered plate. A method of designing a flyer plate taper has been derived using the effective explosive mass (C_{eff}) from the results of Equation 4. The velocity gradient across the plate can be determined from the desired plate rotation rate. The absolute velocities at the edges of the plate can be calculated by adding the velocity at the center of the plate to the velocity differential between the center and edge of the plate. Equation 5 is used to determine the local mass of the flyer plate that will give the desired velocity at that location. The thickness of the flyer can then be determined by knowing the mass density of the flyer material. In the reverse manner, if the flyer plate taper is known, then the expected rotation rate for a given explosive system can be calculated.

The radial width of the guard ring is chosen to be equal to the explosive length (l) times the tangent of the discount angle. It is expected that the main pressure gradient across the back of the plate occurs in this outer annular region.

A computer program has been written which incorporates the concepts of this method and allows calculation of terminal velocities and rotation rates for a tube-confined explosive system.

THEORETICAL-EXPERIMENTAL CORRELATION

Data from experimental work of Mathews and Duggin [1,2,3,9] were available to the author and were used for comparison to this theory. The experiments consisted of detonating explosive systems similar to the one shown in Fig. 1 and measuring the flyer plate velocity and rotation rate. A flash X-ray system was used to obtain multiple shadowgraphs of the flyer plate at known times after the

explosive initiation. Compensation for the effects of air drag on the plate and parallax associated with the X-ray system was made [1,2,3]. The results of the experiments were taken directly from Mathews' and Duggin's data with no additional adjustments being made.

Table I shows the results of 16 non-rotating tests with the tube confinement mass/explosive mass ratio (N/C) varying from 0.06 to 4.4 and with the explosive mass/flyer mass ratio (C/M) ranging from 2.99 to 20.14. The values of calculated final velocity (using the method of this report) were within $\pm 5\%$ of the measured velocity.

Even for charges of length greater than the charge radius/tangent of the discount angle the agreement is excellent (in these cases the apex of the cone of the discount volume is within the explosive). Possible errors in experimental technique are of the same magnitude as the theoretical-experimental variance observed from the data.

Table II shows results on rotating systems. The agreement between the measured and calculated rotation rate magnitude is good. Experiments are currently being designed to further investigate the rotation process which will hopefully give even better agreement between the theory and experiment.

The theory was checked against three experiments using an explosive made up of two explosives: PBX-9404 and Composition C-4 at a ratio of 8:2. The explosive volume was adjusted analytically to an equivalent volume of PBX-9404 explosive by replacing the Composition C-4 volume by an energy equivalent volume of PBX-9404. The energy equivalency was based on the Gurney velocity of the explosive as shown in Equation 6.

$$\text{Volume}_{\text{(PBX-9404)}} = \text{Volume}_{\text{(C-4)}} \frac{\sqrt{2E_{\text{(C-4)}}}}{\sqrt{2E_{\text{(PBX-9404)}}}} \quad (6)$$

All three tests were designed for flyer rotation. The results are shown in Table III. The agreement in velocity is excellent and the agreement in rotation rate is acceptable. In every case, the measured value of rotation rate is less than the calculated values.

SUMMARY AND CONCLUSION

A theory for predicting the velocity and rotation rate of a tube-confined explosively driven flyer plate has been developed. A scheme for determining the mass of the explosive that is effective in driving the plate by discounting a quantity of explosive based on the amount of lateral tamping present has been devised. The technique predicts terminal velocity of a tube-confined flyer plate to

within +5% and rotation rates that are about 10% higher than measured. Experimentation is continuing to further investigate the rotation process. The theory has also been used to predict, with equally good results, the performance of tube-confined systems with multiple explosives.

APPENDIX

Determination of γ for the explosive used in the tube-confined, flyer-plate system is important since the final plate velocity (V_F) is nearly linearly dependent on its value. (see Equation A-1).

$$V_F = D \sqrt{\frac{8}{\gamma^2 - 1}} \left(\left(\frac{1 + \frac{32 C_{eff}}{27 M}}{\gamma^2 - 1} \right)^{1/2} - 1 \right) \quad (A-1)$$

where

D = Detonation velocity of the explosive

C_{eff} = Effective explosive mass

M = Flyer plate mass

Through calculations performed by Baum [4] and Gurney [6] it has been found that for this system 90% of the final flyer-plate velocity is attained after the explosive has expanded to 2.36 times its initial volume (95% at 3.15 times the initial volume). These values of percent of final flyer velocity vs expansion ratio are not affected by the quantity of lateral tamping because of the nature of the explosive mass discount process.

The average value of γ for use in Equation A-1 is determined by using the JWL equation-of-state for various explosive product gases.

$$P = A e^{-R_1 V} + B e^{-R_2 V} + \frac{C}{V(w-1)} \quad (A-2)$$

where

P = Pressure

\bar{V} = Instantaneous volume

V_0 = Initial volume

$V = \bar{V}/V_0$ = Specific volume

A, B, C, R_1, R_2 = Empirically determined constants¹⁰

γ at any expansion V can be determined using Equation A-3 leading to a plot of γ vs V .

$$\gamma = - \frac{V}{P} \left(\frac{\partial P}{\partial V} \right)_S \quad (A-3)$$

Figure A-1 shows the plots of γ vs V for the explosive Composition C-4 and PBX-9404. The average value of γ over a given expansion is determined from the data of the γ vs V plots by using the averaging Equation A-4.

$$\text{Average} = \frac{\int_1^V \gamma dv}{\int_1^V dv} \quad (A-4)$$

The results show that the average γ for Composition C-4 for $V = 2.36$ (90% of final velocity) is 2.94 and for $V = 3.15$ (95% of final velocity) is 2.91. For PBX-9404, the average γ for $V = 2.36$ is 2.96 and for $V = 3.15$ is 3.12. These values justify the use of $\gamma = 3$ for the process involved in the barrel-tamped explosive system for propelling flyer plates to high velocities.

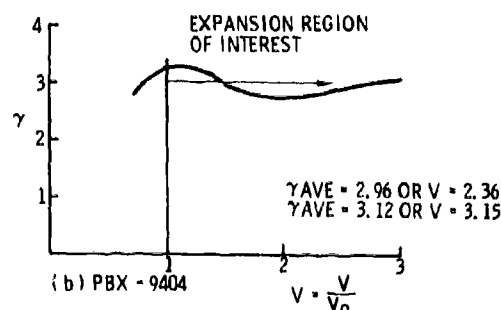
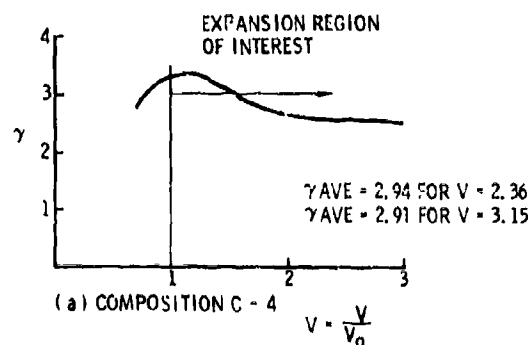


Fig. A-1 - γ VS V PLOT FOR EXPLOSIVES OF INTEREST

TABLE 1
Theory vs Experiment Correlation, Nonrotation Flyer Plates

Test ¹	C/M	N/C	Charge length (cm)	Average Measured (m/s)	Velocity		Comments
					Calculated (m/s)	$\frac{V_{\text{Measured}}}{V_{\text{Calculated}}}$	
10	4.478	1.67	7.62	2236	2288	.98	
20	6.076	1.75	3.81	3195	3315	.96	
21	8.110	1.77	5.08	3504	3516	1.00	
22	11.990	1.78	7.62	3792	3650	1.04	
23	20.140	1.76	12.70	3991	4044	.99	Cone apex inside HE Volume @ 9.65 cm
25	3.340	.06	3.81	1924	1872	1.03 ²	
26	4.438	.06	5.08	2089	1998	1.05 ²	Cone apex inside HE Volume @ 4.83 cm
3	4.458	4.40	7.62	2670	2689	.99	
5	6.698	4.40	7.62	3221	3245	.99	
6	12.116	4.40	7.62	4140	4054	1.02	
19	5.368	4.40	3.81	3320	3339	.99	
1	2.980	4.40	5.08	2310	2414	.96	
B	7.137	4.40	12.70	2730	2792	.98	
11	4.530	.84	7.62	2088	2039	1.02	Cone apex inside HE Volume @ 7.37 cm
24	5.986	.88	3.81	3115	3117	1.00	
15	6.240	.84	12.70	2527	2443	1.03	Cone apex inside HE Volume @ 7.37 cm

¹See Figure 1 for description of terms.

²Flyer broken allowing venting and, therefore, lower terminal velocity.

NOTES:

1. All explosive is Composition C-4, $\sqrt{Z_E} = 2750$ m/s, detonation velocity = 8040 m/s.
2. All charges initiated by a single detonator placed on the axis of the charge opposite the flyer; all charge diameters are 5.08 cm.
3. The mass of the cushion material is included in the flyer mass to determine M.
4. Reference 9.

TABLE II
Theory vs Experiment Correlation, Large Systems Rotating
and Nonrotating Configurations

Test No.	C/M	N/C	Charge Length (cm)	Velocity		$\frac{V_{\text{Measured}}}{V_{\text{Calculated}}}$	Rotation Rate	
				Average Measured (m/s)	Calculated (m/s)		Measured (rad/s)	Calculated (rad/s)
1-22	8.06	2.72	77.80	3012	3027	.99	570	600 ¹
1-28	8.24	2.66	79.58	3018	3018	1.00	636	600
1-13	4.99	2.71	76.43	2317	2407	.96	0	0
1-29	8.06	2.72	77.88	3041	3027	1.00	616	600 ¹
1-21	8.05	2.69	78.74	2959	3005	.98	-	-
1-26	5.15	2.70	78.84	2350	2407	.98	316	400 ²

¹ Good resolution on rotation data
² Poor resolution on rotation data

NOTES:

1. All explosive is Composition C-4, $\sqrt{Z_E} = 2750$ m/s, detonation velocity = 8040 m/s.
2. Reference 9.
3. All charge diameters are 40.79 cm.

TABLE III

Theory vs Experiment Correlation, Large Systems Multiple Explosive

Test No.	C/M	N/C	Velocity		$\frac{V_{\text{Measured}}}{V_{\text{Calculated}}}$	Rotation Rate	
			Charge Length (cm)	Average Measured (m/s)		Measured (R/S)	Calculated (R/S)
29	9.478	2.10	74.57	3570	1.01	680	750
32	9.85	2.09	74.83	3582	1.00	~173	200
33	9.478	2.10	74.57	3527	1.00	692	750
NOTES: 1. All charge diameters are 41.59 cm. 2. Reference 9. Explosive is Composition C-4 and PBX-9404 ($\sqrt{Z_E} = 2900$ m/s Detonation Velocity 8800 m/s)							

REFERENCES

1. F. H. Mathews, "Explosively Propelled Rotation Plates for Oblique Impact Experiments," Shock and Vibration Bulletin, No. 45, Part 4, June 1975.
2. F. H. Mathews and B. W. Duggin, "Barrel-Tamped, Explosively Propelled Plates for Oblique Impact Experiments," Shock and Vibration Bulletin, No. 46, Part 2, pp 145-154, August 1976.
3. F. H. Mathews and B. W. Duggin, "Barrel-Tamped Explosively Propelled Rotating Plastic Plates," Shock and Vibration Bulletin, No. 47, Part 1, pp 113-119, September 1977.
4. F. A. Baum, K. P. Stanyukovich, and B. I. Shekhter, Physics of an Explosion, p 335, 506, Moscow, 1959. (English translation from Federal Clearinghouse, AD 400 151.)
5. J. E. Kennedy, "Explosive Output for Driving Metal," Behavior and Utilization of Explosives in Engineering Design, 12th Annual Symposium ASME Published by the New Mexico Section of ASME, March 2-3, 1972.
6. R. W. Gurney, "The Initial Velocities of Fragments from Bombs, Shells, and Grenades," BRL Report 405, 1943.
7. A. K. Aziz, H. Hurwitz, and H. M. Sternberg, "Energy Transfer to a Rigid Piston Under Detonation Loading," Physics of Fluids 4, 380-84, 1961.
8. E. L. Lee, H. C. Hornig, and J. W. Kury, Adiabatic Expansion of High Explosive Detonation Products, Lawrence Radiation Laboratory Report, UCRL-50422, TID-4500, UC-4, CHEM., May 2, 1968.
9. F. H. Mathews and B. W. Duggin, Private Communication.
10. E. Lee, M. Finger, and W. Collins, JWL Equation-of-State Coefficients for High Explosives, Lawrence Livermore Laboratory Report, UCID-16189, January 16, 1973.

A STABILITY THEOREM FOR A DYNAMICALLY LOADED LINEAR VISCOELASTIC STRUCTURE

D. W. Nicholson
Naval Surface Weapons Center
White Oak, Silver Spring, Maryland 20910

The response of a linear viscoelastic structure to a dynamic load is considered. For the finite element equation of dynamic equilibrium a representation of the solution is derived using the exponential matrix function, and this representation permits application of the highly efficient method of Gaussian quadrature. Positive definiteness and other properties of the system mass, damping and stiffness matrices are shown to entail satisfaction of an inequality ensuring a physical and a numerical type of stability.

INTRODUCTION

We consider a damped linear system under dynamic loading. Positive definiteness of the system matrices is shown to ensure satisfaction of a condition both for physical and numerical stability. A general solution is obtained using the matrix exponential function, and computation can be performed using the efficient method of Gaussian quadrature. Our results appear to be new.

Of course, stability of linear viscoelastic and other time invariant linear systems has been extensively studied before. Primarily, physical stability was investigated and an approach (Lyapunov's first method) was followed which obviated the need for establishing a certain mathematical fact (namely, that the norm of the transition matrix not exceed unity). However, because certain additional physical and numerical stability results are thereby obtained, this fact is worth demonstrating. Here, apparently for the first time, the demonstration is given, and several consequences are described.

RESPONSE OF DAMPED LINEAR SYSTEMS

1. General Form of the Solution

In finite element analysis and elsewhere, the dynamic response of a linear viscoelastic structure may be

represented as the linear system [1]

$$M\ddot{x} + D\dot{x} + Kx = f(t) \quad (1)$$

where M , D and K are, respectively, the mass, damping and stiffness matrices, x is the displacement vector and f is the force vector. The matrices are n by n and real, constant, Hermitian and positive definite (RCHPD), the vectors are real and n by 1, and the superposed dot denotes differentiation with respect to time t . The vector $f(t)$ is considered known as a function of time. For wave propagation analyses, the mass matrix is diagonal [2].

We introduce the matrix exponential function defined for the nonsingular matrix $X(t)$ by the power series [3]

$$\text{Exp}(Xt) = \sum_{j=0}^{\infty} (Xt)^j / j! \quad (2)$$

This function is completely analogous to the scalar exponential function, and in particular we will need the useful properties

$$\text{Exp}(Xt) \text{Exp}(-Xt) = I \quad (3a)$$

$$\text{Exp}(Xt_1) \text{Exp}(Xt_2) = \text{Exp}(X(t_1 + t_2)) \quad (3b)$$

$$\frac{d}{dt} \text{Exp}(Xt) = X \text{Exp}(Xt) = \text{Exp}(Xt)X \quad (3c)$$

$$\int_0^t \text{Exp}(Xt) dt = (\text{Exp}(Xt) - I) X^{-1}. \quad (3d)$$

Equation (1) may be rewritten as

$$\dot{A}q + Bq = h(t) \quad (4a)$$

where

$$A = \begin{bmatrix} M & O \\ O & K \end{bmatrix} \quad B = \begin{bmatrix} D & K \\ -K & O \end{bmatrix}$$

$$q = \begin{bmatrix} \dot{x} \\ x \end{bmatrix} \quad h(t) = \begin{bmatrix} f(t) \\ 0 \end{bmatrix}.$$

Using Equation (3c), Equation (4a) is readily shown equivalent to

$$\text{Exp}(-A^{-1}Bt) \frac{d}{dt} \text{Exp}(A^{-1}Bt)q = A^{-1}h(t).$$

After elementary integration and the application of Equation (3c), we have

$$q = \text{Exp}(-A^{-1}Bt) \int_0^t \text{Exp}(A^{-1}B\eta) A^{-1}h(\eta) d\eta \quad (4b)$$

$$= \int_0^t \text{Exp}(-A^{-1}B\tau) A^{-1}g(\tau) d\tau \quad (4c)$$

where

$$g(\tau) = \begin{bmatrix} f(t-\tau) \\ 0 \end{bmatrix}.$$

The foregoing integral representation of the solution suggests a powerful method of integration, namely Gaussian quadrature, as discussed below.

2. Application of Gaussian Quadrature

The numerical integration can be facilitated by exploiting the useful properties of the exponential matrix function, particularly Equation (3b). Divide the interval of integration into N subintervals of length Δt . The Gaussian quadrature points in the i th such interval are designated $\tau_1^{(i)}, \tau_2^{(i)}, \dots, \tau_k^{(i)}$. But for equal intervals Δt , these points have the relation

$$\tau_j^{(i)} = \tau_j^{(1)} + (i-1) \Delta t \quad (5)$$

where $i = 1$ corresponds to the interval $0 \leq \tau \leq \Delta t$. The interval for the i th interval is now evaluated as [4]

$$\int_{(i-1)\Delta t}^{i\Delta t} \text{Exp}(-A^{-1}B\tau) A^{-1}q(\tau) d\tau \quad (6)$$

$$\approx \frac{\Delta t}{2} \sum_{j=1}^k \text{Exp}[-A^{-1}B\tau_j^{(i)}] A^{-1}q(\tau_j^{(i)}).$$

Now Equation (3b) together with Equation (5) implies a kind of recursion relation:

if

$$J_j^{(i)} = \text{Exp}(-A^{-1}B\tau_j^{(i)}),$$

then

$$J_j^{(i)} = \text{Exp}(-A^{-1}B\Delta t) J_j^{(i-1)}$$

$$= \text{Exp}(-A^{-1}B\Delta t)^{i-1} J_j^{(1)}.$$

Equation (6) is conveniently rewritten as

$$\int_{(i-1)\Delta t}^{i\Delta t} \text{Exp}(-A^{-1}B\tau) A^{-1}q(\tau) d\tau$$

$$\approx \frac{\Delta t}{2} \text{Exp}(-A^{-1}B\Delta t)^{i-1} \sum_{j=1}^k J_j^{(i-1)} A^{-1}q(\tau_j^{(i)}).$$

So the application of the Gaussian quadrature method, which itself is most efficient, is facilitated by the recursive relations derived from the properties of the matrix exponential function.

We will subsequently prove a strong stability theorem for the present numerical method which will be then seen to offer strong attractions compared to the more common methods, including mode superposition and direct numerical integration. These latter two methods are sometimes inconvenient or unstable [5]. But one very serious disadvantage of the present method is the fact that the exponential matrix function can be fully populated even when M , D and K are sparse and banded, so that storage limitations may be

bothersome. We hope to determine in future work how this difficulty can be obviated.

STABILITY CONDITIONS

In this section we derive an inequality ensuring both a physical and a numerical type of stability. In the subsequent section we prove that the inequality is satisfied by the damped linear system represented by Equation (1).

1. Physical Stability

For impulse loading expressed by

$$f(t) = f_0 \delta(t)$$

where f_0 is a constant vector and $\delta(t)$ is the Dirac function, the solution expressed by Equation (4b) becomes [6]

$$q = \text{Exp}(-A^{-1}Bt)A^{-1} \begin{Bmatrix} f_0 \\ 0 \end{Bmatrix}.$$

The present system will be called physically stable if its response to an impulse loading is nonincreasing in time. Let $||\cdot||$ denote some vector norm and let $||\cdot||$ denote some consistent matrix norm [7]: i.e., for a vector y and a matrix Y ,

$$||Yy|| \leq ||Y|| ||y||.$$

Physical stability obtains if for some such norms

$$||q||/||A^{-1} \begin{Bmatrix} f_0 \\ 0 \end{Bmatrix}|| \leq 1.$$

It is sufficient if

$$||\text{Exp}(-A^{-1}Bt)|| \leq 1 \quad (7)$$

for all $t \geq 0$. Hereafter the system of interest will be called physically stable if Ineq. (7) is satisfied.

To consider physical stability further, consider the constant amplitude oscillatory input

$$f = f_0 \text{Exp}(i\omega t) = f_0 \text{Exp}(Ii\omega t).$$

(That $f_0 \text{Exp}(i\omega t) = f_0 \text{Exp}(Ii\omega t)$ is readily proved from Equation (2).) Now referring back to Equation (4b) we find

$$q = \text{Exp}(-A^{-1}Bt) \left[\text{Exp} \left[(A^{-1}B + i\omega I)t \right] - I \right] \cdot (A^{-1}B + i\omega I)^{-1} A^{-1} h_0$$

assuming $[A^{-1}B + i\omega I]$ is nonsingular, which we will subsequently prove it to be. Rewriting gives

$$q = [\text{Exp}(i\omega t) - \text{Exp}(-A^{-1}Bt)] \cdot (A^{-1}B + i\omega I)^{-1} A^{-1} h_0.$$

By virtue of norm properties,

$$|q| \leq \{ ||\text{Exp}(i\omega t)|| + ||\text{Exp}(-A^{-1}Bt)|| \} \cdot ||(A^{-1}B + i\omega I)^{-1} A^{-1} h_0||.$$

But

$$||\text{Exp}(Ii\omega t)|| = |\text{Exp}(i\omega t)| = 1,$$

where in this instance the vertical bars denote the magnitude. By the physical stability condition, Ineq. (7), it follows that

$$|q|/2 ||(A^{-1}B + i\omega I)^{-1} A^{-1} h_0|| \leq 1.$$

Otherwise stated, the physical stability condition implies a bound on the response to a constant amplitude oscillatory input. By using the Fourier representation

$$f(t) = \sum_{n=0}^{\infty} f_n \text{Exp}(in\omega t)$$

one may prove that the present condition of physical stability leads to a corresponding bound on the response for a very general class of input functions.

2. Numerical Stability

Computational error will arise in the foregoing numerical approach from several important sources, including quadrature error and "propagated initial error." A computational method will be called stable with respect to a given source of error if this error increases at most linearly with the number of time steps over which computation is performed. Of primary concern in this regard is that error at one time step might be amplified in subsequent steps. At first glance, such a difficulty would be expected here because of the presence of $\text{Exp}(-A^{-1}Bt)$ in the integral of

Equation (4c). In this section we focus on the computation of $\text{Exp}(-A^{-1}Bt)$.

Owing to property (3b), if $t=m\Delta t$ for some integer, then

$$\begin{aligned}\text{Exp}(-A^{-1}Bt) &= \text{Exp}(-mA^{-1}B\Delta t) \\ &= [\text{Exp}(-A^{-1}B\Delta t)]^m.\end{aligned}$$

Suppose that computation of $\text{Exp}(-A^{-1}Bt)$ introduces a "small" error E such that the actual computed matrix C is given by

$$C = \text{Exp}(-A^{-1}B\Delta t) + E,$$

where $\|E\|/\|C\| \ll 1$. (Rapid computation of $\text{Exp}(-A^{-1}B\Delta t)$ is discussed in the appendix.) Assume that subsequent matrix operations introduce no further error, and now at the m^{th} time step

$$\begin{aligned}C^m &= \text{Exp}(-A^{-1}B\Delta t)^m \\ &\quad + m \text{Exp}(-A^{-1}B\Delta t)^{m-1}E \dots\end{aligned}$$

Define the m^{th} error E_m as $E_m = C^m - \text{Exp}(-A^{-1}B\Delta t)^m$, and for $\|E\|$ sufficiently small we obtain

$$E_m \approx m [\text{Exp}(-A^{-1}B\Delta t)]^{m-1}E.$$

In terms of matrix norms,

$$\|E_m\| \leq m \|\text{Exp}(-A^{-1}B\Delta t)\|^{m-1} \|E\|.$$

Clearly, the present error grows stably, i.e., at most linearly with m , if

$$\|\text{Exp}(-A^{-1}B\Delta t)\| \leq 1,$$

and by Equation (3b) this condition holds if and only if

$$\|\text{Exp}(-A^{-1}Bt)\| \leq 1$$

for all t . But this last inequality was previously given in Ineq. (7) as the condition for physical stability. Recapitulating, Ineq. (7) states a condition for both a physical and a numerical type of stability.

In the subsequent sections we prove that Ineq. (7) holds under the assumption that M , D and K are real, constant, Hermitian and positive

definite (RCHPD).

STABILITY THEOREM

A suitable matrix norm [7] can be found such that Ineq. (7) is satisfied if and only if

$$\rho(\text{Exp}(-A^{-1}B\Delta t)) \leq 1$$

where ρ denotes the spectral radius of the matrix $\text{Exp}(-A^{-1}B\Delta t)$. (For the eigenvalues $\lambda_i(\text{Exp}(-A^{-1}Bt))$,

$$\begin{aligned}\rho(\text{Exp}(-A^{-1}Bt)) &= \\ &\max_i |\lambda_i(\text{Exp}(-A^{-1}B\Delta t))|.\end{aligned}$$

Now [8]

$$\lambda_i(\text{Exp}(-A^{-1}B\Delta t)) = \text{Exp}(-\lambda_i(A^{-1}B)\Delta t)$$

and upon writing $\lambda_i(A^{-1}B) = \alpha_i + \beta_i$, we have

$$\begin{aligned}\rho[\text{Exp}(-A^{-1}B\Delta t)] &= \\ &= \max_i |\text{Exp}(-\alpha_i\Delta t)\text{Exp}(-i\beta_i\Delta t)| \\ &= \max_i |\text{Exp}(-\alpha_i\Delta t)| \\ &= \text{Exp}[-(\min_i \alpha_i)\Delta t].\end{aligned}$$

So now proving stability reduces to proving that $\min_i \alpha_i \geq 0$, that is, to

proving that the eigenvalues of $A^{-1}B$ have only nonnegative real parts. In this event $A^{-1}B$ is called a stable matrix.

A matrix will be called strongly stable if its eigenvalues have only positive real parts. Our strategy in proving that Ineq. (7) is satisfied in the present system is to show that the positive definiteness and other properties of M , D and K entail that, for every $\epsilon > 0$, $A^{-1}(B + \epsilon I)$ is similar to a strongly stable matrix, and is therefore itself strongly stable.

It is convenient to introduce an intermediate notion. Specifically, a matrix Y will be called positive real [7] if and only if $y^H Y y$ is a positive

real number for every nonvanishing real vector y . (Here y^H is the Hermitian transpose of y .) By a theorem attributed to Wachspress [7], necessary and sufficient conditions for Y to be positive real are that $Y + Y^H$ be positive definite.

For every real $\epsilon > 0$, $B + \epsilon I$ is positive real since

$$B + \epsilon I + (B + \epsilon I)^H = \begin{bmatrix} 2(D + \epsilon I) & 0 \\ 0 & 2\epsilon I \end{bmatrix}$$

is positive definite (block diagonal with positive definite blocks). Now the RCHPD matrix A^{-1} can be written as $A^{-1} = A^{-1/2} A^{-1/2}$ where $A^{-1/2}$ is likewise RCHPD [7]. Further, for every nonvanishing real vector y , $y^H A^{-1/2}$ $(B + \epsilon I) A^{-1/2}$ can be written as $(A^{-1/2} y)^H (B + \epsilon I) (A^{-1/2} y)$ and hence is a positive real number since $B + \epsilon I$ is positive real. (That $A^{-1/2}$ is nonvanishing follows from positive definiteness of $A^{-1/2}$.) Hence $A^{-1/2} (B + \epsilon I) A^{-1/2}$ is also positive real.

We now invoke a theorem attributed to Lyapunov [7]. A matrix X is strongly stable if and only if there exists a positive definite, Hermitian matrix Y such that $XY + YX^H$ is positive definite. With the identification $Y = I$, it follows that the positive real matrix $A^{-1/2} (B + \epsilon I) A^{-1/2}$ is strongly stable.

But note that

$$A^{-1} (B + \epsilon I) = A^{-1/2} [A^{-1/2} (B + \epsilon I) A^{-1/2}] A^{1/2}.$$

So $A^{-1} (B + \epsilon I)$ is similar to a strongly stable matrix and is therefore itself strongly stable. For every $\epsilon > 0$, its eigenvalues have positive real parts.

Hence $A^{-1} B$ is a stable matrix, and the satisfaction of the stability condition, Ineq. (7), is proved for the system represented by Equation (1).

CONCLUSION

We have considered a damped linear system with positive definite mass, damping and stiffness matrices. A solution permitting application of the efficient method of Gaussian quadrature

has been derived using the matrix exponential function. A stability condition has been derived ensuring stable response to a broad class of dynamic inputs, and also ensuring numerical stability with respect to propagated error. A theorem has been proved showing that the stability condition is satisfied under the assumptions on the system matrices, particularly positive definiteness.

REFERENCES

1. R. D. Cook, Concepts and Applications of Finite Element Analysis, John Wiley and Sons, New York, 1974
2. C. J. Constantino, "Finite Element Approach to Stress Wave Problems," Proc ASCE, J.E.M. Div., Vol 93, 1967
3. A. Householder, The Theory of Matrices in Numerical Analysis, Blaisdell, New York, 1964
4. G. Dahlquist and A. Bjork, Numerical Methods, Prentice-Hall, Inc., Englewood Cliffs, New Jersey, 1974
5. K. C. Park, Evaluating Time Integration Methods for Nonlinear Dynamics Analysis, in Finite Element Analysis of Transient Nonlinear Structural Behavior, ed. T. Belytschko, et al, ASME, 1975
6. W. Flügge, Viscoelasticity, Blaisdell Publishing Co., London, 1967
7. D. M. Young, Iterative Solution of Large Linear Systems, Academic Press, New York, 1971
8. W. L. Brogan, Modern Control Theory, Quantum Publishers, New York, 1974

APPENDIX

Rapid Computation of $\exp(-A^{-1} B \Delta t)$

The exponential matrix function satisfies the equation [8]

$$\exp(-A^{-1} B \Delta t) = \lim_{m \rightarrow \infty} \left[I - \frac{A^{-1} B}{m} \right]^m$$

One may derive the approximation

$$\begin{aligned} \text{Exp}(-A^{-1}B\Delta t) &= (I - \frac{A^{-1}B\Delta t}{m})^m + f_1(m)\Delta t^2 \\ &\quad + f_2(m)\Delta t^3 + O(\Delta t^4). \end{aligned}$$

The present method involves both "extrapolation" and "telescoping."

A representation accurate to order $O(\Delta t^4)$ is obtained by eliminating Δt^2 and Δt^3 in the system

$$\begin{aligned} \text{Exp}(-A^{-1}B\Delta t) &= (I - \frac{A^{-1}B\Delta t}{m})^m + f_1(m)\Delta t^2 \\ &\quad + f_2(m)\Delta t^2 \end{aligned}$$

$$\begin{aligned} \text{Exp}(-A^{-1}B\Delta t) &= (I - \frac{A^{-1}B\Delta t}{m+1})^{m+1} \\ &\quad + f_1(m+1)\Delta t^2 + f_2(m+1)\Delta t^3 \end{aligned}$$

$$\begin{aligned} \text{Exp}(-A^{-1}B\Delta t) &= (I - \frac{A^{-1}B\Delta t}{m+2})^{m+2} \\ &\quad + f_1(m+2)\Delta t^3 + f_2(m+2)\Delta t^3 \end{aligned}$$

This leads to an expression of the form

$$\begin{aligned} \text{Exp}(-A^{-1}B\Delta t) &= O(\Delta t^4) \\ &\quad \sum_{i=1}^3 \left\{ q_i(m) \left[I - \frac{A^{-1}B\Delta t}{m-1+1} \right]^{m-1+i} \right\} \end{aligned}$$

where $q_1(m)$, $q_2(m)$ and $q_3(m)$ are readily derived.

Suppose now that $m = 2^k$ for a k positive integer. Then computation of

$(I - \frac{A^{-1}B\Delta t}{m})^m$ requires only $\ln m / \ln 2$

matrix multiplications according to the scheme

$$j_1 = 1$$

$$j_k = m \quad q = 1, 2, \dots, k$$

$$j_{q+1} = 2j_q$$

$$(I - \frac{A^{-1}B\Delta t}{m})^{j_{q+1}} = \left[(I - \frac{A^{-1}B\Delta t}{m})^{j_q} \right]^2.$$

ANALOG DOUBLE INTEGRATION OF SHOCK PULSES

Kalman Peleg, Associate Professor
School of Packaging
Michigan State University
East Lansing, Michigan
On Leave of Absence From
Technion Israel Institute of Technology

and

Richard A. Lund
MTS Systems Corporation
Minneapolis, Minnesota

Conventional monitoring and evaluation in shock testing is based mainly on acceleration pulse recordings from a shock machine and a tested product. For product fragility boundary establishment, shock machine velocity change is either computed from drop height, measured by an optical velocity meter or single integration of the acceleration time pulse.

An approach to acceleration transient analysis is described whereby a real-time double integrator circuit provides analog readout of velocity and displacement as well as acceleration. Absolute and relative velocity changes and displacements are obtained by means of consecutive integration of signals from acceleration transducers.

Although an analog double integration circuit is featured in this work, the applications also apply to digital double integration.

INTRODUCTION

Since the advent of shock machines for shock testing [1], monitoring and evaluation of test results is based mainly on acceleration pulse recordings of shock machine and tested product. For product fragility boundary establishment [1,4], shock machine velocity change is either computed from drop height measured by an optical velocity meter or single integration of the acceleration pulse [2,3,4].

Real-time double integration can significantly extend the capability of acceleration transient analysis whereby absolute and relative velocity changes and displacements can be measured by means of consecutive integration of signals from acceleration transducers (accelerometers) [5].

In a recent study conducted by the authors at MTS Systems Corporation, a practical single and double integration electronic network was developed utilizing a small analog/hybrid computer. This prototype network will serve as a basis for development of a commercial Analog

Double Integrator (A.D.I.) for simultaneous real-time recording of velocities and displacements as well as the source acceleration signals.*

An A.D.I. in conjunction with the availability of extremely light weight and high sensitivity accelerometers provides the capability of measuring relative displacements of very delicate product component parts with good accuracy.

In shock machine testing, absolute table and product velocity changes and displacements as well as velocities and displacements of the product in relation to the table or product component parts in relation to the product itself can be measured. Some additional practical application possibilities are:

1. Hammer/Anvil configurations.

- A. Measuring dynamic displacement of

*Readers interested in details of the electronic network of A.D.I. are referred to the second author.

the programmers of a shock machine [1,4].

- B. Velocity changes and recoil displacements of inertia activation mechanisms (automatic weapons, canons, dies, etc.).

2. Packaging problems.

- A. Measuring velocity changes and dynamic displacements of cushioned items and product component parts.
- B. Measuring dynamic cushion deflection in shock machines, cushion testers, or free fall drop tests of packaged products to detect "bottoming" strains (maximal cushion deflection).
- C. Detecting critical dynamic deflections of containers or product component parts. This is especially important in product fragility testing whereby unacceptable deformation (non-destructive assessment) of components on the verge of elasticity limits rather than actual failure (destructive assessment) serve as product fragility criteria.

The A.D.I. also affords estimation of the energy involved in shock by real-time plotting of the acceleration signal versus the displacement calculated by double integration. This type of analysis creates a completely new dimension in shock analysis, since the area under the acceleration (force) deformation curve represents the energy involved in the dynamic test. Thus, it is possible to estimate energy absorption of cushioning materials, shock absorbers, etc., or plot dynamic hysteresis curves of any material subjected to transient loads.

Although an analog double integration circuit is featured in this work, the applications apply to digital double integration as well.

PRINCIPLES OF OPERATION

There are two possibilities of A.D.I. application: "absolute" and "relative" mode. In the Absolute Mode only one accelerometer is used for determination of absolute velocity change ΔV and displacement ΔX . In the Relative Mode two accelerometer signals are subtracted from each other to obtain relative acceleration G_R , whereupon relative velocity change ΔV_R and relative displacement ΔX_R are generated by A.D.I.

Absolute Mode

Figure 1a is a schematic of the absolute mode setup for shock machine testing.

The signal G_1 from a probe accelerometer attached to the place where displacement measurement is desired, is fed into the A.D.I. circuit through a suitable accelerometer conditioner. This mode requires setting of initial conditions for velocity V_0 and displacement X_0 at the instant of collision. However, initial conditions are not required for measuring total velocity change ΔV alone. Thus, by running a preliminary test and single integrating the acceleration signal, V_0 can be computed by:

$$V_0 = \frac{\Delta V}{1 + C_r} \quad (1)$$

where C_r is the coefficient of restitution of the colliding surfaces.

C_r is either known from physical tables or can be easily determined by independent tests. For example, an optical velocity change meter can be used for this purpose, whereby

$$V_0 = \frac{\Delta V}{1 + t_1/t_2} \quad (2)$$

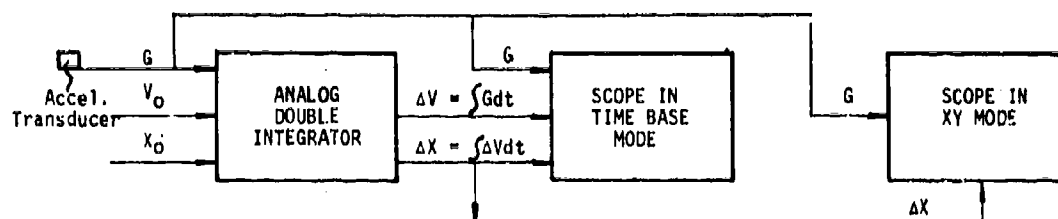
Here, t_1 and t_2 are optical velocity change meter readout times corresponding to incidence and rebound times respectively.

The oscilloscope traces in Figure 2-42 were obtained with $V_0 = 0$ setting. Note that the velocity trace does not pass through zero at the transition between incidence and rebound, consequently the displacement signal "Ramps Off". Thus, displacement cannot be measured but total velocity change is readily obtainable (about 2.2 m/sec in Figure 2-42). When $V_0 \neq 0$, the accuracy of the displacement trace will depend strongly on the exactness of the V_0 setting at the instant of collision.

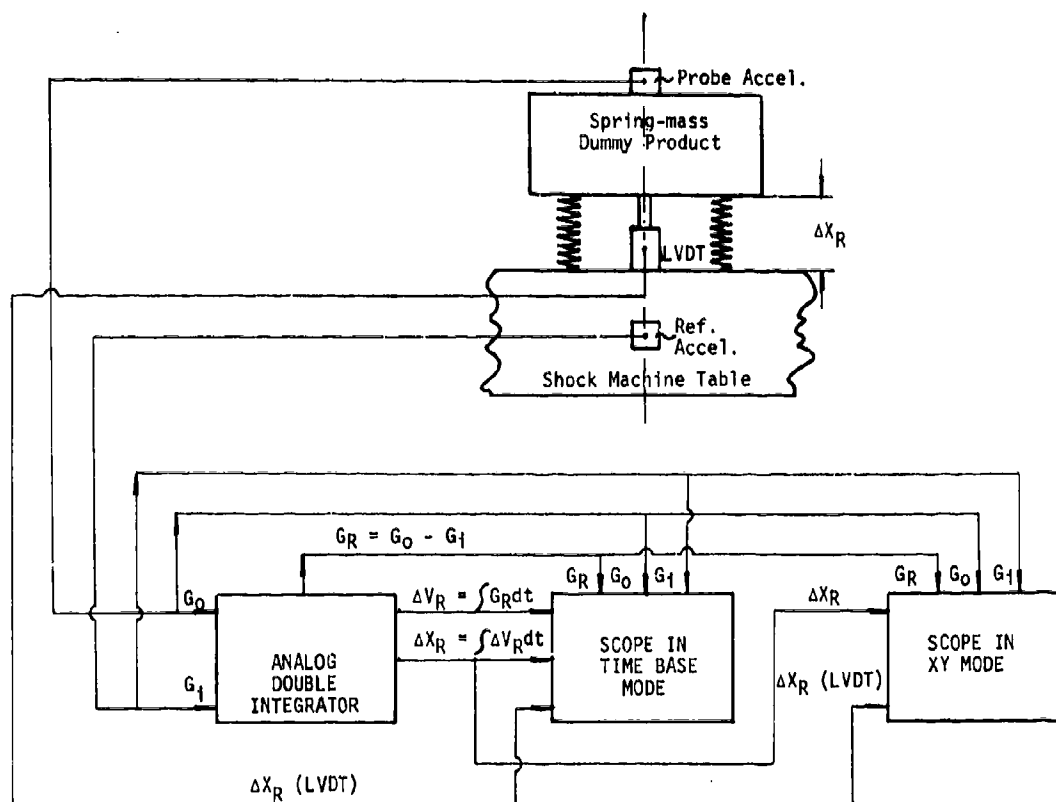
This may be facilitated by using electro-optical rather than a mechanical microswitch for triggering the A.D.I. Assuming $X_0 = 0$ at the instant of collision and given accurate estimates of V_0 , an accurate A.D.I. calculation of dynamic displacement is possible.

Figure 2-41 is an example of this mode. Retaining the same input pulse as in Figure 2-42 the total velocity change remains the same (2.2 m/sec) whereas the setting of initial velocity to $V_0 = 1.1$ m/sec results in about 5.5 mm displacement.

Oleson [5] described this mode of double integration, however, the real advantage of double integration in shock testing lies in the ability to measure relative displacement by double integrating a differential acceleration signal between two accelerometers.



a. Absolute ADI Mode



b. Relative ADI Mode

Fig. 1 - Schematics of Analog Double Integration setups.

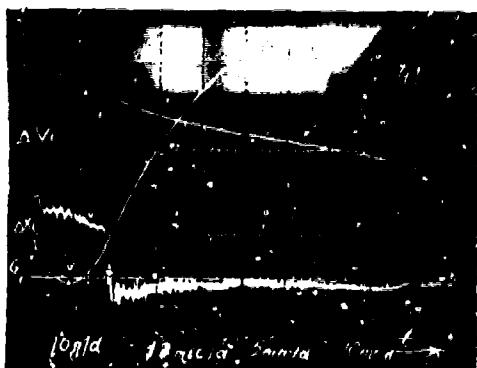


Fig. 2 - Example of absolute mode A.D.I. with initial conditions $V_0 = 0$ (42) and $V_0 = 1.1$ m/sec (41). $\Delta V_i = 2.2$ m/sec in both cases.

Relative Mode

In the relative mode there is no need to know V_0 in advance. A second accelerometer is used as a reference and acceleration differences are double integrated.

Let G_R be the relative acceleration (differential acceleration signal),

$$G_R = G_0 - G_i \quad (3)$$

where G_0 is the output of probe acceleration and G_i is the input or reference acceleration signal. A good example is shock machine testing, where G_i is the signal from an accelerometer mounted on the table while G_0 is generated by a probe accelerometer on the specimen.

The first integration, to obtain the relative velocity $V_R(t)$ is:

$$\int G_R(t) dt = V_R(t) + \text{Constant} \quad (4)$$

where the constant of integration is the initial relative velocity between specimen and table at the instant of collision. In most practical cases this can be assumed to be zero.

Thus, the relative displacement X_R is obtained simply by:

$$\int V_R(t) dt = X_R(t) + \text{Constant} \quad (5)$$

Again, the constant of integration may be assumed to be zero since the relative movement between the table of the shock machine and specimen prior to collision is negligible compared to the displacement during the shock.

Figure 1b is a schematic of the relative mode setup for A.D.I. Note that the LVDT (Linear Variable Displacement Transformer) is not required for A.D.I. calculations. It was used in our experimental setup for estimation of A.D.I. displacement error by comparing A.D.I. and LVDT results.

The oscilloscope traces in Figure 3-13, 19, 37 are examples of shock machine tests of the same specimen with elastomer, plastic, and gas cylinder programmers respectively. Note the relationship between the three signals G_i , G_0 and G_R . It can be seen that G_0 changes sign during the input pulse period. That is, the specimen is accelerated in relation to the table at the beginning of the shock and decelerated at the end of the shock.

The oscilloscope traces in Figure 3-14, 20, 38 are examples of double integration of the corresponding G_R signals in Figure 3-13, 19, 37 respectively. For comparison, simultaneous traces of ΔX_R by the LVDT are shown together with the A.D.I. traces. Note that only the first "half cycle" represents the "shock", while the traces following the first half cycle represent residual reciprocating motion of the specimen following the shock. These can be used for calculating the logarithmic decrement of the system, i.e. the damping characteristics.

DYNAMIC FORCE DEFLECTION CURVES

The dynamic force acting on the specimen during a shock can be approximated for most typical specimens as G_0 times the mass of the specimen. Thus, plots of G_0 versus ΔX_R are essentially dynamic force deformation curves of the specimen during the shock. Such curves are very useful in materials testing where measurement of resistance to transient loading is desired.

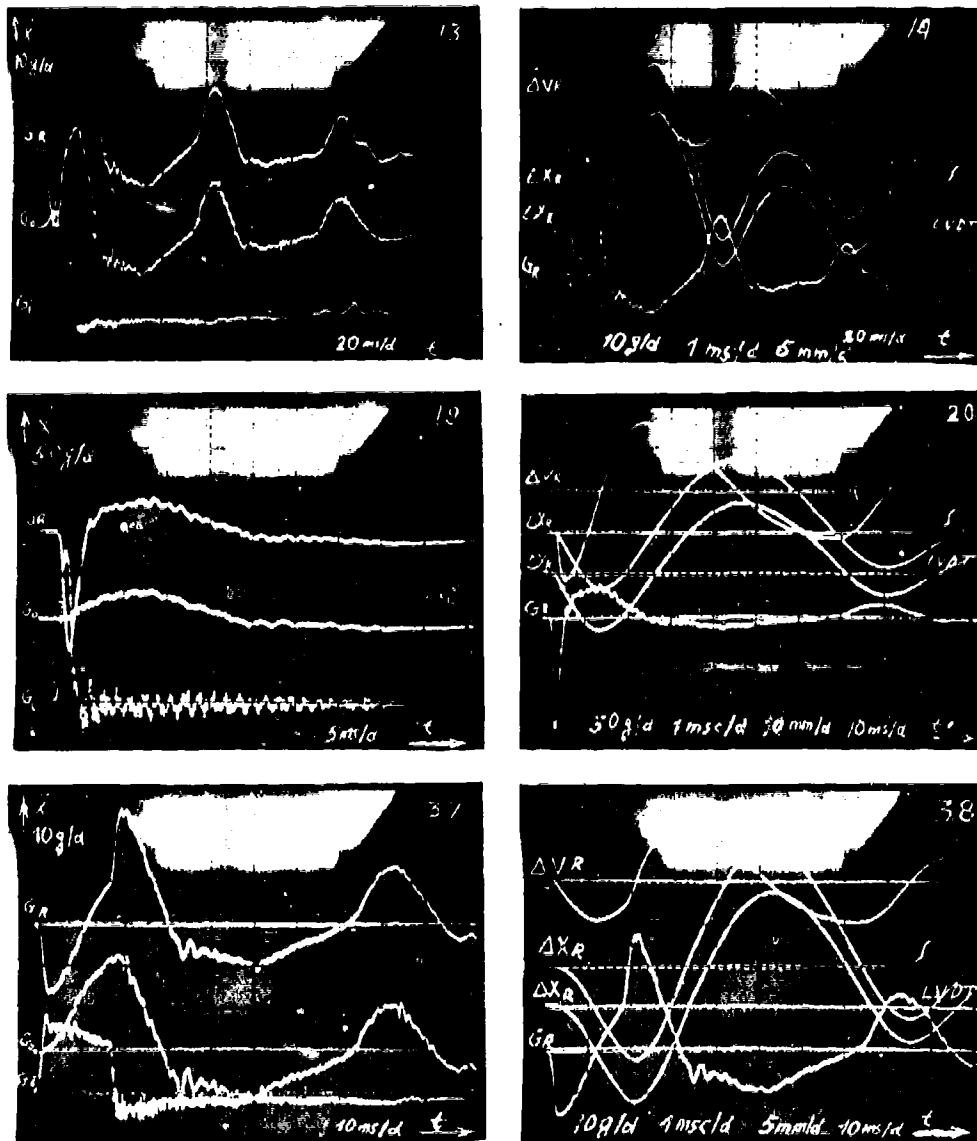


Fig. 3 - Traces of accelerometer signals for elastomer, plastic and gas cylinder programmers (13, 19, 37 respectively). Corresponding velocity changes and relative displacements obtained by A.D.I. (14, 20, 38 respectively).

The oscilloscope traces on the left side of Figure 4-10, 21, 39 are G_0 versus ΔX_R plots of the three example input pulses in Figure 3 respectively, while the right side curves were obtained by plotting G_0 versus the LVDT signal for comparison. These curves are actually dynamic hysteresis loops, with the outer loop representing the first cycle (shock pulse) while the consecutive inner loops represent residual reciprocating specimen motion following the shock.

Also, the area enclosed by the loops represents the energy dissipated by the specimen during the test. The portion of the area enclosed in the loops to the left of the G_0 axis represents the energy dissipated by the specimen during incidence (compression of specimen) while the area to the right of the G_0 axis represents the energy dissipated during rebound (expansion of the specimen).

It is interesting to observe that the relatively long square (trapezoidal) input pulse of about 13 g (Figure 3-37) produced similar response to the 24 g haversine pulse (Figure 3-13). This can be seen by comparing the shape and size of the loops in Figure 4-10 to those of Figure 4-39.

Also, the response of the specimen to the short duration 170 g peak pulse of Figure 3-19 is only slightly greater than the previous (compare Figure 4-21 to Figure 4-10, 39). This demonstrates, in a very simple way, the relative role of peak acceleration, pulse shape and duration in shock testing [1,3].

In addition to G_0 versus ΔX_R plots, the A.D.I. affords plotting of any two signals out of the group - G_i , G_0 , G_R , ΔV_R , ΔX_R , ΔX_i - against each other. Of practical interest are G_i versus ΔX_i and G_R versus ΔX_R plots. The traces in Figure 5-16, 24, 43 are examples of the former while the traces in Figure 4-11, 22, 40 are examples of the latter for the three example input pulses of Figure 3.

G_i versus ΔX_i plots may be considered as shock machine "programmer signatures". Compare the gradual deflection and rebound of the elastomer programmer (Figure 5-16) creating a half-sine pulse to the "spike" force deflection curve of plastic programmers (virtually no deflection - Figure 5-24) to a gas cylinder programmer (Figure 5-43) reaching maximum force at almost zero deflection then keeping up the maximum force throughout its deflection followed by sudden rebound. "Programmer signature" curves are useful in optimal programmer design.

The traces in Figure 4-11, 22, 40 are traces of G_R versus ΔX_R for the three example input pulses in Figure 3 as before. Since $G_R = G_0 - G_i$, the G_R versus ΔX_R plots are affected by both G_i and G_0 . The input pulse tends to be of short duration relative to the specimen response. Consequently, G_R is dominated initially by $-G_i$ and therefore shows the

$-G_i$ pulse. After completion of the G_i pulse the trace becomes G_0 versus ΔX_R and therefore also shows the dynamic hysteresis loops.

ACCURACY OF A.D.I.

The inherent difficulty in double integration of shock pulses is that the integrator gains must be very high in order to provide useable scaling on displacement. Gains of 245 volts per sec. per volt for the first integrator and 400 volts per sec. per volt for the second integrator were used in this work. This provides a net gain of 98000 through the two integrators. As a result, displacement error builds up at a rate of $0.049t^2$ times the DC offset in the first integrator.

This effect is minimized by use of an automatic balancing circuit to correct DC offset, and a trigger mechanism to initiate integration at the instant the shock table contacts the programmer. Additional sources of error in A.D.I. applications are:

1. Poor matching of reference and probe accelerometers in the relative mode.
2. Inaccurate triggering and electrical trigger noise.
3. Friction noise in guide posts and bearings of a shock machine.
4. Electronics components sensitivity to temperature and other environmental changes.
5. Due to filtering effects which may be introduced by the accelerometers and conditioners, there may be a small phase error between the real acceleration time history and the accelerometer signal used for the integration with the accelerometer signal having a phase lead at low frequencies with respect to the real acceleration.
6. Slight displacement amplitude errors can be introduced due to A.D.I. scaling errors or accelerometer conditioner loading by the A.D.I. circuit.

All of these errors can be reduced to acceptable values by accurate matching of accelerometers, photoelectric triggering, proper cable shielding and high quality electronics. Friction noise, filtering effects and A.D.I. scaling errors can be reduced by suitable pre-calibration.

Velocity Change Accuracy

Throughout the tests, velocity change from an optical velocity change meter were compared with integrator results. The table below shows some representative results for 12 inches

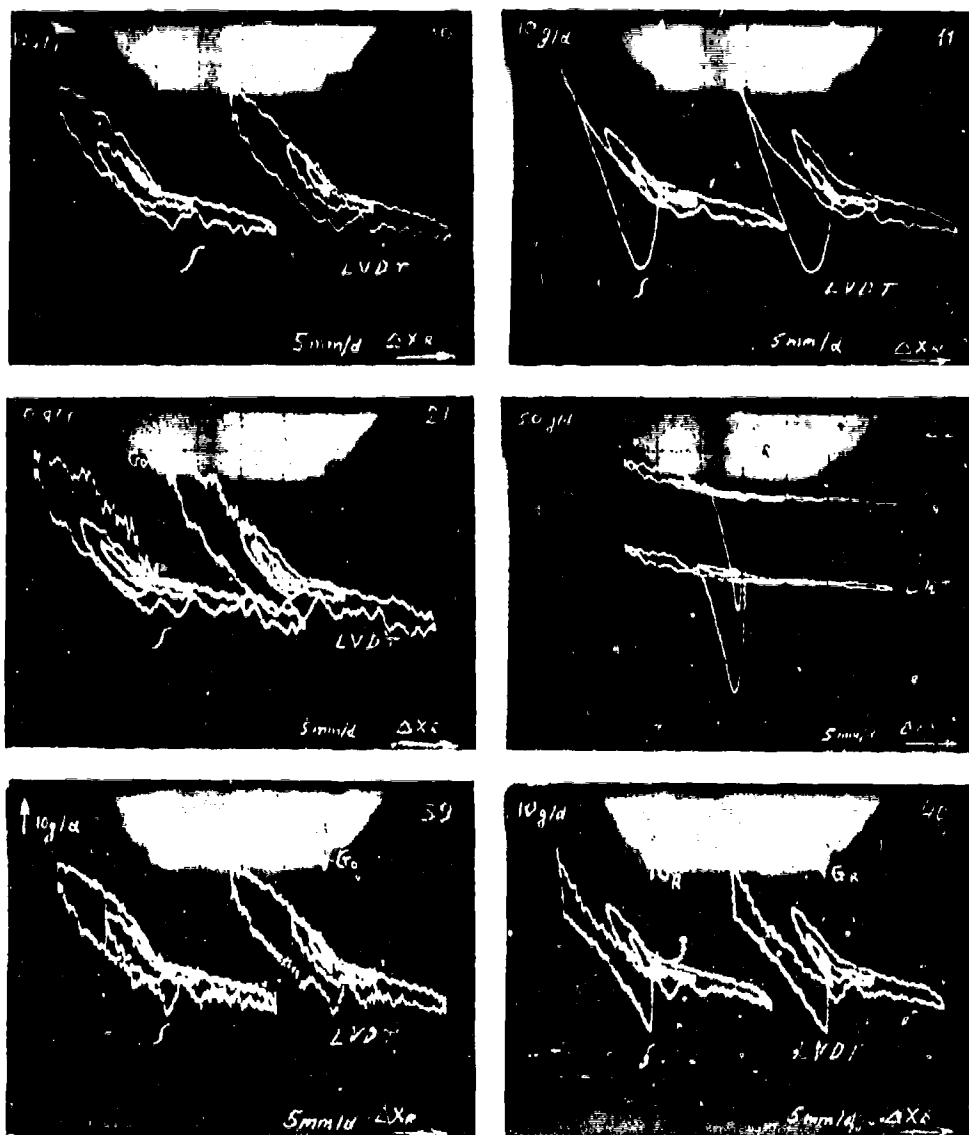


Fig. 4 - Hysteresis loops of the same specimen subjected to the three different shock pulses (10, 21, 39 respectively). Corresponding "specimen signatures" (11, 22, 40 respectively).

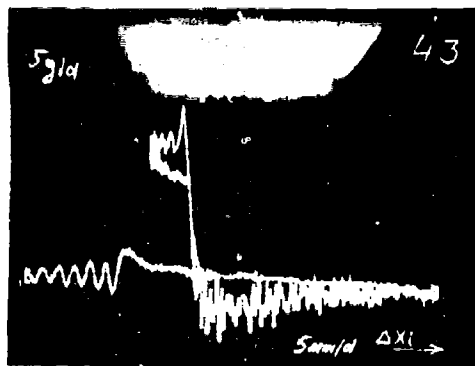
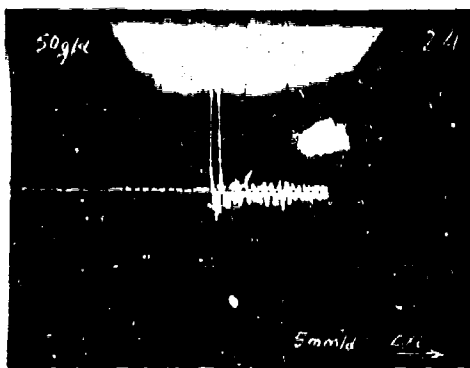
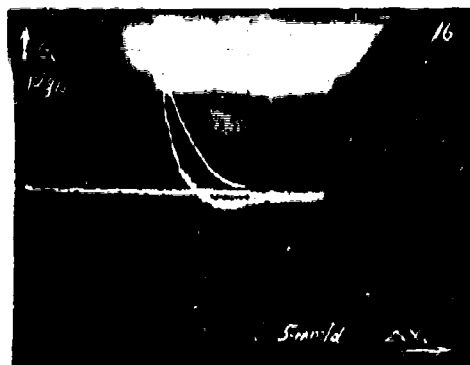


Fig. 5 - Elastomer, plastic and gas cylinder "programmer signatures" (16, 24, 43 respectively).

effective drop height with plastic programmers.

ΔV_i Optical m/sec	ΔV_i Integrated m/sec
1.92	2.00
1.96	1.95
1.96	1.90
2.05	2.10
2.11	2.20

It can be seen that the agreement is quite good.

Absolute Displacement Accuracy

Theoretical displacement of shock machine programmers were calculated using the following formula:

$$\text{Half sine pulses: } \Delta X = 3.898 \times 10^{-5} \times \text{ACC} \times t^2$$

$$\text{Square pulses: } \Delta X = 4.83 \times 10^{-5} \times \text{ACC} \times t^2$$

where ACC is in g, t in ms, and ΔX in inches.

The table below compares some of the theoretically calculated values to the integration results: (12 inches effective drop height)

	ΔX_i Theoretical mm	ΔX_i Integrated mm
Plastic Programmers	0.928	1.25
Elastomer Programmers	13.1	13.0
Gas Programmers (100 psi)	7.28	7.55

Again, the agreement seems to be quite good.

Relative Displacement Accuracy

Throughout the tests, relative displacement readings obtained by A.D.I. were compared with those of the LVDT.

Visual inspection of the ΔX_R traces generated by the LVDT, versus ΔX_R traces obtained by A.D.I., reveals good agreement up to about 100 ms time histories (Figure 4 and Figure 3-14, 20, 38). Note that comparing LVDT and A.D.I. results involves an inherent error due to the phase shift effect as mentioned earlier. This effect will tend to reduce the area enclosed within the A.D.I. hysteresis loop. On the other hand, the phase as measured by an LVDT will tend to lag the true phase angle between the real acceleration and displacement. Thus, the

area within the LVDT hysteresis loop will be slightly increased in comparison to the true value.

Consequently, it appears that A.D.I. results do not carry larger errors of velocity change and displacement than conventional optical velocity change meters or LVDT's.

CONCLUSION

The feasibility and some application possibilities of A.D.I. were demonstrated and the accuracy was shown to be adequate for processing time histories of up to 100 ms. These results were obtained with a small commercial analog computer. The use of better electronic circuit design would result in superior accuracy and dependability. Nevertheless, the results achieved in the study are comparable to those obtained by conventional optical velocity change meters and LVDT's. The flexibility afforded by measuring velocity and relative displacement from accelerometer signals, rather than cumbersome fixturing of velocity meters or LVDT's, renders A.D.I. a powerful tool in shock testing.

The economics are also favorable since the additional cost for A.D.I. electronics are largely offset by the elimination of velocity change meters, LVDT's, conditioners and displays.

NOTATION

Sign convention for all values: Up \oplus Down \ominus

- G_i - Input acceleration (shock machine acceleration) - g.
- G_o - Output acceleration (product component acceleration) - g.
- G_R - Relative acceleration (product versus shock machine acceleration) - g.
- ΔV_i - Input velocity change (shock machine table versus machine base) m/sec.
- ΔV_o - Output velocity change (product versus machine base) m/sec.
- ΔV_R - Relative velocity change (product versus shock machine table, product component versus product, etc.) m/sec.
- V_o - Initial velocity for integration (ideally $V_o - V_i$) m/sec.
- ΔX_i - Absolute displacement of input accelerometer (deflection of programmers) mm.
- ΔX_o - Absolute displacement of output accelerometer (displacement of product versus machine base) mm.

ΔX_R - Relative displacement (product versus shock machine table) mm.

t_1, t_2 - Optical ΔV meter readouts, ms.

t - time msec.

C_r - Coefficient of restitution.

LVDT - Linear Variable Differential Transducer (displacement transducer).

REFERENCES

1. Newton, R. E., Fragility Assessment: Theory and Test Procedure, Naval Postgraduate School, Monterey, CA, 1968.
2. Kelly, R. D. and G. Richman, "Principles and Techniques of Shock Data Analysis", SMV-5, Shock and Vibration Center, U.S. Dept. of Defense, Ch. 7, 1969.
3. Kipp, W. I., "Impact with Rebound; An Advanced Tool for Laboratory Crash Simulation", Compendium International Automobile Safety Conference, pp. 886-875, 1970.
4. Baird, T. W. and R. L. Kuhn, "Shock Machine Testing: New Methods of Measuring Velocity Change", Package Development and Systems, pp. 19-21, July/August 1977.
5. Oleson, M. W., "Integration and Double Integration: A Practical Technique", Shock and Vibration Bulletin 35 Part 4, February 1966.